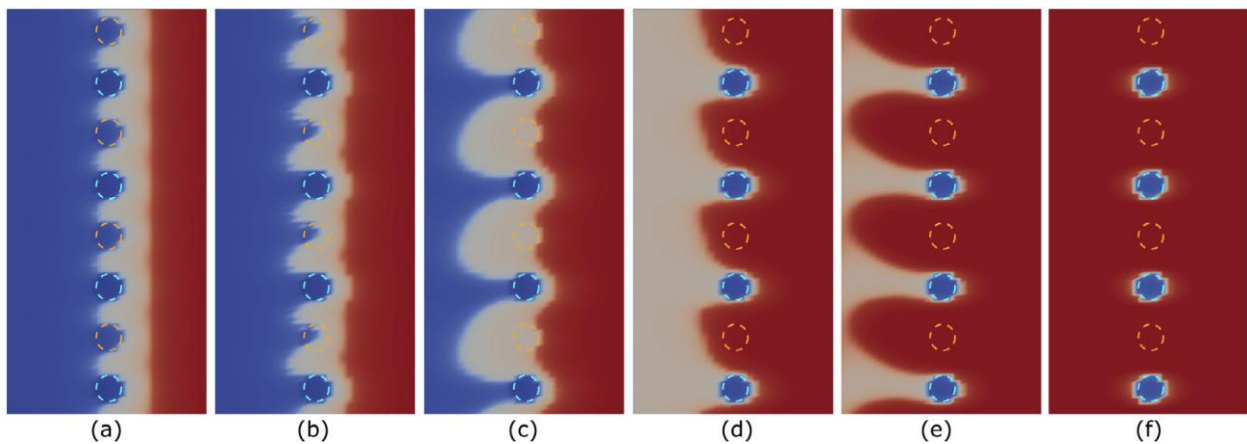
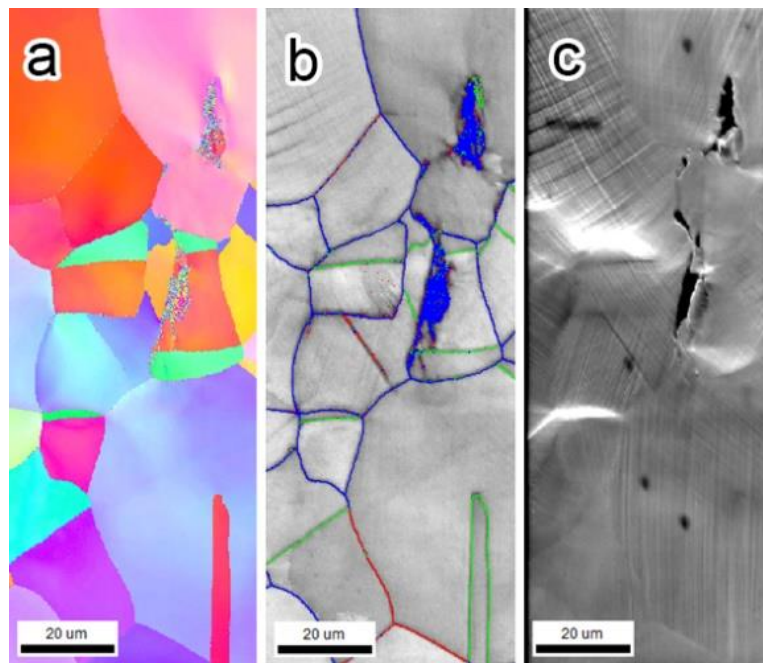


Mechanical Behavior and Radiation Effects 2022 Principal Investigators' Meeting

November 2–3, 2022



U.S. DEPARTMENT OF
ENERGY

Office of
Science

Materials Sciences and Engineering Division
Office of Basic Energy Sciences

Cover

Top: EBSD characterization of a fatigue crack. (a) IPF map; (b) IQ map with grain character labelled (blue $> 15^\circ$ rotation, red $< 15^\circ$, green twin boundary); (c) Secondary electron image of the same region. (Kacher, Georgia Tech)

Bottom: Snapshots of selected configurations for an edge dislocation bypassing four FCC $\text{Cu}_{0.8}\text{Nb}_{0.2}$ precipitates (cyan circles) and four amorphous precipitates (orange circles) in a Cu matrix. The applied stress is constant and is slightly higher than the critical stress for a dislocation to overcome the array of obstacles. Snapshots are colored by the disregistry field along the x direction, ξ_x , where blue and red correspond to $\xi_x = 0$ and b , respectively. The light brown region is the intrinsic stacking fault between two Shockley partial dislocations. (Mara and Beyerlein, University of Minnesota and UCSB)

Foreword

This volume comprises the scientific content of the 2022 Mechanical Behavior and Radiation Effects Principal Investigators' (PI) Meeting sponsored by the Division of Materials Sciences and Engineering (DMS&E) in the Office of Basic Energy Sciences (BES) of the U.S. Department of Energy (DOE). The meeting, held on November 2–3 virtually through Zoom and GatherTown, is the eighth such meeting on this topic and is one among a series of research theme-based PI Meetings being held by DMS&E. The meeting's focus is on research in mechanical behavior and radiation effects of materials, and it also features research that cuts across several other BES core research program areas and Energy Frontier Research Centers where appropriate and relevant.

The studies of mechanical behavior and radiation effects have a long and important history with respect to the generation, transmission, utilization and conservation of energy. It is a tribute to the researchers that they have continued to move the field forward into a number of important areas, as can be seen by the diversity of projects being presented at this meeting. Attendees will note a number of new projects and research directions since the previous meeting, including several recipients of Early Career Research Program awards. These new projects add to the exciting areas of research and cutting-edge techniques that are a hallmark of this program.

The purpose of the Mechanical Behavior and Radiation Effects PI Meeting is to bring together researchers funded by DMS&E in this important area of research on a periodic basis (approximately every two years, though due to the pandemic, it has been three years since the last one) in order to facilitate the exchange of new results and research highlights, to nucleate new ideas and collaborations among the participants, and to identify needs of the research community. The meeting will also help DMS&E in assessing the state of the program, identifying new research directions and recognizing programmatic needs.

I would like to express my sincere thanks to all of the attendees for their active participation and for sharing their ideas and new research results. Of special note, I have greatly appreciated the help of Dr. Saryu Fensin from LANL, who is helping me as a detail to my program and helped tremendously with this meeting. I would also like to express my sincere gratitude to Ms. Teresa Crockett in DMS&E, and Ms. Tia Moua (plus others) of the Oak Ridge Institute for Science and Education (ORISE) for their dedicated and outstanding work in taking care of all the logistical aspects of the meeting, including running the Zoom and GatherTown systems.

John Vetrano
Program Manager
Mechanical Behavior and Radiation Effects
Division of Materials Sciences and Engineering
Office of Basic Energy Sciences
U.S. Department of Energy

Table of Contents

Foreword	i
Agenda	ix
Poster Sessions	xv
 Abstracts	
<i>Stacking Fault Energy and Elastic Constants in Multi-principal Elemental Alloys</i> Dilpuneet Aidhy	3
<i>Establishing Defect-Property Relationships for 2D-Materials[†]</i> Assel Aitkaliyeva	7
<i>Center for PRedictive Integrated Structural Materials Science – PRISMS Center</i> John Allison, A. Bucsek, V. Gavini, A. Misra, B. Puchala, L. Qi, V. Sundararaghavan, K. Thornton, and A. Van der Ven	9
<i>Understanding Multiscale Defect Formation Process and Domain Switching Behavior in Shape Memory Functional Oxides</i> Mohsen Asle Zaeem	14
<i>Global Aspects of Microstructural Evolution in Irradiated Alloys: Effects of Self-Organization</i> Pascal Bellon, Robert S. Averback, and Shen J. Dillon	19
<i>Role of Subgrain Heterogeneous Processes in Slip Localization in Polycrystalline Metals During Cyclic Plasticity</i> Irene J. Beyerlein, Tresa M. Pollock, M. P. Miller	24
<i>Nanomechanics and Nanometallurgy of Boundaries</i> Brad L. Boyce, Khalid Hattar, Doug Medlin, and Remi Dingreville	29
<i>Effect of Heterogeneous Architectures on the Mechanical Behavior of Metallic Glasses</i> Paulo Branicio	34
<i>Beyond Shear: Improving the Prediction of Plastic Deformation Activation in HCP Materials*</i> Ashley Bucsek and Huseyin Sehitoglu	39

[†] Early Career Project

* Newly funded in 2022

<i>Elucidating the Influence of Bulk Slip Morphology on Hydrogen Environment-Assisted Cracking Behavior in Precipitation-Hardened Alloys*</i> James T. Burns	44
<i>Data Driven Approach to Dislocation-Based Plasticity Models of Face-Centered Cubic Metals</i> Wei Cai	47
<i>The Role of Local Chemical Order on Defect Kinetics in Alloys under Irradiation[†]</i> Penghui Cao	52
<i>Twinning and Phase Transformations in Hexagonal Close Packed Metals: Network Formation Process and Effects on Plastic Response</i> Laurent Capolungo, K. Q. Dang, A. Kumar, R. J. McCabe, and C. Tome	56
<i>Understanding the Effect of Stress on Complexion Transitions and the Interplay with Creep in Thermally Stabilized Nanocrystalline Materials*</i> Maarten P. de Boer, Gregory S. Rohrer, and Elizabeth C. Dickey	61
<i>Improving Radiation Response of Solid State Interfaces via Control of Curvature</i> Michael J. Demkowicz and Kelvin Y. Xie	64
<i>Coupled Effects of Stress and Hydrogen on Stress Corrosion Cracking of Fe-based Alloys[†]</i> Arun Devaraj	69
<i>Understanding the Mechanics of Reverse Phase Transformation and Detwinning in BCC*</i> Avinash M. Dongare	74
<i>Fundamental Insights into Defect Generation and Transport Phenomena at Grain Boundaries in Advanced Nuclear Fuel Candidates*</i> S. Finkeldei, S. Dillon, J. White, M. Cooper, and D. Andersson	76
<i>The Role of Anisotropy on the Self-Organization of Gas Bubble Superlattice</i> J. Gan, C. Sun, C. Jiang, A. Jokisaari, L. Aagesen, E. Jossou, S. Gill, A. Schneider, and Y. Zhang	80
<i>Insight into the Stability and Deformation Processes of “High Entropy” Alloys with bcc/B2-type Microstructure</i> Maryam Ghazisaeidi and Michael J. Mills	86
<i>Kinetically-driven Microstructure as a Governing Factor in Enhanced Mechanical Properties of Hydrogel Infusion Additive Manufacturing (HIAM)-produced Metals</i> Julia R. Greer	90

[†] Early Career Project
* Newly funded in 2022

<i>Towards Ductile, Nanostructured Metallic Glasses</i> [†] Wendy Gu	93
<i>Elucidating the Mechanical and Thermal Response of Nanotwinned Ni Alloys</i> Kevin J. Hemker	96
<i>Computational and Experimental Investigation of Cryogenic Grain Boundary Motion for Enhanced Mechanical Properties</i> Eric R. Homer and Gregory B. Thompson	101
<i>Understanding the Role of Surface Energy in the Deformation of Metal Nanoparticles</i> Tevis D. B. Jacobs and Ashlie Martini	106
<i>Fundamental Study of Fatigue Crack Initiation at Grain and Twin Boundaries in Austenitic Stainless Steel</i> [†] Josh Kacher	111
<i>Fundamental Mechanisms of Newtonian Viscous Creep in Structural Alloys</i> ^{*†} Boopathy Kombaiiah	116
<i>Elucidating Grain Growth in Thermo-Magnetic Processed Materials by Transfer Learning and Reinforcement Learning</i> Amanda R. Krause, Michael R. Tonks, Joel P. Harley, and Michael S. Kesler	118
<i>Far-From-Equilibrium Processing of Materials under Extreme Conditions</i> Maik Kurt Lang	123
<i>Mechanical Properties of Metals at the Micrometer Scale in Different Environments</i> Seok-Woo Lee	127
<i>The Role of Strain Localization at Interfaces on Fatigue Crack Initiation in Highly Textured Magnesium Alloys</i> ^{*†} Aeriel D. M. Leonard	131
<i>Fatigue Crack Initiation and Growth in Ultrafine-Grained Magnesium Deformed at Subfreezing Environmental Temperatures</i> Qizhen Li	132
<i>Influence of 3D Heterophase Interface Structure on Deformation Physics</i> N. A. Mara and I. J. Beyerlein	137
<i>Chemical Partitioning and Radiation Damage in Concentrated Alloys</i> [*] Emmanuelle Marquis, Fadi Abdeljawad, Enrique Martinez, and Suveen Mathaudhu	142

† Early Career Project

* Newly funded in 2022

<i>Taming Martensitic Transformations by Defect Engineering</i> Michael J. Mills, Yunzhi Wang, and Peter M. Anderson	144
<i>Metal-Ceramic Interfaces at High Temperatures*</i> Yuri Mishin	149
<i>Plasticity of High-Strength Multiphase Metallic Composites</i> Amit Misra and Jian Wang	152
<i>Determining the Rate-Controlling, Grain-Boundary-Mediated Mechanisms in Ultrafine Grained Au Films</i> Olivier Pierron, Josh Kacher, and Ting Zhu	157
<i>NanoMechanics: Elasticity and Friction of Nano-Objects</i> Elisa Riedo	162
<i>Damage-Tolerance in Structural Materials</i> Robert O. Ritchie, Mark Asta, and Andrew M. Minor	167
<i>Improving Interfacial Damage Tolerance with Amorphous Complexion Transitions</i> Timothy J. Rupert	172
<i>Segregation and Shear Localization in Nanocrystalline Alloys</i> Frederic Sansoz	177
<i>Crack Tip Mechanisms Driving Environmental Degradation</i> D. K. Schreiber, C. Wang, M. J. Olszta, K. Kruska, M. L. Sushko, and K. M. Rosso	182
<i>Discovery and Design of Stable Nanocrystalline Alloys: The Grain Boundary Segregation Genome</i> Christopher A. Schuh	187
<i>New Experimental Views on the Role of Temperature in Extreme Strain Rate Mechanics</i> Christopher A. Schuh and Keith A. Nelson	192
<i>Radiation Response of Low Dimensional Carbon Systems</i> Lin Shao	196
<i>Toughening Mechanisms in Ceramic Nanocomposite</i> Brian W. Sheldon, Jun Lou, Huajian Gao, and Nitin Padture	201
<i>Dynamic Fracture in Dealloying Induced Stress-Corrosion Cracking</i> Karl Sieradzki	206

† Early Career Project

* Newly funded in 2022

<i>Micromechanics of Migrating Interfaces: Martensitic Transformations</i> Ryan Sills	208
<i>Localizing Energy Dissipation in Molecular Dynamics Simulations of Nanostructured Elastomers</i> David S. Simmons	212
<i>Role of Nanoscale Coherent Precipitates on the Thermo-mechanical Response of Martensitic Materials</i> Alejandro Strachan and Michael Titus	216
<i>Radiation Effects and Corrosion in Carbides and Borides</i> Izabela Szlufarska	220
<i>Grain Boundary Microstates: Exploring the Metastability of Sink Efficiency</i> Mitra Taheri, Michael Falk, Jaime Marian, and David Srolovitz	225
<i>Irradiation Defect Formation and Evolution in Doped Metallic Interfaces</i> Jason R. Trelewicz, Andrea M. Hodge, and David J. Sprouster	230
<i>Disorder & Diffusion in Complex Oxides: Towards Prediction & Control</i> Matthew Janish, Cortney Kreller, Ghanshyam Pilania, Yongqiang Wang and Blas Pedro Uberuaga	234
<i>Understanding the Competition between Plastic Flow and Fracture in BCC Transition Metals</i> Christopher R. Weinberger and Gregory B. Thompson	239
<i>Irradiation Tailoring of Deformation-Induced Phase Transformations[†]</i> Janelle P. Wharry	242
<i>Mesoscale Defect Interaction Mechanisms in Structural Alloys[†]</i> Haixuan Xu	247
<i>Deformation Mechanisms of Nanotwinned Al and Binary Al Alloys</i> Xinghang Zhang and Jian Wang	252
Author Index	257
Participant List	261

† Early Career Project
* Newly funded in 2022

**Mechanical Behavior and Radiation Effects
Principal Investigators' Meeting Agenda**

Wednesday, November 2, 2022

11:00 – 11:10 am *Introductory Remarks and Program Overview*
John Vetrano

Session I Chairs: **Mitra Taheri (Johns Hopkins University) and
Ryan Sills (Rutgers University)**

11:10 – 11:25 am **Rob Ritchie – LBNL**
Damage-Tolerance of Structural Materials

11:25 – 11:40 am **Wendy Gu – Stanford University**
Deformation of Nano-Metallic Glasses Made using Colloidal Synthesis

11:40 – 11:55 am **Tim Rupert – University of California, Irvine**
*Microstructure-within-a-Microstructure: Uncovering Fundamental Scaling
Laws Connecting Complex Network Descriptors to Damage Tolerance*

11:55 – 12:10 pm **Eric Homer – Brigham Young University**
*Computational and Experimental Investigation of Cryogenic Grain Boundary
Motion for Enhanced Mechanical Properties*

12:10 – 12:13 pm **Xinghang Zhang – Purdue University**
Deformation Mechanisms of Nanotwinned Al and Al Alloys

12:13 – 12:16 pm **Wei Cai – Stanford University**
*Data Driven Approach to Dislocation-Based Plasticity Models of Face-
Centered Cubic Metals*

12:16 – 12:19 pm **Amit Misra – University of Michigan**
Plasticity of High-Strength Multiphase Metallic Composites

12:19 – 12:22 pm **Karl Sieradzki – Arizona State University**
Dynamic Fracture in Dealloying Induced Stress Corrosion Cracking

12:22 – 12:25 pm **Avinash Dongare – University of Connecticut**
*Understanding the Mechanics of Reverse Phase Transformation and
Detwinning in BCC Metal Microstructures*

12:25 – 12:28 pm **Laurent Capolungo – LANL**
*Multi-Scale Study of the Role of Microstructure in the Deformation Behavior of
Hexagonal Materials*

- 12:28 – 12:43 pm **Chris Schuh – MIT**
Discovery and Design of Stable Nanocrystalline Alloys: The Grain Boundary Segregation Genome
- 12:43 – 12:58 pm **Seok-Woo Lee – University of Connecticut**
Mechanical Properties of Metals at the Micrometer Scale in Different Environments
- 1:00 – 1:30 pm **BREAK**
- Session II** Chair: **Remi Dingreville (Sandia National Laboratories)**
- 1:30 – 1:45 pm **Dan Schreiber – PNNL**
Crack-Tip Mechanisms Driving Environmental Degradation
- 1:45 – 2:00 pm **Amanda Krause – Carnegie Mellon University**
Elucidating Grain Growth in Thermo-Magnetic Processed Materials by Transfer Learning and Reinforcement Learning
- 2:00 – 2:03 pm **Paulo Branicio – University of Southern California**
Effect of Gradient Architectures on the Strength, Deformation and Failure of Nanoglasses
- 2:03 – 2:06 pm **Yuri Mishin – George Mason University**
Metal-Ceramic Interfaces at High Temperatures
- 2:06 – 2:09 pm **Jimmy Burns – University of Virginia**
Elucidating the Influence of Bulk Slip Morphology on Hydrogen Environment-Assisted Cracking Behavior in Precipitation-Hardened Alloys
- 2:09 – 2:12 pm **Irene Beyerlein – University of California, Santa Barbara**
The Role of Subgrain Heterogeneous Processes in Slip Localization in Polycrystalline Metals During Cyclic Plasticity
- 2:12 – 2:15 pm **Mohsen Asle Zaeem – Colorado School of Mines**
Understanding Multiscale Defect Formation Process and Phase-Switching Behavior in Shape Memory Functional Oxides
- 2:15 – 2:18 pm **Kevin Hemker – Johns Hopkins University**
Elucidating the Mechanical and Thermal Response of Nanotwinned Ni Alloys
- 2:18 – 2:21 pm **Tevis Jacobs – University of Pittsburgh**
Understanding the Role of Surface Energy in the Deformation of Metal Nanoparticles
- 2:21 – 2:50 pm **BREAK**

2:50 – 3:05 pm **Maryam Ghazisaeidi – The Ohio State University**
Mechanisms of Deformation and Slip Transmission in Two Phase BCC/B2 Refractory High Entropy Alloys

3:05 – 3:20 pm **David Simmons – University of South Florida**
Nanoscale Origins of Nonlinear Energy Dissipation and Toughness in Elastomeric Nanocomposites

3:20 – 3:35 pm **Izabela Szlufarska – University of Wisconsin, Madison**
Radiation Effects in Carbides and Borides

Poster Session I Chair: **Saryu Fensin (Los Alamos National Laboratory)**

Poster session introductions:

3:36 – 3:37 pm **Ryan Sills – Rutgers University**
Micromechanics of Migrating Interfaces: Martensitic Transformations

3:37 – 3:38 pm **Josh Kacher – Georgia Tech**
Fundamental Study of Fatigue Crack Initiation at Grain Boundaries in Austenitic Stainless Steel

3:38 – 3:39 pm **Blas Uberuaga – LANL**
Disorder and Diffusion in Complex Oxides: Towards Prediction and Control

3:39 – 3:40 pm **Boopathy Kombaiah – INL**
Fundamental Mechanisms of Newtonian Diffusional Creep in Structural Alloys

3:40 – 3:41 pm **Aeriel Leonard – The Ohio State University**
The Role of Strain Localization at Interfaces on Fatigue Crack Initiation in Highly Textured Magnesium Alloy

3:41 – 3:42 pm **DP Aidhy – Clemson University**
Understanding Twinning and Deformation in High Entropy Alloys

3:42 – 3:43 pm **Maarten de Boer – Carnegie Mellon University**
Understanding the Effect of Stress on Complexion Transitions and the Interplay with Creep in Thermally Stabilized Nanocrystalline Materials

3:43 – 3:44 pm **Chris Weinberger – Colorado State University**
Understanding the Competition between Plastic Flow and Fracture in BCC Transition Metals

3:44 – 3:45 pm **Ashley Bucsek – University of Michigan**
Beyond Shear: Improving the Prediction of Plastic Deformation Activation in HCP Material

4:00 – 5:00 pm **Poster Session in Gathertown**

Session III	Chairs: Irene Beyerlein (University of California, Santa Barbara) and Kevin Hemker (Johns Hopkins University)
11:00 – 11:10 am	Dr. Andrew Schwartz – Director, Materials Sciences and Engineering Division, BES
11:10 – 11:25 am	Janelle Wharry – Purdue University <i>Irradiation Tailoring of Deformation-Induced Phase Transformation</i>
11:25 – 11:40 am	Nathan Mara – University of Minnesota <i>Influence of 3D Heterophase Interface Structure on Deformation Physics</i>
11:40 – 11:55 am	Brad Boyce – SNL <i>Nanomechanics and Nanometallurgy of Boundaries</i>
11:55 – 11:58 am	Qizhen Li – Washington State University <i>Fatigue Crack Initiation and Growth in Ultrafine-Grained Magnesium Deformed at Subfreezing Environmental Temperatures</i>
11:58 – 12:01 pm	Lin Shao – Texas A&M <i>Radiation Response of Low Dimensional Carbon Systems</i>
12:01 – 12:04 pm	Michael Demkowicz – Texas A&M <i>Improving Radiation Response of Solid-State Interfaces via Control of Curvature</i>
12:04 – 12:07 pm	Chris Schuh – MIT <i>Microparticle Supersonic Impact: A Testbed for the Exploration of Metals under Extreme Conditions</i>
12:10 – 12:25 pm	Mike Mills – The Ohio State University <i>Taming Martensitic Transformations by Defect Engineering</i>
12:25 – 12:40 pm	Brian Sheldon – Brown University <i>Toughening Mechanisms in Ceramic Nanocomposites</i>
12:40 – 12:55 pm	Alejandro Strachan – Purdue University <i>Role of Nanoscale Coherent Precipitates on the Thermo-Mechanical Response of Martensitic Materials</i>
12:55 – 1:25 pm	BREAK

- Session IV** Chair: **Ashlie Martini (University of California, Merced)**
- 1:25 – 1:40 pm **Jian Gan – INL**
The Role of Anisotropy on the Self-Organization of Gas Bubble Superlattices
- 1:40 – 1:55 pm **John Allison – University of Michigan**
Center for PRedictive Integrated Structural Materials Science PRISMS Center
- 1:55 – 2:10 pm **Jason Trelewicz – Stony Brook University**
Irradiation Defect Formation and Evolution in Doped Metallic Interfaces
- 2:10 – 2:13 pm **Julia Greer – California Institute of Technology**
A Fundamental Study on the Link between Mechanical Properties and Atomic-level Microstructure in Chemically-Derived, Nanocrystalline Metals
- 2:13 – 2:16 pm **Elisa Riedo – New York University**
NanoMechanics: Elasticity and Friction in Nano-Objects
- 2:16 – 2:19 pm **Mitra Taheri – Johns Hopkins University**
Grain Boundary Microstates: Exploring the Metastability of Sink Efficiency
- 2:20 – 2:35 pm **Assel Aitkaliyeva – University of Florida**
Establishing Defect-Property Relationships for 2D-Nanomaterials
- 2:35 – 2:50 pm **Pascal Bellon – University of Illinois, Urbana-Champaign**
Global Aspects of Microstructural Evolution in Irradiated Alloys: Effects of Self-Organization
- 2:50 – 3:25 pm **BREAK**
- Poster Session II** Chair: **Kelvin Xie (Texas A&M)**
- Poster session introductions:**
- 3:25 – 3:26 pm **Arun Devaraj – PNNL**
Coupled Effects of Stress and Hydrogen on Stress Corrosion Cracking of Fe-based Alloys
- 3:26 – 3:27 pm **Sarah Finkeldei – University of California, Irvine**
Advancing Clean Energy through Fundamental Insights into Defect Generation and Transport Phenomena at Grain Boundaries in Nuclear Energy Materials
- 3:27 – 3:28 pm **Penghui Cao – University of California, Irvine**
The Role of Local Chemical Order on Defect Kinetics in Alloys under Irradiation

- 3:28 – 3:29 pm **Olivier Pierron – Georgia Tech**
Fundamental Investigation of Grain Boundary Dislocation Mechanisms in Ultrafine Grained Metallic Films
- 3:29 – 3:30 pm **Frederic Sansoz – The University of Vermont**
Role of Heterogeneous Segregation on Shear Localization Mechanisms in Nanocrystalline Alloys
- 3:30 – 3:31 pm **Emmanuelle Marquis – University of Michigan**
Chemical Partitioning and Radiation Damage in Concentrated Alloys
- 3:31 – 3:32 pm **Blas Uberuaga – LANL**
FUTURE EFRC
- 3:32 – 3:33 pm **Dave Hurley – INL**
TETI EFRC
- 3:33 – 3:34 pm **Haixuan Xu – University of Tennessee, Knoxville**
Mesoscale Defect Interaction Mechanisms in Structural Alloys
- 3:45 – 5:00 pm **Poster Session in Gathertown**

Mechanical Behavior and Radiation Effects Principal Investigators' Meeting

POSTER SESSION I

Wednesday, November 2, 2022

Chair: Saryu Fensin, LANL

- 1) **Micromechanics of Migrating Interfaces: Martensitic Transformations**
Ryan Sills, Rutgers University
- 2) **Fundamental Study of Fatigue Crack Initiation at Grain Boundaries in Austenitic Stainless Steel**
Josh Kacher, Georgia Tech
- 3) **Disorder and Diffusion in Complex Oxides: Towards Prediction and Control**
Blas Uberuaga, LANL
- 4) **Fundamental Mechanisms of Newtonian Diffusional Creep in Structural Alloys**
Boopathy Kombaiah, INL
- 5) **The Role of Strain Localization at Interfaces on Fatigue Crack Initiation in Highly Textured Magnesium Alloy**
Ariel Leonard, The Ohio State University
- 6) **Understanding Twinning and Deformation in High Entropy Alloys**
DP Aidhy, Clemson University
- 7) **Understanding the Effect of Stress on Complexion Transitions and the Interplay with Creep in Thermally Stabilized Nanocrystalline Materials**
Maarten de Boer, Carnegie Mellon University
- 8) **Understanding the Competition between Plastic Flow and Fracture in BCC Transition Metals**
Chris Weinberger, Colorado State University
- 9) **Beyond Shear: Improving the Prediction of Plastic Deformation Activation in HCP Material**
Ashley Bucsek, University of Michigan

Mechanical Behavior and Radiation Effects Principal Investigators' Meeting

POSTER SESSION II Thursday, November 3, 2022 Chair: Kelvin Xie, Texas A&M

- 1) **Coupled Effects of Stress and Hydrogen on Stress Corrosion Cracking of Fe-based Alloys**
Arun Devaraj, PNNL
- 2) **Advancing Clean Energy through Fundamental Insights into Defect Generation and Transport Phenomena at Grain Boundaries in Nuclear Energy Materials**
Sarah Finkeldei, University of California, Irvine
- 3) **The Role of Local Chemical Order on Defect Kinetics in Alloys under Irradiation**
Penghui Cao, University of California, Irvine
- 4) **Fundamental Investigation of Grain Boundary Dislocation Mechanisms in Ultrafine Grained Metallic Films**
Olivier Pierron, Georgia Tech
- 5) **Role of Heterogeneous Segregation on Shear Localization Mechanisms in Nanocrystalline Alloys**
Frederic Sansoz, The University of Vermont
- 6) **Chemical Partitioning and Radiation Damage in Concentrated Alloys**
Emmanuelle Marquis, University of Michigan
- 7) **FUTURE EFRC**
Blas Uberuaga, LANL
- 8) **TETI EFRC**
Dave Hurley, INL
- 9) **Mesoscale Defect Interaction Mechanisms in Structural Alloys**
Haixuan Xu, University of Tennessee, Knoxville

Abstracts

Stacking fault energy and elastic constants in multi-principal elemental alloys

Dilpuneet Aidhy, Clemson University

Keywords: Stacking fault energy, elastic constants, density functional theory, charge density, machine learning

Research Scope

#1 Charge density and stacking fault energy in alloys: Recent experiments in multi principal element alloys (MPEAs) have observed a correlation between stacking fault energy (SFE) and alloy composition.[1] However, the guiding principles to tailor SFE via composition don't yet exist. Over the years, the SFE-composition correlation has been investigated in dilute alloys, particularly Ni. It had been postulated that the radius of the dopant is a key factor that controls SFE.[2] However, our work shows that the argument likely fails in Cu. As shown in Figure 1a and 1b, when dopants of large radii are added, while the SFE decreases in Ni, it increases in Cu. The contrast between the two matrices is shown in Figure 1c. In this project, we have elucidated that a quantified charge density explains these contrasting results.

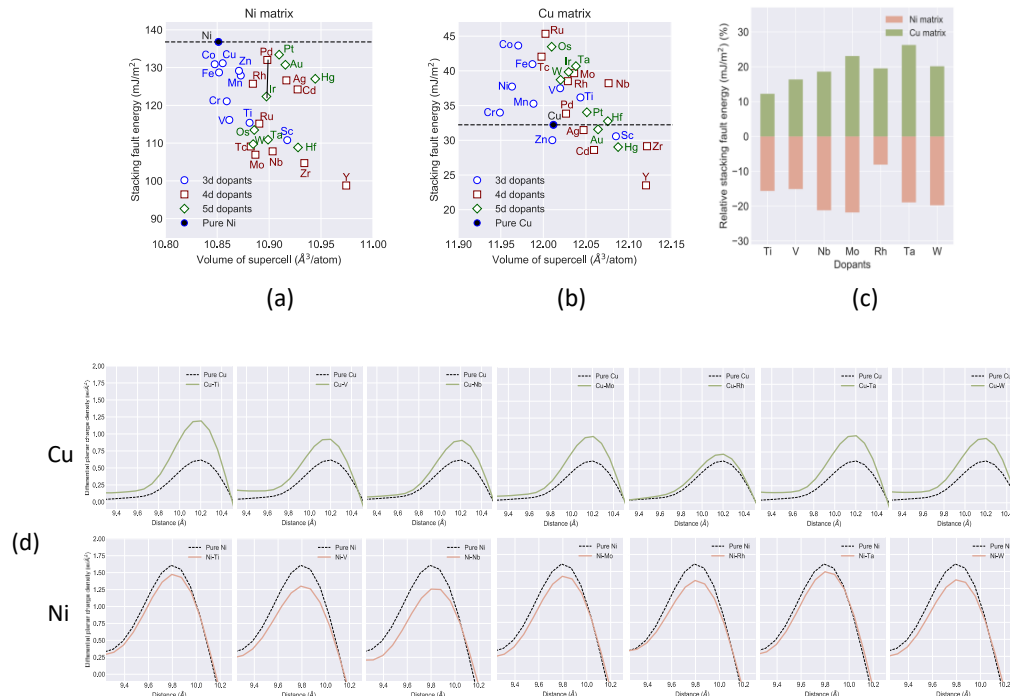


Figure 1. (a and b) SFE in Ni and Cu due to different dopants. (c) Contrasting change in SFE due to addition of same dopants in Ni and Cu. (d) Comparison of DPCD between doped and pure metals.

We find that differential planar charge density (DPCD) plays a critical role. The planar charge density (PCD) is the charge density of each plane calculated in density functional theory (DFT) whereas DPCD is the difference in the charge density before and after shearing the plane. Figure

1d shows DPCD comparisons between doped and pure Cu (upper panel), and between doped and pure Ni (lower panel) for the seven elements. It is observed that while the DPCD is consistently lower in doped-Ni than pure Ni, it is consistently higher in doped-Cu than pure Cu. A higher charge density after shearing due to the addition of the dopants makes shearing difficult and raises SFE in Cu, whereas opposite happens in Ni.

#2 ML model for SFE prediction: Based on the important role of charge density, we have developed a support vector regression (SVR) ML model to predict SFE in ‘model’ concentrated alloys as shown in Figure 2. The training data consists of binary and ternary compositions, and the predictions are made in quaternary alloys. The true and predicted SFEs are shown in the table. As observed, the model correctly predicts SFEs both quantitatively and qualitatively. For example, the lower SFEs in NiCrWV and NiScCrCo compared to higher SFEs in NiFeCrCo and NiMnCrCo are correctly predicted. Similarly, the trends within three compositions of NiFeCrCo that differ by nearest neighbor environments are also correctly predicted.

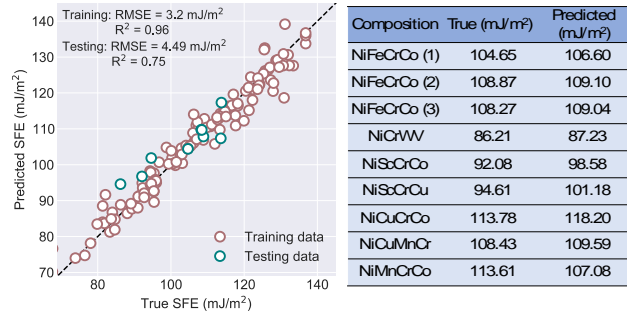


Figure 2. (a) Predicted SFE vs DFT ‘true’ SFE in quaternary alloys from ML model based on charge density of the sheared plane. (b) Comparison of SFE values in different model concentrated alloys between true DFT and ML predicted.

In ML modeling, one of the major bottlenecks is the identification of correct descriptors to predict a given property. We have developed a ML model that can bypass descriptor search. Here, we use image recognition technique where the charge density images of stacking faults are used to predict SFE. The model is based on convolutional neural network (CNN). Charge density images such as Figure 3a are used as training data. The SFE predictions in various alloys are shown in Figure 3b. A good predictive capability represented by R^2 and RMSE of 0.87 and 6.18 mJ/m² respectively is achieved. The model learns and recognizes the patterns of charge density images and predicts SFEs of complex alloys.

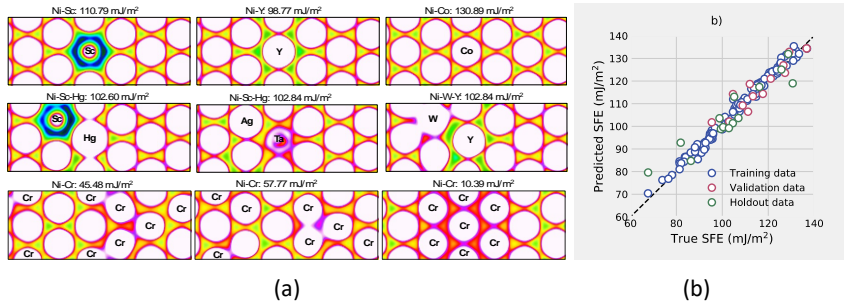


Figure 3. (a) Examples of charge density images used to train image recognition ML model to predict SFE. (b) ML predicted SFE from image recognition method.

#3 Bond stiffness and elastic constants in MPEAs: The stiffness of a bond is analogous to bond strength. In our previous work, we had observed that stiffness of a A-B simply depends on the bond length, i.e., larger bond length indicated lower bond stiffness.[3, 4] We had further found that bond stiffness is independent of the alloy chemistry. Using this understanding and correlation, we have developed an ML model to predict bond stiffness in MPEAs to overcome the computational expense which is a major bottleneck in phase space exploration and property prediction. The model predicts elastic constants in MPEAs simply from the database of binary alloys and enables exploration of full dimensionality of the elastic constant space as a function of alloy composition. Figure 4 shows a comparison of Voigt-Reuss-Hill (VRH) Young’s modulus, Poisson’s ratio, shear and bulk moduli in Ni-Cu-Au-Pd-Pt system.

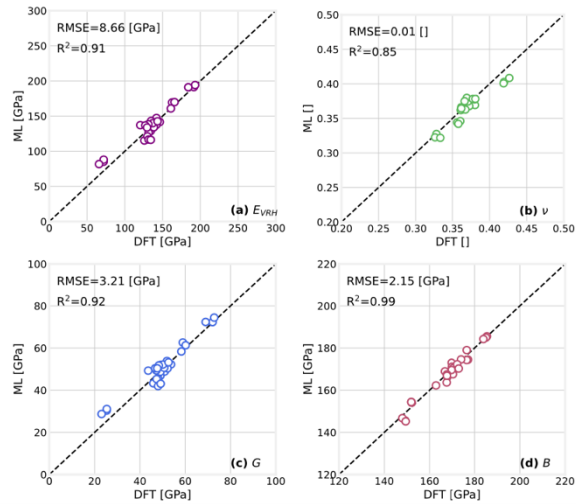


Figure 4. (a) Voigt-Reuss-Hill Young’s modulus, (b) Poisson’s ratio, (c) shear modulus, and (d) bulk modulus predictions in Ni-Cu-Au-Pd-Pt quinary system from the database of binary systems.

Recent Progress

SFE has been a major focus area in the MPEA community because it controls deformation mechanisms. There is a lack of guiding principles as to how to control SFE via composition. We have observed that, among other factors, charge density after shearing in the twin region is a critical factor that should be considered to determine SFE.

Using charge density, we have developed two ML models (one based on SVR and the other on image recognition), that can predict SFE of any alloy composition with high precision. The latter model has opened a door to develop ML models without encountering the vexing issue of descriptor search.

We have developed a ML model that can predict elastic constants in fcc alloys. This model opens the door to explore large compositional phase space of MPEAs.

Future Plans

We will focus on understanding the effect of nearest neighbor environment and short-range order on SFE in MPEAs. We will extend our elastic constant model to elements beyond fcc structures.

References

- [1] Z. Li, K.G. Pradeep, Y. Deng, D. Raabe, C.C. Tasan. Metastable high-entropy dual-phase alloys overcome the strength-ductility trade-off, *Nature* 534 (2016) 227-230.
- [2] S.L. Shang, C.L. Zacherl, H.Z. Fang, Y. Wang, Y. Du, Z.K. Liu. Effects of alloying element and temperature on the stacking fault energies of dilute Ni-base superalloys, *Journal of physics. Condensed matter : an Institute of Physics journal* 24 (2012) 505403.
- [3] A. Manzoor, D.S. Aidhy. Predicting vibrational entropy of fcc solids uniquely from bond chemistry using machine learning, *Materialia* 12 (2020).
- [4] G. Arora, D.S. Aidhy. Machine learning enabled prediction of stacking fault energies in concentrated alloys, *Metals* 10 (2020) 1072.

Publications

G Arora, A Manzoor and DS Aidhy, Charge-density based evaluation and prediction of stacking fault energies in Ni alloys from DFT and machine learning, *under review*.

G Arora, P Tahmasebi, S Kamrava and DS Aidhy, Charge-density informed convolutional neural network for stacking fault energy prediction in Ni-based concentrated alloys, *under review*.

N Linton and DS Aidhy, A machine learning framework for elastic constants predictions in multi-principal element alloys, *under review*.

Establishing defect-property relationships for 2D-nanomaterials

Assel Aitkaliyeva, University of Florida

Keywords: 2D-nanomaterials, defects, defect-induced property changes

Research Scope

This project aims to provide insight into the evolution of non-equilibrium concentration of defects in two-dimensional nanomaterials (2DNMs). Nanoscale materials are postulated to be resistant to extreme environments, but the grand challenge is to discover fundamental physical mechanisms that control their degradation. The main goals of the projects are to: i) tailor defect configurations and defect densities in 2DNMs using irradiation, ii) use defects to control physical properties of 2DNMs, and iii) investigate self-healing mechanisms in low dimensional materials. Molybdenum disulfide (MoS_2) has been selected as a model system for establishing defect-property relationships in 2DNMs because it is more complex than previously investigated mono-elemental graphene and more representative of 2DNM family.

The project is designed to include both experimental and modeling components. The modeling component includes density-functional theory (DFT) calculations to guide experimental irradiation campaigns needed to obtain a comprehensive understanding of the formation and evolution of defects in MoS_2 in response to radiation. Experimental approach is based on thorough characterization of intrinsic defect densities in MoS_2 , various in-situ and ex-situ irradiation campaigns, and characterization (and property measurements) of irradiated specimens.

Recent Progress

We were able to successfully characterize the defects that can be formed in MoS_2 with irradiation. As shown in Figure 1a, as-fabricated MoS_2 is uniform and does not contain defects. The structure of the MoS_2 before irradiation is 2H (ground state). Irradiation can induce phase transitions that have been captured in Figure 1b. The 1T phase is thermodynamically metastable and dominated in regions of disorder from a combination of lattice strain and charge transfer inducing S atoms to glide to a lower energy atomic position under stress. The α (amorphous) phase is generated from high Mo and S vacancy concentrations, leading to the destruction of translational periodicity in the crystal. Lastly, the 3R phase (AB) is seen primarily during the 300°C irradiation. We observe all possible defect configurations in MoS_2 and

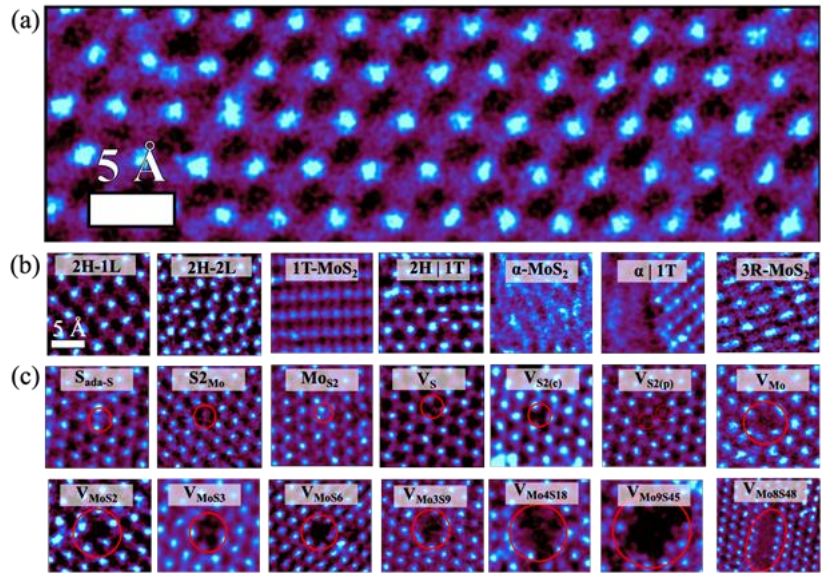


Figure 1: Atomically resolved HAADF-STEM images of defect complexes and phases in MoS_2 . (a) Pristine lattice of MoS_2 with no defects present. (b) Micrographs displaying phases and phase boundaries present throughout the lattice. (c) Micrographs displaying commonly found defects in MoS_2 induced by Au ion irradiation.

show them in Figure 1c. In addition to these defects, Au irradiation produced large nanopores that induced rotational misalignment within the periodic boundary conditions of dissimilar hexagonal lattices. During characterization, we observe misorientation boundaries and phase boundaries. These misorientation boundaries resemble ripples or elastic surface waves. It is therefore not unreasonable to assume that nanopores introduce stresses to the material and excite SAWs, which could be responsible for the observed moiré patterns. We hypothesized that thermoelastic stresses and strains around nanopores not only deform atomically thin MoS₂ layers normal to the 2D plane, but they also excite surface acoustic waves (SAWs), which induce relative rotation between the layers to generate Moiré patterns seen in our electron microscopy images. To test this hypothesis, we performed MD simulations and mapped out the time evolution of in-plane and out-of-plane atomic deformations, stress distributions, relative rotations, and Moiré patterns in the bilayer at various temperatures. The simulation results validate our hypothesis: out-of-plane atomic deformations, z , and thermoelastic stresses in the bilayer provide direct evidence for SAWs emanating from nanopores.

Future Plans

In year 5, we will concentrate our efforts on investigating the effects of substrate on MoS₂. We plan to investigate the role of substrates on radiation stability of MoS₂ and have identified three substrates (plus free-standing MoS₂). We will compare samples irradiated at different energies to elucidate the effects of nuclear vs. electronic stopping in the new series of experiments. We will also investigate the difference in damage production mechanisms between monolayer and bulk MoS₂.

Publications

1. K. Burns, B. Bischoff, C.M. Barr, K. Hattar, A. Aitkaliyeva, “Photo-exfoliation of MoS₂ Quantum Dots from Nanosheets: An In-Situ Transmission Electron Microscopy Study”, *Nanotechnology* 33, 085601 (2021). <https://doi.org/10.1088/1361-6528/ac357c>
2. K. Burns, A.M.Z. Tan, H. Gordon V, T. Wang, A. Gabriel, L. Shao, R.G. Hennig, A. Aitkaliyeva, “Defect-modulated biaxial strain in two dimensional MoS₂”, *Physics Review B* 102(8) 085421 (2020). <https://doi.org/10.1103/PhysRevB.102.085421>
3. K. Burns, A.M.Z. Tan, A. Gabriel, L. Shao, R.G. Hennig, A. Aitkaliyeva, “Controlling neutral and charged excitons in MoS₂ with defects”, *J. Mater. Research*, Invited Feature Paper (2020). <https://doi.org/10.1557/jmr.2019.404>

Center for PRredictive Integrated Structural Materials Science – PRISMS Center

PI: J. Allison, University of Michigan (UM)

Co-PIs: A. Bucsek (UM), V. Gavini (UM), A. Misra (UM), B. Puchala (UM), L. Qi (UM), V. Sundararaghavan (UM), K. Thornton (UM), A. Van der Ven (UCSB).

Keywords: Software, data repository, magnesium alloys, microstructural evolution, mechanical behavior.

Program Scope

The goal of the PRISMS Center is to establish a unique scientific platform that will enable accelerated predictive materials science. The platform has three key thrust areas:

1. **PRISMS Integrated Computational Software:** Develop and establish a suite of integrated, multi-scale, open-source computational tools for predicting the microstructural evolution and mechanical behavior of structural metals.
2. **The Materials Commons:** Develop and deploy “The Materials Commons,” a knowledge repository and virtual collaboration space for curating, archiving and disseminating information from experiments and computations.
3. **PRISMS Integrated Science Use Cases:** The use cases demonstrate the application of the integrated PRISMS platform of experiments, theory and simulation for making major advances in the quantitative and predictive understanding of microstructural evolution and mechanical behavior of magnesium alloys.

Recent Progress and Future Plans

In addition to eight faculty members, the PRISMS Center currently has four full time software staff members and over the past two years has supported fourteen graduate students, post-doctoral fellows and part time staff. We hold an annual workshop to develop our external PRISMS collaborative community and to train external users of PRISMS software tools and Materials Commons. More than 370 users have attended these workshops. In addition, a PRISMS Center You-Tube channel has been established with training for PRISMS software. It currently has over 480 subscribers and over 26,500 combined views. Additional information can be found at <http://prisms-center.org>.

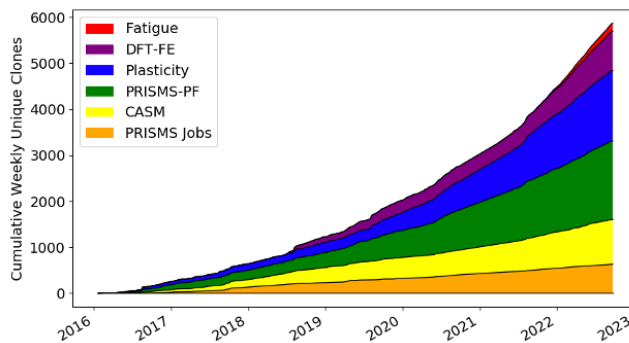


Figure 1. Cumulative clones of PRISMS codes since January 2016.

PRISMS Integrated Open-Source Computational Software

Currently four primary codes make up the PRISMS Open-Source Integrated software: *CASM*, *PRISMS-PF*, *PRISMS-Plasticity*, and *DFT-FE*. All codes are available on GitHub and have major upgrades every year. Software GitHub pages have been viewed more than 250,000 times and over 6200 unique clones (copies) have been downloaded as shown in Figure 1. Codes are also available on an easy-to-install virtual machine. Each software package includes a substantial user manual, formulation notes, commented source code and unit tests.

CASM: CASM, a Clusters Approach to Statistical Mechanics, provides functionality for symmetry identification, enumeration of symmetrically unique supercells and configurations, use of automatically determined or custom reference states for formation energy calculation, and

convex hull identification. Major updates to CASM include features for local cluster expansion fitting and updated Monte Carlo and kinetic Monte Carlo implementations. New Python packages were implemented for interfacing with the CASM crystallography and structure mapping libraries. These are being used to develop tools for studying twinning energetics. Future plans include implementing kinetic Monte Carlo calculations around extended crystal defects such as grain boundaries and Python packages for interfacing with the CASM configuration enumeration and Monte Carlo methods. <https://github.com/prisms-center/CASMCode>.

DFT-FE: *DFT-FE* is a massively parallel code for large-scale real-space DFT calculations using spatially adaptive higher-order finite-element basis. Important upgrades occurred culminating in the *DFT-FE* v1.0 release. The benchmarking of *DFT-FE* v1.0, which is the combined CPU-GPU version, shows a ~20x CPU-GPU speedup by using GPU acceleration. This has resulted in a dramatic reduction of wall-times for large-scale DFT calculations, with single-point ground-state calculations on systems containing ~15,000-20,000 electrons now possible in ~1-2 mins of wall-time on GPU nodes. *DFT-FE* is over 100x faster than traditional DFT calculations (Figure 2).

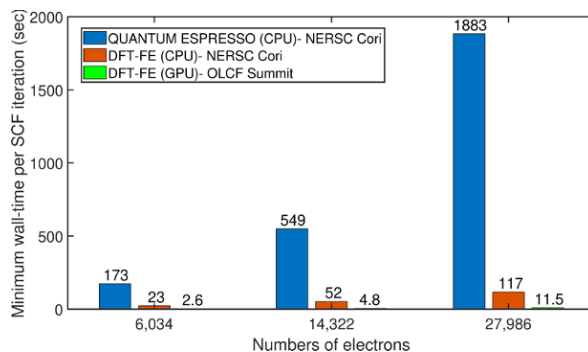


Figure 2. Computational efficiency of new *DFT-FE* GPU implementation compared to CPU implementations of *DFT-FE* and *Quantum Espresso*.

DFT-FE is being used to conduct high precision calculations of <c+a> slip modes in Mg-Y alloys. Future plans include implementation of hybrid exchange-correlation functionals (on CPUs) and extending the formulation to periodic systems. <https://github.com/dftfeDevelopers/dftfe>

PRISMS-PF: The *PRISMS-PF* phase field code uses the deal.ii open-source finite element library and is a massively scalable numerical framework for implementing phase field models for the multiscale materials modeling effort of PRISMS. New developments of the *PRISMS-PF* framework consisted of the release of new applications, improvements in performance, ease of use, integration with other tools, and efforts to increase widespread adoption and development by the members of the phase-field community. A total of 30 applications, including precipitate evolution, micro-galvanic corrosion and solidification, are available. Two new applications are under development: one for static recrystallization that includes nucleation of pristine crystallites and another for twin evolution. Future plans include development of an integrated *PRISMS-PF/PRISMS Plasticity* application to simulate twin microstructure evolution and dynamic recrystallization in polycrystalline metals. This application will also be directly coupled with CASM, which will provide kinetic and thermodynamic data from first principles. <https://github.com/prisms-center/phaseField>

PRISMS-Plasticity: The *PRISMS-Plasticity* code is a massively parallel numerical framework for implementing continuum and crystal plasticity finite element (CPFE) models using the deal.ii open source library. A variety of crystal and continuum plasticity material models have been implemented. A significant new feature, *PRISMS-Plasticity TM*, which is a rapid texture evolution analysis pipeline based on the Taylor model, has been integrated into *PRISMS-Plasticity*. This pipeline has been linked to an unsupervised machine learning (ML) model to identify process sequences which lead to improved properties. *PRISMS-Fatigue* is a new PRISMS software tool co-developed with external open-source developers for characterizing fatigue indicator

parameters. A new pipeline was developed to include grain size and morphology effects in *PRISMS-Plasticity*. New simulation pipelines for indentation and a new rate-dependent twin/detwin constitutive model have also been implemented. Future plans include integration with PRISMS-PF to capture twinning and dynamic recrystallization. <https://github.com/prisms-center/plasticity>

Materials Commons: The *Materials Commons* is a publicly available information repository and virtual collaboration space for curating, storing and disseminating materials information from experiments and computations. *Materials Commons 2.0* debuted in 2021 and represents a complete rework of this information repository which is continually updated with new features. There are over 630 registered users of *Materials Commons 2.0* which has over 3 million data files. Materials Commons use doubled over the past year. Published datasets have been viewed over 14,500 times and downloaded more than 7000 times. New features include an advanced query and search interface for data and relationships, a Python API for integration of computational applications with *Materials Commons*, a spreadsheet loader that allow users to directly upload data from spreadsheets and integration with Globus for fast, reliable upload/download of large data sets. Future plans include support for computational, visualization, machine learning and analysis tools for data stored in Materials Commons. <https://materialscommons.org>

PRISMS Use Cases

The PRISMS Use Cases serve as demonstrations and test beds for the development and demonstration of the PRISMS platform combining experiments, theory and simulation. Highlights from these use cases are summarized below.

Grain Boundary Strengthening Use Case

Theoretical/computational methods have been integrated with advanced experiments to understand grain boundary strengthening behavior in Mg alloys. This involves atomistic to continuum multiscale investigation of how texture, grain and twin boundaries, as well as chemistry, affect the micro-Hall Petch coefficients used to capture grain size effects in *PRISMS-Plasticity*. High resolution EBSD experiments have been used to quantify slip mode effects on grain boundary (GB) pile-ups (see Figure 3). Using DFT-FE and atomistic simulations a novel mechanism of how GBs and solute clusters at GBs promote the nucleation of $\langle c+a \rangle$ dislocations has been identified. GB segregation of solutes in Mg alloys have been characterized using high resolution STEM and atomistic simulations informed using large scale DFT-FE calculations.

Plans: Atomistic simulations are being used to measure the slip nucleation and transmission energy barriers at pure and solute-segregated Mg GBs, and further study the effects of solute segregation on the micro-Hall-Petch relationship. DFT-FE will be used to study the influence of dislocation-solute interactions on the $\langle c+a \rangle$ pyramidal I/II screw dislocation cross-slip barrier in dilute binary Mg-Y alloys. Multi-modal HEDM results of 3D measurement of grain size effects on twinning and slip modes in Mg-Nd, Mg-Y, Mg-Al alloy specimens are being used to validate *PRISMS-Plasticity* simulation parameters.

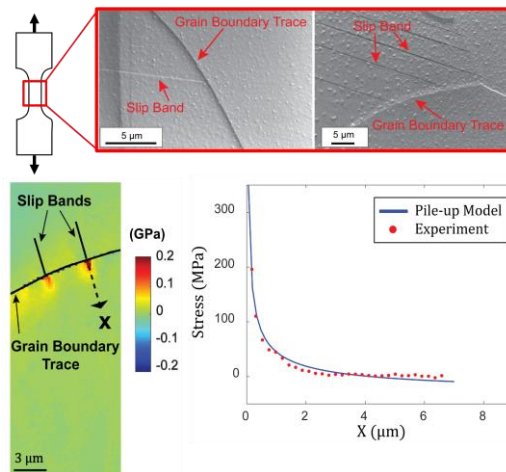


Figure 3. High resolution EBSD is used to characterize dislocation pile-up of prismatic dislocations at a grain boundary.

Fatigue Behavior Use Case

A multiscale graph theory-based approach was developed to predict the microscale crack path in polycrystalline materials. The model was validated against experimentally measured 2D fracture path using multi-modal HEDM (APS) on thin foil Mg alloy specimens. The *PRISMS-Fatigue* framework was used to study microstructure effects on the grain-scale fatigue indicator parameters in extremely large (up to 160,000 grain) microstructural simulations.

Plans: The graph theory model will be demonstrated by predicting the 3D fatigue crack path in Mg alloy samples characterized using multi-modal HEDM. Studies have been initiated to validate *PRISMS-Fatigue* grain-level predictions and explore pre-twin effects on fatigue behavior.

Alloying Effects on Twinning Use Case

This use case is studying alloying effects on twinning and detwinning behavior of cyclically deformed materials. New experimental in-situ EBSD capability and multi-modal HEDM data

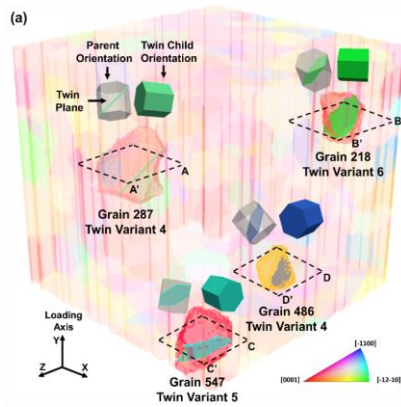


Figure 4. Multi-modal HEDM characterization of grain-scale twinning in Mg-Nd.

analysis techniques have been developed and used to quantify alloying effects on twin and detwinning during cyclic deformation and, in conjunction with *PRISMS-Plasticity* simulations, quantify alloy effects on the CRSS for twinning. We have significantly expanded the use of HEDM in the twinning and texture evolution use cases by utilizing new tools available at UM, CHESS, APS and EPFL. A revolutionary lab-scale HEDM instrument has been designed, developed, installed and demonstrated by the Bucsek group. The first-ever lab-HEDM measurements were taken on this one-of-a-kind X-ray microscope and used to measure 3D grain maps in Al, Mg, and Ti alloys. This instrument utilizes Excillum's next-generation Liquid MetalJet source, the brightest-ever lab-scale x-ray source, to conduct in-house near-field and far-field HEDM.

Plans: A coupled *PRISMS-PF/PRISMS-Plasticity* twin model is under development and will be parameterized with CASM inputs and validated on unalloyed Mg and Mg-Al. Analysis of HEDM characterization of twinning and detwinning during cyclic deformation of Mg, Mg-Al and Mg-Y will be used to validate the coupled model. Twin embryo formation and propagation will be characterized in Mg-Al using multi-modal HEDM (HEDM+ X-Ray toptomography).

Texture Evolution Use Case

This use case is exploring the effect of processing and alloying on deformation and recrystallization textures in Mg-Zn-Ca alloys to produce improved textures and promote sheet formability. Using *PRISMS-Plasticity TM* we have predicted the influence of Ca, Zn and Ca/Zn in combination on deformation texture. Gleeble thermo-mechanical processing protocols were developed combined with EBSD and synchrotron X-ray experiments. Multi-modal HEDM results showed the emergence and evolution of over 1200 individual grains during in-situ annealing. Early in recrystallization, grains with a moderately weak basal texture were observed to have a significant and persistent nucleation advantage.

Plans: A coupled *PRISMS-PF/PRISMS-Plasticity* code will be used to simulate dynamic recrystallization. Grain boundary segregation/co-segregation thermodynamics for different solute elements (e.g. Ca & Zn) will be investigated using atomistic simulations and DFT-FE calculations. Multi-modal (far field / intermediate field & near field / dark field) HEDM experiments on Mg-Zn-Ca samples will be used to characterize recrystallization kinetic processes.

2020-2022 Ten major PRISMS Center Publications acknowledging DOE-BES support (out of a total of 39 publications in past two years).

1. M. Yaghoobi, J.E. Allison, V. Sundararaghavan, “Multiscale modeling of twinning and detwinning behavior of HCP polycrystals” *International Journal of Plasticity*, 127, (2020) 102653.
2. S. DeWitt, S. Rudraraju, D. Montiel, W.B. Andrews, K. Thornton, “PRISMS-PF: A General Framework for Phase-Field Modeling Employing a Matrix-Free Finite Element Method”, *npj Computational Materials (Nature)*, 6:29(2020).
3. Sambit Das, Phani Motamarri, Vishal Subramanian, David Rogers, Vikram Gavini, “DFT-FE 1.0: A massively parallel hybrid CPU-GPU density functional theory code using finite-element discretization” *Computer Physics Communications*, 280 (2022) 108473.
4. M Yaghoobi, K. Stopka, A. Lakshmanan, V. Sundararaghavan, J. Allison, D. McDowell, “PRISMS-Fatigue computational framework for fatigue analysis in polycrystalline metals and alloys *npj Computational Materials* (2021) 38.
5. M. Andani, A. Lakshmanan, V. Sundararaghavan, J. Allison, A. Misra, “Estimation of micro-Hall-Petch coefficients for prismatic slip in Mg-4Al as a function of grain boundary parameters”, *Acta Materialia*, 226 (2022) 117613.
6. Z. Chen, C. Torbet and J. Allison, “*In-situ* Characterization of Deformation Twinning in Magnesium during Cyclic Loading via Electron Backscatter Diffraction”, *JOM* (2022) pp 2577-2591.
7. R. Roumina, S. Lee, T. Berman, K. Shanks, J. Allison, A. Bucsek, “The dynamics of recrystallized grains during static recrystallization in Mg-Zn-Ca sheet alloy using in-situ far field high-energy diffraction microscopy” *Acta Materialia* 234 (2022) 118039.
8. M. Yaghoobi, Z. Chen, A. Murphy-Leonard, V. Sundararaghavan, S. Daly, J. Allison, “Deformation twinning and detwinning in extruded Mg-4Al: in-situ experiment and crystal plasticity simulation” *International Journal of Plasticity*, 155 (2022) 103345.
9. Q. Shi, A. Natarajan, A. Van der Ven, J. Allison, “Segregation of Ca to precipitates in a Mg-rare earth alloy”, *Materials Research Letters*, in press (2022).
10. Y. Hu, V. Menon, L. Qi, “Formation of I1 stacking fault by deformation defect evolution from grain boundaries in Mg” *Journal of Magnesium and Alloys*, in press (2022)

Understanding Multiscale Defect Formation Process and Domain Switching Behavior in Shape Memory Functional Oxides

Mohsen Asle Zaeem, Colorado School of Mines

Keywords: Shape memory; ceramics; domain switching; ferroelastic; defects.

Research Scope

Shape memory ferroic (ferroelastic, ferroelectric, and ferromagnetic) materials undergo recoverable phase transition or switching under different stimuli (mechanical, thermal, or electrical), providing advanced properties for different applications. In general, ferroelectric and ferromagnetic materials are also ferroelastic, which leads to multiferroicity. By developing and using atomistic and microscale computational modeling algorithms, this project aims to study the effect of defects on phase/domain switching in functional oxides. Since ferroelasticity mediates most ferroelectric and ferromagnetic properties, it is also important to understand the mechanisms of ferroelastic domain nucleation (FDN) and ferroelastic domain switching (FDS) and their competition with martensitic phase transformation to properly design any ferroic material. In the following, we summarized our recent atomistic and microscale studies on fatigue of tetragonal to monoclinic phase transformation (TMPT) in yttria stabilized tetragonal zirconia (YSTZ) nanoparticles, ferroelastic domain switching in yttria stabilized zirconia (YSZ), and the effect of dislocations and deformation on polarization switching in bismuth ferrite (BiFeO_3) nanofilms. Then, we presented our research plans for the near future, that includes study the mechanisms of FDN and FDS, dislocation dynamics, and defects generation/evolution in ferroelastic ceramics.

Recent Progress

Superelasticity and shape memory effect in zirconia nanoparticles

Superelasticity and shape memory effect are two key properties of zirconia-based ceramics which are mediated by the reversible TMPT. Although experimental studies discovered that the shape memory behavior of ceramics can be improved by reducing the grain boundary density, degradation in shape memory response still happens after a few cycles of loading-unloading-heating-cooling. We studied the superelastic and shape memory properties of single crystalline and polycrystalline YSTZ nanoparticles by atomistic simulations [1]. Fully recoverable superelastic strain (8.3%) was observed in a single crystalline nanoparticle by merely removing the compressive load. However, the shape memory behavior degrades with the increase of loading-unloading-heating-cooling cycles. In other words, a higher temperature is required for an additional strain recovery, but certain residual displacement may still remain after few cyclic loadings. In a polycrystalline YSTZ nanoparticle, most amorphous phase transfer back to the original tetragonal structure, however, a small amount of monoclinic phase is restrained by some

grain boundaries at the end of cyclic loading, causing degradation of shape memory behavior. We are studying the interactions of TMPT and grain boundaries to determine if certain types of grain boundaries can help reducing the localized effects.

Ferroelastic domain switching in YSZ

Under certain conditions, the t' -phase in YSZ forms that has a herringbone structure with low tetragonality and can adopt three possible domains or twin variants. Instead of the well-known TMPT in YSTZ, t' -YSZ displays a completely different deformation behavior, including FDN and FDS, during which one or multiple variants mechanically reorient their c -axis to minimize the elastic energy of the system [2]. Despite its large grain size, t' -YSZ does not transform to monoclinic phase due to the coherent nature of its domains and/or twin boundaries.

To date, existing experimental works could neither clearly explain the details of the deformation process of ferroelastic ceramics nor establish explicit relations between FDN/FDS, dislocation behavior, and intrinsic texture and extrinsic features. We aim to study the deformation and domain switching of ferroelastic ceramics by advanced computational models.

Most of the current phase-field simulations of domain switching are based on ferroelectricity coupled with ferroelasticity problems. A very few phase-field simulations are actually performed to study ferroelasticity solely. So far, the phase-field simulations have studied domain switching with arbitrary initial domain. However, experimental work suggests that there is an influence of residual thermal stress. We have formulated a new phase-field model to appropriately capture the transformation of paraelastic to ferroelastic phase and simultaneously simulate the evolution of domains (Figure 3). Subsequently, the domain switching will be studied with more realistic initial domains.

Effects of defects on domain switching in ferroelectric ceramic nanofilms

The polarization switching process triggered by an applied electric field determines the performance of ferroelectric ceramics. Often this polarization switching is accompanied by ferroelastic domain switching as well. We first aimed to decouple the polarization switching from ferroelastic domain switching, and primarily study the effect of controlling factors on the polarization switching characteristics. We have developed an atomistic-scale computational framework to study the domain switching process of BiFeO₃ nanofilms [3]. We also needed to develop new interatomic potentials for Bi [4] and BiFeO₃ (not published) for our study. Through

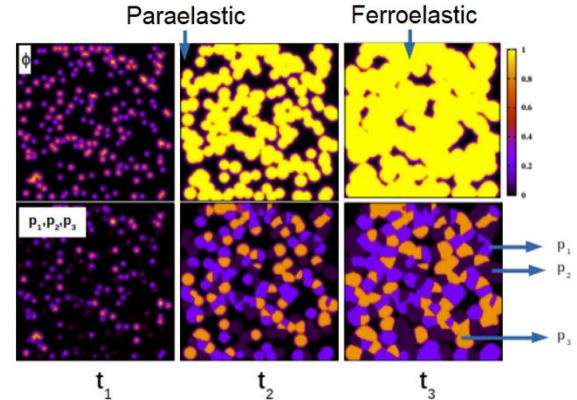


Figure 1. Initial phase-field simulation results for t to t' -YSZ transition.

a series of atomistic simulations, the effects of duration and magnitude of an electric field, domain size and nanofilm thickness on the domain switching behavior were investigated. We first studied the evolution of domains under different magnitudes and durations of the applied electric field, and the results of unswitched and switched cases are summarized in a switching map (Figure 1). Analysis of various nanofilms reveals that by increasing the film thickness, the switching time is increased. Furthermore, the nanofilms with different domain sizes and configurations are examined, and the minimum domain size for complete reversal switching is obtained. These results are helpful to predict and tune the switching process in ferroelectric materials.

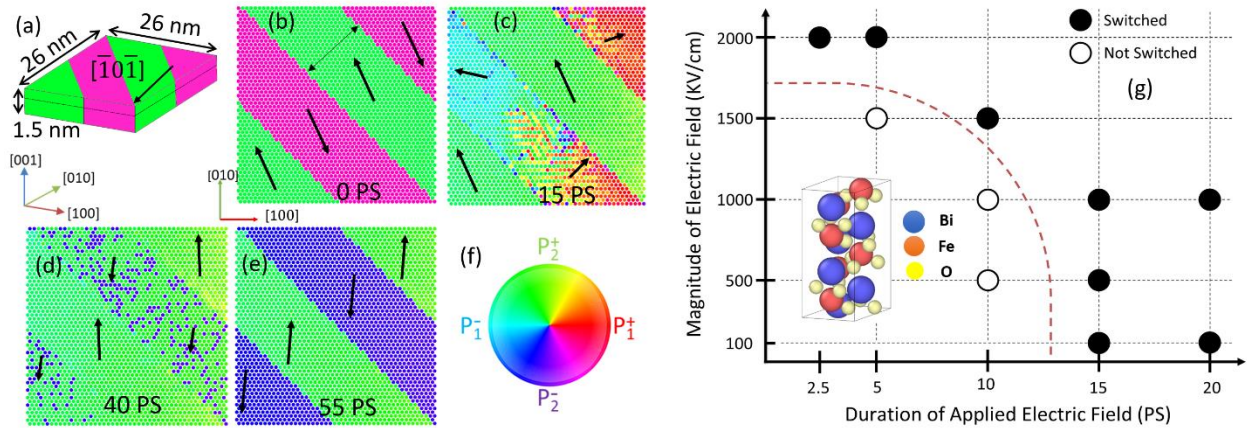


Figure 2. Evolution of domains in BiFeO₃ nanofilm with 180° DW: (a) the schematic view of BiFeO₃ nanofilm under an applied electric field along with the $[\bar{1}0\bar{1}]$, (b-e) domain evolution via polarization map in (001) plane, DC electric field of 1000 kV/cm was applied for 10 PS then the structure was relaxed for 40 PS, (f) the polarization wheel, and (g) map of magnitude versus duration of the applied electric field showing switched and not switched nanofilms with 180° DWs (inset shows the crystal structure of BiFeO₃). [3]

Then, we studied the effects of edge dislocations and applied strain on the polarization switching and hysteresis loop (Figure 3). Our atomistic framework, for the first time, provides fundamental information on how dislocation can change the polarization switching and consequently affect the hysteresis loop. The simulations also show that applied tension and compression results in narrowing and widening the hysteresis loop, respectively.

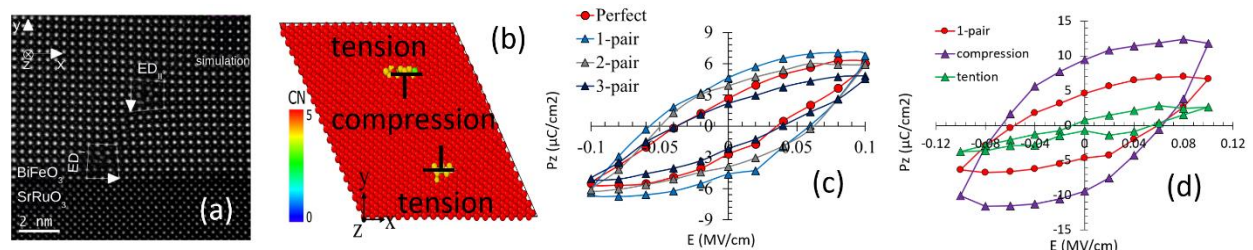


Figure 3. (a) High resolution HAADF-STEM of 2 perpendicular edge dislocations; (b) A pair of edge dislocations colored based on coordination number; (c) Effect of different configurations of edge dislocations on polarization response of BFO; (d) Comparison between change in polarization in tension and compression and one pair of dislocation in BFO. (Not published)

Future Plans

Study thermomechanical deformation and defect nucleation/ evolution in ferroelastic ceramics

A precursor for understanding the texture effects on the mechanical behavior of ferroelastic t' -YSZ, we will examine and interpret the deformation process of single crystals. The experimentally derived semi-empirical potential will be tested to describe the interaction between ions of Zr^{4+} , Y^{3+} , and O^{2-} in YSTZ. A model consisting of few million atoms will be deformed mechanically by applying a compressive strain up to 10% and then unloading. We will investigate the deformation mechanisms considering various crystallographic orientations with respect to the loading direction. To study the effect of defects and dislocations in the cubic phase on the FDN, some specimens will be deformed at a high stress level before the cooling process. We will also study the effect of yttria concentration, which is expected to find its origin at the atomistic scale. Additionally, we will study dislocations emission and motions, and the effect of preexisting defects on the nucleation and switching of ferroelastic tetragonal phase. Numerous small and planar defects were reported during a second deformation along a direction perpendicular to the first loading. We will conduct cyclic loading simulations to understand the defect formation mechanisms.

Study ferroelastic transition and switching, & defect nucleation/evolution in ferroelastic materials

We are developing a 3D multiphase field model (MPFM) to predict the microscale domain nucleation and switching in any ferroelastic materials. To this end, we are advancing our PFM that was developed for TMPT and transformation toughening in YSTZ [5], and martensitic transformation and elastocaloric effect in shape memory alloys. We will modify the total free energy function of this model to include the ferroelastic nucleation and switching process and will consider dislocations and defects nucleation and motion. The MPFM will be used to study the mechanisms of FDN and FDS, dislocation dynamics, and defects generation/evolution in microscale t' -YSZ samples, considering various crystal orientations with respect to loading direction, preexisting dislocations, and specimen sizes. Possible competition between FDS and TMPT will also be investigated by mechanically deforming the specimens at low temperatures under monotonic and a few cyclic loadings.

References

1. N. Zhang and M. Asle Zaeem, *Superelasticity and shape memory effect in zirconia nanoparticles*, *Extreme Mechanics Letters* **46**, 101301, 8 pages (2021).
2. D. Baither, M. Bartsch, B. Baufeld, A. Tikhonovsky, A. Foitzik, M. Rühle, and U. Messerschmidt, *Ferroelastic and Plastic Deformation of t' -Zirconia Single Crystals*, *Journal of the American Ceramic Society* **84**(8), 1755-1762 (2001).
3. H. Nobarani and M. Asle Zaeem. *A molecular dynamics study of domain switching in $BiFeO_3$ nanofilm under DC electric field*, *Computational Materials Science* **199**, 110718, 9 pages (2021).
4. H. Zhou, D. Dickel, M.I. Baskes, S. Mun, and M. Asle Zaeem. *A modified embedded atom method interatomic potential for bismuth*. *Modelling and Simulations in Materials Science and Engineering* **29**, 065008, 15 pages (2021).
5. C. Cissé and M. Asle Zaeem, *A phase-field model for non-isothermal phase transformation and plasticity in polycrystalline yttria-stabilized tetragonal zirconia*, *Acta Materialia* **191**, 111-123 (2020).

Publications

1. H. Nobarani and M. Asle Zaeem. *A molecular dynamics study of domain switching in BiFeO₃ nanofilm under DC electric field*. Computational Materials Science **199**, 110718, 9 pages (2021).
2. N. Zhang and M. Asle Zaeem. *Superelasticity and shape memory effect in zirconia nanoparticles*. Extreme Mechanics Letters **46**, 101301, 8 pages (2021).
3. H. Zhou, D. Dickel, M.I. Baskes, S. Mun, and M. Asle Zaeem, *A modified embedded atom method interatomic potential for bismuth*, Modelling and Simulations in Materials Science and Engineering **29**, 065008, 15 pages (2021).
4. C. Cissé and M. Asle Zaeem, *A phase-field model for non-isothermal phase transformation and plasticity in polycrystalline yttria-stabilized tetragonal zirconia*, Acta Materialia **191**, 111-123 (2020).
5. N. Zhang and M. Asle Zaeem, *Nanoscale flaw tolerance behaviour of polycrystalline tetragonal zirconia nanopillars*, International Journal of Mechanical Sciences **173**, 105405, 7 pages (2020).
6. N. Zhang and M. Asle Zaeem, *Effects of grain orientations and pre-existing defects on mechanical properties and deformation mechanisms of polycrystalline yttria-stabilized tetragonal zirconia*, Materialia **9**, 100553, 7 pages (2020).
7. N. Zhang and M. Asle Zaeem, *Effects of twin boundaries and pre-existing defects on mechanical properties and deformation mechanisms of yttria-stabilized tetragonal zirconia*, Journal of the European Ceramics Society **40**, 108-114 (2020).

Global aspects of microstructural evolution in irradiated alloys: Effects of self-organization

Pascal Bellon, Robert S. Averback, Shen J. Dillon

Department of Materials Science and Engineering, University of Illinois at Urbana-Champaign, Urbana, IL

Keywords: Irradiation, self-organization, compositional patterning, grain boundaries, severe plastic deformation

Research Scope

The next generation of nuclear power systems requires structural materials that can operate safely and economically in harsh conditions, in particular resisting to high levels of radiation damage at elevated temperature. Such materials, driven far from equilibrium, constitute dissipative systems that have a strong tendency for developing self-organized microstructures. One strong attractive characteristic of these self-organized microstructures is they are stable steady states, thus ensuring that materials properties are stable over time. Furthermore, it has been recognized recently that some of these microstructures contain a high number density of nanoscale features that can promote both the recombination of point defects and trapping of rare gas atoms, thus improving the overall alloy stability under irradiation. Most of the past works on self-organization under irradiation focused on isolated elements of the microstructure, such as precipitates [1], voids and bubbles, [2,3] grain boundaries [4-6]. Recent results, as well as critical re-analysis of past results, suggests however that self-organization takes place globally, coupling all the elements of the microstructure. Our research effort aims at elucidating these global aspects of microstructural evolution under irradiation, including the validity of a local forcing analysis and the dynamical coupling of sub-systems of the microstructure. Fundamental understanding of global self-organization under irradiation is expected to offer new ideas about designing new radiation resistant materials. This project considers also a related case of dissipative systems, where alloys are driven into nonequilibrium state by severe plastic deformation. It is expected that this broad research program stimulates and guides research on other aspects of self-organization in dissipative materials systems, the so-called driven alloys.

Recent Progress

We investigated whether irradiation (1) could induce compositional patterning (CP) at GBs or other sinks and, if it is the case (we show below it indeed is), (2) whether this CP could co-exist with CP at grain interiors. We also investigated (3) whether the concept of effective temperature and effective thermodynamics is broadly applicable to alloys driven into nonequilibrium steady states by irradiation and plastic deformation. For all three questions, we combined modeling and experiments to provide a more solid and comprehensive understanding of these complex materials systems. We summarize below the key results obtained so far.

1. Compositional patterning under irradiation: Phase-field modeling was used as the main modeling tool as it allows for an integration of all relevant physical processes and related length scales and rates, such as defect production rates, range R and frequency Γ_b of ballistic recoil mixing events, coupled transport equations, and integration of sinks, e.g., symmetric-tilt twin boundaries (STGB), general grain boundaries and dislocation loops. We considered two broad families of alloys: (i) alloys where irradiation does not lead to radiation induced segregation (RIS) and precipitation (RIP), i.e., segregation and precipitation in these alloys are solely due to thermodynamic driving forces, and (ii) alloys where irradiation can induce RIS and RIP due to flux coupling between point defects and vacancies. In the former family of alloys, it was found that when the range of atomic relocation is smaller than the GB width, δ , compositional patterning did not take place, but that the effect of forced mixing could be rationalized with effective segregation isotherms [7], extending the concept of effective temperature initially introduced by Martin for bulk evolutions under irradiation for small R values. When R was greater than δ , CP was observed first at GBs for the most dilute compositions, then at GBs and grain interiors for more concentrated alloys but their behavior could not be simply rationalized. This first study suggests that CP at GBs is not guaranteed in this family of alloys since atomistic simulations indicate that R ranges are typically a few Å to ≈ 1 nm, and therefore R will rarely exceed δ , which is commonly assumed to be ≈ 1 nm.

In the second family of alloys, those where irradiation can induce non-equilibrium segregation and precipitation due to kinetic coupling between point defects and solutes fluxes, CP was however found to take place much more readily at GBs and sinks than in the grain interiors. A typical steady state phase diagram, see Fig. 1, displays an extended region of compositional patterning in the (R, Γ_b) parameter space [8]. Furthermore, when the solute advection from RIS is sufficiently strong (represented by a large Péclet number), it is found that CP at GBs can even take place in the absence of ballistic mixing, in sharp contrast with bulk response, where ballistic mixing is required for CP to take place [1]. Fig. 2 illustrates CP at a STGB in a dilute alloy mimicking Al-5at.% Sb. A finite number of precipitates is found at large irradiation damage levels, and these microstructures are long-lived metastable ones. A theoretical and numerical analysis indicates that these structures are stabilized by strong solute convection by RIS and large diffusion anisotropy near GBs [8]. Two distinct alloys systems, Al-Sb and Ni-Ge have been selected for testing these predictions, experimentally, since past works and recent first principles calculations indicate that solute atoms bind strongly to vacancies. This leads to substantial radiation-induced segregation over a range of temperatures easily accessible experimentally. Preliminary results suggest that irradiation-induced CP does take place in these alloys but a systematic investigation employing advanced transmission electron microscopy (TEM), scanning TEM (STEM), and atom probe tomography (APT) is in progress to provide a comprehensive picture. We are combining these techniques on the same sample regions, using the so-called correlative microscopy, thus integrating the structural and chemical information of both techniques at the sub-nanometer scale.

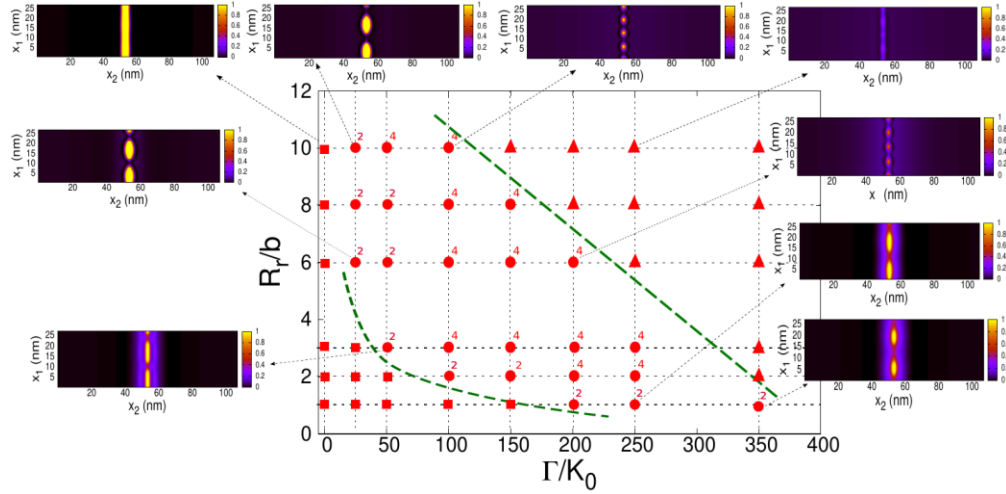


Figure 1: Steady-state phase diagram obtained by phase field modeling for a dilute Al-5at.%Sb alloy irradiated at 300K at $K_0=10^{-3}$ dpa/s as a function of the number of replacement per displacement, Γ/K_0 , and the average ballistic relocation distance R_r rescaled by the Burgers vector \mathbf{b} . The simulation cell contains one STGB with a disorientation $\theta = 9.55^\circ$ in the middle of the cell. Note the large domain for compositional patterning in the central region of the diagram.

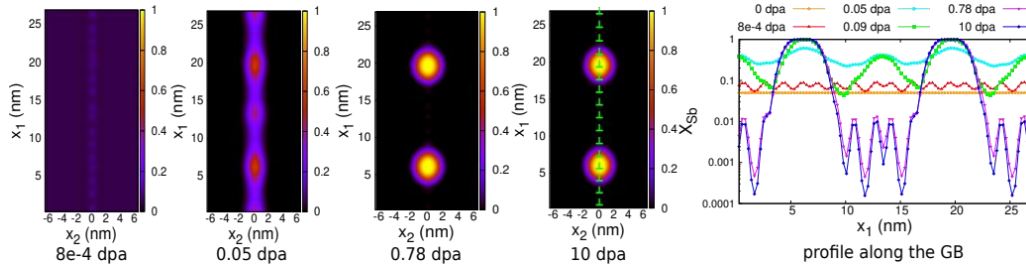


Figure 2: Evolution with dose of the same STGB as in Fig. 1 but for a smaller grain size and in the absence of ballistic mixing. Strong solute advection nevertheless results in the stabilization of a composition pattern with a two-precipitate structure, which is stable over large irradiation dose.

As part of this research component of our program, we also elucidated the role solute elements such as Sc, Cr, Sb, W in nanocrystalline Al thin films, showing that these solutes promote high hardness near room temperature by solute strengthening of GBs [9]. Moreover, irradiation of Al-1.2 at.% Sb indicated strong flux coupling and RIS to GBs, which in fact motivated the phase field modeling of this system. We also developed techniques to derive free energy functionals for phase separating [10] and for ordering alloy, expanding on the original derivation by Cahn and Hilliard for the contribution of inhomogeneities. Our approach allows the derivation of higher order terms, responsible for anisotropic interface energies, and it can directly be extended to atomic interactions extending beyond pair interactions, on contrast to past methods.

2. Immiscible alloys subjected to severe plastic deformation: Severe plastic deformation (SPD) is another means to drive alloys into nonequilibrium steady states. In our past BES-funded research we established experimentally that in highly immiscible systems subjected to SPD at low temperature, the mutual solubilities of coexisting phases could be affected by the use by solute alloying [11]. Atomistic simulations by molecular dynamics (MD) now establish that the effect of forced atomic mixing induced by SPD on steady-state microstructures could be captured by using the concept of an effective temperature, which would reach a high but finite value at deformation temperature where point defect diffusion is negligible. We have extended these results to the case of two-phase alloys doped by a ternary solute [12], and established for the first time that (i) SPD steady states deformed near 100 K are indeed equivalent to equilibrium states reached at a higher, effective temperature, (ii) SPD can lead to segregation of solute at interphase boundaries despite the very low temperature deformation, and (iii) that this segregation strengthens the composite material and thereby increases the effective temperature of the alloy. This work establishes a direct link between alloy strength and effective temperature, and thus it is beginning to provide a scientific basis for the complex microstructural evolutions involved in SPD processing of strongly immiscible and reactive alloys.

Future Plans

Building on this ensemble of results, a renewal proposal is in preparation, which will focus on a holistic approach to the self-organization of alloy microstructures under irradiation.

References

- [1] R. A. Enrique and P. Bellon, *Phys Rev Lett* **84**, 2885 (2000).
- [2] Y. P. Gao, Y. F. Zhang, D. Schwen, C. Jiang, C. Sun, and J. Gan, *Materialia* **1**, 78 (2018).
- [3] Y. P. Gao, Y. F. Zhang, D. Schwen, C. Jiang, C. Sun, J. Gan, and X. M. Bai, *Sci Rep-Uk* **8**, 6629, 6629 (2018).
- [4] N. M. Ghoniem and D. Walgraef, *Instabilities and self-organization in materials* (Oxford University Press, Oxford ; New York, 2008), Oxford science publications, 63.
- [5] A. J. Ardell and P. Bellon, *Curr Opin Solid St M* **20**, 115 (2016).
- [6] M. Nastar and F. Soisson, in *Comprehensive Nuclear Materials* (2012), pp. 471.
- [7] Q. Li, PhD thesis, University of Illinois, 2021.
- [8] G. F. Bouobda Moladje, P. Bellon, and R. S. Averback, (in preparation).
- [9] S. E. Kim, N. Verma, S. Özerinç, S. Jana, S. Das, P. Bellon, and R. S. Averback, *Materialia* **26**, 101564 (2022).
- [10] P. Bellon and Q. Li, *Acta Mater* **215**, 117041 (2021).
- [11] N. Pant, N. Verma, Y. Ashkenazy, P. Bellon, and R. S. Averback, *Acta Mater* **210**, 116826 (2021).
- [12] N. Pant, S. Das, P. Bellon, R. S. Averback, M. Krief, and Y. Ashkenazy, *Acta Mater* **240**, 118333 (2022).

Publications

- [1] N. Pant, S. Das, P. Bellon, R.S. Averback, M. Krief, Y. Ashkenazy, *Role of interfaces on phase formation during severe plastic deformation*, Acta Mater **240** (2022) 118333.
- [2] S.E. Kim, N. Verma, S. Özerinç, S. Jana, S. Das, P. Bellon, R.S. Averback, *Strengthening of nanocrystalline Al using grain boundary solute additions: Effects of thermal annealing and ion irradiation*, Materialia **26** (2022) 101564.
- [3] N. Pant, N. Verma, Y. Ashkenazy, P. Bellon, R.S. Averback, *Phase evolution in two-phase alloys during severe plastic deformation*, Acta Mater **210** (2021) 116826.
- [4] Q. Li, R.S. Averback, P. Bellon, *Compositional patterning in irradiated alloys: Effective potentials and effective interfacial energy*, Phys. Rev. B **103**(10) (2021) 104110.
- [5] G.S. Jawaharram, C.M. Barr, K. Hattar, S.J. Dillon, *Evidence for a high temperature whisker growth mechanism active in tungsten during in situ nanopillar compression*, Nanomaterials **11**(9) (2021) 11092429.
- [6] P. Bellon, Q. Li, *Anisotropic Cahn-Hilliard free energy and interfacial energies for binary alloys with pairwise interactions*, Acta Mater **215** (2021) 117041.
- [7] P. Bellon, R.S. Averback, F. Ren, N. Pant, Y. Ashkenazy, *A Review: Microstructural and Phase Evolution in Alloys during Extended Plastic Deformation*, JOM **73**(7) (2021) 2212-2224.
- [8] R.S. Averback, P. Bellon, S.J. Dillon, *Phase evolution in driven alloys: An overview on compositional patterning*, J Nucl Mater **553** (2021) 153015.
- [9] Q. Li, X. Shang, B. Janicek, P.Y. Huang, P. Bellon, R.S. Averback, *Evolution of Nb oxide nanoprecipitates in Cu during reactive mechanical alloying*, J Mater Res **35**(1) (2020) 98-111.
- [10] G.S. Jawaharram, C.M. Barr, A.M. Monterrosa, K. Hattar, R.S. Averback, S.J. Dillon, *Irradiation induced creep in nanocrystalline high entropy alloys*, Acta Mater **182** (2020) 68-76.

Role of Subgrain Heterogeneous Processes in Slip Localization in Polycrystalline Metals During Cyclic Plasticity

Irene J. Beyerlein, Tresa M. Pollock, University of California at Santa Barbara

M. P. Miller, Cornell University

Keywords: slip localization, lattice rotation, crystal plasticity, triple junction, irreversibility

Research Scope

Fatigue of ductile polycrystalline metals is a microstructure-sensitive localization process, beginning with cyclic plasticity-driven production of subgrain inhomogeneities and ending with the eventual development of cracks across many grains. While the failure mechanisms of materials under cyclic conditions have been studied extensively, *designing a material for extended fatigue life is rarely performed based on knowledge of how instabilities first form and grow below the scale of the grain*. The overarching goal of this research project is to establish a fundamental understanding of how slip events develop in polycrystalline microstructures and escalate to form fatigue cracks during cyclic loading. This understanding will be embodied in new computational capabilities that can guide the development of processing paths for damage-resistant materials.

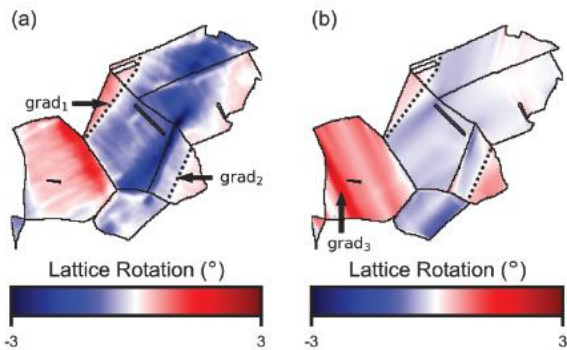
The main challenge lies in identifying *when, where, why and how* cyclic loading leads to the formation and intensification of rare but terminal material instabilities, such as slip localizations and cracks. Our approach involves bringing together multimodal datasets, from in-situ testing and characterization to 3D microstructural characterization, and to 3D microstructure-explicit micromechanical modeling. The *central hypothesis* that drives our work is that the irreversible growth of intragranular lattice rotations and slip localizations during cyclic loading emerge from specific polycrystalline microstructural features. Research activities in all tasks are driven to address three scientific questions: 1) Why do some intragranular orientation gradients, formed during cyclic loading, “intensify” and become life-limiting structural slip localizations? 2) What are the combined microstructural and micromechanical characteristics at triple lines that provide high probability conditions for slip band formation? 3) Which properties, material states and crystallographic neighborhood configurations have the highest probability of producing conditions for runaway propagation of slip localizations under cyclic loading?

To address these questions, we have grouped the research activities into three main tasks. The first task aims to understand when and where lattice rotation gradients increase to the level that they can form these structural localizations and the role played by the response of neighboring grains and the local stress state. The second task examines the link between fundamental aspects of the polycrystalline microstructure, namely local grain neighborhoods and their junctions, and rare events, such as slip localizations, that emerge from them under deformation using methodologies

developed in the first phase of this program. The final task seeks to identify the material properties and neighborhood configurations that produce high probability conditions for runaway propagation of dislocation-rich localized slip bands under cyclic loading.

Recent Progress

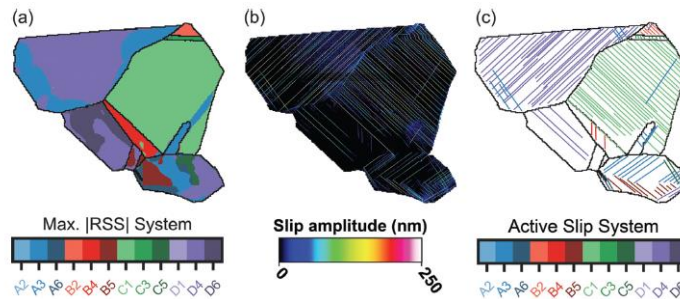
In this last year, we investigated the evolution of intragranular lattice rotations and slip activity during monotonic and cyclic loading in a high performance, polycrystalline face centered cubic material, IN718. We engaged in-situ high-resolution digital image correlation (HR-DIC) experiments and 3D full-field crystal plasticity (CP) modeling.



Lattice rotation maps from the (a) experimental and (b) modeling analysis of a local region in the microstructure

With our setup, highly resolved, spatial maps of lattice rotation can be obtained in time during deformation from both in-situ HR-DIC testing and CP modeling for the same microstructure, at the same fine resolution, and under the same boundary conditions. Direct point-by-point comparisons of the measured and calculated intragranular fields (stress, strain, lattice rotations) are not only possible in time but also over a large field of view, encompassing

several tens of grains. With no adjustment to model material parameters, the model captured sub-grain features of the lattice rotation fields observed experimentally, including the gradients in the amount and sign of lattice rotation within individual grains, as well as across multiple grains, in monotonic and cyclic loading. Both experiment and model revealed that individual grain deformation proceeds heterogeneously, primarily by dividing into domains of distinct orientation, creating intragranular

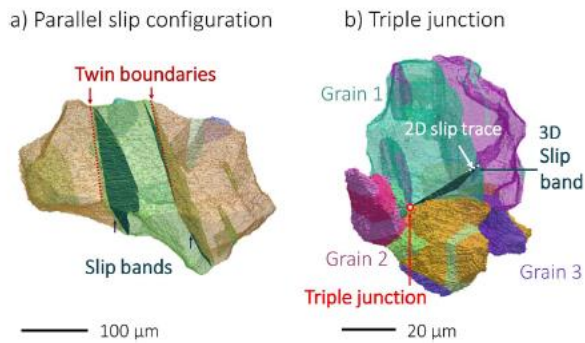


Maps of the (a) calculated resolved shear stress, (b) experimental slip trace analysis of slip amplitude and (c) active slip.

boundaries or precisely, lattice rotation gradients. The model shows that single or dual slip operates in each domain, putting into question the conventional view that grains need to operate by homogeneously activating five or more slip systems. Importantly, we found that some of the observed lattice rotation gradients can be considered “polarized”, that is, associated with a change in the sign of lattice rotation (e.g., from clockwise to counterclockwise). The calculations and testing found that, during a tension-compression loading cycle, the misorientation across polarized orientation gradients increase rather than recover. This implies polarized orientation gradients

formed during the first loading step are the ones that would progressively increase under cyclic loading.

In the same polycrystalline nickel-base superalloy IN718, we investigated the role of microstructural features on the strong slip localizations generated during monotonic tensile loading. We combined HR-DIC and 3D EBSD to reconstruct the planes for a statistically significant number of slip localizations (several hundred) in nickel-base superalloy Inconel 718



Two types of slip band locations seen in the deformed 3D microstructure: (a) parallel to annealing twins and (b) at a triple junction

(IN718) after monotonic deformation. The analysis revealed that over half of the localizations originated from triple junction lines. The most intense bands were those that simultaneously formed parallel and close to annealing twin boundaries. To understand the incipient slip processes that would lead to localization, we built a full-field 3D crystal plasticity model of the triple junction and its microstructure neighborhood without any slip localizations. The model accurately forecasted the slip system on which the slip localization would form. More importantly,

the model revealed that triple junctions that tend to form localizations are associated with one grain in which slip activity is dominated by one slip system. The main finding from these first-time 3D analyses is that slip localizations form from triple junctions into grain(s) that deform in single slip.

In-situ far-field High Energy X-ray Diffraction Microscopy (ff-HEDM) yields the critical evolution information needed to understand *when* localized deformation becomes fatal under cyclic loading. While these point-to-point measurements are rich in grain-scale data, they are coarse in evolution data, only capture discrete portions of the material response, and typically rely on slow strain rates (10^{-6} /s), which are unrealistic for a fatigue experiment with a considerable number of cycles. We developed an innovative real-time analysis technique to “fill in the gaps” of these point-to-point measurements. This real-time technique leverages machine learning in the form of principal component analysis (PCA), a dimensionality reduction tool, to investigate polycrystal diffraction pattern spots under limited sample rotation. With this real-time PCA technique, we were able to: 1) finely characterize the deformation history of a cyclically loaded IN718SS sample (128 cycles) and a cyclically loaded IN718DP sample (128 cycles) with LODI measurements, and 2) correlate physical meaning to PC patterns to inform full ff-HEDM measurement collection on future cycles.

These informed ff-HEDM measurements permitted focus on the evolution of lattice rotations and stress states to better understand their connection to fatal localized slip. To understand how they evolve in time, we combined an actual far-field High Energy Diffraction Microscopy (ff-HEDM) during in situ cyclic loading and a synthetic ff-HEDM experiment using a virtual diffractometer

built from spatially resolved orientation data our 2D-EBSD and TriBeam 3D-EBSD experiments. We anticipated that elevated statistical moments of these distribution would act as a signature of localized deformation. We label these grains as *grains experiencing microscale localized deformation inside (gremlins)*. We found that grains with high skewness and high kurtosis correlated to grains with microvolumes (regions of high orientation gradients) and these grains defined a signature for gremlins. This correlation will enable discovering a signature of localized deformation, and ff-HEDM measurements to identify when and where gremlins arise during in-situ cycling without destroying the sample.

Future Plans

One key question that remains concerns why only a small fraction of triple lines leads to either a slip localization or a microvolume (a local region of high orientation gradients). Our future plans include expanding the investigation to include hundreds of triple junctions. The two key quantities that will be mapped in the three adjoining grains and at the common triple line region are the lattice rotations and active slip systems. The driving hypothesis is that the slip patterns prompted at the triple line identify which grain and which slip systems will produce a slip localization.

In the next year, we also plan to link when and where orientation gradients become critical and their link to slip localizations and fatigue cracks. We intend to bring together our full suite of techniques and apply them to both cyclic loading and very high cycle fatigue loading (VHCF). One effort involves building upon the real-time principal component analysis (PCA) of limited omega diffraction image (LODI) measurements made on IN718 alloys, either in solid solution or precipitation hardened, both cyclically loaded to 128 cycles made by the HEDM experiment in this last year. When the PCA and LODI are paired with a virtual diffractometer we can compare and link local material characteristics, like neighbor configurations and stress states, to localized slip under cyclic loading. In another effort, we will expand our study to include high-strength Ti alloy, which also is prone to localization in fatigue. We plan to examine, for the same microstructure, the evolution of the orientation distributions within the grains computed by the model and measured in the ff-HEDM experiments. We will especially focus on grain neighborhoods that result in microvolumes and slip localization that are quantified with the TriBeam/HR-DIC experiments. With the model, we aim to identify more nuanced differences in the higher order moments of the orientation distributions that would distinguish grains with slip localizations vs. microvolumes.

Finally, we plan to link when and where orientation gradients become critical and their link to slip localizations and fatigue cracks. We will bring together our full suite of techniques and apply them to both cyclic loading and very high cycle fatigue loading (VHCF). To this end, we plan to build upon the real-time principal component analysis (PCA) of limited omega diffraction image (LODI) measurements made on the IN718SS and IN718DP samples, both cyclically loaded to 128 cycles made by the HEDM experiment in this last year.

Publications

1. M.A. Charpagne, J.M. Hestroffer, A.T. Polonsky, M.P. Echlin, D. Texier, V. Valle, I.J. Beyerlein, T.M. Pollock, and J.C. Stinville, *Slip localization in Inconel 718: A three-dimensional and statistical perspective*, Acta Materialia **215**, 117037 (2021).
2. M. I. Latypov, J.-C. Stinville, J. R. Mayeur, J. M. Hestroffer, T. M. Pollock, and I. J. Beyerlein, *Insight into microstructure-sensitive elastic strain concentrations from integrated computational modeling and digital image correlation*, Scripta Materialia **192**, 78–82 (2021).
3. M. I. Latypov, J. M. Hestroffer, J.-C. Stinville, J. R. Mayeur, T. M. Pollock, and I. J. Beyerlein, *Modeling lattice rotation fields from discrete crystallographic slip bands in superalloys*, Extreme Mechanics Letters **49**, 101468 (2021).
4. J. M. Hestroffer, M. I. Latypov, J.-C. Stinville, M.-A. Charpagne, V. Valle, M. P. Miller, T. M. Pollock, and I. J. Beyerlein, *Development of grain-scale slip activity and lattice rotation fields in Inconel 718*, Acta Materialia **226**, 117627 (2022).
5. J. M. Hestroffer and I. J. Beyerlein, *XtalMesh Toolkit: High-Fidelity Mesh Generation of Polycrystals*, Integrating Materials and Manufacturing Innovation **11**, 109–120 (2022)
6. J.-C. Stinville, J. M. Hestroffer, M.-A. Charpagne, A. T. Polonsky, M. P. Echlin, C. J. Torbet, V. Valle, K. E. Nygren, M. P. Miller, O. Klaas, A. Loghin, I. J. Beyerlein, and T. M. Pollock, *Multi modal Dataset of a Polycrystalline Metallic Material: 3D Microstructure and Deformation Fields*, Scientific Data **9**, 460 (2022).
7. M.-A. Charpagne, J.-C. Stinville, A. T. Polonsky, M. P. Echlin, T. M. Pollock, *A Multi-modal Data Merging Framework for Correlative Investigation of Strain Localization in Three Dimensions*, JOM **73**, 3263–3271 (2021).
8. M. P. Miller, K. E. Nygren, and D. J. Shadle, *Using real-time data analysis to conduct next-generation synchrotron fatigue studies*, International Journal of Fatigue **164**, 107113 (2022).
9. J.-C. Stinville, P. G. Callahan, M.-A. Charpagne, M. P. Echlin, V. Valle, and T. M. Pollock, *Direct measurements of slip irreversibility in a nickel-based superalloy using high resolution digital image correlation*, Acta Materialia **186**, 172-189 (2020).
10. D.J. Shadle, K.E. Nygren, J.C. Stinville, M.A. Charpagne, T.J.H. Long, M.P. Echlin, C.J. Budrow, A.T. Polonsky, T.M. Pollock, and M.P. Miller, *Bringing to Life a Newly Discovered Signature of Fatigue Crack Initiation via Multimodal Characterizations*, Nature Communications (2022), Accepted.

Nanomechanics and Nanometallurgy of Boundaries

Brad L. Boyce, Khalid Hattar, Doug Medlin, Remi Dingreville

Sandia National Laboratories

Keywords: nanostructured metals, GBs, mechanical properties, irradiation, defects

Research Scope

Nanostructured materials are inherently unstable due to the high density of non-equilibrium defects that provide a substantial driving force for anomalous or unexpected evolution. Departing from most mesoscale models for grain boundaries (GBs), there is a clear recognition that GB properties are not single-valued for a given material, but widely disparate depending on the configuration of the particular boundary and its neighboring grain. Taking this one step further, the core hypothesis for the proposed program is that both GB character and GB defects control the kinetics and thermodynamics of chemical and physical processes in response to mechanical, thermal, and irradiation stimuli. The result is a heterogeneous response to external stimuli, setting up triggered incipient processes such as abnormal grain growth which can be driven by several mechanistic processes (see Fig. 1). We propose to elucidate the effect of defected GBs and their networks by examining model FCC systems, *e.g.* Pt and Pt-Au. In our work moving forward, we are focusing specifically on the role of GB defects such as disconnections, facet junctions and triple junctions on thermally-, mechanically-, and radiation-induced migration in both pure systems and in solute-segregated GBs. This effort ranges from fundamental characterization and theory of the structure of these GB defect types to the role of different extended GB networks on properties such as fatigue and radiation tolerance.

Recent Progress

Our core hypothesis is that heterogeneous GB character and GB defects strongly influence the macroscopic properties in response to external stimuli. This hypothesis was a central theme in our recent paper [1] where the details of GB

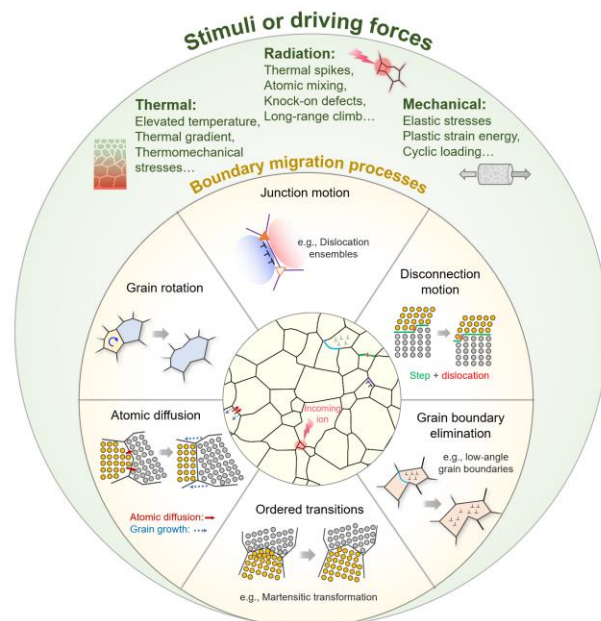


Fig.1 A summary of the stimuli and migration processes that influence the mechanical behavior and radiation response of nanostructured metals.

migration are distilled into multiple contributing processes at GB defects, specifically, faceted junctions in a $\{112\}$ -faceted $\Sigma 3$ GB in Pt. Prior models, based on boundary curvature alone and ignoring the details of GB defects, would have anticipated migration counter to the present observations. While prior models consider only the local cascade rearrangements, we find that both short- and long-range interactions are necessary to explain the observations. The short-range effect involves local atomic shuffling, cascade progression, and thermal spikes. The long-range effect includes the superimposed stress field associated with defect evolution. Our future work will build on these findings by considering more complex and chemically modified grain boundaries as well as boundary network effects.

Going beyond pure metals, we are interested in alloys with controlled boundary stability, and in particular binary alloys with thermodynamically stabilized boundaries. To this end, we employed atomic-resolution Chemi-STEM, automated crystallographic orientation mapping, molecular dynamics simulations, and phase field simulations to elucidate the nature of heterogeneous segregation as a function of GB configuration/misorientation [2]. This study revealed that in "thermodynamically-stabilized" systems like Pt-Au, where the solute was chosen for its ability to lower the thermodynamic driving force for boundary migration, the mobility of GBs is still limited primarily by the *kinetic* contribution of solute drag rather than the *thermodynamic* contribution.

Thermodynamic models for boundary stability typically ignore the structural details of the GB, and in particular the role of GB defects. In [3], we used atomistic modeling and dislocation structural analysis to show that a characteristic defect configuration, resulting from the disconnection of the disconnection through the emission of a stacking fault, is responsible for the transition from a bilayer to a trilayer segregation patterning. We showed that this phenomenon can be ascribed to a break of the stress-field symmetry across the disconnection, the associated reduction of local pressure, and an increase of the segregation volume induced by the presence of the stacking fault at the disconnection.

Ultimately, control of boundary stability is intended to have a strong influence on mechanical properties. With respect to high-cycle fatigue response, fatigue-induced grain growth has been shown to initiate cracking in nanocrystalline metals. As a potential strategy to suppress such grain growth, particular solute additions are known to stabilize GBs through both thermodynamic and kinetic mechanisms. In previous work, Au additions in nanocrystalline Pt were confirmed to stabilize grain boundaries against thermally-driven GB migration, however, the corresponding effect on fatigue resistance was unknown. In [4], we compared the high-cycle fatigue performance of stabilized Pt-10at.% Au to reference pure Pt with a similar initial grain size, using a combination of ex-situ and in-situ scanning electron microscope fatigue tests. *Ex-situ* tests revealed that the Pt-10at.% Au exhibits substantial improvement in overall fatigue life over Pt, including a 75% elevation of the fatigue endurance limit. The improvement was attributed to enhanced crack initiation resistance, since the Pt-10at.% Au exhibited diminished resistance to crack propagation compared to Pt. Electron backscatter diffraction, transmission Kikuchi diffraction, and

transmission electron microscopy showed that the pure Pt exhibited extensive fatigue-induced abnormal grain growth, with the largest grains growing to 10 times the size of the initial grain size, whereas the Pt-10at.%Au exhibited inhibited grain growth, with the largest grains growing by approximately a factor of two. This study provides clear evidence that thermodynamic strategies used to impart thermal stability can also contribute to improved high-cycle fatigue resistance via suppression of grain-growth induced crack initiation.

Using a newly developed radiation-fatigue ion accelerator end-station, we have revealed surprising initial observation that a nanocrystalline Ni-Fe alloy exhibited improved fatigue resistance under He⁺ irradiation compared to unirradiated conditions [5]. We have attributed this improved fatigue performance to the role of He⁺ irradiation in pinning GBs. The new capability will enable future combined environment studies with ion beam modification, heating up to 1200 °C, uniaxial loading up to 4.5 kN, or cyclic loading at rates of up to 50 Hz.

Future Plans

Fundamentals of GB and junction instability under thermal, mechanical, and irradiation stimuli. We recently elucidated how radiation damage and interfacial defects interplay to control the motion of a $\Sigma 3$ GB by highlighting the role of local atomic shuffling near the boundary due to ion interactions but also the longer range interactions associated with line defects such as facet junction and disconnections. Recognizing the important role of this short vs. long range partition on the stability of GBs, we will further investigate the mechanisms controlling the stability of boundaries for which the short- and long-range atomic interactions are more complex. A fundamental question is how the local disorder and GB defect structure interact at the junction between two or more boundaries. We will examine this question by investigating the correlation between the distribution of short-range atomic configurations and long-range (elastic) interactions of far-from-equilibrium boundaries with their stability. Far-from-equilibrium boundaries will be fabricated by tailoring the energy distribution of the deposition species yielding various degrees of disorder at boundaries. We will examine measure the structure and stability of these boundaries by using a combination of atomic-resolution scanning transmission microscopy and nanomechanics testing and compare these observations with atomistic and phase-field models of these boundaries. The modeling effort will inform our knowledge on the possible unit mechanisms and their interactions within GB network to predict subsequent stability behaviors.

Alloying effects at boundary defects. Going beyond pure metal GBs, previous work from our group and others has shown that local solute segregation at GBs depends on the atomic structure of the boundaries, with high-angle boundaries generally accommodating a greater degree of segregation. However, with the growing recognition that boundary migration is often regulated or influenced by defect migration within the boundary, our intent is to examine the local segregation potential of the atomic region surrounding typical boundary defects such as disconnections, facet junctions, or triple junctions. Not only do we intend to explore how different defect types uniquely segregate solute, but then examine how that solute affects the

stability/mobility of those defects. This study will primarily focus on atomistic modeling using molecular dynamics simulations of Pt-Au and other segregating binary alloy pairs. However, we intend to consider the possibility of experimental confirmations using either our group's Chemi-STEM capabilities and/or a synergistic collaboration with the Atom Probe group (Deveraj) at PNNL. The question of segregation susceptibility at GB defects leads to a question about how the overall segregation potential of a GB evolves as its defect content evolves, as opposed to the current belief that GBs have a fixed segregation potential.

Compositionally gradient nanostructures. Following on our recent model of gradient grain size distributions induced by compositional gradients [6], we are embarking on experimental confirmation of the stabilized gradient nanostructure. A compositional multilayer of Pt-Au consists of top and bottom layers of Pt-10at% Au, with intermediate layers at 5%, 1%, and 0%, with compositional step increments every 200 nm, in a stack that has a total thickness of 2000 nm. Initial experiments indicate that the starting grain size is uniform throughout the stack, but after subsequent annealing a substantial grain size gradient is induced. This grain size gradient is far steeper (~ 100 nm/ μm) than gradients induced by severe plastic deformation. Our intent is to explore the thermal stability of this gradient multilayer. Since the gradient is induced compositionally, we expect that subsequent thermal exposures would only serve to further exacerbate the grain size gradient. In addition, we expect that thermal exposures well below the initial annealing treatment would be inconsequential to the established grain size gradient. Beyond thermal stability, a key question is the mechanical properties. We intend to explore these properties through nanoindentation and thin film tension studies, comparing the hardness gradient, tensile properties and fatigue-crack initiation resistance to uniform nanocrystalline Pt and fully stabilized Pt-10at% Au.

High-throughput characterization of fatigue and irradiation-fatigue response of nanocrystalline metals. Ultimately, our interest is to understand how nanostructured metals, with a high grain-boundary density, respond at the macroscale to thermal-, mechanical-, and irradiation-stimuli. In particular we seek to answer the basic question, are thermally-stabilized GBs also stabilized against thermal and mechanical evolution? We will compare pure nanocrystalline Pt to stabilized Pt-Au under high-cycle fatigue loading conditions. We anticipate that the stabilized Pt-Au alloy will resist fatigue-induced grain growth, resulting in a suppression of the crack initiation process and enhancement of total fatigue life. However, it is unclear if the embrittling nature of the Au solute at the GBs will counteract this enhancement and lead to an overall degradation in fatigue response. In parallel, we will complete our two-year development of a MEMS-based in-situ SEM high-cycle fatigue testing platform that can enable at least a dozen simultaneous, independent fatigue tests in the SEM. Such a tool is expected to play a figurative role in future work, where we can more thoroughly address questions around weakest-link microstructural features and rare, incipient process in GB evolution under mechanical loading.

Publications

1. C.M. Barr, E.Y. Chen, J.E. Nathaniel II, P. Lu, D.P. Adams, R. Dingreville, B.L. Boyce, K. Hattar, and D.L. Medlin, *Irradiation-induced GB facet motion: in-situ observation and atomic-scale mechanisms*, *Sci. Adv.* **8**, abn0900 (2022):.
2. C.M. Barr, S.M. Foiles, M. Alkayyali, Y. Mahmood, P.M. Price, D.P. Adams, B.L. Boyce, F. Abdeljawad, and K. Hattar, *The role of GB character in solute segregation and thermal stability of nanocrystalline Pt-Au*, *Nanoscale* **13**, 3552-3563 (2021).
3. C. Hu, D.L. Medlin, and R. Dingreville, *Disconnection-mediated transition in segregation structures at twin boundaries*, *J. Phys. Chem. Lett.* **12**, 6875-6882 (2021).
4. N.M. Heckman, A. Barrios, C.M. Barr, D.P. Adams, T.A. Furnish, K. Hattar, and B.L. Boyce, *Solute segregation improves the high-cycle fatigue resistance of nanocrystalline Pt-Au*, *Acta Mater.* **229**, 117794 (2022).
5. S.A. Briggs, M. Steckbeck, N.M. Heckman, T.A. Furnish, D.C. Bufford, D. Buller, B.L. Boyce, and K. Hattar, *A combined thermomechanical and radiation testing platform for a MeV linear accelerator*, *Nuclear Inst. Methods B*, **509**, 39-47 (2021).
6. J.M. Monti, E.M. Hopkins, K. Hattar, F. Abdeljawad, B.L. Boyce, and R. Dingreville, *Stability of immiscible nanocrystalline alloys in chemical and thermal gradients*, *Acta Mater.* **226**, 117620 (2022).
7. D. Vizoso, C. Deo, and R. Dingreville, *The effects of dose, dose rate, and irradiation type and their equivalence on radiation-induced segregation in binary alloy systems via phase-field simulations*, *J. Nucl. Mater.* **569**, 153924 (2022):.
8. P.D. Zarnas, B.L. Boyce, J. Qu, and R. Dingreville, *Stress-induced transition from vacancy annihilation to void nucleation near microcracks*, *Int. J. Solids and Struct.* **213**, 103-100 (2021).
9. [invited] L. Lu, Q. Pan, K. Hattar, and B.L. Boyce, *Fatigue and fracture of nanostructured metals and alloys*, *MRS Bulletin* **46**, 258-264 (2021).
10. R.D. Moore, T. Beecroft, G.S. Rohrer, C.M. Barr, E. Homer, K. Hattar, B.L. Boyce, and F. Abdeljawad, *The GB stiffness and its impact on equilibrium shapes and boundary migration: Analysis of the $\Sigma 5$, 7, 9, and 11 boundaries in Ni*, *Acta Mater.* **218**, 117220 (2021).

SNL is managed and operated by NTESS under DOE NNSA contract DE-NA0003525.

Effect of heterogeneous architectures on the mechanical behavior of metallic glasses

Paulo Branicio, University of Southern California

Keywords: metallic glasses, nanoglasses, nanoporous metallic glasses, mechanical behavior, molecular dynamics

Research Scope

This research program aims to understand the intrinsic mechanical behavior mechanisms in heterogeneous metallic glasses (MGs) and nanoglasses (NGs) leading to their deformation and failure. Our work focuses on designing, generating, and characterizing the mechanical properties of heterogeneous MGs by employing MD simulations, visualization, and data analytics. We perform large-scale MD simulations to describe the structure and mechanical behavior and use data analysis to clarify the underpinning mechanisms controlling their mechanical response. This research employs copper-zirconium amorphous alloys. The working hypothesis is that the presence of heterogeneous architectures in the structure of MGs and NGs materials will influence their expected mechanical behavior, enhancing delocalization of deformation and constraining early deformation, consequently augmenting the strength, allowing the generation of structures exceeding the currently achievable strength-to-ductility relationship of MGs and NGs. The recent accomplishments of this research program are briefly summarized below.

Recent Progress

Structural characterization of inert gas condensation (IGC) synthesized nanoparticles based CuZr NG: While NGs can be generated directly by Voronoi tessellation, experimental NG samples are commonly generated by high-pressure consolidation of glass nanoparticles synthesized by IGC. It is fair to question if the two approaches are equivalent. We used MD simulations to investigate the IGC processes leading to the synthesis of $\text{Cu}_{64}\text{Zr}_{36}$ amorphous nanoparticles. We investigated the growth of nanoparticles up to 7.3 nm diameter using long simulations of up to 130 ns, under relatively low pressures in the range of 4 to 10 bars. Results indicate a significant pressure effect on the amorphous nanoparticles' final structure, yet no clear influence on the segregation of Cu atoms to its surface. Cu segregation occurring at all pressures results in a thin Cu-rich layer, about 2.5 Å thick, that coats all nanoparticles. Statistics of Voronoi polyhedra shows that the fraction of full icosahedra in the nanoparticles produced at 4 bars is equivalent to that of BMG produced by melt and quench at 10^9 K/s. Higher pressures result in a lower fraction of full icosahedra. We follow up by using MD simulations to generate an NG model by consolidating IGC-prepared $\text{Cu}_{64}\text{Zr}_{36}$ nanoparticles following a workflow similar to that of experiments. The resulting structure was compared to those of NGs produced following direct generation employing Voronoi tessellation and consolidation of spherical nanoparticles carved from an MG sample. We focused on the characterization of the excess free volume and the Voronoi polyhedral statistics in order to identify and quantify contrasting features of the glass-glass interfaces (GGI) in the three

NG samples prepared using distinct methods. Results indicate that GGIs in IGC-based NGs are thicker and display higher structural contrast with their parent MG structure. Nanoparticle-based methods display excess free volume exceeding 4%, in agreement with experiments. IGC-prepared nanoparticles, which display Cu segregation to their surfaces, generate the highest GGI excess free volume levels and the largest relative interface volume with excess free volume higher than 3%. Voronoi polyhedral analysis indicates a sharp drop in the full icosahedral motif fraction in the GGI in nanoparticle-based NG compared to their parent MG. These results were reported in a recent publication in Scientific Reports (1).

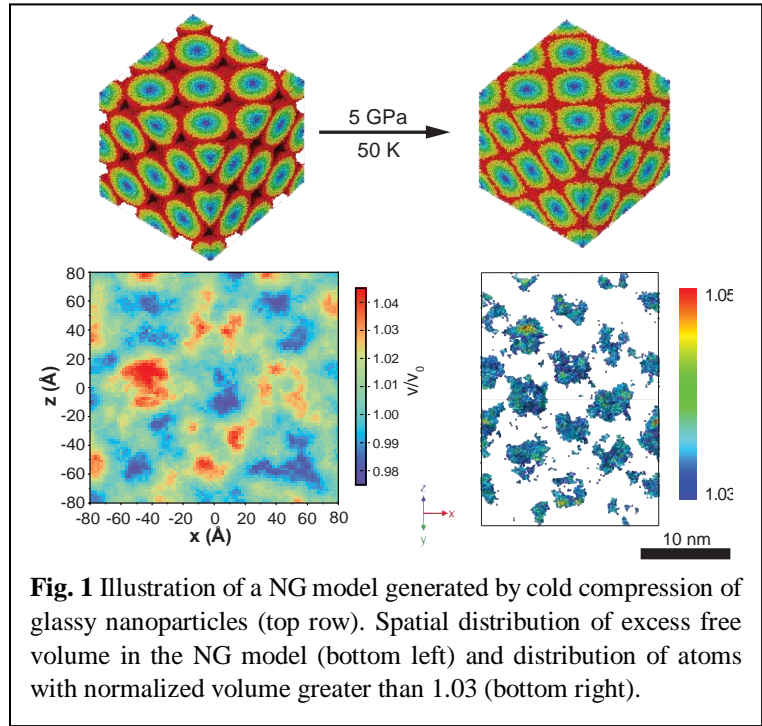


Fig. 1 Illustration of a NG model generated by cold compression of glassy nanoparticles (top row). Spatial distribution of excess free volume in the NG model (bottom left) and distribution of atoms with normalized volume greater than 1.03 (bottom right).

Tuning the mechanical properties of MG and NG composites with brick-and-mortar designs: In a programmatically related investigation, we studied the mechanical behavior of MG-NG composites under uniaxial tensile loading conditions. Samples were constructed from a 3 nm-grain-size $\text{Cu}_{64}\text{Zr}_{36}$ NG matrix and an MG second phase following a brick-and-mortar design. By tuning the volume fraction and arrangement of the second phase, distinct deformation mechanisms

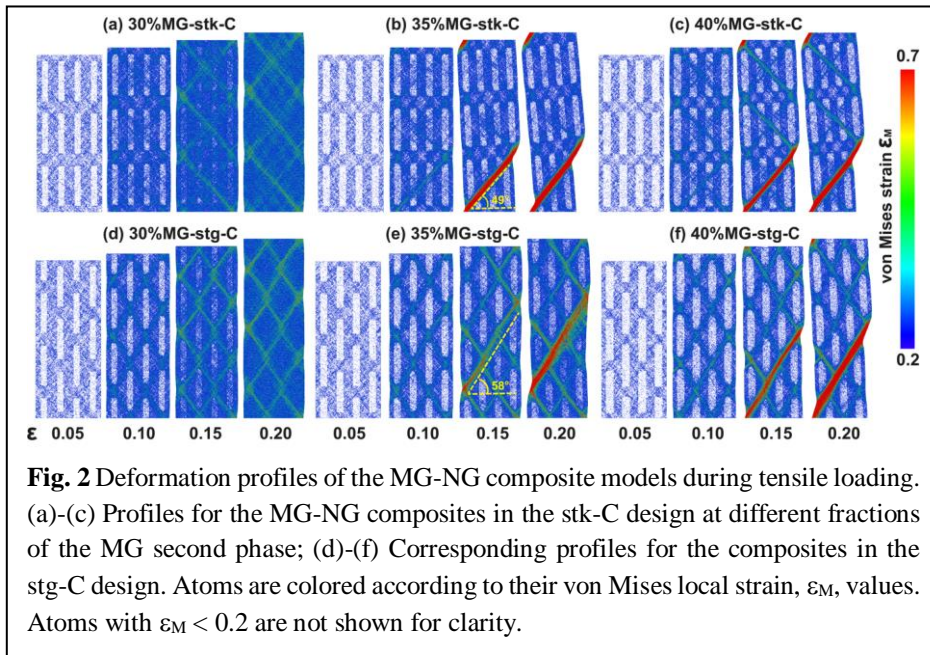


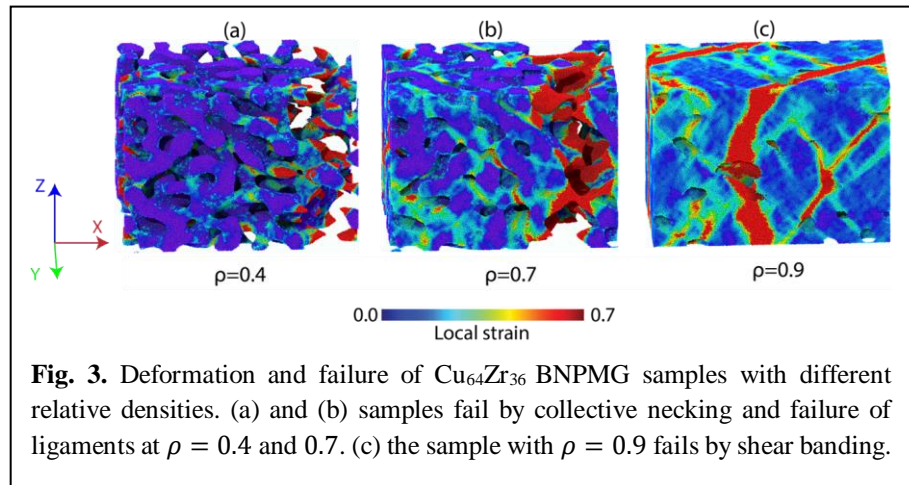
Fig. 2 Deformation profiles of the MG-NG composite models during tensile loading. (a)-(c) Profiles for the MG-NG composites in the stk-C design at different fractions of the MG second phase; (d)-(f) Corresponding profiles for the composites in the stg-C design. Atoms are colored according to their von Mises local strain, ϵ_M , values. Atoms with $\epsilon_M < 0.2$ are not shown for clarity.

were observed. With 30% MG second phase, the composite displayed significantly enhanced overall strength compared with an NG counterpart while preserving the superplasticity of the NG matrix. Higher MG volume fractions resulted in higher strength while sacrificing ductility.

At the same phase fractions, an optimized mechanical synergy of the two phases can be achieved by arranging the MG phase in a staggered way. Such an architecture is able to effectively delocalize local plastic deformation and hence delay the generation of critical shear bands. These results pointing out to new possibilities in the field of MG composites, were published in Scripta Materialia (2).

Mechanical properties and scaling laws of bicontinuous nanoporous MGs: In this investigation of heterogeneous MGs, we focused on the mechanical behavior of porous MG with a bicontinuous topology. Such materials synergize the outstanding properties of MGs and open-cell nanoporous materials. The low-density and high-specific surface area of bicontinuous nanoporous structures have the potential to enhance the applicability of MGs in catalysis, sensors, and lightweight structural designs. We used MD simulations of tensile loading deformation and failure of bicontinuous nanoporous $\text{Cu}_{64}\text{Zr}_{36}$ MG with 55% porosity and 4.4 nm ligament size. Simulation results indicate an anomalous MG mechanical behavior featuring abnormal plastic deformation preceding a typically ductile failure by fracture following successive necking and rupture of ligaments. This work demonstrates that a bicontinuous nanoporous design is able to effectively delocalize strain localization in an MG by utilizing the size-induced brittle-to-ductile transition of MG nanopillars and nanowires. These results were published in Scripta Materialia (3).

We followed up this investigation by studying the scaling laws in bicontinuous nanoporous metallic glasses. MD simulations were employed to study the mechanical properties of nanoporous $\text{Cu}_x\text{Zr}_{1-x}$ MGs with five different compositions, $x = 0.28, 0.36, 0.5, 0.64,$ and 0.72 , and porosity in the range $0.1 < \phi < 0.7$. Results from tensile loading simulations indicate a strong dependence of Young's modulus, E , and Ultimate Tensile Strength (UTS) on porosity and composition. By increasing the porosity from $\phi = 0.1$ to $\phi = 0.7$, the topology of the nanoporous MG shifts from closed cell to open-cell bicontinuous. The change in nanoporous topology enables a brittle-to-ductile transition in deformation and failure mechanisms from a single critical shear band to necking and rupture of ligaments. Genetic Programming (GP) was employed to find scaling laws for E and UTS as a function of porosity and composition. A comparison of the GP-derived scaling laws against existing relationships shows that the GP method is able to uncover expressions that can accurately predict both the values of E and UTS in the whole range of porosity and compositions considered. These results were published in Scripta Materialia (4).



Future Plans

The future goals of this research program are to focus on gradient NGs (GNGs) and are three-fold: i) Elucidate the structure and properties of GGI in IGC-GNGs; ii) Understand the overall mechanical behavior of IGC-GNGs; iii) Understand how the deformation in a GNG relates to the deformation of gradient nanostructured metals and to theoretical predictions of strain gradient plasticity. To enable the emergence and adequately identify the underlying atomistic mechanisms responsible for the strength, deformation, and failure of GNGs, it is imperative to employ fully atomistic models. We will investigate CuZr GNG models with glassy particle sizes in the range of 3 to 20 nm. The research is planned to follow four aims, which will provide the essential ingredients to further our understanding of the mechanical behavior of GNGs:

1) Establish the methodology and construct realistic IGC-GNG atomistic models for mechanical testing at different conditions and characterize the nanostructures generated; 2) Investigate the GGI potential energy landscape and its diffusional properties. 3) Perform MD simulations of tensile and compressive loading on different

IGC-GNG models; 4) Analyze the relationship between the GNG deformation profile and intrinsic deformation mechanisms to those of gradient nanostructured metals, gradient MGs, and theoretical predictions.

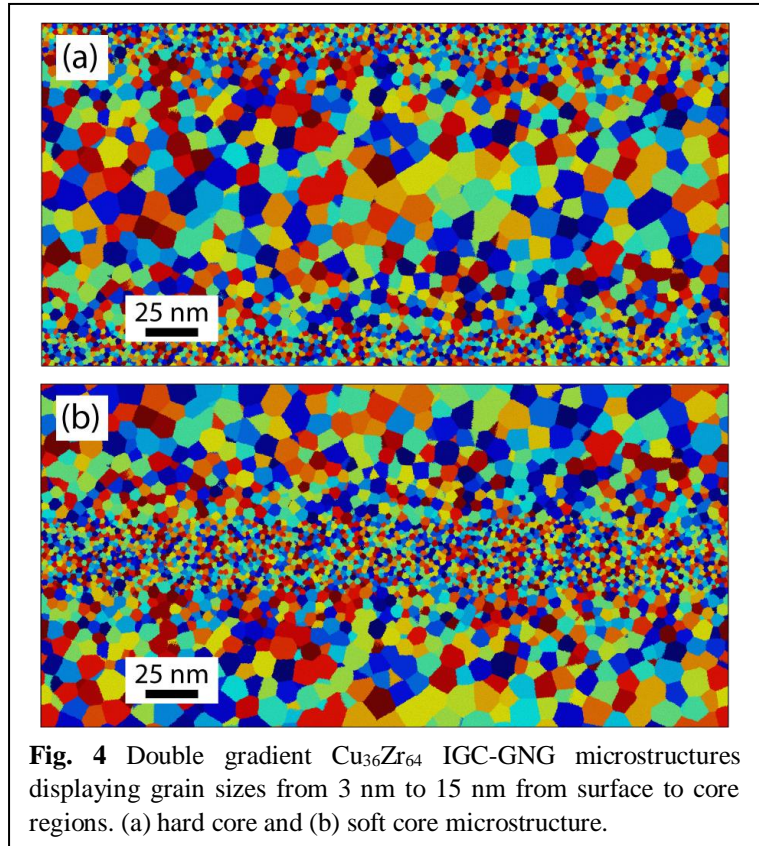


Fig. 4 Double gradient Cu₃₆Zr₆₄ IGC-GNG microstructures displaying grain sizes from 3 nm to 15 nm from surface to core regions. (a) hard core and (b) soft core microstructure.

References

1. K. Zheng, S. Yuan, H. Hahn, and P. S. Branicio, *Excess free volume and structural properties of inert gas condensation synthesized nanoparticles based CuZr nanoglasses*, *Scientific Reports*, **11**, 19246 (2021).
2. S. Yuan and P. S. Branicio, *Tuning the mechanical properties of nanoglass-metallic glass composites with brick and mortar designs*, *Scripta Materialia*, **194**, 113639 (2021).
3. C. Liu, S. Yuan, and P. S. Branicio, *Bicontinuous nanoporous design induced homogenization of strain localization in metallic glasses*, *Scripta Materialia* **192**, 67 (2022).
4. C. Liu, S. Yuan, J. Im, F. P. J. de Barros, S. F. Masri, and P. S. Branicio, *Mechanical properties, failure mechanisms, and scaling laws of bicontinuous nanoporous metallic glasses*, *Acta Materialia* **239**, 118255 (2022).

Publications

1. C. Liu, S. Yuan, J. Im, F. P. J. de Barros, S. F. Masri, and P. S. Branicio, *Mechanical properties, failure mechanisms, and scaling laws of bicontinuous nanoporous metallic glasses*, *Acta Materialia* **239**, 118255 (2022).
2. K. Zheng, S. Yuan, H. Hahn, and P. S. Branicio, *Excess free volume and structural properties of inert gas condensation synthesized nanoparticles based CuZr nanoglasses*, *Scientific Reports*, **11**, 19246 (2021).
3. S. Yuan and P. S. Branicio, *Tuning the mechanical properties of nanoglass-metallic glass composites with brick and mortar designs*, *Scripta Materialia*, **194**, 113639 (2021).
4. C. Liu, S. Yuan, and P. S. Branicio, *Bicontinuous nanoporous design induced homogenization of strain localization in metallic glasses*, *Scripta Materialia* **192**, 67 (2022).
5. H. Li, Q. X. Pei, Z. D. Sha, and Paulo S. Branicio, *Intrinsic and extrinsic effects on the fracture toughness of ductile metallic glasses*, *Mechanics of Materials* **162**, 104066 (2021).

Beyond Shear: Improving the Prediction of Plastic Deformation Activation in HCP Materials

Ashley Bucsek¹, Huseyin Sehitoglu²

¹University of Michigan, ²University of Illinois at Urbana-Champaign

Keywords: plastic deformation, deformation twinning, hcp metals, titanium, x-ray diffraction

Research Scope

The goal of this research program is to improve the prediction of the onset of plastic deformation in hcp materials by studying the sensitivities of slip and twin activation to the local 3D stress state. Slip and twinning activation is predicted using a critical resolved shear stress (CRSS) criterion that states that a specific deformation mode will initiate when its unique CRSS value is exceeded: This is known as *Schmid's law*. Although Schmid's law was originally derived for fcc materials, today, Schmid's law is applied for materials across all crystallographic structures. For hcp materials, reports showing a breakdown of Schmid's law called non-Schmid behavior are prolific. In addition to microscale explanations for non-Schmid behavior (e.g., grain neighborhood effects), research has shown that the 3D anisotropic atomic configurations involved with slip in non-fcc materials can lead to sensitivities to the full 3D stress state (i.e., *beyond* the resolved shear stress). Because the atomic configuration between slip and twin nucleation are closely related, this implies that non-fcc twinning will also be sensitive to the full 3D stress state. We hypothesize that accounting for these sensitivities can improve the prediction of slip and twinning in hcp materials and, as a result, improve the prediction of the onset of deformation in lightweight hcp metals. To test this hypothesis, we propose an integrated theoretical and experimental approach to connect the atomic-scale origins of non-Schmid behavior to microscale crystal plasticity and macroscale yield phenomena. Using titanium (Ti) as a model hcp material system, slip/twin dislocation core structures will be determined with atomistic simulations and high-resolution transmission electron microscopy (HRTEM) and used to develop a modified Schmid law based on a modified Peierls Nabarro formalism that includes sensitivities to the 3D stress state. Then, the modified Schmid law will be informed and validated by microscale measurements of the local, intragranular 3D stress state and subsequent slip/twin modes in single and polycrystalline samples using in-situ point-focused high-energy diffraction microscopy (pf-HEDM).

Recent Progress

2.1 Analytical Prediction of CRSS in Ti Undergoing Slip: The CRSS is determined from the intrinsic lattice resistance to overcome for dislocation motion. The lattice resistance is associated with atomic-scale restoring forces operating across the slip plane of the dislocation. In order to quantify this resistance, a clear understanding of the dislocation core is required. In Ti,

the slip mechanism is complex and involves a mechanism called a “locking-unlocking mechanism” [1], which is due to the transition between the sessile-glissile configurations under applied stress. (This mechanism is schematically depicted in **Fig. 1**, consisting of the sessile (a), intermediate (b,c) and, glissile (d) configurations.) Under applied stress, the sessile core spreads on the pyramidal plane and cross-slips to the pyramidal plane and starts gliding. However, the core spread in a prismatic plane is metastable, in contrast to the stable configuration on the pyramidal plane. Hence, this mechanism will result in a deviation from conventional Schmid behavior (which only considers specific plane for glide and does not account for the cross-slipping). An analytical model to predict this mechanism is currently not available. We aim to develop a predictive

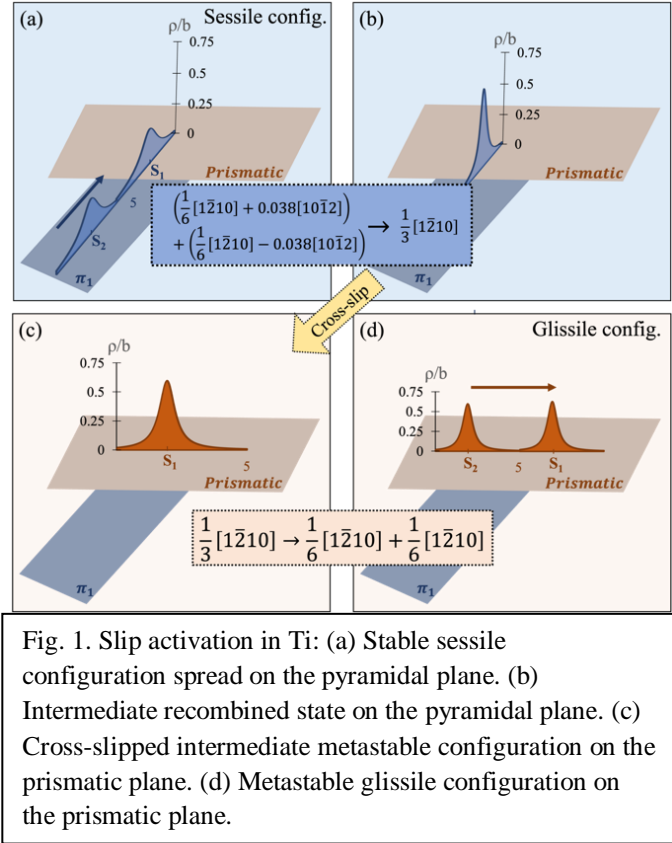


Fig. 1. Slip activation in Ti: (a) Stable sessile configuration spread on the pyramidal plane. (b) Intermediate recombined state on the pyramidal plane. (c) Cross-slipped intermediate metastable configuration on the prismatic plane. (d) Metastable glissile configuration on the prismatic plane.

model that captures this non-trivial slip activation mechanism for an accurate estimation of the associated critical stress. The total energy of the structure is calculated by utilizing anisotropic Eshelby-Stroh formalism and a new Wigner-Seitz Cell misfit model [2].

2.2 Energetics of the $\{11\bar{2}1\}$ Twin Mode: Our progress so far has focused on determining the energetics of $\{11\bar{2}1\} \langle 11\bar{2}6 \rangle$ twin system. The $\{11\bar{2}1\}$ twin is one of the most well studied hcp twin modes, yet, key challenges remain regarding the twin boundary (TB) structure. The inherent corrugation of $\{11\bar{2}1\}$ planes prevents the construction of equilibrium TB as a reflective TB. Here, we have utilized the concept of lattice offsets. Lattice offsets describe the relative positioning of the twin variants necessary for energetically favorable equilibrium structure while satisfying volume invariancy criteria [3]. Our work has revealed that only the lattice offset along $\langle \bar{1}100 \rangle$ takes a non-zero value. The next step in our study of Ti $\{11\bar{2}1\}$ twinning is the determination of shear-shuffle partitioning of TB migration mechanism. TB migration or twinning mechanism is the displacement pathway that the atoms follow as one twin variant consumes the other. As one twin variant grows at the expense of the other, complementary movements called shuffles are needed to complete the twinning. Our work elucidated that atoms shuffle in opposite directions with equal magnitude along $\langle \bar{1}100 \rangle$ direction during TB migration, and the shuffle magnitude is $0.083|\langle \bar{1}100 \rangle|$.

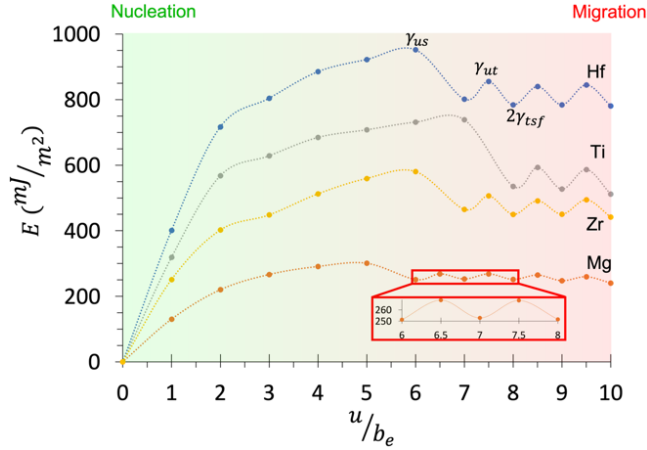


Fig. 2. GPFE curves for the $(11\bar{2}1)$ twin mode for select hcp metals. The peak point of the a curve represents the twin nucleation energy barrier γ_{us} and is followed by periodic dips indicating the TB migration regime. These energetically degenerate points indicate the energy of dual TBs encapsulating a twin nucleus $2\gamma_{tsf}$. The TB migration barrier is dictated by the height of the periodic peaks in TB migration portion, i.e. $\gamma_{TBM} = \gamma_{ut} - 2\gamma_{tsf}$. Inset shows the TB migration portion of the GPFE for Mg.

Finally, there is a lack of GPFE curves for $\{11\bar{2}1\}$ twin system in literature. The calculation of the GPFE curve requires one to prescribe the twinning shear displacement while selectively allowing the shuffling motions. Unambiguous determination of shear-shuffle partition enables us to calculate GPFE curves reliably through ab-initio DFT (Fig. 2). On a GPFE curve, the first peak characterizes the energy barrier for twin nucleation γ_{us} . Subsequent periodic dips in the curve marks the interface energy of two TBs encapsulating a twin embryo $2\gamma_{tsf}$. We have discovered the thickness of the smallest twin embryo which is dictated by the placement of the first $2\gamma_{tsf}$ dip varies from metal to metal.

2.3 Local, Intragranular Deformation Characterization Using pf-HEDM: The

ability to “watch” local, intragranular, sub-surface stress concentrations develop (e.g., Fig. 3) and then activate specific plastic deformation modes across large, statistically relevant volumes does not currently exist. PI Bucsek is working toward achieving these capabilities for the purpose of testing the atomic-scale-derived CRSS values and modified Schmid law that Co-PI Sehitoglu is developing. Pf-HEDM, also known as scanning 3D X-ray diffraction (scanning 3DXRD), is capable of intragranular orientation and intragranular elastic strain tensor measurements inside and across bulk 3D specimens (nondestructively) (Fig. 4). Previously only demonstrated at the European Synchrotron Radiation Facility (ESRF), PI Bucsek recently demonstrated pf-HEDM capabilities on 1-ID at the Advanced Photon Source (APS) in collaboration with APS scientists. These preliminary measurements were taken on a Ti sample that was strained to 7% with a residual strain of 6.5%, demonstrating the ability to apply this technique to even severely deformed materials. These first results were used to develop a new pf-HEDM reconstruction algorithm that incorporated the unique overlapping peak separation capability of the APS software MIDAS. This algorithm was then used to measure the intragranular misorientation and 3D elastic strain tensor across the Ti specimens (Fig. 3, Fig. 4). Note: This is the first-ever intragranular misorientation map measured using pf-HEDM (or scanning 3DXRD), as this aspect of the microstructure was not resolvable via pf-HEDM using other existing data

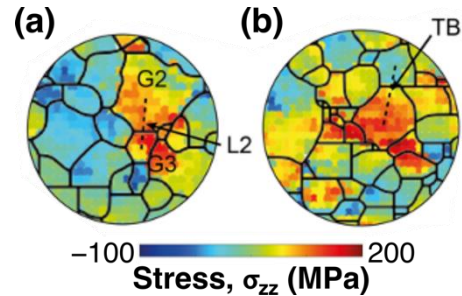


Fig. 3. Local stress σ_{zz} concentrations at grain (a) and twin (b) boundaries measured inside a bulk 3D volume using pf-HEDM.

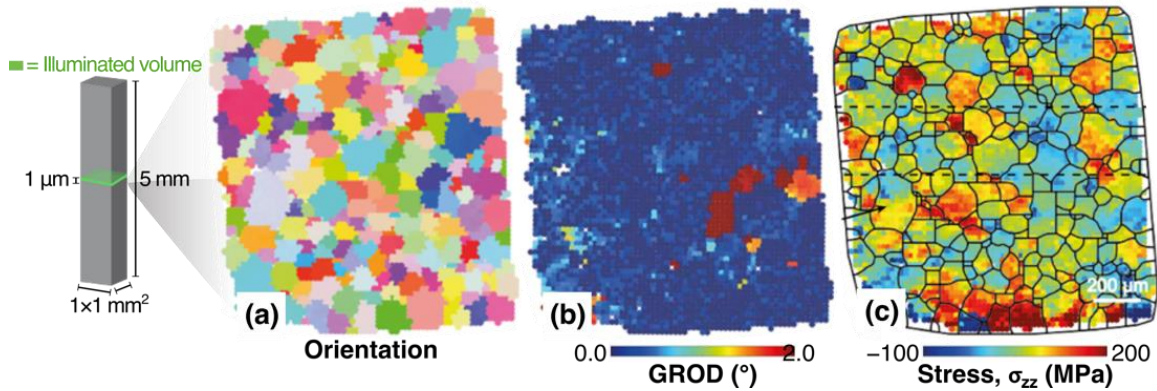


Fig. 4. Pf-HEDM measurements on 1-ID at the APS, analyzed using a new reconstruction algorithm. These reconstructions show the spatially resolved crystallographic orientation (a), grain reference orientation distribution (GROD) or intragranular misorientation (b), and stress calculated from the 3D elastic strain tensor (c) corresponding to one 2D layer inside a bulk Ti specimen that was plastically deformed to 6.5% residual strain (spatial resolution $1 \mu\text{m} \times 10 \mu\text{m}$).

reduction procedures. More recently, PI Bucsek conducted pf-HEDM measurements during in-situ loading of a Ti specimen, capturing the initial microstructure, the microstructure just before macroscopic yield, and the microstructure just after macroscopic yield. These measurements will be used to develop procedures for identifying the local activation of new slip and twin systems, including the local 3D stress state at stress concentration points that precedes this activation.

Future Plans

Our future aims include the following tasks:

- (1) Determine the CRSS for the major slip and twin systems in Ti by considering the complexity of the interfaces and a novel theoretical framework (Sehitoglu). These values will be tested using in-situ pf-HEDM measurements of slip and twin activation in a multi-grain environment as a function of stress state (Bucsek).
- (2) Determine the deviations from Schmid law upon cross-slip from pyramidal to prismatic slip planes accounting for the energy barriers (Sehitoglu). The in-situ pf-HEDM experiments will be used to test this proposed mechanism, and the theory will be modified based on experimental observations (Bucsek).
- (3) Develop a model for slip/twin dislocation core interactions and elevation of the CRSS (Sehitoglu) and compare with experimental measurements of such interactions on stress-strain curves (Bucsek).
- (4) Develop a modified Schmid law (for slip and twinning) that will be informed and validated by microscale measurements of the local 3D stress state and subsequent slip/twin modes using in-situ pf-HEDM (Bucsek-Sehitoglu).

References

- [1] E. Clouet, D. Caillard, N. Chaari, F. Onimus, D. Rodney, Dislocation locking versus easy glide in titanium and zirconium, *Nature Materials* 14(9) 931-936, (2015).
- [2] A.S.K. Mohammed, O.K. Celebi, H. Sehitoglu, Critical stress prediction upon accurate dislocation core description, *Acta Materialia* 233 117989, (2022).
- [3] G. Gengor, A.S.K. Mohammed, H. Sehitoglu, $\{101^{-} 2\}$ Twin interface structure and energetics in HCP materials, *Acta Materialia* 219 117256, (2021).

Elucidating the influence of bulk slip morphology on hydrogen environment-assisted cracking behavior in precipitation-hardened alloys

James T. Burns, Associate Professor, University of Virginia

Keywords: H-embrittlement, cracking, grain boundary, slip

Research Scope

The exposure of metallic structural components to hydrogen (H)-producing/containing environments can lead to a degradation in mechanical performance characterized by increased crack growth rates, reduced fracture toughness, and decreased ductility and fracture stress. The hydrogen embrittlement (HE) phenomenon has been extensively studied in the over the past half-century. However, despite these efforts, HE remains a prominent failure mode in aerospace, marine, energy, chemical, and infrastructure applications. In addition to these ongoing challenges, the recent exploration of H-based renewable energy solutions for transportation and commercial applications has reinvigorated the field. However, there remains foundational knowledge gaps in (1) the understanding of the governing damage physics, (2) how the failure mode depends on material microstructure, and (3) the link between the micromechanical failure mechanisms and the macroscale material properties.

The overarching objective of the proposed research is to elucidate the mechanistic influence of bulk slip morphology on the HEAC behavior of a model precipitation-hardened alloy by coupling high-fidelity fracture mechanics testing methods with a state-of-the-art multiscale characterization strategy that leverages correlative S-EBSD, HR-EBSD, FIB/TEM, and PED. The following specific research questions will be addressed. First, for a constant global mechanical driving force (*e.g.*, stress intensity factor), grain size, grain orientation, and hydrogen uptake behavior, do differences in bulk slip morphology result in quantitatively different (both spatially and in intensity) near-crack plastic deformation distributions during HEAC? Addressing this question will rigorously establish the causal role of bulk slip morphology on HEAC susceptibility by controlling possible obfuscating factors. Second, how does the observed deformation distributions proximate to the crack at a constant stress intensity factor vary as a function of grain orientation and environmental severity (*e.g.*, hydrogen uptake behavior) for a given bulk slip morphology? Addressing this question will establish the sensitivity of observed deformation distributions for a given bulk slip morphology to two expected modifying influences. This will provide insights into (1) the mechanistic contribution of H content on crack propagation and (2) the impact of grain orientation on the deformation responsible for crack propagation. Third, differences in bulk slip morphology impact the deformation distribution *in front* of the crack tip for a constant applied stress intensity factor and hydrogen uptake behavior? Any observed variations in deformation distribution and grain boundary-deformation interactions proximate to the crack tip can provide a mechanistic pathway to understand *how* bulk slip morphology may

induce differences in HEAC propagation metrics for a constant stress intensity factor and H uptake behavior.

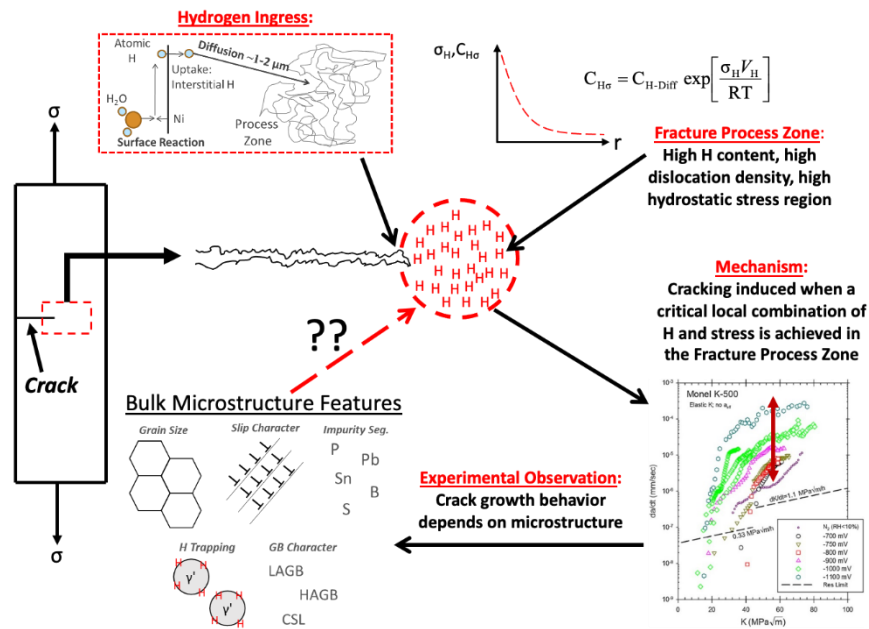


Figure 1 - Overview of hydrogen (H) environment-assisted cracking process and the mechanistic importance of understanding how bulk microstructure features impact the local hydrogen and stress distributions in the fracture process zone that are ultimately responsible for crack propagation.

Recent Progress

Grant logistics being finalized. A PhD student (Javon Smith) has joined the research group and has begun training on executing the proposed EAC testing and characterization. Additionally, we have engaged with American Elements to get the quote and procure the material.

Future Plans

Once the grant logistics are finalized and the funding is available work will begin on executing the tasks laid out in the proposal. Task #1 will focus on obtaining material and identify targeted heat treatment protocols. The objective of this task will be to develop heat treatment protocols to obtain desired grain size and precipitate morphology for subsequent tasks. Task #2 will aim to establish variations in precipitate morphology, bulk slip morphology, and diffusible hydrogen concentration as a function of aging time. The objective of this task will be two-fold. First, to confirm that bulk slip morphology and precipitate character varies as expected for the selected aging times. Second, to isolate the effect of hydrogen uptake when assessing HEAC susceptibility as a function of aging time in subsequent tasks. Task #3 will aim to assess HEAC susceptibility via high-fidelity fracture mechanics testing. The objective of this task will be to

establish the HEAC susceptibility of each aging condition for a range of environmental severities (quantified by the hydrogen uptake data collected in Task #2) to identify conditions of interest for further evaluation. Task #4 will leverage a multiscale characterization approach to develop mechanistic links between bulk deformation character and near-crack deformation as a function of pertinent variables. The objective of this task will be to couple local and global evaluations of the deformation proximate to the crack path to elucidate the mechanistic influence of hydrogen content, bulk slip morphology, and grain orientation on HEAC behavior.

References

None.

Publications

None

Data Driven Approach to Dislocation-Based Plasticity Models of Face-Centered Cubic Metals

Wei Cai, Stanford University

Keywords: dislocation dynamics, crystal plasticity, strain hardening

Research Scope

Dislocation dynamics controls plastic deformation, mechanical strength, and failure of crystalline materials. It also governs fatigue resistance under cyclic loading, creep resistance at elevated-temperature, and radiation resistance for reactor applications. There is a compelling need for understanding fundamental dislocation mechanisms for deformation because virtually all structural metals used in energy systems are fabricated to desired forms and shapes by deformation processes. To date, the most outstanding problem in a physics-based multiscale model of crystal plasticity is the lack of quantitative connections between continuum plasticity (CP) models with the lower scale dislocation models. As a result, existing CP models used in engineering applications are still phenomenological, while evidence continues to mount that they can make inaccurate predictions under realistically complex scenarios.

This project will take advantage of the recent advances in high-performance discrete dislocation dynamics (DDD) simulations and data science approaches to establish the first fully connected multiscale plasticity model for pure face-centered cubic (FCC) single crystals. In particular, we will use large scale DDD simulation to provide quantitative connections to: continuum plasticity models, high strain rate deformation experiments, and molecular dynamics models. Our research will answer the following fundamental questions in the plastic response of FCC metals. (1) What are the dominant microstructural features (beyond total dislocation density) that need to be retained when coarse-graining the discrete dislocation network into a continuum field description? (2) What dislocation properties (such as mobility and initial structure) influence the stress-strain response of single crystals at the 10^3 - 10^4 s⁻¹ strain rates as measured by Kolsky bar experiments? (3) How dislocation interaction mechanisms at the atomistic scale (e.g., jog formation) influence dislocation multiplication and pattern formation?

Recent Progress

1. Rate of Dislocation Cross slip

Cross slip of screw dislocations in crystalline solids is a stress-driven thermally activated process essential to many phenomena during plastic deformation, including dislocation pattern formation, strain hardening, and dynamic recovery. Molecular dynamics (MD) simulation has played an important role in determining the microscopic mechanisms of cross slip. However, due to its limited timescale, MD can only predict cross-slip rates in high-stress or high-temperature conditions. The transition state theory can predict the cross-slip rate over a broad range of stress

and temperature conditions, but its predictions have been found to be several orders of magnitude too low in comparison to MD results. This discrepancy can be expressed as an anomalously large activation entropy whose physical origin remains unclear.

We have resolved this long-standing discrepancy by showing that the large activation entropy results from anharmonic effects, including thermal softening, thermal expansion, and soft vibrational modes of the dislocation. We expect these anharmonic effects to be significant in a wide range of stress-driven thermally activated processes in solids. We will submit this work for publication shortly [1].

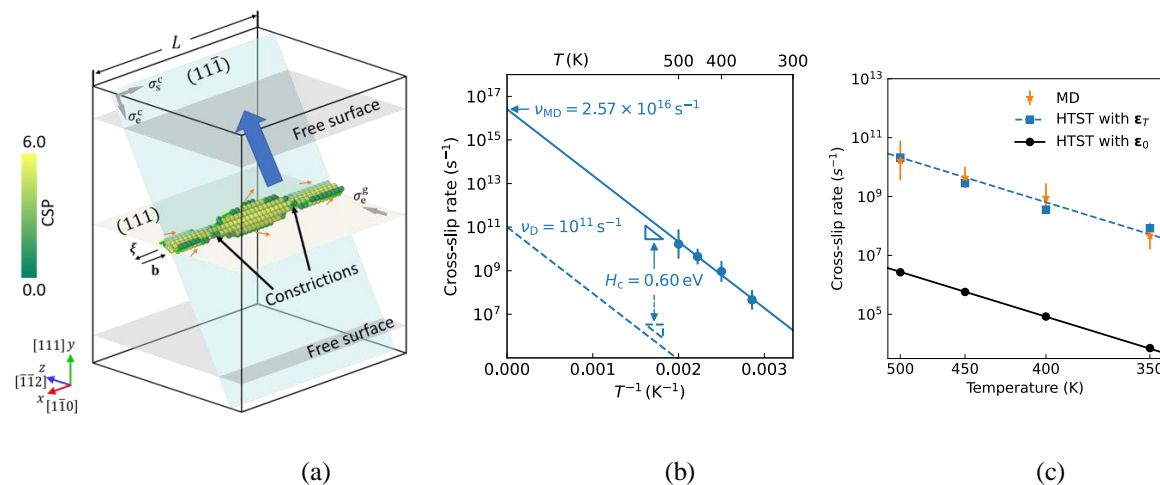


Figure 1. (a) Simulation cell containing a screw dislocation along the x -direction. (b) Cross-slip rates at different temperatures obtained by MD simulations (solid line) and predicted by transition state theory (TST). (c) With proper account for the anharmonic effects, the TST predictions (squares) are now in very good agreement with MD simulations (arrows).

2. The First Direct Comparison between Experiments and Dislocation Dynamics

A long-standing challenge in computational materials science is to establish a quantitative connection between the macroscopic properties of plastic deformation with the microscopic mechanisms of dislocations in crystalline materials. Although the discrete dislocation dynamics (DDD) simulation method has been developed for several decades with the goal of addressing this challenge, a one-to-one comparison between the DDD predictions on single crystal stress-strain curves and experimental measurements under identical conditions has not been possible to date. Such a comparison is an essential step towards establishing a dislocation-physics based theory of plasticity and a multiscale framework of the plastic behaviors of crystalline materials. Here we provide direct comparisons between the stress-strain curves of Cu single crystals under high strain rate loading in the $[0\ 0\ 1]$ and $[0\ 1\ 1]$ directions obtained from miniaturized desktop Kolsky bar experiments and those from DDD simulations under identical loading conditions.

With an appropriate set of parameters, DDD simulations can produce stress-strain curves that are in reasonable agreement with the experimental results. However, the dislocation mobility values needed to achieve this agreement are an order of magnitude lower than expected based on

previous measurements and atomistic simulations. We attribute this discrepancy to possible drag forces from jogs and point defects produced during the plastic deformation. Cross-slip of screw dislocations is also found to be necessary to capture the experimental stress-strain behavior, especially for the [0 1 1] loading direction. This work provides an example of how direct comparisons between DDD simulations and experimental measurements can provide new insight into the fundamental mechanisms of plastic deformation. This work is currently under review in Acta Materialia [2].

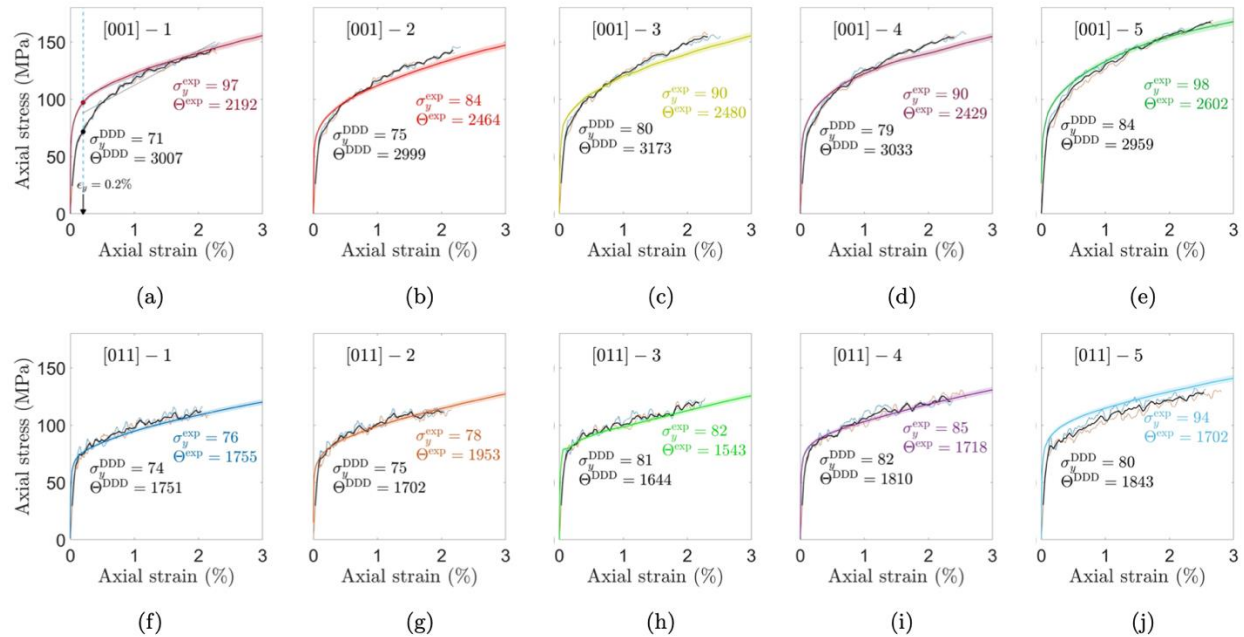


Figure 2. Comparison of stress-strain curves from experiments and DDD simulations. In each case, two different initial configurations were used to perform simulations, results of which are shown by thin lines. Thick black lines show the averaged values of two simulations. Experiments are shown in color with 2% error margin.

3. Mechanisms of Strain Hardening from Dislocation Dynamics

We have previously extracted a crystal plasticity flow rule from a large database of Discrete Dislocation Dynamics (DDD) simulations of face-centered cubic (FCC) Cu. The flow rule predicts the plastic shear rate $\dot{\gamma}_i$ on slip system i given the resolved shear stress τ_i and the dislocation density ρ_j on all slip systems $j = 1, \dots, 12$. We now succeeded in obtain more insights on the dislocation mechanisms underlying such a (homogenized) flow rule, by connecting the plastic shear rate $\dot{\gamma}_i$ with the structure and dynamics of dislocation links on slip system i .

First, we show that the length of dislocation links on every one of the 12 slip systems (from DDD simulations of >100 loading orientations) satisfy a statistical distribution that is either a sum

of two exponentials,
$$n_i(l) = \frac{N_i^{(1)}}{\bar{l}_i^{(1)}} e^{-l/\bar{l}_i^{(1)}} + \frac{N_i^{(2)}}{\bar{l}_i^{(2)}} e^{-l/\bar{l}_i^{(2)}}$$
 or a single exponential (see Fig. 3). The second exponential corresponds to a very small fraction of dislocations that are much longer (e.g. 10 times

average length) than the majority of the dislocation lines, and are only present in active slip systems. They may be considered as ‘long-tails’ in the distribution, associated with ‘run-away’ mobile dislocations.

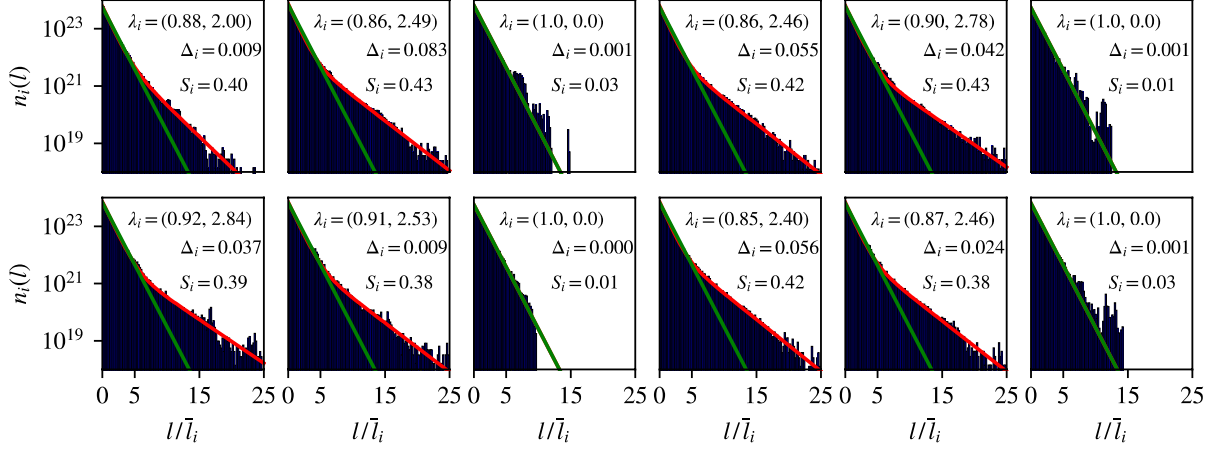


Figure 3. Link length distribution of dislocations on (12) individual slip systems corresponding to a DDD simulation along the [3 5 98] loading orientation, averaged over shear strain window in the range of 0.9 – 1.1%. The link lengths on active slip systems satisfy double-exponential distribution, while those on inactive slip systems satisfy single exponential distribution.

Second, we obtained a dislocation link velocity function, $\bar{v}(\tau_i, l_i)$, which predicts the average velocity of a dislocation link of length l_i under resolved shear stress τ_i for any slip system i . The average velocity function provides the connection between the microscopic link length distribution $n(l_i)$ and the macroscopic shear rate $\dot{\gamma}_i$ through a generalized Orowan’s equation.

$$\dot{\gamma}_i = \int_0^{\infty} \dot{\gamma}_i(l) dl = \int_0^{\infty} n_i(l) \bar{v}(\tau_i, l) b l dl$$

Future Plans

1. We will test our hypothesis that the anomalously large activation entropy in dislocation cross-slip also occurs in a wide range of stress-driven thermally activated processes in solids. We will start with the kink pair nucleation mechanisms of screw dislocation motion in BCC metals.
2. We are testing the hypothesis that jogs are responsible for the gap in dislocation mobility values obtained by comparing DDD simulations to experiments and those in the literature (from MD simulations). We will proceed by examining the effect of jogs on dislocation mobility in MD simulations, and by accounting for jog formation in DDD simulations.
3. We are preparing a journal publication reporting the dislocation link length statistics and kinetics during DDD strain hardening simulations. We believe the average dislocation link velocity function provides a good way to link the macroscopic shear rate on slip system with the microscopic dynamics of dislocations.

References

1. Y. Wang and W. Cai, *Stress-dependent activation entropy in thermally activated cross-slip of dislocations*, to be submitted.
2. Sh. Akhondzadeh, M. Kang, R. B. Sills, K. T. Ramesh, W. Cai, Direct Comparison between Experiments and Dislocation Dynamics Simulations of High-Rate Deformation of Single Crystal Copper, submitted to *Acta Materialia* (2022).

Publications

1. H. D. Deng, H. Zhao, N. Jin, L. A. Hughes, B. H. Savitzky, C. Ophus, D. Fraggedakis, A. Borbely, Y.-S. Yu, E. G. Lomeli, R. Yan, J. Liu, D. A. Shapiro, W. Cai, M. Z. Bazant, A. M. Minor, W. C. Chueh, “Correlative image learning of chemo-mechanics in phase-transforming solids”, *Nature Materials*, **21**, 547 (2022).
2. Sh. Akhondzadeh, N. Bertin, R. B. Sills, W. Cai, “Slip-free multiplication and complexity of dislocation networks in FCC metals”, *Materials Theory*, **5**, 2 (2021).
3. N. Bertin, W. Cai, S. Aubry, V. V. Bulatov, “Core energies of dislocations in bcc metals”, *Phys. Rev. Mater.*, **5**, 025002, (2021).
4. Sh. Akhondzadeh, R. B. Sills, N. Bertin, W. Cai, “Dislocation Density-Based Plasticity Model from Massive Discrete Dislocation Dynamics Database”, *J. Mech. Phys. Solids*, **145**, 104152, (2020).
5. W. P. Kuykendall, Y. Wang, W. Cai, “Stress Effects on the Energy Barrier and Mechanisms of Cross-Slip in FCC Nickel”, *J. Mech. Phys. Solids*, **144**, 104105, (2020).
6. I. Ryu, J. D. Gravell, W. Cai, W. D. Nix, H. Gao, “Intrinsic size dependent plasticity in BCC micro-pillars under uniaxial tension and pure torsion”, *Extreme Mechanics Letters*, **40**, 100901, (2020).
7. N. Bertin, R. B. Sills, W. Cai, “Frontiers in the Simulation of Dislocations”, *Annual Review of Materials Research*, **50**, 437 (2020).
8. E. Van der Giessen, et al. “Roadmap on Multiscale Materials Modelling”, *Model. Simul. Mater. Sci. Eng.*, **28**, 043001 (2020).
9. D. Vorselen, Y. Wang, M. Footer, W. Cai, J. Theriot, “Microparticle traction force microscopy reveals subcellular force exertion patterns in immune cell-target interactions”, *Nature Comm.*, **11**, 20 (2020).

The Role of Local Chemical Order on Defect Kinetics in Alloys under Irradiation

Penghui Cao, University of California, Irvine

Keywords: Irradiation, Local chemical order, Defects, Dislocation, Vacancy

Research Scope

As an emerging class of materials, multi-principal element alloys (MPEAs) have attracted increasing attention owing to their extraordinary properties, including diminished radiation defects, enhanced swelling resistance, and suppressed solute segregation when compared to traditional solid solutions. While the fundamental atomic mechanisms and their correlation to the improved radiation performance remain to be elucidated, this project speculates that the hidden local chemical order¹ may be the salient feature that makes MPEAs distinct from traditional alloys, plays a vital role in radiation defect dynamics and kinetics, and contributes to the improved radiation tolerance. The overarching goal of this research is to understand the role of local chemical order on the kinetics of defects in MPEAs under irradiation and to evaluate the mechanistic strategy for controlling radiation defects migration and evolution through tailoring the degree of local ordering at the nanoscale. The research focuses on single-phase MPEAs and addresses the following fundamental questions regarding local ordering: (i) how does the local chemical order influence defect migration, coalescence, and growth; (ii) what are the new atomistic mechanisms and processes enabled by local order that could lead to radiation damage reduction; and (iii) is tuning the degree of local ordering able to promote defect recombination and to alleviate radiation-induced damage accumulation? Specifically, research activities are driven by three mechanistic hypotheses pertaining to the role of local ordering on point defects, defect clusters, and grain boundaries: (1) the presence of local chemical order raises migration energy barriers of point defects and localizes their diffusion; a localized diffusion can promote defects recombination and mitigate defect cluster growth; (2) local chemical order roughens the potential energy landscape, which can locally pin a dislocation loop and reduce its diffusivity; and (3) the introduced local ordering in the grain matrix increases grain boundary migration energy and lowers its mobility. These hypotheses will be evaluated in single-phase MPEAs using integrated theoretical and computational techniques, including molecular dynamics, Monte Carlo, accelerated molecular dynamics, climbing image nudged elastic band method, and a machine learning tool. The modeling and theoretical predictions will be validated by targeted experiments, including energy-dispersive x-ray spectroscopy characterization and in-situ ion irradiation. Evaluation of these hypotheses will advance the fundamental understanding of atomistic mechanisms underlying the extraordinary properties of MPEAs, facilitate material design strategies to manipulate defect behaviors via tailoring nanoscale features, and result in tunable material properties.

Recent Progress

Dislocation: revealing the role of chemical short-range order on dislocation motion in MPEAs.

This study² samples and reconstructs the energy landscape formed by concentrated solid solutions and reveals the saddle point activation events along minimum energy pathways that trigger individual mechanisms (Peierls mechanism, kink-pair formation, and lateral kink glide) underlying

screw dislocation motion. Considering a model bcc MoNbTaW alloy using a state-of-the-art machine learning interatomic potential that captures solute interactions and ordering, we reveal that the potential energy landscape (PEL) demonstrates hierarchical structures with large metabasin encompassing a bundle of small local basins - a striking feature resulting from random MPEAs solid solutions (right panel of **Fig. 1**). The energy landscape, sensitive to local chemical order, can be altered by introducing SRO,

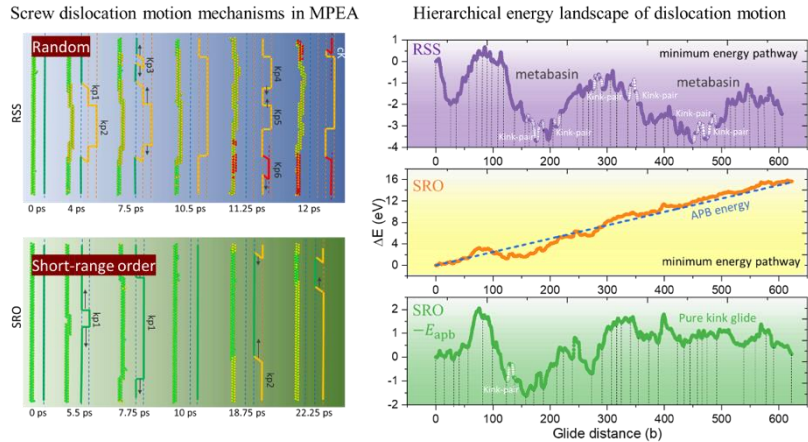


Figure 1. (Left) Atomic structure evolution and motion mechanisms of screw random solid solution (RSS) and short-range order (SRO) systems. Atoms are colored by their positions along the glide plane normal direction to illustrate cross slip. (Right) The hierarchical potential energy landscape of kink gliding over 615b distance in RSS (upper panel). The unfilled symbols indicate kink-pair events. Middle panel shows the energy landscape of kink gliding in SRO (orange curve) and the associated diffuse APB energy due to order breaking.

which transfers the predominance of individual mechanisms as the rate-limiting step for screw dislocation motion. The detailed analysis of the PEL in the random solid solution (RSS) alloy shows that, in contrast with both the very recent understanding of screw dislocation glide, kink-pair nucleation can be a rate-limiting mechanism that competes with kink pair propagation in concentrated solid solutions. The PEL of the SRO system highlights the various roles of breaking chemical order and consequent diffuse anti-phase boundary (APB) generation in modifying the energy barriers of elementary motion processes.

Vacancy: Predicting path-dependent vacancy diffusion barrier spectrum in vast compositional space of MPEAs

Since vacancy diffusion in MPEAs is highly heterogeneous, significantly depending on the local environment, revealing the diffusion processes and the chemical short-range order formation is a challenging task. To overcome it, we aim to develop the kinetic Monte Carlo (kMC) modeling approach enabled by the convolution neural network (CNN) model to resolve individual ion diffusion pathways underpinning chemistry evolution. As the first and critical step, we developed the CNN model³ that is now capable of predicting path-dependent ion diffusion barrier spectra at any sites of MPEAs, which enables simulation and modeling of diffusion kinetics and short-range order formation.

The CNN model, accurately and efficiently predicting the ion diffusion barrier, is solely based on its local atomic environment (**Fig. 2** demonstrates the CNN structure and its results for Ta-Nb-Mo systems). In this deep learning (DL) framework, the discrete local atomic environments will be described using a new structure representation—spatial density maps (SDMs) to replace

2. Wang, X., Maresca, F. & Cao, P. The hierarchical energy landscape of screw dislocation motion in refractory high-entropy alloys. *Acta Mater.* **234**, 118022 (2022).
3. Fan, Z., Xing, B. & Cao, P. Predicting path-dependent diffusion barrier spectra in vast compositional space of multi-principal element alloys via convolutional neural networks. *Acta Mater.* **237**, 118159 (2022).

Twining and phase transformations in hexagonal close packed metals: network formation process and effects on plastic response

L. Capolungo, KQ. Dang, A. Kumar, R.J. McCabe, C. Tome

Los Alamos National Laboratory

Keywords: Phase transformation, twinning, microscopy, phase field, atomistic simulations

Research Scope

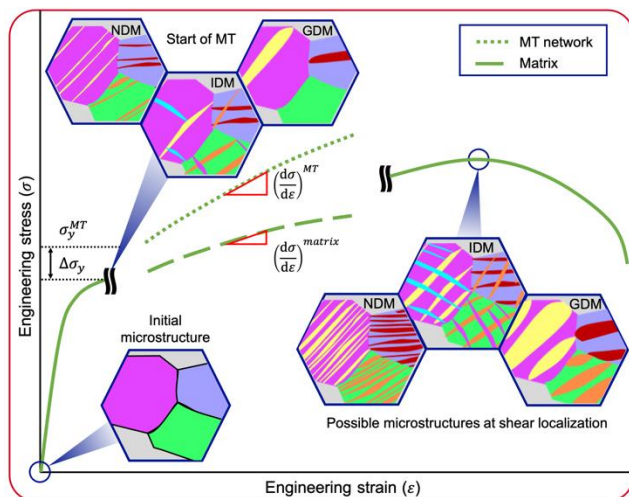


Figure 1: Schematic illustrating the mechanical response of materials conditioned by the nucleation, growth, and percolation of martensitically transformed (MT) domains (i.e. twins or new crystallographic phase). IDM: Interaction dominated network, NDM: Nucleation dominated network, GDM: growth dominated network.

Plastic deformation in metals can be accommodated by numerous deformation modes including dislocation slip, twinning, and martensitic phase transformations. Twinning and martensitic transformations are diffusionless transformations (DTs) whose activation leads to rapid and drastic microstructure changes within the host crystals (see Figure 1). Naturally, the mechanical response (e.g., yield strength, strain hardening rates, strain rate sensitivity, ductility) of materials exhibiting DTs is controlled by the activity of the DTs and their interactions. The role of both twinning and martensitic transformations on the mechanical response is complex as the generation of subvolumes within the host crystals can provide the material with a new route/path for strain hardening and continued plastic

deformation (see Figure 1). At the same time, the formation of complex subdomain networks and the rates at which these form can also deteriorate the overall ductility due to the creation of microstructural configurations that lead to incompatible plastic flow. Throughout the literature, DTs are equally praised and blamed for conferring materials (e.g. twinning induced plasticity, transformation induced plasticity, high entropy alloys, shape memory alloys etc.) with either high or low ductility.

The long-term objective of this research program is to comprehensively rationalize the effects of both twinning and martensitic phase transformations on the plastic response and eventual failure in metals due to localization of plastic flow. Our efforts over the past few years have aimed at understanding the mechanisms and processes mediating the formation of complex three-dimensional domain networks in metals with the hexagonal close packed (HCP) crystal symmetry. Future efforts will aim to more broadly comprehend how the kinetics and morphology of these

complex networks evolving in a plastically flowing microstructure relate to the onset of shear localization.

Recent Progress

Since the late 1990s, the hexagonal close packed metals research community has been able to rationalize and predict how volume fractions of twins evolve as a function of load and crystallographic texture. Yet understanding of the mechanisms leading to the formation of complex 3D networks, of the likely differences in processes mediating twinning and martensitic transformations, and the nature/morphology of dense networks remained elusive. In this context, the work performed over the past few years aimed to answer the following questions:

- What are the mechanisms and driving forces mediating the growth of twins and PT domains in HCP metals?
- How do twin networks form (i.e., twin-grain boundary interactions, twin-twin interactions)?
- What is the 3D morphology of complex twin networks?

Using phase field modeling (PF), atomistic simulations (AS), high-resolution transmission electron microscopy (HR-TEM), and high energy x-ray synchrotron diffraction, the processes of twin expansion was comprehensively studied. Overall, twin propagation is found to be mediated by the motion of minimum energy facets that bound three-dimensional twin domains [1]. Twin propagation and thickening is enabled by nucleation and expansion of disconnection loops whose relative rates were found to largely depend on local stress states. Consequently, two migration regimes with intrinsically distinct facet mobilities were found. Characterization of the internal stress state within an evolving twinned microstructure (APS experiment) further showed that both regimes could be activated during mechanical loading due to the profound heterogeneity in the internal stresses within a polycrystal [2]. Importantly, it was also found that facets can adopt distinct states (e.g. coherent and semi-coherent) depending on the local stress magnitude [3]. The ability of facets to migrate is conditioned by this state, and relaxed facets must first change state to migrate. In addition, within a host crystal, twin domains necessarily interact with dislocations. TEM analysis revealed the mechanism by which complex dislocation structures with limited mobilities form as dislocations from the host crystal interact with twin domains. While these interactions were found to lead to local bursts in growth of twin domains as they provoke the nucleation of disconnections, they did not emerge as the dominant contributor to twin growth.

With regard to martensitic transformations, we studied the thermodynamics of ω domain formation within pure Zr and pure Ti using both Eshelbian micromechanics and AS. It was found that both nucleation and growth of these volumes with simple hexagonal crystal symmetry are aided both by the flow and presence of dislocations. Particularly, the stress field emanating from prismatic dislocations was found to favor these transformations. The proposed model can rationalize the experimentally reported variations in transformation pressure on the basis of the presence and flow of dislocations. This was further confirmed by inducing an ω phase transformation in pre-deformed samples at the Advanced Photon Source (APS) .

The aforementioned body of work sheds light on the key distinctions between twinning and ω phase transformations thus enabling the study of domain network formation and morphology. This was achieved using METIS; a software developed at LANL that allows for semi-automated extraction of twin network states/statistics using electron back scattering diffraction (EBSD) data. By generating large datasets from deformed microstructures for Ti, Zr and Mg, it was found that commonly accepted metrics/predictors used to rationalize twin transmissions across grain boundaries are neither good descriptors nor appropriate predictors for twin transmission. In parallel, PF modeling and AS simulations revealed that twins crossing grain boundaries are not required to initially adopt a specific habit plane aligning with the crystallographic twin plane in the neighboring grain. Rather, owing to the degrees of freedom resulting from the facets that mediate twin growth, twins are able to punch straight through grain boundaries prior to reorienting.

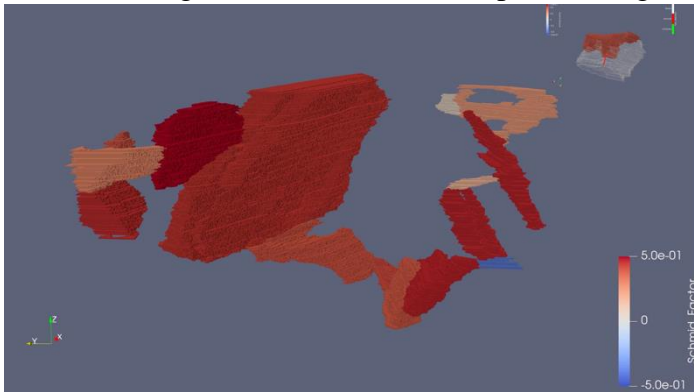


Figure 2: Three-dimensional twin network reconstructed in pure Ti compressed to 2 percent strain. METIS-3D was used. The volume reconstructed is $\sim 100\mu\text{m} \times 80\mu\text{m} \times 80\mu\text{m}$.

Full field crystal plasticity simulations further confirmed that twin transmission is conditioned by maximum energy dissipation rather than solely by geometrical criteria [4]. This confirms that the local stress state within polycrystals largely dictates twin transmission and the development of twin network structures. A consequence of these findings is that twin network morphologies are expected to be particularly convoluted. Thus, the software METIS was extended to three

dimensions and new serial section data acquisition techniques (using Polarized Light Microscopy or Plasma focused ion beam) were utilized to allow for the reconstruction of complex 3D twin networks. Figure 2 shows that twin networks follow far more tortuous paths than previous 2D analysis suggested.

Future Plans

As stated previously, DTs are praised for high ductility in some cases and are blamed for low ductility in other cases they. For instance, HCP Mg and its alloys typically lack ductility while HCP Ti and Zr exhibit considerable ductility. Currently, it is unclear whether this contrast is to be ascribed to DTs, to plastic anisotropy, or to a combination of both. Future work will leverage the modeling and characterization capabilities developed in previously supported work, particularly METIS-3D, to comprehensively rationalize in which scenarios DTs are favorable or unfavorable to strength and ductility. We postulate that to suppress damage nucleation/growth/coalescence and delay shear localization, it is necessary that: (i) high strength DT domains form rapidly/instantaneously, (ii) the DT domains significantly strengthen the host crystals, (iii) both DT and host phases must co-deform plastically (i.e., the strain hardening rates of both phases must

be relatively similar, no plastically incompatible microstructures are generated), and (iv) the expansion rate of DT domains is sluggish (absent this, localization could be exacerbated by the shear induced by DT domain growth). We thus hypothesize that: the ductility of metals can be modulated by controlling the morphology and kinetics of evolution of the MT domain network. The guiding principle is that by controlling the network it is possible to simultaneously modulate (i-iv). To test this hypothesis, the coupled contributions of (i-iv) to shear localization will be quantified as a function of network morphologies and of the intrinsic responses of the host crystals. Specifically, the following three questions will be addressed:

- What is the role of co-deformation on shear localization in microstructures containing MT domains?
- What is the role of the kinetics of MT domain expansion on shear localization in microstructures containing MT domains?
- What is the role of the nucleation rates of MT domains on shear localization?

Three types of DT network morphologies will be studied, see Figure 1. In nucleation dominated microstructures (NDM), the expansion rate of DT domains is rate-limiting due to either slowly migrating facets and/or internal stresses emanating from multiple parallel MT domains. In interaction dominated microstructures (IDM), multiple DT variants in the same crystal are co-activated. Finally, in growth dominated microstructures (GDM), DT domains can expand relatively freely within the host crystal due to factors such as easy facet migration. The degree to which NDM, IDM, or GDM are more favorable to ductility depends on the plastic flow within the host material. These questions will be answered by modeling and characterizing network evolution effects in three material systems: high-purity Ti, Ti-16%V and Ti-20%V. The latter two materials systems are body center cubic (BCC) with Ti-16%V exhibiting a martensitic transformation and Ti-20%V exhibiting deformation twinning.

References

1. M. Gong, J. Graham, V. Taupin, and L. Capolungo, "The effects of stress, temperature and facet structure on growth of $\{10\bar{1}2\}$ twins in Mg: A molecular dynamics and phase field study," *Acta Materialia*, **vol. 208**, p. 116 603, (2021).
2. R. J. McCabe, M. Arul Kumar, W. Liu, C. N. Tome, and L. Capolungo, "Revealing the effect of local stresses on twin growth mechanisms in titanium using synchrotron x-ray diffraction," *Acta Materialia*, **vol. 221**, p. 117 359, (2021).
3. K. Dang, S. Wang, M. Gong, R. J. McCabe, J. Wang, and L. Capolungo, "Formation and stability of long basal-prismatic facets in mg," *Acta Materialia*, **vol. 185**, pp. 119–128, (2020).
4. M. Arul Kumar, R. J. McCabe, C. N. Tome, and L. Capolungo, "m' measure for twin transmission: A predictor or descriptor?" *Materials Today Communication*, **104634**, (2022).

Publications

1. K. Dang, S. Wang, M. Gong, R. J. McCabe, J. Wang, and L. Capolungo, "Formation and stability of long basal-prismatic facets in mg," *Acta Materialia*, **vol. 185**, pp. 119–128, (2020).
2. M. Gong, J. Graham, V. Taupin, and L. Capolungo, "The effects of stress, temperature and facet structure on growth of $\{10^{-12}\}$ twins in Mg: A molecular dynamics and phase field study," *Acta Materialia*, **vol. 208**, p. 116 603, (2021).
3. R. J. McCabe, M. Arul Kumar, W. Liu, C. N. Tome, and L. Capolungo, "Revealing the effect of local stresses on twin growth mechanisms in titanium using synchrotron x-ray diffraction," *Acta Materialia*, **vol. 221**, p. 117 359, (2021).
4. S. Wang, K. Dang, R. J. McCabe, L. Capolungo, and C. N. Tome, "Three-dimensional atomic scale characterization of $\{11^{-22}\}$ twin boundaries in titanium," *Acta Materialia*, **vol. 208**, p. 116 707, (2021).
5. K. Dang, J. Graham, R. J. McCabe, V. Taupin, C. N. Tom´e, and L. Capolungo, "Atomistic and phase field simulations of three dimensional interactions of $\{10^{-12}\}$ twins with grain boundaries in Mg: Twin transmission and dislocation emission," *Materialia*, **vol. 20**, p. 101 247, (2021).
6. K. Dang, C. N. Tome, and L. Capolungo, "The $\{10^{-12}\}$ non-cozone twin-twin interactions in Mg: A stability and mobility study using 3-D atomistic simulations," *Scripta Materialia*, **vol. 200**, p. 113 913, (2021).
7. M. Wronski, M. Arul Kumar, R. J. McCabe, K. Wierzbanski, and C. N. Tome, "Deformation behavior of CP-titanium under strain path changes: Experiment and crystal plasticity modeling," *International Journal of Plasticity*, **vol. 148**, p. 103 129, (2022).
8. M. Arul Kumar, K. Dang, V. Taupin, R. J. McCabe, C. N. Tom´e, and L. Capolungo, "Numerical and experimental characterization of twin transmission across grain boundaries along the forward and lateral directions," *Materialia*, **vol. 23**, p. 101 437, (2022).
9. R. J. McCabe, D. Savage, A. Bhattacharyya, R. Gogusetti, and D. Alexander IV, "Microstructure segmentation using multi-angle polarized light microscopy," *Materials Characterization*, **192**, 112197, (2022).
10. M. Arul Kumar, R. J. McCabe, C. N. Tome, and L. Capolungo, "‘m’ measure for twin transmission: A predictor or descriptor?" *Materials Today Communication*, **104634**, (2022).

Understanding the effect of stress on complexion transitions and the interplay with creep in thermally stabilized nanocrystalline materials

¹Maarten P. de Boer, ²Gregory S. Rohrer, ²Elizabeth C. Dickey

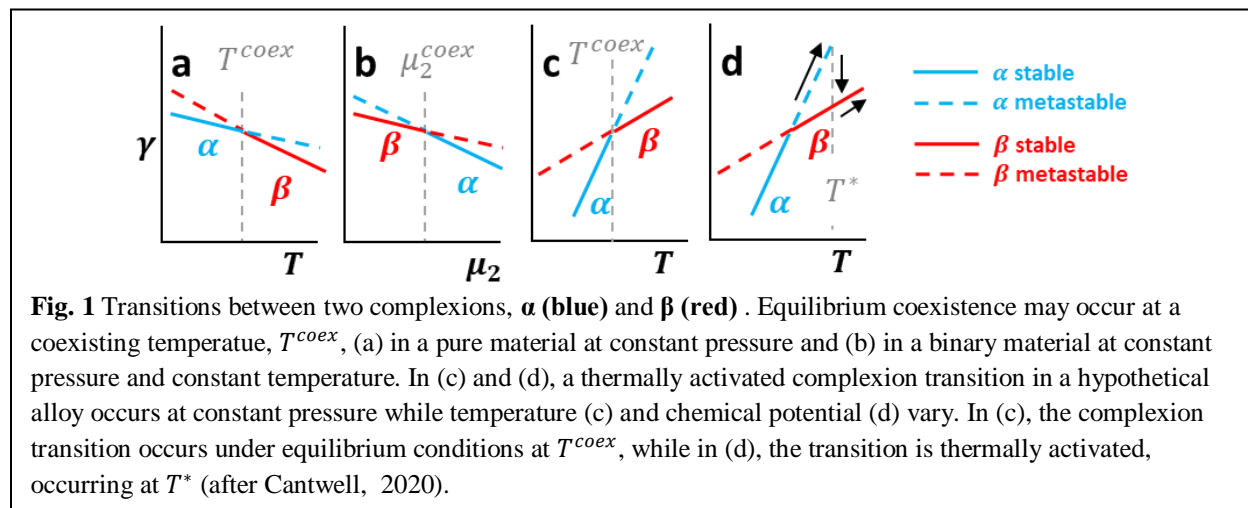
¹Mechanical Engineering, ²Materials Science

Carnegie Mellon University, Pittsburgh, PA, 15213

Keywords: Complexion transitions, stress, microscopy

Research Scope

The phase of a bulk material depends on thermodynamic variables such as temperature, composition, and pressure. Most metals are polycrystalline and the crystals are separated by grain boundaries (GBs). Phases of GBs, known as complexions, influence mechanical properties such as strength and toughness. Such complexions have been studied to date as a function of temperature and composition. A schematic overview of some of their behaviors [1] is given in Fig. 1.



Externally applied stress is also theorized to affect the complexion state [2, 3], but experimental data is lacking. Thermally-stabilized nanocrystalline materials consist of a high volume fraction of GBs. A thermally stabilized nanocrystalline alloy system that forms relatively thick complexions at elevated temperatures is selected as a model material for experimentation. Complexion transitions are likely to be initiated by stress in such an alloy.

In this project, which began September 1, 2022, a versatile nanomechanical platform that can apply a controlled stress over a wide range of temperature to a freestanding nanocrystalline metal in thin film form [4] will be employed to search for stress-induced complexion transitions. A bird's eye view of this platform is shown in Fig. 2. An atomic force microscopy method by which GB energy is measured at thermal grooves will be extended so that it can be applied to nanocrystalline metals. By making measurements on many grooves, the average relative GB energy and the width of its energy distribution can be measured at different stress levels; discontinuous changes will be interpreted as signals of a GB complexion transition. High-

resolution transmission electron microscopy will be used to determine the structure and composition of boundaries equilibrated at different stresses and correlated to changes in the relative energies measured from the thermal grooves. Over time at elevated temperature, the material is likely to creep, which will be associated with a slow stress relaxation. If complexions transform from an amorphous to an ordered state, they will become denser, which will slow diffusion and hence a change in creep rate should be observable. Creep rates will be monitored to search for these transitions.

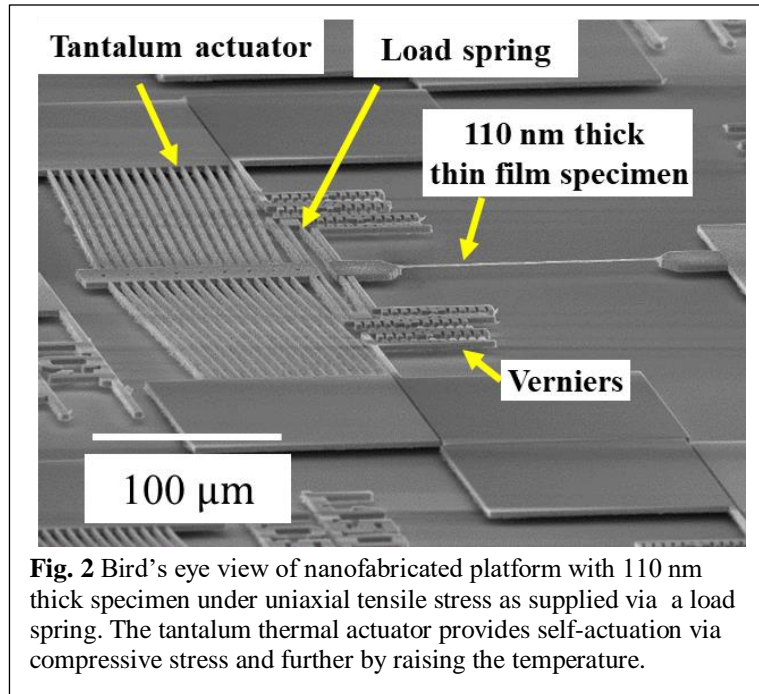


Fig. 2 Bird's eye view of nanofabricated platform with 110 nm thick specimen under uniaxial tensile stress as supplied via a load spring. The tantalum thermal actuator provides self-actuation via compressive stress and further by raising the temperature.

Recent Progress

We have hired students, and they are being trained in nanofabrication, nanomechanical testing methods, atomic force and transmission electron microscopy.

Future Plans

Year 1 plan – develop fabrication and characterization protocols

- Adapt nanofabricated platform to apply well-known stress levels to nanocrystalline metal thin films that exhibit complexion transitions.
- Determine appropriate thermal cycle protocols.
- Characterize film and grain boundary structures by transmission electron microscopy.
- Investigate atomic force microscopy methods to characterize grain boundary energies.

References

- [1] P. R. Cantwell, T. Frolov, T. J. Rupert, A. R. Krause, C. J. Marvel, G. S. Rohrer, J. M. Rickman, and M. P. Harmer, "Grain boundary complexion transitions," *Annual Review of Materials Research*, vol. 50, pp. 465-492, 2020.
- [2] T. Frolov and Y. Mishin, "Thermodynamics of coherent interfaces under mechanical stresses. I. Theory," *Physical Review B*, vol. 85, no. 22, p. 224106, 2012.
- [3] T. Frolov and Y. Mishin, "Thermodynamics of coherent interfaces under mechanical stresses. II. Application to atomistic simulation of grain boundaries," *Physical Review B*, vol. 85, no. 22, p. 224107, 2012.
- [4] L. Ni and M. P. de Boer, "Self-actuating isothermal nanomechanical test platform for tensile creep measurement of freestanding thin films," *Journal of Microelectromechanical Systems*, vol. 31, no. 1, pp. 167-175, 2022.

Publications

None to date.

Improving radiation response of solid state interfaces via control of curvature

Michael J. Demkowicz, Kelvin Xie (Texas A&M Engineering Experiment Station)

Keywords: radiation, interface, curvature, nanocomposite, microstructure

Research Scope

The goal of this project is to discover the effects of curvature on the radiation response of solid-state interfaces and explore strategies for elevating the radiation resistance of composite materials *via* control of interface curvature. Materials that are simultaneously resistant to numerous forms of radiation-induced degradation call for intricate, hierarchical microstructures composed of multiple, interpenetrating phases with high curved interfaces. Yet the majority of previous studies dedicated to radiation response of interfaces have focused on nearly flat interfaces, leaving the effect of interface curvature unexplored. Underlying our work is the recognition that curvature changes the atomic-level structure of interfaces by introducing defects that may not be present in flat interfaces, such as facet junctions or disconnections. We expect these defects to influence interface radiation response.

Recent Progress

Synthesis of model materials: Our research relies on the fabrication of nanocomposite samples of mutually insoluble metals, with one metal forming a flat layer embedded within a matrix of the other metal. The embedded layer is not continuous but terminates along a straight edge within the composite. We synthesize these samples using a new method based on *in situ* physical masking during vapor deposition. This approach requires handling of samples between deposition of successive layers without breaking vacuum. Thus, we used specialized facilities at the Center for Integrated Nanotechnology (CINT) at Los Alamos National Laboratory (LANL) to perform this work. The outcome are compositionally pure, flaw-free samples, such as the copper (Cu)-niobium (Nb) composite shown in the FIB cross section SEM image in Fig. 1.a). In this image, the Cu layer is approximately 250nm thick and tapers gradually to the terminated edge.

High temperature microstructure evolution: We annealed the terminated edge samples in vacuum at 800°C for times of 1 to 10 hours. The resulting microstructure evolution, illustrated in Fig. 1.b), yields several insights. First, we see no evidence of the dramatic breakdown in film cohesion reported in previous studies and attributed to melting point depression. However, we did see such breakdown when we replaced the non-reactive, Nb substrates shown in Fig. 1 with Si substrates. Therefore, we believe that substrate-film reactions are responsible for the thermally induced instabilities reported in the literature, not melting point depression.

Second, the tip of the terminated edge retracts upon annealing, leaving behind a series of pinched-off Cu particles. We interpret this observation based on prior phase field simulations, which modeled the evolution of a terminated layer using the Cahn-Hilliard equation, $\dot{c} = \nabla \cdot (M\nabla c)$. If

the mobility, M , is taken to be composition independent, then layer retraction does not generate any pinched off particles. However, if mobility is restricted to heterophase interfaces through the composition-dependent mobility function $M = M_0|1 - c^2|$ (where $c = \pm 1$ correspond to pure phases and $c = 0$ denotes the interface), then layer retraction gives rise to strings of pinched off particles, as shown in Fig. 1.c). The occurrence of these particles in our experiments is therefore consistent with transport in the Cu-Nb system being limited to interfaces. Moreover, the product $M_0\Delta F$ (where M_0 is the mobility prefactor and ΔF mixing energy) may be inferred from the average distance D between the particles and the average time Δt between successive particle formation, as illustrated in Fig. 1.c). Our experiments allow us to conclude that $M_0\Delta F \approx 24 \pm 12 \text{ nm}^2/\text{s}$. Estimating ΔF from previous density function theory calculations, we obtain $M_0 \approx 264 \pm 132 \text{ nm}^5/\text{eVs}$. This is the first quantitative, experimental constraint on the mobility of Cu-Nb or, indeed, any binary system of phase separating metals.

III.c) Radiation response of curved interfaces:

As shown in Fig. 1.b), high temperature annealing gives rise to high-curvature interfaces in our samples. To investigate their response to radiation, we prepared TEM foils and irradiated them with 200 keV He ions at LANL. At this energy, most of the ions pass through the foil, resulting in displacement damage, but no impurity implantation. Fig. 2 shows that high curvature interfaces have much wider defect depleted zones (DDZs) than nearly flat ones. This work provides the first direct

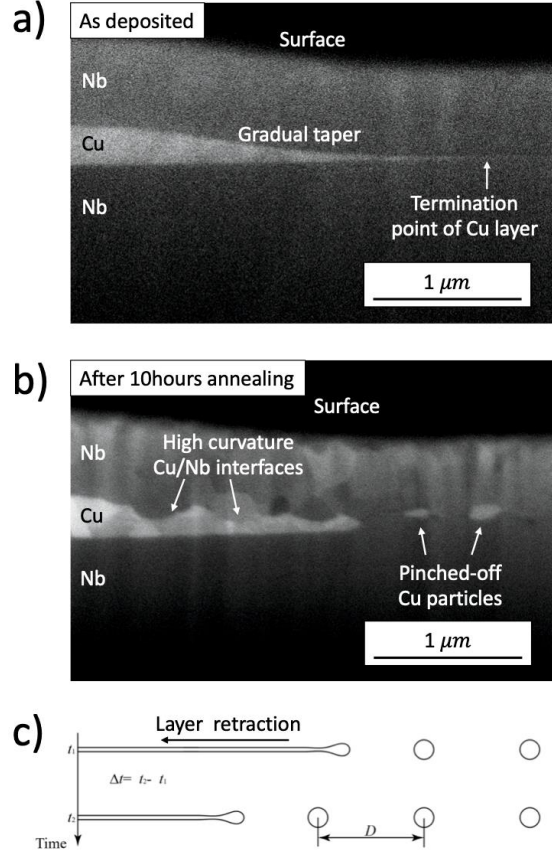


Fig. 1: Cross sectional, secondary electron SEM images of a layer of Cu terminating along a straight, tapered edge within a matrix of Nb in a) as-deposited condition and b) after 10 hours of annealing at 800°C. Phase field modeling predictions for formation of pinched off particles during annealing are shown in c).

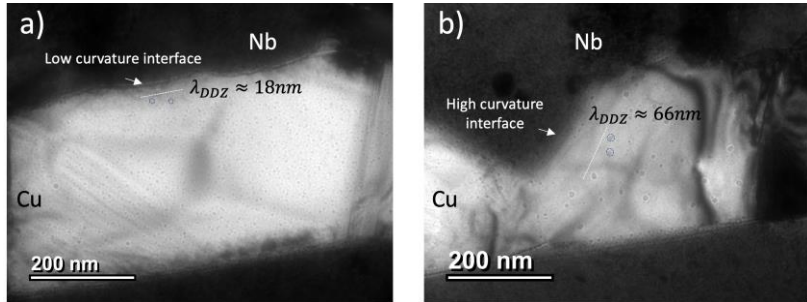


Fig. 2: Defect depleted zones (DDZ) are noticeably wider near b) high curvature interfaces than near a) low curvature interfaces. White dashed lines indicate the approximate extent of the DDZs.

evidence of the effect curvature on radiation response. Analysis of these experiments is ongoing and atomistic modeling of the structure of the curved interfaces in our samples is in progress.

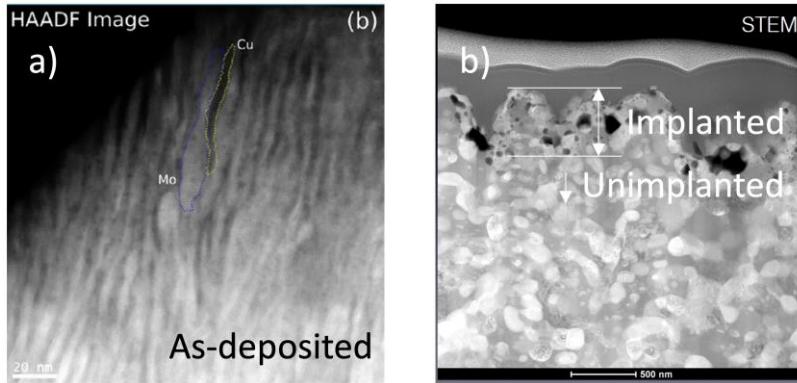


Fig. 3: Cu-Mo nanocomposites a) contain sub-10nm domains in their as-deposited state, but b) coarsen substantially after He implantation at 750°C. The microstructure of the implanted region (within ~100nm of the surface) is comparable to that of the unimplanted region deeper down.

Michigan) in its as-processed state to its structure after implantation at 750°C. The high implantation temperature causes comparable coarsening in both the implanted (near surface) and unimplanted (near substrate) regions of the material. Thus, implantation does not improve the thermal stability of these Cu-Mo composites. However, we see that microstructure evolution alters the form of damage generated by irradiation significantly: defect clusters are much larger in microstructures that coarsened during irradiation than in ones that remained static.

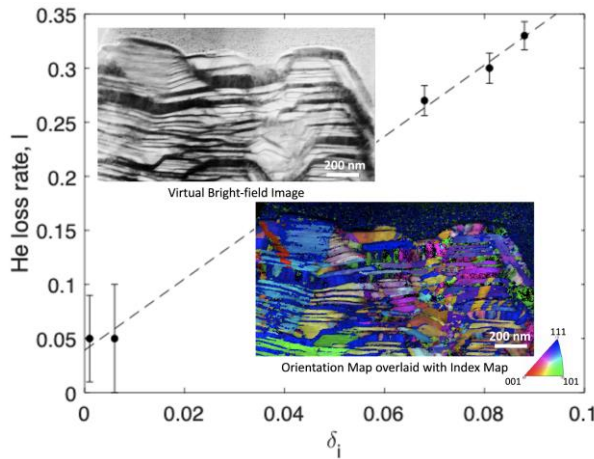


Fig. 4: He removal rate, I , is correlated to the total interface density, δ_i (nm^2/nm^3) in Cu-W co-deposited composites (see top left inset; dark phase is W). δ_i was determined by PED analysis (bottom right inset).

$$\rho = -\frac{4\ln(1-f)}{\pi\bar{d}^2t}$$

Radiation response of metal nanocomposites with high curvature interfaces: To investigate the effect of a high density of curved interfaces on radiation response, we performed He implantation on three nanocomposite metals with interpenetrating constituents of complex shape. Fig. 3 compares a vapor co-deposited Cu-Mo nanocomposite (provided by the group of A. Misra at U. of

Through combined He^{3+} implantation and nuclear reaction analysis (NRA), we demonstrated substantial (>30%), damage-free escape of implanted He from vapor co-deposited Cu-W nanocomposites. The total density, δ_i , of phase and grain boundaries in these materials (obtained using precession electron diffraction) is directly correlated to the amount of outgassing, as shown in Fig. 4. Thus, both heterophase interfaces and grain boundaries are short-circuit paths for He diffusion. Finally, in a study of He implanted titanium Ti/Ta nanocomposites, we developed an analytical formula for He bubble density, ρ , that corrects for bubble overlap in TEM images:

Here, f is the image area fraction covered by bubbles, \bar{d} is mean bubble diameter, and t is foil thickness. This formula improved our estimates of ρ and provided quantitative insights into the relationship between He bubble sizes and densities in our work on Cu-W nanocomposites.

Ir-Cu interatomic potential: In anticipation of future research on the effect of lattice misfit on the radiation response of curved interfaces, we constructed an embedded-atom method (EAM) potential for Cu-Ir by developing a new, single-element Ir EAM potential and joining it to the Mishin Cu EAM potential with a cross-interaction function. The newly developed Ir potential is fitted to the cohesive energy, lattice parameter, vacancy formation energy, stacking fault energy, and elastic constants. The Cu-Ir cross-interaction function is fitted to cohesive energies of seven hypothetical intermetallic structures as well as the formation enthalpies of $\text{Cu}_x\text{Ir}_{1-x}$ quasirandom solid solutions, which are obtained using first-principles, density-functional theory (DFT) calculations. We used the new potential to investigate the structure and energy of Cu-Ir interfaces formed in two canonical orientation relations (ORs) along $\{111\}$ planes: one in the cube-on-cube OR and the other in the hetero-twin OR.

Healing of nanocracks by collision cascades: Using molecular dynamics simulations, we investigated the interaction between collision cascades and pre-existing nano-cracks in nickel (Ni). Collision cascades cause the cracks to heal whenever a cascade initiates a thermal spike whose core overlaps with the crack, as illustrated in Fig. 5. This work indicates that irradiation may reduce the number of pre-existing crack-like flaws in metallic components, potentially improving their mechanical resilience. It was conducted entirely remotely by undergraduate researcher Advika Chesetti under the guidance of postdoc Peng Chen at the height of the COVID-19 crisis.

Future Plans

Our results so far suggest that curvature extends the range of interactions between interfaces and radiation-induced defects: an effect we hypothesize to be due to the elastic fields of curvature-induced interface defects. Our future plans therefore emphasize experimental characterization and atomistic modeling of curvature-induced elastic fields around interfaces and point defect interactions with these fields. Moreover, our research to date suggests that, rather than reducing interface mobility, defects trapped at interfaces diffuse from regions of high curvature to regions of low curvature. Thus, we hypothesize that radiation-induced defects generated concurrently with microstructure evolution are swept towards locations of low interface curvature. This effect is expected to influence curvature-driven interface mobility under irradiation. We will investigate it through experiments on edge retraction of a terminated layer, such as that shown in Fig. 1.

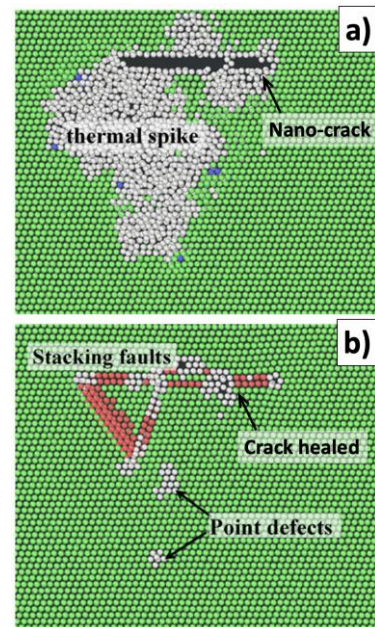


Fig. 5: Collision cascade-induced nano-crack healing in Ni.

Publications

1. S. Xiang, I. McCue, D. Yadav, Y. Q. Wang, J. K. Baldwin, M. J. Demkowicz, K. Xie, *Comparative study of helium bubbles in a Ti-Ta alloy and a Ti-Ta nanocomposite*, Philosophical Magazine Letters **100**, 307 (2020).
2. D. Yadav, D. Zhao, J. K. Baldwin, A. Devraj, M. J. Demkowicz, K. Y. Xie, *Persistence of crystal orientations across sub-micron-scale “supergrains” in self-organized Cu-W nanocomposites*, Scripta Materialia **194**, 113677 (2021).
3. P. Chen, A. Chesetti, M. J. Demkowicz, *Healing of nano-cracks by collision cascades in nickel*, Journal of Nuclear Materials **555**, 153124 (2021).
4. D. Yadav, P. Chen, Y. Q. Wang, J. K. Baldwin, P. Evans, N. Williams, M. J. Demkowicz, K. Y. Xie, *Short circuit transport of implanted He along phase and grain boundaries in vapor co-deposited Cu-W nanocomposites*, Acta Materialia **240**, 118306 (2022).
5. P. Chen, T. Duong, M. J. Demkowicz, *An embedded-atom method potential for the Cu-Ir binary system*, Modelling and Simulation in Materials Science and Engineering **submitted** (2020).
6. E. Sheu, Y. F. Zang, H. Kim, D. J. Williams, J. K. Baldwin, M. J. Demkowicz, *Evolution of the edge of a terminated Cu nanolayer within a Nb matrix upon annealing*, **submitted** (2022).
7. D. Yadav, B. Derby, Y. Q. Wang, M. Powers, A. Misra, M. J. Demkowicz, K. Y. Xie, *Microstructure evolution in Cu-Mo nanocomposites under concurrent He implantation and high temperature annealing*, **in preparation** (2022).

Coupled effects of stress and hydrogen on stress corrosion cracking of Fe-based alloys

Arun Devaraj, Pacific Northwest National Laboratory

Keywords: Stress corrosion cracking, steel, hydrogen, deformation, correlative microscopy

Research Scope

The overarching goal of this project is to develop predictive, mechanistic understanding of the coupled influence of applied stress, H concentration and distribution, and intergranular oxidation on propagation of stress corrosion cracking (SCC) in Fe-based alloys in high-temperature water environments. When steels are subjected simultaneously to an applied tensile stress and high-temperature water environment, it is hypothesized that a combination of H-assisted mechanisms and intergranular oxidation leads to intergranular stress corrosion cracking (SCC), which can cause catastrophic failures. Although SCC mechanisms of steels has been studied for decades, crucial knowledge gaps still exist, especially due to the complexity of the coupled mechanisms. This project correlates results from unique, state-of-the-art microscopy and spectroscopy capabilities housed at Pacific Northwest National Laboratory and at synchrotron light source user facilities to quantitatively analyze the influence of hydrogen, oxidation, and local deformation in Fe-based alloys from the atomic scale to the mesoscale. Additionally, judiciously selected in situ and in operando methods and computational simulations are used to unravel the coupling between H and the chemical and mechanical factors that influence SCC mechanisms. This project also investigates the SCC mechanisms operating at defected grain boundaries, revealing the influence of high defect density, modified grain boundary structure, and solute segregation to facilitate predictive control of H-assisted and oxidation-based SCC mechanisms of Fe-based alloys.

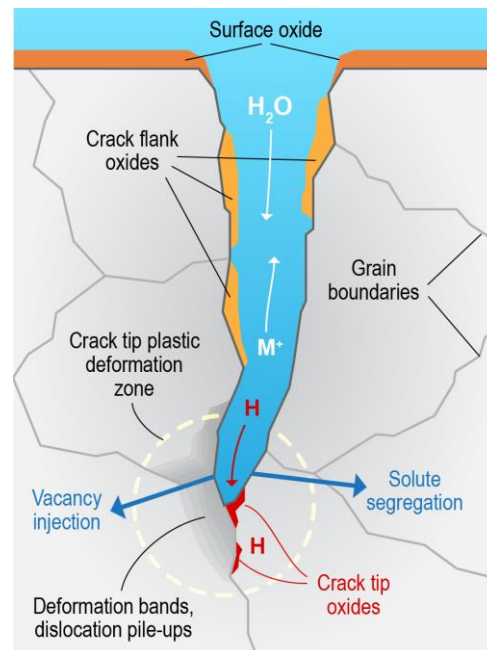


Figure 1. The crack tip phenomenon during SCC of Fe-based alloys in high-temperature water is a complex, multiscale problem. This proposed work will develop a predictive, mechanistic understanding of the coupled influence of applied stress, H, and intergranular oxidation on propagation of SCC in Fe-based alloys in high-temperature water environments.

Recent Progress

Atomic-scale in situ observations revealed that during the high-temperature oxidation of an iron–chromium–nickel (Fe-18 wt. % Cr-14 wt. % Ni) alloy (from here onward denoted as Fe18Cr14Ni), cations diffuse out to the surface faster than oxygen migrates inward [1]. Developing such an atomic-scale understanding of steel oxidation is critical for developing more robust, next-

generation alloys for nuclear and structural applications exposed to high temperatures and corrosive environments. We also established a rapid high throughput in situ atom probe tomography approach for studying material degradation mechanisms.

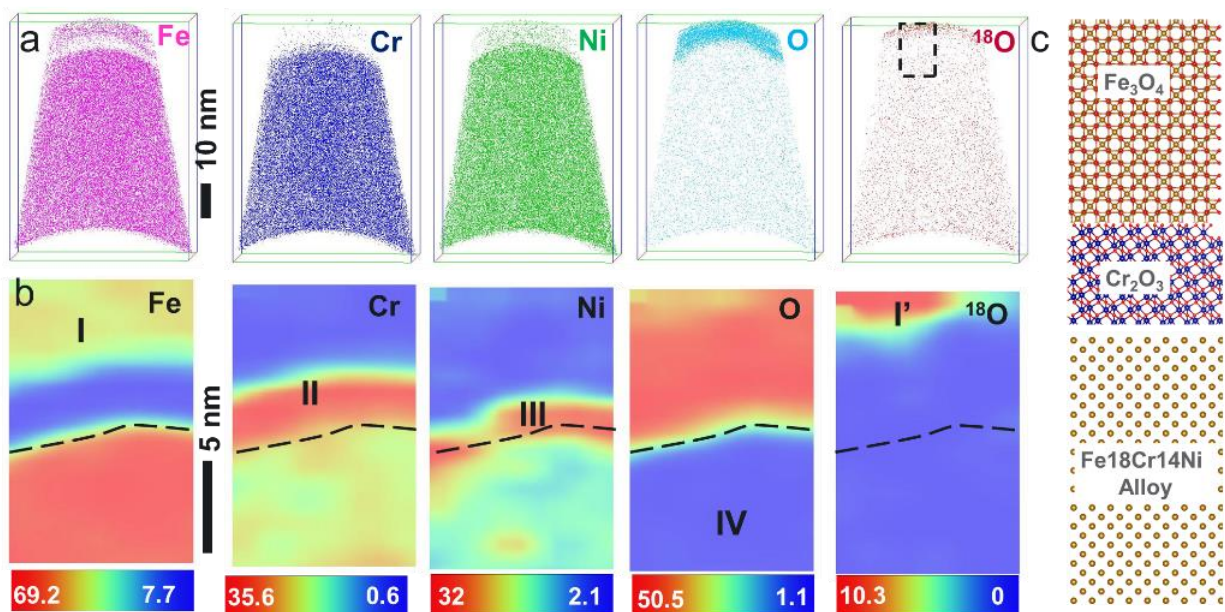


Figure 2: Using in situ atom probe tomography, the Fe-18 wt. % Cr- 14 wt. % Ni alloy was first oxidized in natural abundance O₂ followed by oxidation in ¹⁸O₂, revealing the formation of an outer Fe₃O₄ and inner Cr₂O₃ layer with Ni enrichment at the oxide-metal interface (a, b). The ¹⁸O rich oxide formed on the outer surface of the pre-existing oxide, which agreed with the predictions of PNP-cDFT simulations, confirming outward cation diffusion to be the dominant mechanism.

The oxidation mechanism of these alloys at 300 °C was investigated using a unique environmental reactor chamber attached to the atom probe tomography (APT) vacuum system to analyze the diffusional events that drive the early stages of oxidation [2]. Site-specific APT needle samples from the center of selected austenite grains were oxidized at 300 °C while 10 mbar oxygen with either natural-abundance or isotopically enriched ¹⁸O₂ was flowed into the reactor chamber for specific time durations varying from 5 to 30 min. After the oxidation experiments, the samples were analyzed again with APT to understand the compositional changes due to oxidation. We also correlated the in situ APT results with the multimodal analysis of the structure and oxidation state of the oxides as well as with coupled Poisson-Nernst-Planck (PNP) transport kinetics model and classical density functional theory (cDFT) simulations. Oxidation at 300 °C for 5 min and 30 min in natural-abundance oxygen allowed us to identify the composition and thickness of the double oxide layers (an Fe₃O₄ layer on the surface with a Cr₂O₃ underlayer and Ni segregation to the oxide-metal interface) as a function of time. A double-stage oxidation experiment, which involved a first stage of exposing an Fe₁₈Cr₁₄Ni alloy to natural-abundance O₂ followed by a 15 min exposure to ¹⁸O enriched O₂, revealed that the ¹⁸O- rich oxide layer formed on top of the pre-existing oxide and not at the prior oxide-metal interface (Figure 2(a) and (b)). This observation helped confirm that the outward diffusion of cations is the dominant diffusional mechanism. A secondary, less-dominant mechanism of inward diffusion of oxygen was also observed. The PNP-

cDFT simulated compositional profile from the oxide surface to bulk alloy agreed with all the experimental results (Figure 2(c)). This correlated multimodal experimental and computational approach is now allowing us to additionally study the influence of grain boundaries, deformation induced defects, and hydrogen on the oxidation mechanisms of these alloys.

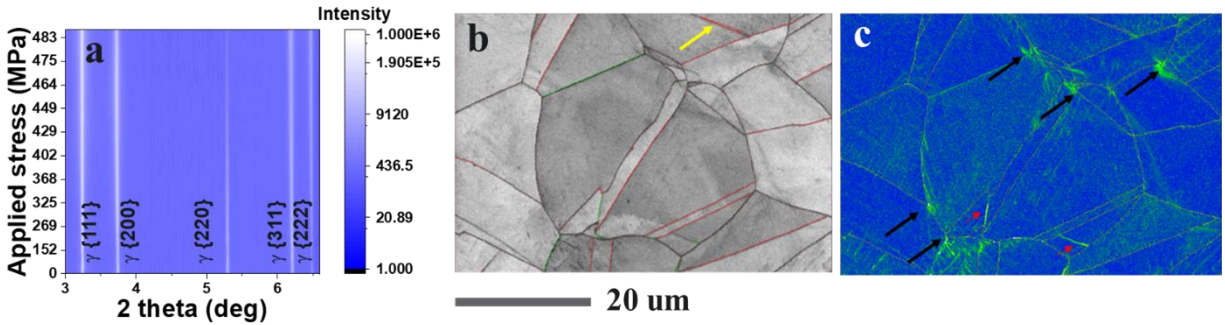


Figure 3: (a) In situ synchrotron high energy X-ray diffraction of Fe18Cr14Ni alloy during tensile deformation, followed by (b, c) ex situ microstructural analysis by electron back scatter diffraction revealing strain accumulation at slip bands near grain boundaries (red arrows) and triple junctions (black arrows) in the kernel average misorientation map in (c).

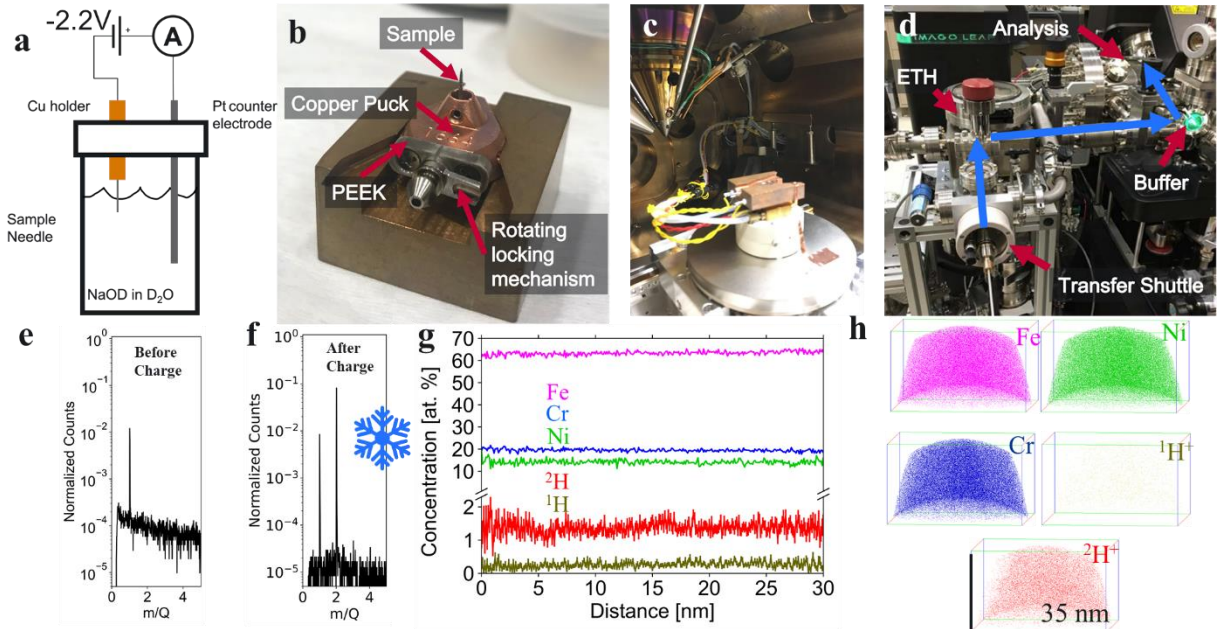


Figure 4: Complete workflow for analyzing deuterium segregation in Fe-based alloys by (a) electrochemical charging of deuterium followed by (b) transfer of the APT sample to (c) the cryogenic focused ion beam stage and (d) environmental transfer hub in to the APT analysis chamber. The comparison of H peaks in the APT mass-to-charge spectra (e) before charging and (f) after charging followed by cryogenic transfer APT successfully revealed the distribution of deuterium in the charged Fe18Cr14Ni alloy (g-h).

The deformation mechanism of Fe18Cr14Ni alloy was studied using in situ synchrotron based high energy X-ray diffraction and ex situ electron microscopy. The slip and twin activities in the alloy were quantified using the microstrain and magnitude of the X-ray diffraction peak

broadening (Figure 3 (a)). Postmortem electron backscatter diffraction revealed pronounced strain accumulation at grain boundaries and especially triple junctions in the microstructure (Figure 3(b, c)).

The sub-nanometer scale spatially resolved hydrogen segregation and embrittlement mechanisms of Fe18Cr14Ni alloys were studied using fully optimized deuterium (^2H) electrochemical charging (Figure 4(a)) followed by APT or mechanical testing [3]. The ^2H charged samples (Figure 4(b)) were plunge frozen in liquid nitrogen and cryogenically sharpened to an APT sample using the cryogenic dual beam focused ion beam system (Figure 4(c)). The final sample was then transferred in vacuum and at cryogenic temperatures to APT using the environmental transfer hub (Figure 4(d)). Clear evidence for ^2H segregating into austenite phase in Fe18Cr14Ni was obtained using the cryogenic transfer APT. The comparison of APT mass-to-charge spectra before charging (Figure 4(e)) and after cryogenic transfer APT revealed a clear signature of ^2H at 2Da (Figure 4(f–h)). This capability is currently being used to analyze the nanoscale distribution and clustering of hydrogen at grain boundaries in Fe-based alloys as a function of applied stress and temperature.

Future Plans

Building from the atomic-scale understanding of individual mechanisms underpinning the oxidation, hydrogen embrittlement, and tensile deformation of Fe-Cr-Ni alloys, we will now investigate the coupled influences of these factors on SCC mechanisms. We will reveal the influence of applied stress and temperature on the hydrogen concentration and distribution at grain boundaries in Fe-based alloys subjected to high-temperature water corrosion. Additional efforts will focus on finding linkages between the stress corrosion crack propagation rates and the grain boundary hydrogen concentration and clustering. Finally, we will also aim to tailor the defect density, free volume, and non-equilibrium solute excess at grain boundaries to modify H segregation and clustering. This in turn will be used to modify the oxidation processes at those grain boundaries, allowing to predictively control the crack growth during intergranular SCC of Fe-based alloys.

References

1. A. Devaraj, Barton, D. J., Li, C.-H., Lambeets, S. V., Liu, T., Battu, A., Vaithiyalingam, S., Thevuthasan, S., Yang, F., Guo, J., Li, T., Ren, Y., Kovarik, L., Perea, D. E., Sushko, M. L., *Visualizing the Nanoscale Oxygen and Cation Transport Mechanisms during the Early Stages of Oxidation of Fe–Cr–Ni Alloy Using In Situ Atom Probe Tomography*, *Advanced Materials Interfaces*, **9**, 2200134 (2022).
2. S.V Lambeets, E. J Kautz, M. G. Wirth, G. J. Orren, A. Devaraj, D. E. Perea, *Nanoscale perspectives of metal degradation via in situ atom probe tomography*, *Topics in Catalysis*, **63**, 15, 1606-1622 (2020).
3. Y. S. Chen, P-Y. Liu, R. Niu, A. Devaraj, H-W. Yen, R. K. W. Marceau, J. M. Kairney, *Atom probe tomography for the observation of hydrogen in materials: a review*, *Microscopy and Microanalysis*, In press, (2022).

Publications

1. A. Devaraj, D. J. Barton, C-H. Li, S. V. Lambeets, T. Liu, A. Battu, S. Vaithiyalingam, S. Thevuthasan, F. Yang, J. Guo, T. Li, Y. Ren, L. Kovarik, D. E. Perea, M. L. Sushko, *Visualizing the Nanoscale Oxygen and Cation Transport Mechanisms during the Early Stages of Oxidation of Fe–Cr–Ni Alloy Using In Situ Atom Probe Tomography*, *Advanced Materials Interfaces*, **9**, 2200134, (2022).
2. O. Cojocar-Mirédin, A. Devaraj, *Correlative Microscopy and Techniques with Atom Probe Tomography: opportunities in material science*, *MRS Bulletin*, **47**, 680–687 (2022).
3. Y. S. Chen, P-Y. Liu, R. Niu, A. Devaraj, H-W. Yen, R. K. W. Marceau, J. M. Kairney, *Atom probe tomography for the observation of hydrogen in materials: a review*, *Microscopy and Microanalysis*, In press, (2022).
4. E. Aydogan, O. El-Atwani, B. Erdem, W-Y. Chen, M. Li, A. Devaraj, Bahattin Koc, Stuart A Maloy, *In-situ radiation response of additively manufactured modified Inconel 718 alloys*, *Additive Manufacturing*, 102601, (2022).
5. E. J. Kautz, D. K. Schreiber, A. Devaraj, B. Gwalani, *Mechanistic insights into selective oxidation and corrosion of multi-principal element alloy from high resolution and in situ microscopy*, *Materialia*, 101148, (2021).

Understanding the Mechanics of Reverse Phase Transformation and Detwinning in BCC Metal Microstructures

Avinash M. Dongare, University of Connecticut (Principal Investigator)

Keywords: Twinning, Phase transformation, molecular dynamics simulations, variants, mesoscale

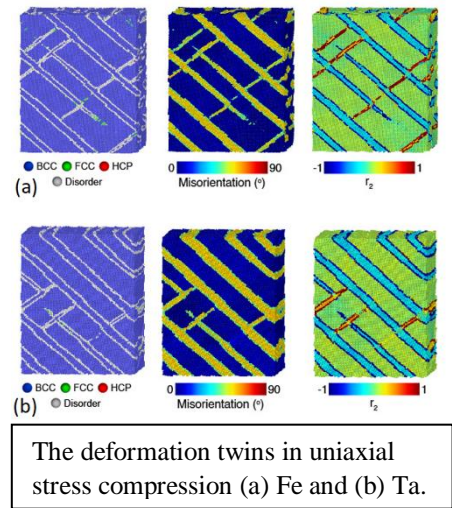
Research Scope

Structural metallic materials that exhibit contributions from twinning-induced plasticity (TWIP) and transformation-induced plasticity (TRIP) can meet the goals of a good combination of strength and ductility. One class of materials exhibiting TRIP/TWIP effects are BCC microstructures of β -titanium alloys. Therefore, the optimization of the TRIP/TWIP contributions requires an understanding of the nucleation and evolution of twins/phases and their contributions to the mechanical behavior of BCC microstructures. The current strategies to understand these mechanisms aim to deform specimens to different strain levels and then unload them to characterize microstructures using electron backscattered diffraction (EBSD) and transmission electron microscopy (TEM). However, a challenge in interpreting the plasticity contributions in these materials is the easy reversibility of the phase-transformed regions and the detwinning behavior upon unloading. Hence, one cannot interpret the individual contributions to plasticity during deformation based on EBSD analysis. While in situ x-ray diffraction (XRD) characterization can provide real-time evidence of these phenomena, the interpretation of the plasticity contributions from diffractograms is non-trivial, especially when multiple deformation modes may be operating. This proposed program uses model BCC metal microstructures (Fe, Ta, Mo, and Nb) and a novel computational framework to understand the evolution of the twinning and phase transformation variants and their contributions to plasticity during deformation and their stability or reverse transformation behavior during unloading. Such an understanding of the variant selections requires investigating the role of grain orientations, the interactions between grains, the stress states on the variant selections, the evolution of their relative fractions, and their contributions to plasticity during deformation under uniaxial or multi-axial loading conditions. In addition, the program aims to understand the mechanics of reverse phase transformation and detwinning to understand the factors that affect the stability of twins in unloaded microstructures. The program will use a novel combination of (a) large-scale molecular dynamics (MD) simulations to model the behavior at the atomic/nanoscales, (b) Quasi-coarse-grained dynamics (QCGD) simulations to model the behavior at the mesoscales, and (c) virtual x-ray diffraction (XRD) and selected area diffraction (SAED) to understand and quantify the dislocation density and twinning contributions to plasticity in MD and QCGD predicted microstructures. The characterization of the phase/twin variants is based on a newly developed virtual texture analysis (VirTex) algorithm by the PI that enables the creation of EBSD maps of the simulated microstructures to compare with experimental EBSD maps. The simulated XRD and SAED analysis on the simulated

microstructures will quantitatively correlate the peak shifts and broadening behavior with the phase/twin variants and their volume fractions and dislocation densities. This understanding will provide critical insights into the interpretation of deformation modes and their contributions to accommodating plastic strain in experimental diffractograms. The proposed effort will provide a rationale for why a particular microstructure will result in the selection of phase/twin variants during deformation and also identify the relative contributions to the flow stress values. In addition, the simulations will also explain why modifications in loading conditions on the same microstructure affect the phase/twin variant selections during deformation and affect the stability and reverse transformation behavior during unloading. This understanding of variant selections and their relative contributions (and fractions) during deformation is critical to allowing the interpretation of plasticity contributions from characterizing unloaded microstructures.

Recent Progress

Molecular dynamics simulations are currently investigating the twinning variants using VirTex analysis [1] in deformed microstructures of Fe and Ta. The VirTex algorithm constructs a rotation matrix to calculate the angle/axis pair and misorientation angle for each atom in the microstructure. The snapshots in Figure show a distribution of twins in the microstructure for both (a) Fe and (b) Ta when deformed under uniaxial compressive stress loading. VirTex analysis confirms two twin variants for Fe and Ta based on the second component of the rotation vector (r_2), and the structures show a large fraction of CTBs and inclined twin boundaries. However, the relative fractions of the two variants are different in Fe and Ta, and the twins in Ta are slightly thicker than that for Fe.



The deformation twins in uniaxial stress compression (a) Fe and (b) Ta.

Future Plans

The MD simulations will investigate the role of stress state on the variant selections and their stability during unloading in polycrystalline BCC microstructures to investigate the role of grain orientations and the misorientations between grains on the variant selections during deformation. This will be followed by an investigation of β -titanium and high entropy alloys.

References

1. A. Mishra, K. Ma, and A.M. Dongare, *Virtual diffraction simulations using the quasi-coarse-grained dynamics method to understand and interpret plasticity contributions during in situ shock experiments*, J. Mater. Sci., **57**, 12782 (2022).

Publications

None to date.

Fundamental insights into defect generation and transport phenomena at grain boundaries in advanced nuclear fuel candidates

S. Finkeldei¹, S. Dillon², J. White³, M. Cooper³, D. Andersson³

¹University of California, Irvine, Department of Chemistry; ²University of California, Irvine, Department of Materials Science and Engineering; ³Los Alamos National Laboratory, Materials Science and Technology Division

Keywords: grain boundaries, defect generation, transport, advanced fuel, internal gelation

Research Scope

Grain boundary transport kinetics in UO₂ affect numerous microstructure processes of considerable importance to nuclear fuel processing, lifetime, and safety. These include influencing sintering kinetics, high temperature creep, interfacial sink behavior, coarsening of secondary phases, fission gas diffusion and bubble evolution that drives swelling. These phenomena have typically been analyzed, modeled, and predicted using diffusional models that assume point defect fluxes impose the rate limiting step. Following this logic, considerable emphasis has been placed on integrating information describing grain boundary diffusional processes into multi-scale models for predicting nuclear fuel evolution. Recent bicrystal creep and sintering experiments, however, suggest that grain boundaries are not ideal sinks for unbalanced continuous fluxes of point defects [1]. Furthermore, those experiments suggest that at individual grain boundaries axial strain, mediated by climb of grain boundary (GB) dislocations, is kinetically rate limited by their nucleation rate up to relatively high stresses. If GB strain is indeed kinetically limited by the nucleation rate of climb mediating point defect sources and sinks, then many aspects of our understanding of interfacial sink behavior, irradiation enhanced GB diffusion, creep, sintering, and bubble nucleation and growth should be revisited.

Recent Progress

In the initial portion of this work, a model for nucleation rate limited creep kinetics was developed and demonstrated to both predict and fit experimental creep data well. These results imply that nucleation rate limited kinetics may indeed be important in understanding GB creep and GB strain under a variety of conditions as originally hypothesized in this work. To the authors' knowledge, a general nucleation rate limited creep model has not been derived previously. The reason this mechanism has been ignored stems from the realization that GB dislocation nucleation requires large local stresses, that often exceed the applied stress by 1 to 2 orders of magnitude. The GB steady-state strain rate, $\dot{\epsilon}$, should follow the general form;

$$\dot{\epsilon} = B'' \frac{\vec{b}^3}{d^3} \dot{\eta}_o \exp\left(-\frac{H^* - S^*T - \sigma V^*}{kT}\right) \quad (1)$$

$\dot{\eta}_o$ is a pre-factor, H^* , S^* , σ , and v^* are the local activation enthalpy, entropy, stress, and volume, respectively, B'' is a geometric constant, \vec{b} is the Burger's vector, and d is the grain size. Note the local stress at the triple line where the GB dislocation likely nucleates is the important parameter rather than the applied stress.

The need for a stress concentration term or the incompatibility between experimentally applied creep stresses and GB dislocation nucleation is reminiscent of another problem in the early creep literature, namely observations of GB creep cavitation at low stresses e.g. on the order of 10 MPa in many oxides. Several models were developed in the open literature to treat this stress concentration based on elastic and viscoelastic response. Here, a simple formulation proposed by Trinkhaus [2] will be used to describe a maximum local stress concentration factor;

$$\Phi \approx 0.5 \sqrt{\left(\frac{a}{l}\right)} \quad (2)$$

where a is the grain edge length, assumed to be $a = 0.5d$, and l is the distance of interest from the singularity, which is taken as the boundary of a spherical activation volume, $l = \sqrt[3]{v^* \left(\frac{3}{4\pi}\right)}$. Dynamic versions of this equation have been developed accounting for more complex viscoelastic response, but predict a maximum stress concentration of similar magnitude [2]. Since local stress concentrations might exhibit a broad distribution depending on local geometry and crystallography, the apparent stress dependence of creep in a polycrystal would be a convolution of this stress distribution and the exponential distribution describing the nucleation kinetics. Accounting for stress concentration effects and assuming H^* , S^* , and $\dot{\eta}_o$ in equation (1) are not stress dependent, a normalized GB dislocation nucleation rate, \dot{N} , may be defined;

$$\dot{N} = \frac{\sum_{i=1}^{i=n} \exp\left(\frac{(\Phi\sigma)_i v^*}{kT}\right)}{n \exp\left(\frac{\sigma_c v^*}{kT}\right)} \quad (3)$$

where, σ_c is the critical local stress at which the system approaches diffusion limited kinetics. The term $\sum_{i=1}^{i=n} \exp\left(\frac{(\Phi\sigma)_i v^*}{kT}\right)$ represents the distribution of local stress concentrations at each of the i^{th} 3- and 4-grain junctions within the microstructure. Arzt et al. [3] made a correction to the diffusional GB limited creep equation to account for the shape of the chemical potential gradient when a finite number of GB dislocations were present;

$$\dot{\epsilon} = \frac{A' \delta D_b \Omega \sigma}{kT d^3} \left\{ \frac{N^2}{N^2 + 1/2} \right\} \quad (4)$$

The creep rate will approach the diffusion limited as $N > 1$. An equation for steady-state nucleation limited creep is then taken as;

$$\dot{\epsilon} = \frac{A' \delta D_b \Omega \sigma}{kT d^3} \left\{ \frac{N^2}{N^2 + 1/2} \right\} \quad (5)$$

and can be tested using physically reasonable values of σ_c and v^* . For simplicity, a Gaussian distribution is utilized to describe the distribution of Φ . The average stress concentration at the singularities is approximated as;

$$\bar{\sigma} = \Phi \sigma f \quad (6)$$

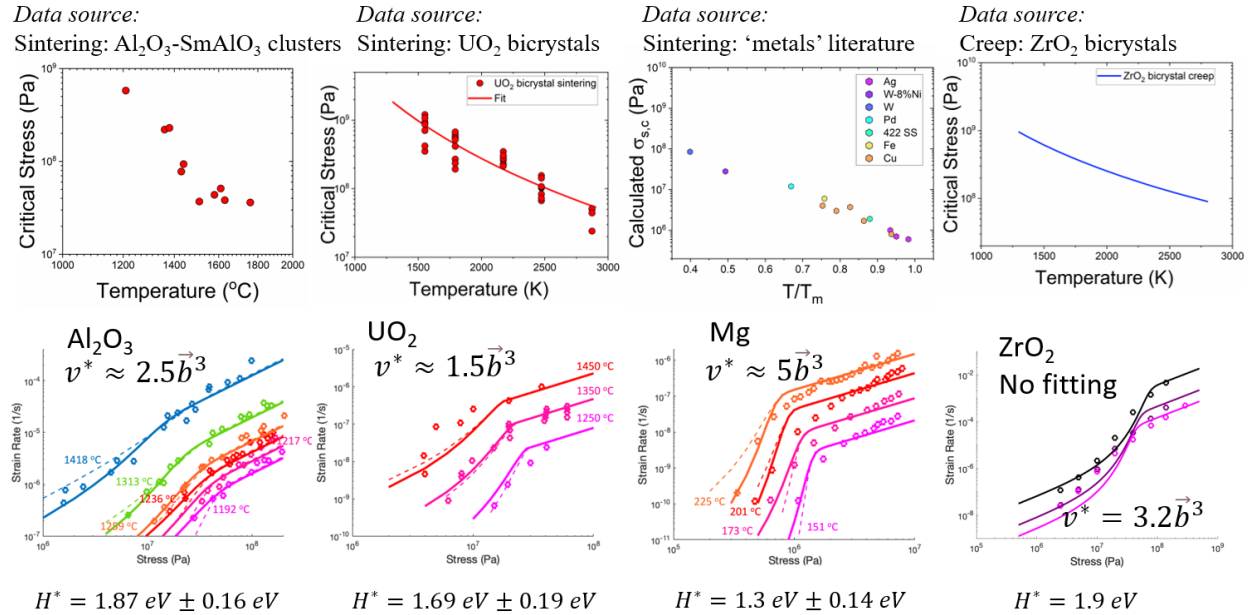
and the standard deviation is taken as;

$$\mu = \Phi \sigma \frac{1-f}{3} \quad (7)$$

where $f < 1$ is utilized as a fitting parameter used to describe the distribution such that the maximum stress occurs at 3 standard deviations above the average. This description is arbitrary, but a single fitting parameter f is favorable for avoiding the introduction of excessive fitting parameters, for all the calculations discussed below $f = 0.5$ is used.

To test this model, input values of $\sigma_c(T)$ and v^* are required. Prior bicrystal creep data from ZrO_2 measured both $\sigma_c(T)$ and v^* providing an opportunity for a reasonable test. Data for $\sigma_c(T)$ from UO_2 , Al_2O_3 , and some simple metals have been obtained based on *in situ* bicrystal sintering, *in situ* polycrystalline sintering, and bulk bicrystal sintering, respectively. These latter data also rely on a recently developed model for nucleation rate limited sintering, which has been shown to work well in describing essentially all aspects of sintering. These three data sets require the use of v^* as a fitting parameter. Using the creep model described above, several data from the literature were either fitted or predicted, for the case of ZrO_2 . Figure 1 shows an example of the data for ZrO_2 predicted without any fitting parameters, and the other systems where v^* is the only fitting parameter. The model works well in both cases, and the values of v^* and H^* are of a reasonable magnitude for GB dislocation nucleation. In fact, the values for UO_2 and Al_2O_3 are comparable to those measured directly from bicrystal creep of ZrO_2 .

The agreement between our model and previously reported data from creep in UO_2 , in particular, supports our hypothesis that GB dislocation nucleation phenomena should play an important role in the performance and processing of UO_2 fuels.



Future Plans

The synthesis of doped UO_2 fuels will be attempted by a classical mixed solid-state liquid salt impregnation method as well as via a sol-gel process [4] to implement dopants leading to advanced fuels with enlarged UO_2 grains with tailored microstructures and chemistry. To understand the role point defects, defect cluster concentrations, their mobilities, as well as GB sink types and their concentrations play towards diffusion enhancement in these fuel candidates under extreme conditions, a combination of experimental and computational efforts will be undertaken to investigate radiation enhanced diffusion at GBs via bicrystal Coble creep experiments. Furthermore, investigations of fission gas diffusion, bubble formation and growth will be realized via Helium-generating neutron irradiation experiments as well as ion implantation experiments. GB FG bubble nucleation and growth are anticipated to depend on the GB creep kinetics in the presence of non-equilibrium concentrations of gas. Utilizing a combined experimental and computational approach, transport phenomena will be evaluated to understand how GB structures could be designed in the future to influence gas bubble nucleation and growth. Lastly, the addition of dopants, such as Cr in advanced UO_2 fuels, is expected to modify the distribution of GB atomic motifs as well as GB defect structures during high temperature irradiation. The role of dopant chemistry in affecting GB structure, creep, and swelling will be investigated by (ion) irradiation experiments and modeling efforts, thus enhancing the understanding of GB structure-property relations under non-equilibrium conditions. This knowledge is expected to be a stepping stone for mechanism-informed developments for fuel forms of the future.

References

1. R.L. Grosso, K.S.N. Vikrant, L. Feng, E.N.S. Muccillo, D.N.F. Mucche, G.S. Jawaharram, C.M. Barr, A.M. Monterrosa, R.H.R. Castro, R.E. Garcia, K. Hattar, S.J. Dillon, *Ultrahigh temperature in situ transmission electron microscopy based bicrystal coble creep in Zirconia II: Interfacial thermodynamics and transport mechanisms*, Acta Mater., **200**, 1008-1021 (2020).
2. H. Trinkaus, M.H. Yoo, *Cavity nucleation under time-dependent stress concentrations*, Philosophical Magazine A, **57**, 543-564 (1988).
3. E. Arzt, M.F. Ashby, R.A. Verrall, *Interface controlled diffusional creep*, Acta Metallurgica, **31**, 1977-1989 (1983).
4. S. Finkeldei, R. D. Hunt, J. O. Kiggans, C. A. Hobbs, B. D. Eckhart, J. W. McMurray, D. Brown, G. W. Helmreich, K. A. Terrani, A. Nelson, *Synthesis and Characterization of UO_2 Feedstocks Containing Controlled Dopants*, ORNL Milestone Report M3FT-19OR020201075 (2019).

The Role of Anisotropy on the Self-Organization of Gas Bubble Superlattice

J. Gan¹, C. Sun¹, C. Jiang¹, A. Jokisaari¹, L. Aagesen¹, E. Jossou², S. Gill²,
A. Schneider³, Y. Zhang³

¹Idaho National Laboratory, ²Brookhaven National Laboratory, ³University of Wisconsin

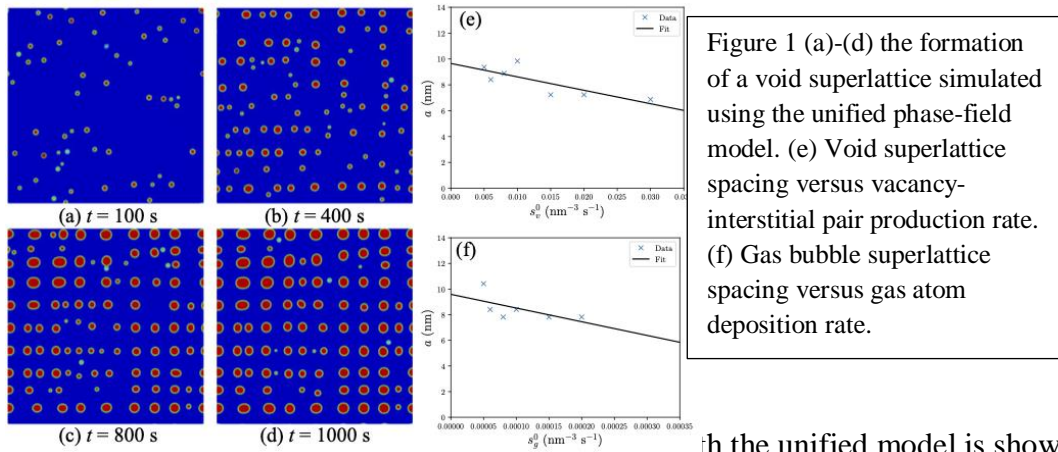
Keywords: diffusion, anisotropy, gas bubble, superlattice, irradiation

Research Scope

Three-dimensionally ordered nanostructures have many potential applications and irradiation is a useful tool for creating them. Gas bubble superlattice (GBS) and void superlattice are the two important ordered nanostructures of great scientific interest. The discovery of the highly ordered face-centered-cubic (fcc) Xe bubble lattice in body-centered-cubic (bcc) U-Mo challenges the widely accepted notion that superlattices are coherent with the host material's crystal structure [1]. The objective of this project is to understand the fundamental mechanisms controlling the self-organization of these patterned structures, to aid the development of materials with novel properties and for applications in conditions involving irradiation. This project takes an integrated experimental and computational approach. The focus is placed on the self-organization mechanisms of nanostructures under irradiation. The studies center on two common self-organization hypotheses: anisotropic elastic interaction between voids or bubbles and anisotropic diffusion such as one-dimensional (1D) diffusion of self-interstitial atoms (SIA) or SIA clusters. In the past three years, the research was focused on addressing the three Science Questions: (1) Can a unified theory be developed for both void and gas bubble superlattices? (2) What is the role of anisotropic diffusion of self-interstitial-atom (SIA) clusters in GBS formation? (3) What is the effect of crystal structure on GBS formation?

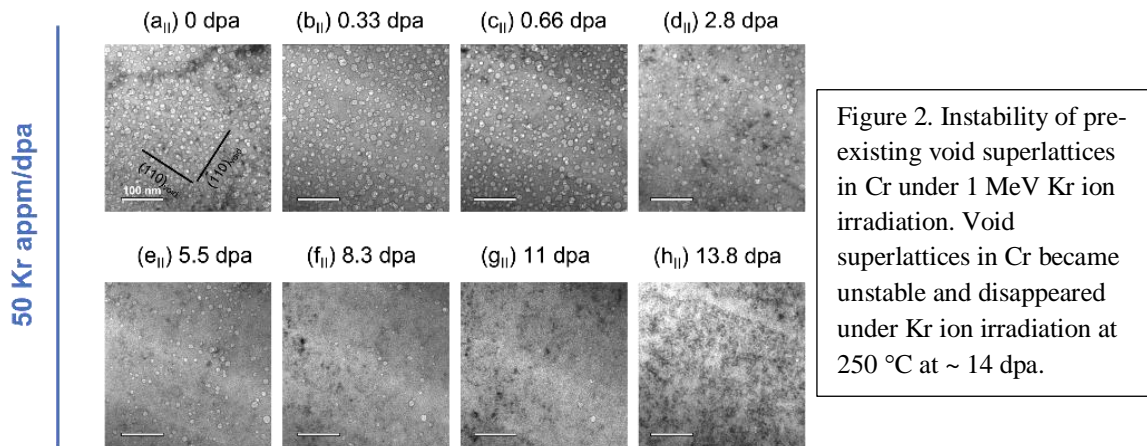
Recent Progress

Models for the formation of void and gas bubble superlattices have been developed in the past with phase-field, kinetic Monte Carlo, and other simulation techniques. However, past phase-field models have focused on void [2,3] or gas bubble superlattice formation [4] independently of one another or have not treated the gas atoms as a distinct defect species from the vacancies [5]. We have recently developed a unified phase-field model for the formation of both void and gas bubble superlattices assuming 1D SIA diffusion and interstitial gas atoms and used the model to understand the relationships between physical parameters and microstructure for these related processes. More details can be found in our recent publication [6]. The model is capable of simulating the phase transformation through either a nucleation and growth or spinodal decomposition-like mechanism; in the initial work using this model, we have focused on the nucleation and growth mechanism due to the prevalence of experimental observations consistent with this mechanism.



Consistent with experimental observations, voids are initially distributed randomly throughout the domain (a), followed by the formation of aligned rows/columns of 3-5 voids at intermediate times (b), and finally by complete superlattice formation (c)-(d). Void and gas bubble superlattice spacing were quantified using a two-point correlation function approach as a function of physical parameters, such as nucleation rate, defect diffusivity, and gas/vacancy ratio. An important finding that was consistent for both void and gas bubble superlattices was that the superlattice spacing decreased with increasing rate of defect production; see (e) for void superlattices and (f) for gas bubble superlattices. A similar dependence of superlattice spacing on flux was found in previous work when the phase transformation occurred by spinodal decomposition-like spontaneous phase transformation.

Using in-situ transmission electron microscopy (TEM) in combination with object kinetic Monte Carlo (OKMC) simulations parameterized using density functional theory (DFT) calculations, the evolution of pre-existing void superlattices in bcc Cr under Kr irradiation at 250°C has been both experimentally observed and modeled. Experimentally, it has been found that both void diameter and void density decrease with increasing Kr irradiation dose. At high doses, the void superlattices become disordered and eventually disappear when void sizes shrink to below TEM resolution at ~ 14 dpa, shown in Figure 2 for 1 MeV Kr irradiation.



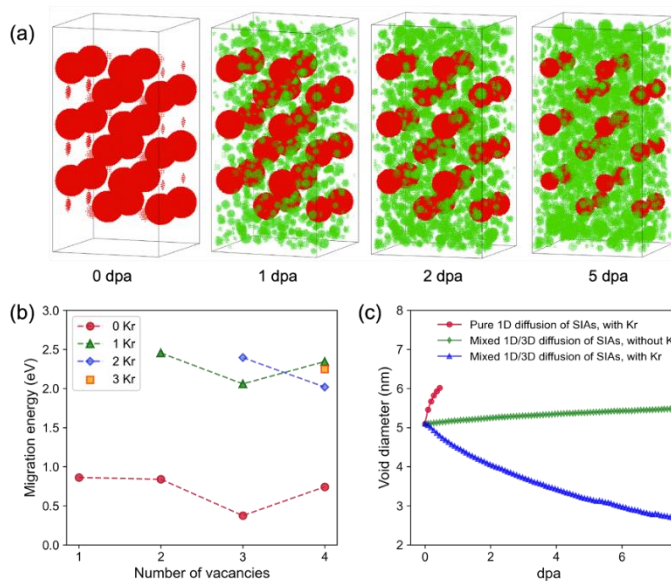


Figure 3. OKMC modeling of microstructural evolution in Cr with pre-existing void superlattices under Kr ion irradiation at 250 °C. (a) Snapshots of void superlattice evolution under irradiation up to 5 dpa. Red and green spheres represent vacancies of pre-existing voids and newly formed Kr bubbles, respectively. (b) Migration energies of small $V_nK_r_m$ ($n \leq 4$, $m \leq 3$) defect complexes. Compared to vacancies, the migration energies of Kr-vacancy complexes are greater. (c) The evolution of void diameter as a function of dpa for three scenarios: pure 1D diffusion of SIAs with injected Kr atoms; mixed 1D/3D diffusion of SIAs without injected Kr atoms; mixed 1D/3D diffusion of SIAs with injected Kr atoms. The last one is consistent with experimental observation.

Under the irradiation with 300 keV Kr ions with high Kr retention, while voids disappear at ~ 80 dpa at a slower rate, new Kr bubbles are also nucleated in between voids, and random Kr bubbles gradually become weakly ordered and form a Kr GBS. Using the OKMC simulations, it was shown that two factors are important to the void shrinkage in the void superlattices: mixed 1D/3D diffusion and the injection of Kr atoms. Our OKMC modeling reveals that the 3D rotation of SIAs occurs once every eight 1D diffusion jumps in Cr at $T=250^\circ\text{C}$. These relatively frequent 3D rotations prevent SIAs that are created in channels from travelling unimpeded to sinks, preventing an excess of vacancies. In addition, injection of Kr atoms increases the migration energy of vacancies by forming Kr-vacancy complexes. The migration energy of vacancies increases from 0.74 eV for V_{a4} to 2.24 eV for $V_{a4}K_r_3$. Thus, at low concentrations of Kr gas atoms, the formation of small Kr-vacancy complexes significantly reduces the mobilities of vacancies and their migration to voids. As a result, more SIAs diffuse to voids, leading to the rapid shrinkage of voids as shown in Figure 3. This work is published, and more detail can be found in the reference [7].

He and Kr irradiation experiments were performed in Ni, Fe, and Cu at temperatures from -120 to 100 °C. Contrary to the conventional wisdom that GBS are formed at temperatures ranging from 0.15 to $0.3T_m$ (T_m is the melting temperature of the host metals), here we report that He GBS are formed at $\sim 0.09T_m$, significantly lower than the low limit of formation temperature reported in the literature. Under He irradiation to a dose of $4 \times 10^{17}/\text{cm}^2$, well-defined He GBS were created in Fe, Cu, and Ni. However, Kr bubbles are weakly ordered in comparison to the He GBS. TEM characterization found that the He GBS lattice constant increases as temperature increases, similar to our previous observation in bcc W and Mo. GBS formation at cryogenic temperatures is intriguing and will be investigated further to elucidate the mechanism.

An analytical physics-based model has been parameterized using systematic DFT calculations on small gas-vacancy clusters containing up to six vacancies and six gas atoms,

which are formed between noble gas atoms (He, Ne, Ar, and Kr) and vacancies in bcc transition metals in group 5B (V, Nb, Ta) and 6B (Cr, Mo, W). Combining this analytical model for gas bubble energetics with kinetic Monte Carlo (KMC) simulations, the lifetimes of noble gas bubbles and their coarsening behavior via the Ostwald ripening mechanism have been predicted [8]. Compared with voids, all gas bubbles exhibit enhanced thermal stability due to reduced thermal vacancy emission rates. The most significant finding is the exceptionally higher thermal stability of Ne, Ar and Kr bubbles compared to He bubbles in bcc metals, conferring them outstanding resistance to Ostwald ripening. Such modeling results provide new insights on the exceptional stability of Xe GBS in U-Mo up to a very high homologous temperature of 0.78 [9].

We also developed a multimodal approach combining synchrotron-based nanoscale X-ray imaging techniques with atomic-scale electron microscopy techniques to elucidate chemical composition change, morphology evolution and lattice distortion in single crystal W under Kr irradiation [10]. Kr-irradiated single crystal W undergoes surface deformation, forming Kr-containing cavities. Furthermore, positive strain fields are observed in Kr-irradiated regions, which lead to compression of underlying W matrix. The structural changes and strain fields in single crystal W induced by 1.8 MeV Kr ion irradiation were studied using nanoscale X-ray microscopy combining X-Ray Fluorescence (XRF) and nanodiffraction imaging. The XRF elemental mapping was successfully employed to study Kr distribution, while nanodiffraction was used to map strain distribution in both the Kr irradiated and interface regions. Our X-ray study reveals a complex network of local defect structures in the irradiated single crystal W. Nanoscale strain imaging reveals strong structural changes from the defect-free tungsten region to the interface and finally to the Kr-irradiated region.

Future Plans

The objective of the future work of this research project is to further develop the unified theory for void and bubble superlattice formation and quantitatively determine factors controlling superlattice formation and ordering. To date, we have focused on determining underlying mechanisms of superlattice formation and in developing a basis for a unified void/GBS theory; that is, answering the fundamental question of why superlattices form. Now, we propose to investigate topics that will move beyond the why to elucidate the how: how are superlattice characteristics (lattice parameter, void/bubble size, degree of ordering, and amount of damage needed to develop a superlattice) controlled and predicted? Our hypothesis will be further examined from the perspective of three interrelated science questions that are inspired from our previous research.

SQ1 – Can a transition in superlattice formation from nucleation to spontaneous phase transformation be predicted and observed?

SQ2 – What mechanisms control the degree of ordering observed in GBS?

SQ3 – What diffusion mechanisms contribute to GBS formation at cryogenic temperatures?

References

1. J. Gan, D.D. Keiser, D. M. Wachs, A. B. Robinson, B. D. Miller, *Transmission electron microscopy characterization of irradiated U-7Mo/Al-2Si dispersion fuel*, J. of Nuclear Materials, 396, 234-239 (2010).
2. Y. Gao, Y. Zhang, D. Schwen, C. Jiang, C. Sun, J. Gan, *Formation and self-organization of void superlattice under irradiation: A phase-field study*, Materialia, 1, 78-88 (2018).
3. Y. P. Gao, A. M. Jokisaari, L. Aagesen, Y. F. Zhang, M. M. Jin, C. Jiang, S. Biswas, C. Sun, and J. Gan. *The effect of elastic anisotropy on the symmetry selection of irradiation-induced void superlattices in cubic metals*. Computational Materials Science, 206, 111252 (2022).
4. H. Yu, and W. Lu, *Dynamics of the self-assembly of nanovoids and nanobubbles in solids*, Acta Materialia 53, 1799 (2005).
5. L. Malerba, C. S. Becquart, C. Domain, *Objective kinetic Monte Carlo study of sink strength*, Journal of Nuclear Materials, 360, 159 (2007).
6. Larry K. Aagesen, Andrea Jokisaari, Daniel Schwen, Chao Jiang, Anton Schneider, Yongfeng Zhang, Cheng Sun, Jian Gan, *A phase-field model for void and gas bubble superlattice formation in irradiated solids*. Computational Materials Science, 215, 111772 (2022).
7. Cheng Sun, Chao Jiang, Yifeng Che, Wei-Ying Chen, Yongfeng Zhang, Andrea M. Jokisaari, Larry K. Aagesen, Lin Shao, Jian Gan, *Unveiling the interaction of nanopatterned void superlattices with irradiation cascades*, Acta Materialia, 239, 118282 (2022).
8. Chao Jiang, Yongfeng Zhang, Larry K. Aagesen, Andrea M. Jokisaari, Cheng Sun, Jian Gan, *Noble gas bubbles in bcc metals: Ab initio-based theory and kinetic Monte Carlo modeling*, Acta Materialia 213, 116961 (2021).
9. J. Gan, D.D. Keiser, Jr.; B.D. Miller; A.B. Robinson, D.M. Wachs, and Mitch Meyer, *Thermal Stability of Fission Gas Bubble Superlattice in Irradiated U-10Mo Fuel*, J. Nucl. Mater. 464, 1-5 (2015).
10. Gill, S. K.; Topsakal, M.; Jossou, E.; Huang, X.; Hattar, K.; Mausz, J.; Elbakhshwan, M.; Yan, H.; Chu, Y. S.; Sun, C.; He, L.; Gan, J.; Ecker, L., *Impact of krypton irradiation on a single crystal tungsten: Multi-modal X-ray imaging study*. Scripta Materialia, 188, 296-301 (2020).

Publications (Oct. 2019 – Oct. 2022) (Selected list of 10 from 13 publications)

- (1) Simerjeet K. Gill, Mehmet Topsakal, Ericmoore Jossou, Xiaojing Huang, Khalid Hattar, Julia Mausz, Mohamed Elbakhshwan, Hanfei Yan, Yong S. Chu, Cheng Sun, Lingfeng He, Jian Gan, Lynne Ecker. *Impact of krypton irradiation on a single crystal tungsten: Multi-modal X-ray imaging study*, Scripta Materialia., 188, 296-301 (2020).
- (2) Cheng Sun, Chao Jiang, Ericmoore Jossou, Mehmet Topsakal, Simerjeet K. Gill, Lynne E. Ecker, Jian Gan. *Self-assembly of solid nanoclusters in molybdenum under gas ion implantation*, Scripta Materialia. 194, 113651 (2021).
- (3) Miaomiao Jin, Yipeng Gao, Yongfeng Zhang, Chao Jiang & Jian Gan, *Dissociated prismatic loop punching by bubble growth in FCC metals*, Scientific Reports, 11:12839 (2021).
- (4) Chao Jiang, Yongfeng Zhang, Larry K. Aagesen, Andrea M. Jokisaari, Cheng Sun, Jian Gan, *Noble gas bubbles in bcc metals: Ab initio-based theory and kinetic Monte Carlo modeling*, Acta Materialia, 213, 116961 (2021).
- (5) Ericmoore Jossou, Anton Schneider, Cheng Sun, Yongfeng Zhang, Shirish Chodankar, Dmytro Nykypanchuk, Jian Gan, Lynne Ecker, and Simerjeet K. Gill, *Unraveling the Early-Stage Ordering of Krypton Solid Bubbles in Molybdenum: A Multimodal Study*, J. Phys. Chem. C, 125, 42, 23338–23348 (2021).
- (6) Yipeng Gao, Andrea M. Jokisaari, Larry Aagesen, Yongfeng Zhang, Miaomiao Jin, Chao Jiang, Sudipta Biswas, Cheng Sun, Jian Gan, *The effect of elastic anisotropy on the symmetry selection of irradiation-induced void superlattices in cubic metals*, Computational Materials Science 206, 111252 (2022). [This paper was marked as Editor's Choice]

(7) Cheng Sun, *A short review of defect superlattice formation in metals and alloys under irradiation*, J. Nucl. Materials 559, 153479 (2022). [Special Issue: JNM Rising Stars in Nuclear Materials]

(8) Anton Schneider, Yongfeng Zhang a, Chao Jiang, Jian Gan, *The effects of temperature and dose rate on the properties of irradiation induced void superlattices*, Materialia 22, 101373 (2022).

(9) Cheng Sun, Chao Jiang, Yifeng Che, Wei-ying Chen, Yongfeng Zhang, Andrea M. Jokisaari, Larry Aagesen, Lin Shao, Jian Gan, *Unveiling the interaction of nanopatterned void superlattices with irradiation cascades*, Acta Materialia, 239, 118282 (2022).

(10) Larry K. Aagesen, Andrea Jokisaari, Daniel Schwen, Chao Jiang, Anton Schneider, Yongfeng Zhang, Cheng Sun, Jian Gan, *A phase-field model for void and gas bubble superlattice formation in irradiated solids*, Computational Materials Science, 215, 111772 (2022).

Insight into the stability and deformation processes of “high entropy” alloys with bcc/B2-type microstructure

Maryam Ghazisaeidi (PI) and Michael Mills (Co-PI), The Ohio State University

Keywords: High entropy alloys, B2 ordering, phase stability, dislocation transfer

Research Scope

The overarching goal of this effort is to provide a fundamental understanding of deformation mechanisms in a new class of two-phase multicomponent concentrated alloys, where disordered bcc and ordered B2-type phases coexist as either matrix or precipitates. In this context, two fundamental questions, need to be addressed: (1) For a specific composition, what are the stable phases at various temperatures, and can a degree of order be defined? (2) What is the effect of order on slip and how does slip transfer between ordered/disordered regions? Motivated by the recent synthesis of the two-phase BCC+B2 refractory complex concentrated alloy (RCCA) ($\text{Al}_{0.5}\text{NbTa}_{0.8}\text{Ti}_{1.5}\text{V}_{0.2}\text{Zr}$), we started our study with this system. However, we found that the B2/BCC microstructure is not stable depending on the various heat treatments. Specifically, the B2 phase, devolves into less symmetric structures which is not conducive to studying the dislocation transfer mechanisms between BCC and B2. We present our progress in characterization of the microstructure and computational prediction of phase stabilities that lead to this conclusion. Based on these results, it is necessary to identify simpler systems that provide a more stable BCC/B2 microstructure which we are currently pursuing.

Recent Progress

Experimental effort:

The initial experimental study for the program has focused on a two-phase, BCC+B2, refractory complex concentrated alloy (RCCA) $\text{Al}_{0.5}\text{NbTa}_{0.8}\text{Ti}_{1.5}\text{V}_{0.2}\text{Zr}$ [1]. We have performed detailed SEM and TEM level investigation of samples that have undergone compressive deformation at 600°C to a true plastic strain of 0.030 at strain rate of 10^{-4} s^{-1} . Detailed scanning transmission electron microscopy (STEM) observations using both diffraction contrast (DF-STEM) and high-angle annular dark field imaging (HAADF), complemented by nanoscale energy dispersive compositional analysis (EDS) has been performed to understand the operative deformation modes. The microstructure was shown to be meta-stable as the original solutionized microstructure, a BCC matrix with B2 nano-clusters, as seen in **Figure 1a** changed after deformation resulting in the B2 phase being aligned along $\langle 100 \rangle$ directions as seen in **Figure 1b**. HAADF-EDS showed the B2 precipitates were Al/Zr rich and Nb/Ta depleted. Deformation was shown to occur via weak pairs of $a/2\langle 111 \rangle$ dislocations as seen in **Figure 1c**, which were often along the screw component. Dislocations were pinned at B2 precipitates with shearing being the expected method of deformation. **Figure 1d** shows an example of the microstructure after additional annealing for 120h. The lower symmetry omega phases begin to emerge and coexist with the B2 phases.

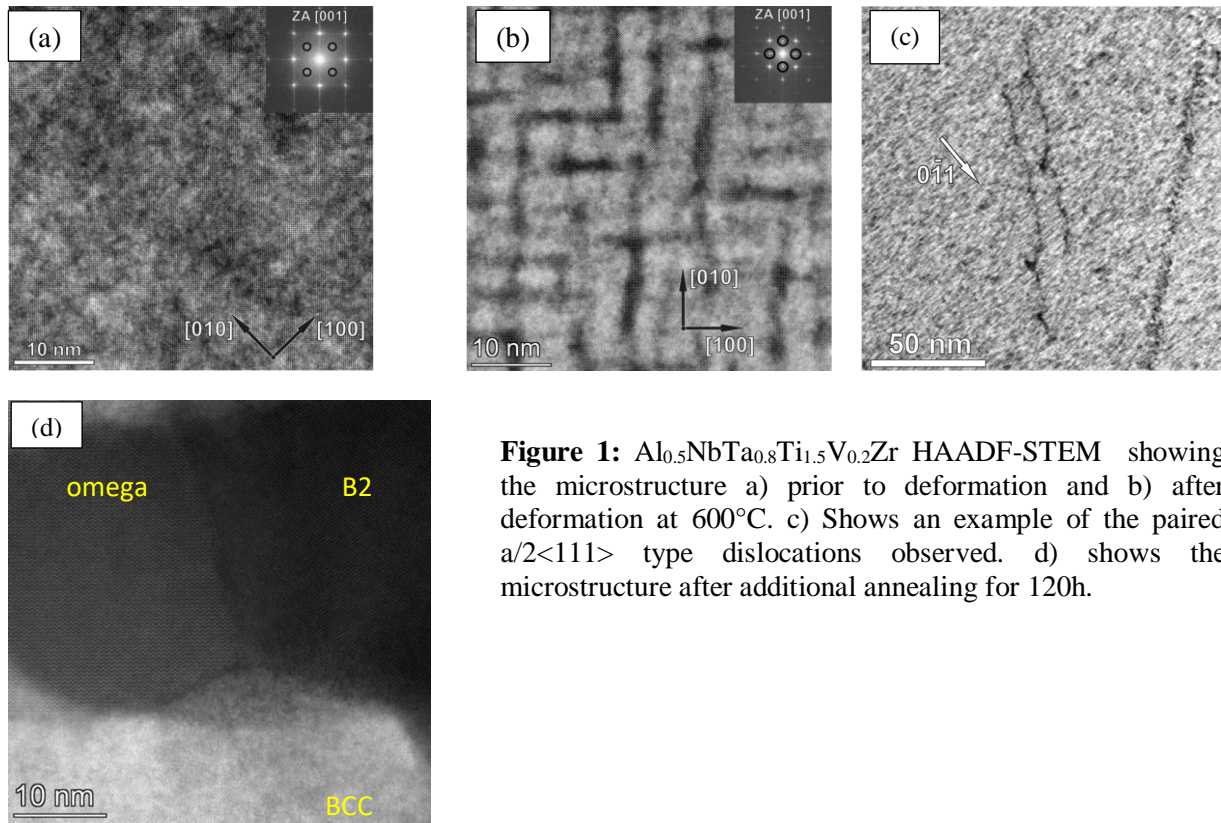


Figure 1: $\text{Al}_{0.5}\text{NbTa}_{0.8}\text{Ti}_{1.5}\text{V}_{0.2}\text{Zr}$ HAADF-STEM showing the microstructure a) prior to deformation and b) after deformation at 600°C . c) Shows an example of the paired $a/2\langle 111 \rangle$ type dislocations observed. d) shows the microstructure after additional annealing for 120h.

Computational effort:

The primary components of the B2 structure in the two-phase BCC+B2 RCCA are Zr (~57 at%), Al (~35 at%), and Ti (~8 at%). We performed Density Functional Theory (DFT) calculations on binary ZrAl to determine its stability as there is no B2 intermetallic phase on the ZrAl phase diagram. The elastic constants of B2 ZrAl were calculated, and the results indicate that the structure has a Born instability ($C_{11} < C_{12}$), rendering it unstable. We incrementally introduced Ti into the structure to determine the effect of Ti on the stability of the B2 phase. Ti is first introduced into the Zr sublattice and the elastic constants were calculated and shown in **Figure 2a-b**. As Ti concentration increases, the B2 structure remains unstable. However, at 3.7 at% Ti, the structure transforms into a tetragonal structure with the space group $P4/mmm$ and $c/a=1.39$. We repeated the process with Ti on the Al sublattice and found the same trend with the only major difference being a slightly smaller c/a ratio. In **Figure 2d**, we calculate the formation energy of Ti on Zr sites vs Ti on Al sites to determine the site Ti prefers to occupy. We found the difference in energy between the two structures to be 48meV/atom and Ti prefers to be on the Zr sublattice. From these results we conclude, the addition of Ti alone does not stabilize the B2 phase regardless of concentration or site occupancy and the stability of the structure is primarily dependent on the interactions between Zr and Al.

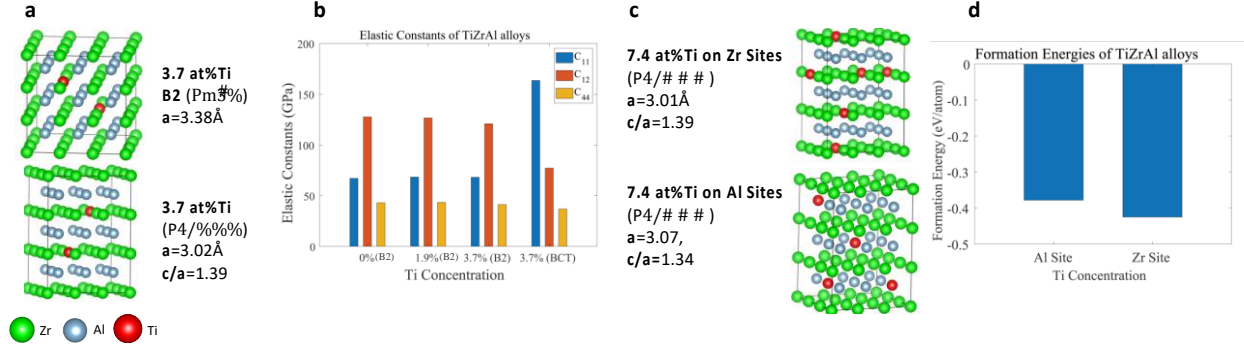


Figure 2: a) Atomic models of the 3.7 at% Ti placed on the Zr sublattice in the B2 and tetragonal structure. b) Elastic Constants as a function of increasing Ti concentration. c) 7.4 at% Ti placed on the Zr and Al sublattice and their corresponding formation energies in (d).

The observed B2 phase exists within a BCC matrix in the alloy. Therefore next, we calculated the energy as a function of strain of the B2 ZrAl structure to determine the effect of strain on the stability of the B2 structure. To isolate the effects of Ti and strain, we first perform the calculations on binary ZrAl. The strain applied is a tetragonal e_3 strain shown given by $e_3 = \frac{1}{\sqrt{6}}(2H_{33} - H_{11} - H_{22})$. Where H is the Hencky-strain, a symmetric matrix whose elements show measure of deformation a lattice must suffer to transform structures [2]. The Hencky-strain is calculated using $\mathbf{H} = \frac{1}{2} \ln(\mathbf{F}^T \mathbf{F})$, where F is the transformation matrix.

The energy vs strain for two different paths of the B2 ZrAl lattice is plotted in **Figure 3a**. We first focus on the Bain path. In the Bain path, the “ a_3 ” axis of the lattice is stretched and held constant at each point while the atomic positions and the “ a_1 ” and “ a_2 ” axes of the lattice are allowed to relax. An e_3 strain of 0, corresponds to the B2 phase with a lattice constant of $a=3.39\text{\AA}$. The point corresponding to this structure exists at a maximum. Upon placing a positive strain (tensile) to the lattice, the tetragonal structure with a $c/a=1.38$ appears, indicating the tetragonal structure is energetically favorable without the presence of Ti. Upon placing a negative strain on the lattice (compression), a second minimum appears with $a=3.62\text{\AA}$ and a $c/a=0.82$ which is stable but is 108meV/atom higher in energy than the former structure.

The energy vs strain for two different paths of the B2 ZrAl lattice is plotted in **Figure 3a**. We first focus on the Bain path. In the Bain path, the “ a_3 ” axis of the lattice is stretched and held constant at each point while the atomic positions and the “ a_1 ” and “ a_2 ” axes of the lattice are allowed to relax. An e_3 strain of 0, corresponds to the B2 phase with a lattice constant of $a=3.39\text{\AA}$. The point corresponding to this structure exists at a maximum. Upon placing a positive strain (tensile) to the lattice, the tetragonal structure with a $c/a=1.38$ appears, indicating the tetragonal structure is energetically favorable without the presence of Ti. Upon placing a negative strain on the lattice (compression), a second minimum appears with $a=3.62\text{\AA}$ and a $c/a=0.82$ which is stable but is 108meV/atom higher in energy than the former structure. Upon further analysis of the structure at the second minimum, it can be seen the structure can be related to a hexagonal structure via a Burgers shuffle illustrated in **Figure 3b**. For the second path, we apply the Burgers shuffle to the relaxed structures from the Bain Path, while fixing the lattice vectors but relaxing the atomic positions. Under tensile strain, the Burgers shuffle path follows the same energy vs strain profile as the Bain Path.

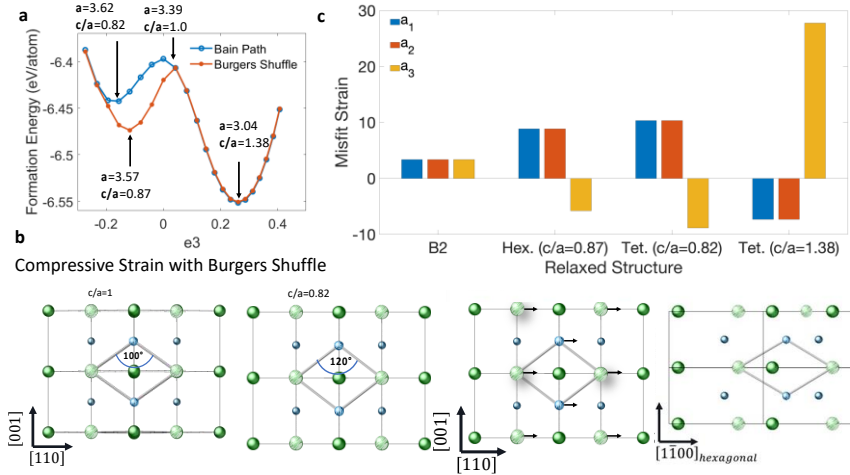


Figure 3: a) Energy as a function of strain in the ZrAl B2 lattice. b) Illustration of how (110) planes of B2 can be transformed to the (0001) planes of hexagonal phase via Burgers shuffle. Shaded atoms are one plane below into the page. d) Misfit strain with BCC matrix of all structures at minimums as well as the unstable B2 structure.

However, under compressive strain, the minimum of the path shifts from a tetragonal structure with a c/a ratio of 0.82 to 0.87. Furthermore, the minimum lowers in energy by 32meV/atom. The misfit strain shown in **Figure 3c**, shows simple atomic shuffles can result in a decrease in lattice strain

Future Plans

Work is still ongoing to determine the effects of Ti and strain on the B2 phase as well as the effect of vacancies and atomic rearrangements on B2-omega transformation pathway. Our results indicate the $Al_{0.5}NbTa_{0.8}Ti_{1.5}V_{0.2}Zr$ does not provide a stable matrix/precipitate microstructure and might be too complicated for studying fundamental mechanisms. Therefore, we are testing simpler, but well-established systems such as $Fe_{0.75}Al_{0.15}Ni_{0.1}$. Other subsets of the bcc HEA are also being investigated, both theoretically and experimentally, with the hope to find single phase B2 compositions.

References

1. V. Soni, B. Gwalani, T. Alam, S. Dasari, Y. Zheng, O. N. Senkov, D.B. Miracle, R. Banerjee, *Phase inversion in a two-phase, BCC+B2, refractory high entropy alloy*. Acta Materialia, 2020. **185**: p. 89-97
2. R. Hill, On Constitutive inequalities for simple materials, Journal of Mechanics and Physics of Solids, Volume 16, Pages 229-242.

Publications

1. J.P Couzinié, M. Heczko, V. Mazánová, Oleg Senkov, Maryam Ghazisaeidi, Rajarshi Banerjee and Michael J. Mills, *High-Temperature Deformation Mechanisms in a BCC+B2 Refractory Complex Concentrated Alloy*, Acta Materialia 233,117995 (2022).

Kinetically-driven Microstructure as a Governing Factor in Enhanced Mechanical Properties of Hydrogel Infusion Additive Manufacturing (HIAM)-produced Metals

Julia R. Greer, California Institute of Technology (Principal Investigator)

Keywords: Microstructure, Additive Manufacturing, Nano-plasticity, Twin Boundaries, Metals

Research Scope. The focus of this work is on the development of a mechanistically accurate paradigm for the understanding and characterizing the link between mechanical properties and microstructure evolution in chemically synthesized nanocrystalline metals. We aim to uncover the

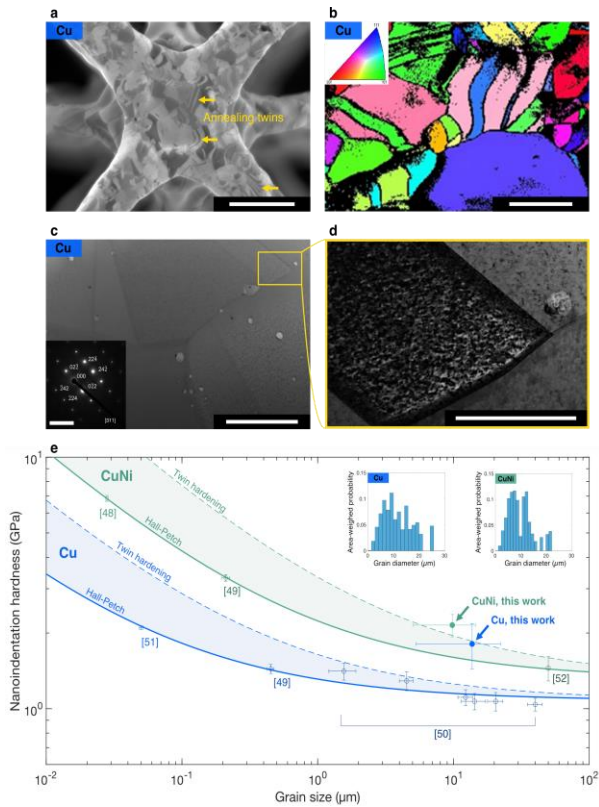


Figure 1 | Microstructure and mechanical properties of HIAM-fabricated metals and alloys. **a**, Ga^+ ion-channeling image and **b**, EBSD map of Cu show a complex micro-grained structure and multiple twinned regions. **c**, **d** TEM images of Cu show well-formed grain boundaries and aluminosilicate inclusions. **e**, Nanoindentation hardness of HIAM Cu and CuNi are higher than reference nanoindentation data and extrapolated Hall-Petch grain size scaling (dashed lines show calculated twin-induced hardening). Insets: area-weighted grain size distribution for Cu ($n = 246$) and CuNi ($n = 309$). Scale bars: **a**, 50 μm ; **b**, 20 μm ; **c**, 2 μm ,

coupled with the experiments and simulations in this work, demonstrate that *micro-sized* Cu and

mechanical deformation and failure mechanisms in micro- and nano-sized metals with complex microstructures, i.e. simultaneously nanocrystalline, ligand- and boundary-containing, and nano-porous. This hierarchical and complex microstructure evolves as a result of the hydrogel infusion-enabled additive manufacturing (HIAM) of sub-micron-sized metals. Some key features of this work include the development of novel methods for the synthesis and of the micro- and nano-mechanical experiments on additively manufactured nanocrystalline and nanoporous metals, as well as conducting thorough microstructural and chemical characterization of these materials. This approach overcomes the inherent ambiguities associated with using the Focused Ion Beam (FIB) to study mechanical behavior of small-scale metallic samples because it alters surface energy state and offers control and versatility of the grain-level and defect-level microstructures. Using EBSD and TEM, we probed the microstructure-driven internal energy landscape of metals that are produced using chemical synthesis of metal ion-containing resins followed by thermal treatment and link them to the mechanical deformation mechanism and properties.

Recent Progress. The new hydrogel infusion additive manufacturing (HIAM) fabrication technique developed by the Greer group, in part under the auspices of the existing BES grant,

CuNi alloys produced via HIAM contain high densities of special boundaries, including coherent twin boundaries, $\Sigma 3$ and other CSL boundaries (Figure 1(a-d)). Nanoindentation revealed the hardness of Cu to be 1.81 ± 0.37 GPa and that of CuNi to be 2.15 ± 0.22 GPa, which are 47% and 15% higher than what is predicted by the Hall-Petch relation¹, $H = H_0 + kd^{1/2}$, which relates nanoindentation hardness H to grain size d for ductile metals, where H_0 is an intrinsic hardness for a single crystalline material and k is a scaling factor related to grain boundary-induced hardening (Figure 1(e)). Twin boundaries disrupt dislocation motion during deformation^{2,3}, increasing measured hardness. To account for this effect, we developed a Hall-Petch based model that accounts for the contribution of twin and grain boundaries (no pores) through $H = H_0 + k \left(\frac{d}{1 + \sum_{i=1}^N p_i N_i} \right)^{-1/2}$ where d is the grain size of the material, N is the average number of twin boundaries per grain, and p_i is the effectiveness of that particular twin boundary as a plasticity barrier. To calculate an upper bound on twin-induced hardening, we assume that twin boundaries and grain boundaries equally impede dislocation motion. The terms inside the summation can account for other types of boundaries with different plasticity barrier coefficients and strengths. The observed high annealing twin densities, formed without the ordinarily requisite melting and recrystallization⁴, highlight the complex interplay of kinetic processes (e.g., solid-state diffusion and grain nucleation) and thermodynamic grain coalescence during oxidation and reduction. Our model indicates that the high boundary density and solid solution hardening alone do not explain an uncharacteristically high hardness measured in HIAM micro-sized Cu, Ni, and cupronickel alloys. Primary candidates for contributing to the high hardness in HIAM metals include (1) twin boundary hardening, (2) broad grain boundary and solid solution strengthening, and (3) special hardening contributions from triple junctions. The 1.5x relative increase in the adjusted hardness of pure metals as compared to alloys hints at a greater material-, microstructure-, and size-dependent relationship to these plasticity processes than seen in other manufacturing methods.

Another key finding from existing BES grant is that when the dimensions of HIAM Ni is reduced to the nanoscale, the microstructure becomes even more complex: nanocrystalline and nanoporous, with a single grain spanning each ligand, that is contained within an individual nano-pillar (Figure 2a). Our most recent findings indicate that the yield strength of these nanocrystalline and nano-porous nano-pillars, with diameters between 160 and 300nm, appears to be ~2x higher than those in reported nanocrystalline Ni nano- and micro-pillar compressions (Figure 2b).

Future Plans

The complex emergent microstructure and the ensuing dramatically altered mechanical response of HIAM-produced pure Ni and Cu, as well as of their alloys with micro- and nano-scale dimensions opens a new avenue for engineering and investigating complex material behavior. Building upon the research findings of the existing DOE BES grant, we will strive to develop a deeper understanding of each kinetic process that occurs during the thermal reduction steps (metal oxide to metal), and to layout the parameter space for attainable microstructures. The microstructural and energetic landscape within these samples will help understand the mechanical properties that correspond to each microstructure. In the future, we will investigate the role of each

microstructural feature class on the mechanical properties with the aim of uncovering the origins of strength amplification observed in Cu and CuNi alloys with micro- and nano-scale dimensions. The model systems for the original and the proposed investigation are pure Cu and Ni, as well as various CuNi alloys through their composition. We will first layout the accessible microstructural space for kinetically-formed metals that are produced using HIAM, with attention dedicated to the thermal reduction step from MO_x to M as the kinetics of this process drive the ensuing microstructure.

Specific research tasks that we propose to study in the renewal proposal include: (1) What parameters define specific microstructural features to be formed in HIAM small-scale metals – i.e. nano-crystallinity (grain size), nano-porosity (pore size), and number of grains per ligand? (2) Are the formed grain boundaries in the metals inherently different from those formed in pure metals and metal alloys produced through traditional methods? (3) What new deformation mechanisms are available to microstructures with dominant characteristics, for example ligands that subtend a single grain vs. multiple ones, the free volume-enabled surface relaxation in the sample interior, and the presence of a dominant grain boundary?

References

1. B. Roy, J. Das *Strengthening face centered cubic crystals by annealing induced nano-twins*. Sci. Rep. **7**, 1–8 (2017).
2. E. O. Hall *The deformation and ageing of mild steel: III Discussion of results*. Proc. Phys. Soc. Sect. B **64**, 747–753 (1951).
3. Lu, L., Shen, Y., Chen, X., Qian, L. & Lu, K. Ultrahigh Strength and High Electrical Conductivity in Copper. *Science (80-.)*. **304**, 422–426 (2004).
4. Bahl, S. *et al. Non-equilibrium microstructure, crystallographic texture and morphological texture synergistically result in unusual mechanical properties of 3D printed 316L stainless steel*. Addit. Manuf. **28**, 65–77 (2019).

Publications

1. M. A. Saccone, R. A. Gallivan, K. Narita, D. W. Yee, and J. R. Greer, "*Additive manufacturing of micro-architected metals via hydrogel infusion*, Nature (**just accepted, 2022**)

Towards Ductile, Nanostructured Metallic Glasses

Wendy Gu, Mechanical Engineering, Stanford University

Keywords: Colloids, nanoparticles, high pressure, interfaces, metal borides

Research Scope

The major goals of this project are to understand deformation mechanisms in metallic glass nanoparticles made using colloidal synthesis, and bulk nano-glasses made using these nanoparticles. Advanced electron microscopy, X-ray measurements and nano-mechanical testing are used to evaluate structure and mechanical performance. The project involves the use of colloidal methods to synthesize ductile metallic glass nanoparticles. The composition of these particles consists of one to five metals in combination with boron. One objective is to understand the relationship between composition, atomistic structure, free volume and mechanical properties. These nanoparticles are also compressed at high pressure inside of a diamond anvil cell to modify the atomistic structure, measure bulk modulus and test the amorphous phase stability. The nanoparticles are sintered together under elevated temperature and pressure to fabricate nanostructured metallic glasses that contain amorphous interfaces of lower density than the surrounding amorphous grains. These structures are used to investigate the connection between structural and/or chemical heterogeneities and mechanical properties such as strength and ductility.

Recent Progress

Bulk, nanostructured metallic glasses were fabricated by sintering nanoparticles together (Figure 1). Iron boride metallic glass nanoparticles were synthesized at the gram-scale. Each batch of nanoparticles is sufficient for the fabrication of several ~ 8 mm x 0.5 mm sized discs.

The nanoparticle size (which controls the size of the amorphous grain in the bulk nano-glass) was controlled by varying the ratio of chemical reagents (metal salt, ligands, chemical reducing

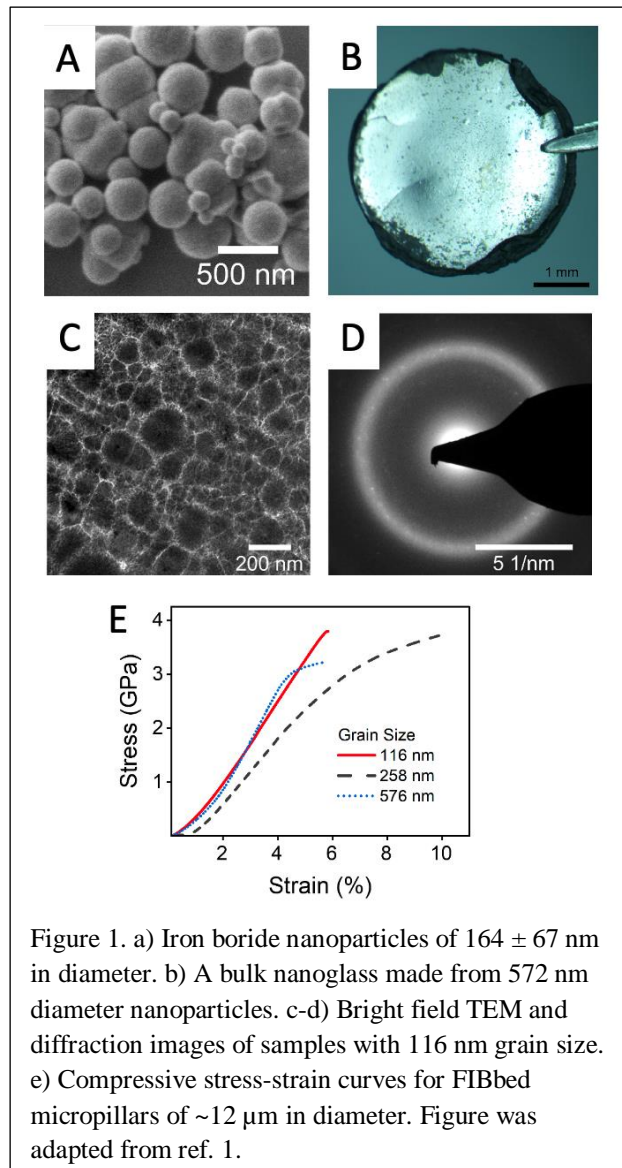


Figure 1. a) Iron boride nanoparticles of 164 ± 67 nm in diameter. b) A bulk nanoglass made from 572 nm diameter nanoparticles. c-d) Bright field TEM and diffraction images of samples with 116 nm grain size. e) Compressive stress-strain curves for FIBbed micropillars of ~ 12 μ m in diameter. Figure was adapted from ref. 1.

agent, solvent). Nanoparticle diameters between ~90 to 600 nm were achieved with ~30-40% size distribution. The optimal pressure and temperature for hot pressing of iron boride nanoparticles into bulk, millimeter scale metallic nanoglasses was determined. The structural (SEM, TEM), thermal (digital scanning calorimetry) and mechanical properties (nanoindentation, micropillar testing) of the nanoparticles and bulk nanoglasses were characterized.

Bulk nanoglasses with grain sizes of 116 nm, 258 nm and 576 nm had mechanical properties (e.g. hardness, yield strength, and ultimate compressive strength) that are on par with bulk metallic glasses. Plasticity of up to ~4% was achieved. Grain size did not have a large influence on the mechanical properties of the nanoglasses. Instead, the presence of nanocrystals governed deformation. Nanocrystals formed within the nanoglasses even when the nanoglasses were fabricated below the crystallization temperature. A higher density of nanocrystals resulted in higher plasticity and lower yield strength in micropillar compression tests.

The deformation mechanism of bulk nanoglasses was determined through a combination of strain rate dependent nanoindentation tests, micropillar compression testing and post-compression imaging of the micropillars. The nanoglasses were observed to fail through crack propagation at the interfaces between grains, rather than shear banding. Thus, previous theory and simulations that propose that high ductility in nanoglasses can be achieved through shear band-mediated mechanism do not appear to apply to nanoglasses with grain sizes above ~100 nm. In addition, the composition of the interfaces between the grains (e.g. impurities or other contaminants, other compositional differences compared to material within grains) may have a large impact on mechanical properties.

In a second project, high pressure compressions and X-ray diffraction of nickel boride metallic glass nanoparticles of two different sizes were performed at the Advanced Photon Source (Figure 2). Surprisingly, the nanoparticles remained amorphous up to pressures of ~40 GPa. In situ high-pressure X-ray diffraction (XRD) was used to track structural changes within the nanoparticles. The ambient pressure pair-distribution functions generated from XRD showed that the smaller sized nanoparticles had a more compact amorphous structure with lower coordination number. The bulk modulus of the nanoparticles was found to be 183 GPa and 178 GPa for two different particle sizes.

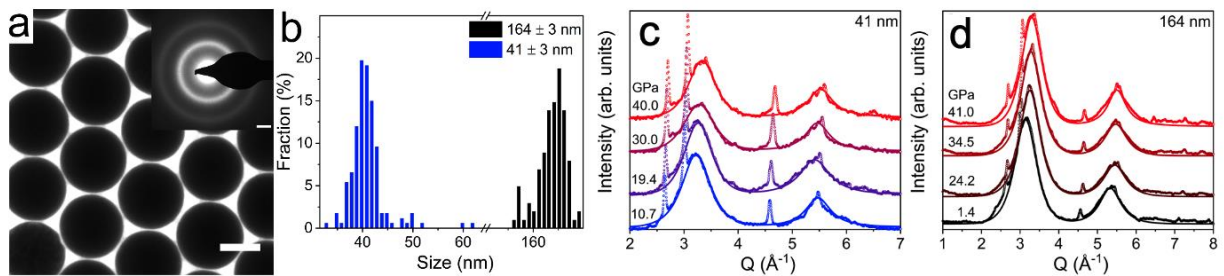


Figure 2. a) TEM image of 164 nm sized $\text{Ni}_{1-x}\text{B}_x$ nanoparticles. Scale bar is 100 nm. Inset showing TEM diffraction pattern for 41 nm $\text{Ni}_{1-x}\text{B}_x$ nanoparticles. Scale bar is 1 nm^{-1} . b) Size distribution of 41 nm and 164 nm sized $\text{Ni}_{1-x}\text{B}_x$ nanoparticles measured using TEM images. Experimental high pressure in situ XRD patterns used for peak fitting and the corresponding fitted amorphous peaks (Re gasket fitted peaks not shown) for a) 41 nm nanoparticles, and b) 164 nm nanoparticles. Figure is adapted from ref. 2.

Future Plans

The next activities in this project will focus on the synthesis of CoB nanoparticles, as well as particles of more compositional complexity (binary, ternary and high entropy metallic glass borides) made up of combinations of Fe, Ni, Co, Mn, Cu, Cr and B. Using these particles, we will investigate the connection between the atomic bonding within metallic glasses (more metallic-like vs. more covalent-like) and mechanical properties. Mechanical tests on these metallic nanoparticles will be compared to our existing data on NiB and FeB binary metallic glass nanoparticles. The elemental composition, mechanical properties, crystal structure, and thermal properties of these nanoparticles will be studied using TEM, in situ SEM compression, and differential scanning calorimetry (DSC). We will also investigate whether multimetallic nanoparticle form intermetallic or high entropy borides when heated above their glass transition temperature.

The second project will investigate how to improve the ductility of the nanostructured bulk metallic glasses. Our current results indicate that the interfaces within the nano-glasses are sites of crack initiation. We hypothesize that stronger and tougher interfaces can be formed if nanoparticles without surface ligands are used. In our previous results, the nanoparticles were coated with a layer of organic surface ligands that decompose at the elevated temperatures used during the sintering process. This likely results in carbon and other impurities at the interfaces. In addition, bulk metallic glasses with multiple, nanoscale glassy phases have been shown to have superior ductility. We will try to achieve this microstructure within our nano-glasses by synthesizing core-shell two-phase metallic glass nanoparticles and using these to form the nano-glasses.

References

1. M.W. Wang, M.T. Kiani, A. Parakh, Yue Jiang, X.W. Gu, *Effect of Grain Size on Iron-Boride Nanoglasses*. Journal of Materials Science and Technology. Accepted.
2. A. Parakh, M.T. Kiani, A.A. Colmenares, A.C. Lee, G. Shen, S. Chariton, V.B. Prakapenka, X.W. Gu, *High Pressure Deformation of Metallic Glass Nanoparticles*. Journal of Non-Crystalline Solids. **597**, 121923 (2022).

Publications

1. M.W. Wang, X. W. Gu, *From Nanocrystals to Nanocrystalline Metals*, Chem, **7**, 285-287 (2021).
2. R.P. Patil, M.T. Kiani, X.W. Gu, *Effect of strain rate on the deformation of hollow CoS nanoboxes and doubly porous self-assembled films*. Extreme Mechanics Letters, **47**, 101354 (2021).
3. M.T. Kiani, L.T. Gan, R. Traylor, R. Yang, C.M. Barr, K. Hattar, J.A. Fan, X.W. Gu, *In-situ TEM Tensile Testing of Bicrystals with Tailored Misorientation Angles*. Acta Materialia, **224**, 117505, (2021).
4. M.T. Kiani, Z. H. Aitken, A. Parakh, Y.W. Zhang, X.W. Gu, *Extraordinary Strain Hardening from Dislocation Loops in Defect-Free Al Nanocubes*, Nano Letters. **22**, 4036-4041 (2022).
5. A. Parakh, M.T. Kiani, A.A. Colmenares, A.C. Lee, G. Shen, S. Chariton, V.B. Prakapenka, X.W. Gu, *High Pressure Deformation of Metallic Glass Nanoparticles*. Journal of Non-Crystalline Solids. **597**, 121923 (2022).
6. M.W. Wang, M.T. Kiani, A. Parakh, Yue Jiang, X.W. Gu, *Effect of Grain Size on Iron-Boride Nanoglasses*. Journal of Materials Science and Technology. Accepted.

Elucidating the mechanical and thermal response of nanotwinned Ni alloys

Kevin J. Hemker, Johns Hopkins University

Keywords: nanotwins, mechanical behavior, shear banding, thermal stability

Research Scope

Our current research aims to elucidate the microscopic origins of the unique mechanical and thermal properties in nanotwinned Ni alloys. Our preceding research has demonstrated ultrahigh strength, very localized plasticity, microstructural stability, and extraordinarily low CTE. Based on in situ and post-mortem TEM experiments, we seek to understand how the nanotwinned structure and local chemistry influence the strain fields that arise during thermal and mechanical loading. Efforts during the current reporting period have been focused on 1) identifying the mechanisms that trigger shear banding; 2) exploring new approaches to control the nanotwin spacing; and 3) evaluating thermal stability and the mechanisms of microstructural evolution.

Recent Progress

Micropillar compression tests of a Mo-rich nanotwinned $\text{Ni}_{84}\text{Mo}_{11}\text{W}_5$ alloy (all compositions are in at.%) have been shown to possess ultrahigh strengths of 3-4 GPa and extremely localized plasticity marked by shear bands [1]. Careful study of a W-rich ($\text{Ni}_{85}\text{Mo}_3\text{W}_{11}$) alloy allowed us to identify the underlying deformation mechanisms that govern the strain localization. Results are summarized in Fig. 1. The W-rich pillars also showed compressive strengths greater than 2.5 GPa with some plasticity before the first strain burst (Fig. 1(a)). Shear banding is very abrupt in the Mo-rich alloy, which prohibits post-mortem observations of these samples at the onset of shear banding. However, for the W-rich samples several tests were strategically stopped before the observation of the first measurable shear band, and FIB lift-

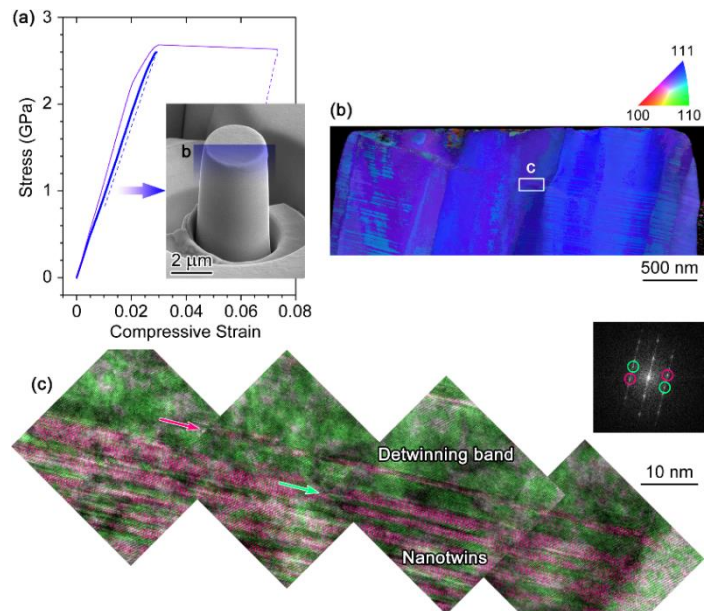


Figure 1. Micropillar compression tests and post-mortem TEM analysis of a W-rich alloy. (a) Examples of stress-strain curves. One test (blue curve) was stopped before the strain burst and the pillar (inset) was sectioned into a thin foil. (b) IPF map of the deformed pillar, colored using orientation in vertical (i.e., film growth) direction. (c) HRTEM image of a portion of the detwinning band, colored with Fourier filtering to distinguish between the two twin variants. Arrows mark fragmented nanotwins.

out was employed to fabricate thin foils of the deformed W-rich pillars. TEM-based crystal orientation mapping (Fig. 1(b)) indicated that the shear bands composed of recrystallized and reoriented nanograins, as seen in other pillars after strain bursts, had not yet developed in the pillar that was terminated before the first strain burst. Closer inspection of HRTEM images (Fig. 1(c)), however, revealed a detwinned (or detwinning) region with a twin-free thickness of 20-30 nm, which is an order of magnitude greater than the twin spacing (2-3 nm) in the as-deposited film. The band extended across the pillar and was parallel to the (111) twin boundaries in the pristine part of the pillar. Moreover, segments of nanotwins were captured between the completely detwinned band and the unaffected nanotwins. These observations allowed us to postulate that detwinning operates as the precursor to shear banding in all nanotwinned Ni-Mo-W alloys. We note that detwinning and shear banding were also observed during the plastic deformation of nanotwinned Cu-Al alloys [2], but the mechanisms therein appear to be different because the initial twin spacing was significantly larger (~10 nm) in Cu-Al than in Ni-Mo-W. As a result, detwinning in Cu-Al was facilitated by the gliding dislocations intersecting with twin boundaries and leading to shear bands that were inclined to the twin boundaries. By contrast, dislocation activity is restricted in Ni-Mo-W and detwinning appears to rely on the in-plane migration of twin boundaries. In the W-rich alloy, formation of the twin-free regions enables dislocation activity, which in turn results in strain localization, and recrystallization in the later stages of deformation.

Rational control of twin spacing was investigated as a route towards concurrently suppressing the strain localization and retaining the ultrahigh strength of nanotwinned Ni- alloys. Our previous attempts indicated that varying the Mo/W ratio in $\text{Ni}_{85}\text{Mo}_{15-x}\text{W}_x$ films and the

deposition rate have little effect in modifying the twin spacing [3]. However, our ongoing collaborations with Prof. Jessica Krogstad at UIUC have shown that the twin spacing can be affected by depositing films with varying Ni content and/or substrate temperatures. As demonstrated in Fig. 2, tuning the power settings for pure Ni and $\text{Ni}_{85}\text{Mo}_{13}\text{W}_2$ targets during co-sputtering at room temperature increased the average twin spacing from 2.9 nm to 3.8 nm when the Ni content was increased from 91.8 at.% to 93.4 at.%. This increase is likely attributable to the change in SFE by alloying, as reported in nanotwinned Cu and Cu-Al alloys [4]. The effect of substrate temperature was more

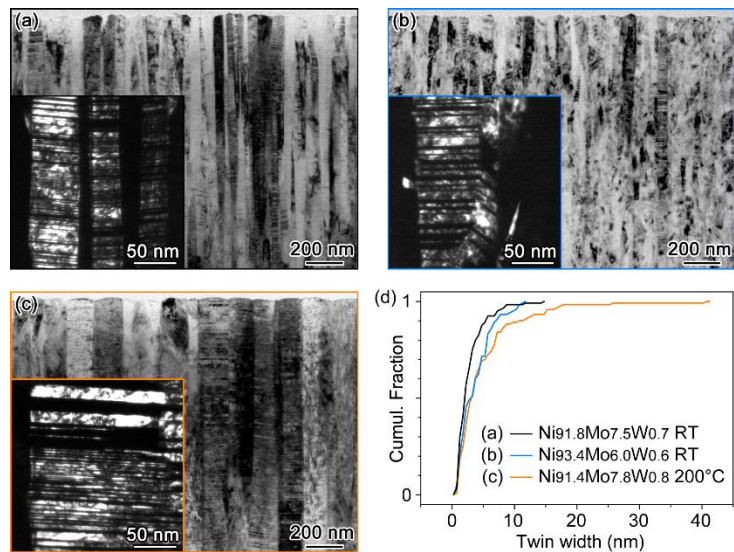


Figure 2. Control of nanotwin spacing in sputtered Ni-Mo-W films. (a-c) Cross-sectional TEM (bright field) images of films made with the compositions and substrate temperatures shown in (d). Inset dark field images show the microstructure (grain size, twin orientation, etc.) of representative columnar grains. (d) Cumulative distributions of nanotwin spacing in films (a-c).

drastic; for a comparable approximate composition of $\text{Ni}_{91}\text{Mo}_8\text{W}_1$, the average twin spacing increased from 2.9 nm at room temperature to 5.0 nm at 200 °C. A significant number of much wider (> 20 nm) individual nanotwins were also observed in the 200 °C film. Our work also revealed that the columnar grains were also affected by the deposition parameters. For instance, increasing the Ni content resulted in a weaker texture and a wider spread in the distribution of twin orientation (Fig. 2(b)), and increasing substrate temperature resulted in a doubling of the columnar grain diameters (Fig. 2(c)).

Our earlier measurements of the CTE for a series of $\text{Ni}_{85}\text{Mo}_{15-x}\text{W}_x$ films evidenced it to be remarkably lower than that of pure Ni. More interestingly, the Mo-rich films (e.g., $\text{Ni}_{85}\text{Mo}_{13}\text{W}_2$) showed nearly temperature-invariant CTE in the range of 20-600 °C. Assessment of thermal stability of the nanotwinned Ni-Mo-W alloys is a prerequisite for understanding their unique thermal expansion behavior. In the current study, in situ heating experiments conducted in the TEAM I STEM at NCEM allowed us to compare and contrast the microstructural evolution in Mo-rich and W-rich alloys. As shown in Fig. 3, atom-resolved STEM images of both films were recorded at both room temperature and during annealing. Twin boundaries and grain boundaries in the Mo-rich film were found to readily migrate at 400 °C (Fig. 3(a2,a3)), whereas in the W-rich film they were almost immobile up to 600 °C (Fig. 3(b2,b3)). Annealing at even higher temperatures induced rapid formation of carbide precipitates in both films. Our findings indicated that W is more effective in stabilizing the nanotwins than Mo, even though first-principles calculations predicted that both elements can equally decrease the SFE in Ni alloys [5].

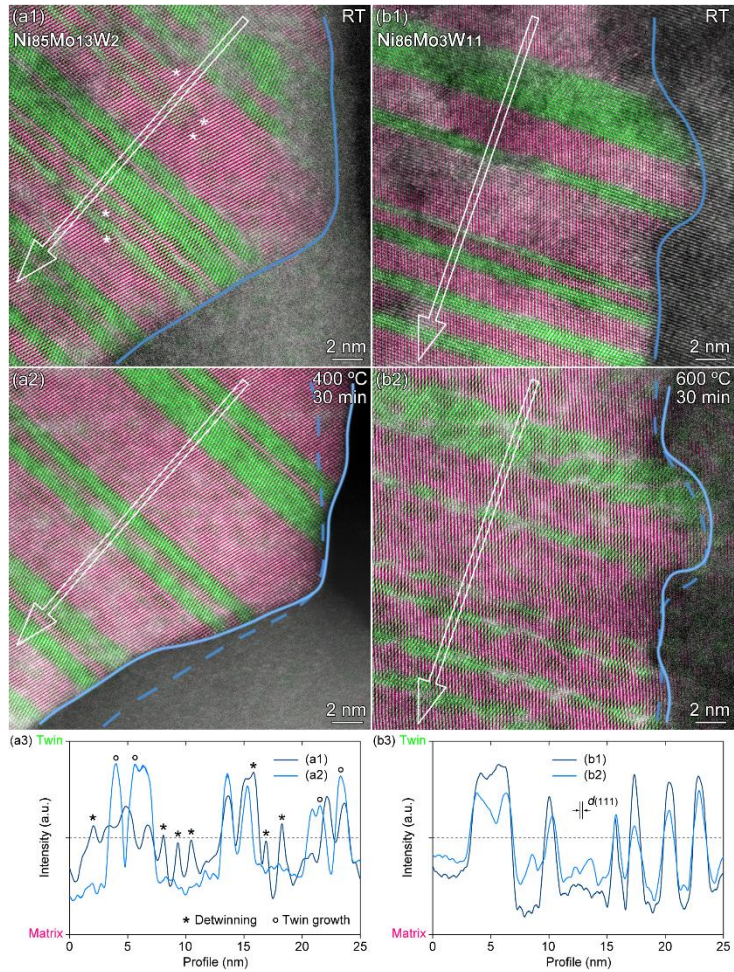


Figure 3. HRSTEM images recorded during in situ heating experiments of (a1,a2) Mo-rich and (b1,b2) W-rich alloy. Nanotwins were colored with Fourier filtering. “*” symbols in (a1) mark the defective sites on twin boundaries. Solid curves in (a1) and (b1) and dash curves in (a2) and (b2) are the initial boundary of columnar grains. Solid curves in (a2) and (b2) indicate grain boundaries after migration. (a3) and (b3) show intensity profiles as measured along the open arrows (white) in (a1,a2) and (b1,b2). The discernible valleys and peaks are identified as matrix and twin variants.

Future Plans

Our work in the coming year will build on these observations and be focused to mature our understanding in three specific areas: 1) synthesis of Ni-Mo-W films with controlled nanotwinned structure (in particular, greater twin spacing); 2) in situ TEM compression experiments to clarify the role of dislocation-CTB interactions in detwinning and strain localization; and in situ TEM heating experiments combining with first-principles calculations to understand the thermal expansion behavior, such as the role of local non-cubic symmetry and local chemistry at twin boundaries.

To create nanotwinned Ni-Mo-W alloys with greater twin spacing, we will return to UIUC to build on the positive trends described above and synthesize films with even higher Ni content at deposition temperatures in the range of 100-300°C. This work will provide greater insight into the growth kinetics of nanotwinned alloys. It will also provide specimens with wider twin spacing that will greatly facilitate the in situ TEM studies that we will undertake to provide more clarity on the deformation mechanisms and to identify the factors that underpin the mechanical and thermal stability of nanotwinned alloys. These in situ loading experiments will be conducted at CINT and will also allow us to elucidate the role of dislocation-coherent twin boundary (CTB) interactions in both detwinning and strain localization. To investigate thermal behavior of nanotwinned Ni alloys, in situ heating experiments at NCEM will combine high-resolution and 4D STEM to quantify the thermal expansion that occurs within individual nanotwins. Here the potential role of crystal anisotropy and local chemistry will be experimentally investigated and unraveled with the aid of ab initio calculations.

References

1. G.M. Valentino, S. Xiang, L. Ma, K.Y. Xie, M.R. He, W.C. Oliver, G.M. Pharr, J.A. Krogstad, T.P. Weihs, and K.J. Hemker, *Investigating the compressive strength and strain localization of nanotwinned nickel alloys*, *Acta Materialia* **204**, 116507 (2021).
2. C.S. Hong, N.R. Tao, X. Huang, and K. Lu, *Nucleation and thickening of shear bands in nano-scale twin/matrix lamellae of a Cu-Al alloy processed by dynamic plastic deformation*, *Acta Materialia* **58**, 3103-3116 (2010).
3. G.M. Valentino, P.P. Shetty, A. Chauhan, J.A. Krogstad, T.P. Weihs, and K.J. Hemker, *Nanotwin formation in Ni-Mo-W alloys deposited by dc magnetron sputtering*, *Scripta Materialia* **186**, 247-252 (2020).
4. L. Velasco, M.N. Polyakov, and A.M. Hodge, *Influence of stacking fault energy on twin spacing of Cu and Cu-Al alloys*, *Scripta Materialia* **83**, 33-36 (2014).
5. S.L. Shang, C.L. Zacherl, H.Z. Fang, Y. Wang, Y. Du, and Z.K. Liu, *Effects of alloying element and temperature on the stacking fault energies of dilute Ni-base superalloys*, *Journal of Physics: Condensed Matter* **24**, 505403 (2012).

Publications

1. G.M. Valentino, P.P. Shetty, J.A. Krogstad, K.J. Hemker, *Fabrication of Freestanding Metallic Ni-Mo-W Microcantilever Beams with High Dimensional Stability*, J. Microelectromech Systems **29**, 329-337 (2020).
2. G.M. Valentino, J.A. Krogstad, T.P. Weihs, K.J. Hemker, *Tailoring the coefficient of thermal expansion of ternary nickel alloys through compositional control and non-contact measurements*, J of Alloys and Compounds **833**, 155024 (2020).
3. G.M. Valentino, P.P. Shetty, A. Chauhan, J.A. Krogstad, T.P. Weihs, K.J. Hemker, *Nanotwin formation in Ni–Mo–W alloys deposited by dc magnetron sputtering*, Scripta Materialia **186**, 247-252 (2020).
4. G.M. Valentino, S. Xiang, L. Ma, K.Y. Xie, M.R. He, W.C. Oliver, G.M. Pharr, J.A. Krogstad, T.P. Weihs, K.J. Hemker, *Investigating the compressive strength and strain localization of nanotwinned nickel alloys*, Acta Materialia **204**, 116507 (2021).

Computational and Experimental Investigation of Cryogenic Grain Boundary Motion for Enhanced Mechanical Properties

PI: Eric R. Homer, Brigham Young University, Provo, UT, USA.

Co-PI: Gregory B. Thompson, University of Alabama, Tuscaloosa, AL, USA.

Keywords: Grain Boundaries, grain boundary migration, cryogenic temperatures

Research Scope

The major goal of the project is to determine the feasibility of cryogenic processing to obtain enhanced mechanical properties by influencing the microstructural network of grain boundaries (GBs). GBs have a significant influence on numerous material properties, including strength and ductility. Whereas high temperature processing would allow all GBs to migrate, cryogenic processing could allow select GBs to migrate (Brons et al., 2014; Zhang, Weertman, & Eastman, 2005). This presents a transformational opportunity to create different microstructural networks at cryogenic temperatures that have enhanced strength and ductility.

In short, work during the first funding period demonstrated that ordered atomic motions are central to cryogenic mobility and that additional thermal energy serves to frustrate the coordinated movements, leading to inverse temperature dependence of GB mobility. The current funding period has focused on testing three hypotheses related to the complexities of different materials, GB structures, and alloying/solute elements. These hypotheses are: (i) The ordered atomic motions predicted by simulations are comparable between interatomic potentials and consistent with experiments and classical models of migration. (ii) Minor changes in local atomic GB structure may slightly alter the ordered atomic motions but the overall mobility behavior will be preserved. (iii) Solutes that do not interrupt the atomic GB structure will not interfere with ordered migration of the GB. The work has combined simulations, used to investigate the atomic mechanisms under various conditions described above, with experiments, focused on examining these various conditions in real materials and relevant conditions, and with theory to provide understanding of the thermally activated processes underlying the observed behaviors.

Recent Progress

Unifying (classical) theory of migration that accounts for Arrhenius and non-Arrhenius behaviors

One particularly important accomplishment is a publication in NPJ Computational Materials, by Homer et al. (2022a), that shows that a forgotten classical model of grain boundary migration can account for non-Arrhenius behaviors observed in the past two decades. It is based on a simple two-state model of atoms jumping between the two grains. The potential energy landscape for jumps between the two states is illustrated in Figure 1a, where the two states are separated by an intrinsic

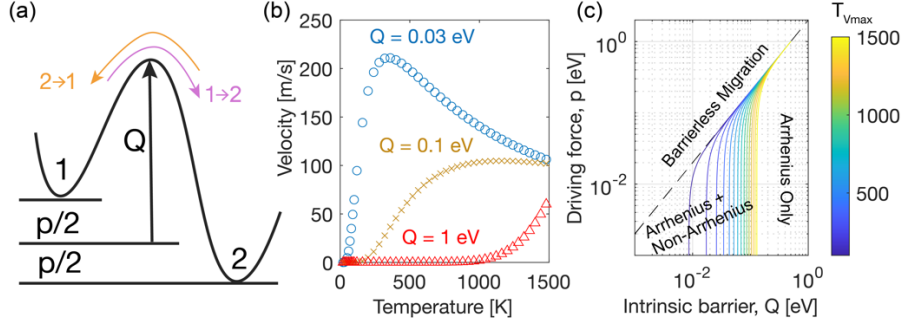


Figure 1. (a) Potential energy landscape of two-state model for atoms jumping between grains, with intrinsic barrier energy, Q , and driving force bias, p . (b) Plot of Equation 1 for several values of Q . (c) Contour plot of conditions under which to expect Arrhenius only migration (e.g. $Q > 0.2$ eV) or Arrhenius and non-Arrhenius migration (e.g. $Q < 0.1$ eV).

energy barrier, Q , and the migration is biased in one direction by magnitude p . A combination of forward and backwards jumps results in the following velocity model

$$v = v_o \exp\left(\frac{-Q}{k_B T}\right) 2 \sinh\left(\frac{-p}{2k_B T}\right) \quad (1)$$

where v is the velocity, v_o is a reference velocity, and k_B is Boltzmann's constant. Equation 1 simplifies to the classical form of $v = Mp$ when $p \ll k_B T$, where M is the mobility. But, this assumption is not always valid, particularly in the case of cryogenic conditions. In such a case, reverting to the full equation leads to interesting insights. Figure 1b provides plots of Equation 1 for several different values of Q . As can be seen, at low values of Q the result is Arrhenius behavior at the lowest temperatures before reaching a maximum and then becoming non-Arrhenius. Figure 1c provides a map of the conditions under which this non-Arrhenius behavior might be observed. The non-Arrhenius behavior results from the increased frequency of “backwards” jumps that inhibit forward migration of the boundary at higher temperatures when the intrinsic barrier, Q , is small. This classical model fits with the observations of what the ordered atomic motions are doing in simulations, they become increasingly frustrated at higher temperatures, leading to the non-Arrhenius behavior.

This classical model and explanation is consistent with the observations of cryogenic coarsening (Brons et al., 2014; Zhang, Weertman, & Eastman, 2005). Furthermore, it reconciles other observations in the literature, described in the paper. Finally, the model provides a way to predict the conditions under which non-Arrhenius boundary migration might occur.

Impact of GB structures variation, interatomic potential, and alloying/solute elements

Simulation work examining incoherent twin boundaries have examined the role of structural variation within the GB, the variation of interatomic potential, as well as the impact of differing levels of solute atoms added. When the structure is varied, as described by Homer et al. (2022a, 2022b), by considering metastable structures of the GB, a spectrum of velocity profiles is

obtained. These velocity profiles can be fit using Equation 1 and reinforce the transition from Arrhenius only behavior to Arrhenius and non-Arrhenius behavior as the intrinsic barrier energy, Q , is increased. Structural variations therefore suggest that a statistical mechanical approach could be applied. But, defects in the GB can have a significant stagnating effect, requiring larger thermal fluctuations to migrate away from the defect. Variation of interatomic potential, as described in work that will be submitted for publication shortly, shows surprisingly good agreement and the behaviors remain unchanged. The addition of solute elements, as described in work that will be submitted for publication shortly, shows the expected slowing of the velocities as solute content is increased. But there is an unexpected transition that is observed where the solute content suddenly leads to stick-slip behavior. This requires “nucleation” events, which have a dramatic impact on the temperature dependence of the boundary migration. Remarkably, all three of these factors appear to have little impact on the ordered atomic motions.

Experimental observations of cryogenic indentation in nano twinned Cu-Al

Earlier experiments suggested that detwinning could play an important role in cryogenic coarsening (Brons et al., 2014). Based on this observation, thin films of copper with 2 at.% and 8 at.% Al in solid solution assess the role of solute content on this growth behavior. Note that aluminum, at these concentrations, reduces copper’s stacking fault energy, which we hypothesized would provide a thermodynamic resistance to detwinning. Through high-rate sputter deposition, the two alloys exhibited a high density of nano twins. Upon cryogenic indentation, the columnar grains for the Cu-2Al alloy bent and tracked along the angle of the indenter tip and too were absent of twins (c.f. Figure 2a). However, unlike the results of Brons et al., the grain size had not coarsened. It is concluded that the indenter impression caused the columnar grains to bend such that a non-zero Schmid force was not on the close packed plane facilitating the passage of Shockley partials to remove the twin. The high fraction of random high angle grain boundary area on either side of the columnar diameter acted as a sink to readily absorbed the passing partials. Consequently, no coarsening was observed. Unlike the Cu-2Al alloy, the highly twinned Cu-8Al alloy did not have its columnar grains bent under the indenter (c.f. Figure 2b). Rather the columnar

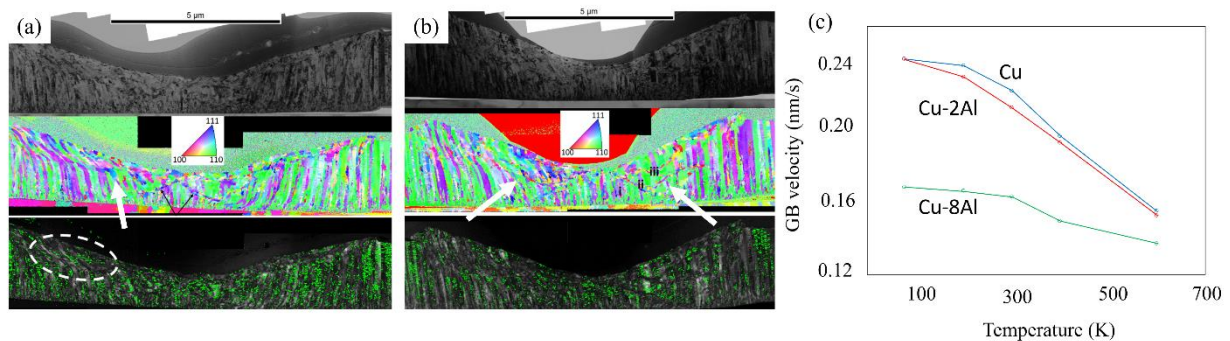


Figure 2. Series of bright field (top), grain orientation (middle), and S3 boundary (bottom) images for (a) Cu-2Al indented at 77K (b) Cu-8Al indented at 77K. Note the white arrows identifying either the bent grains in (a) or the sheared grains in (b). (c) Simulated $\Sigma 3$ grain boundary velocity as a function of increasing temperature. Note the sluggish velocity of Cu-8Al at lower temperatures.

grains sheared with a mirror reflection of the indenter geometry in its microstructure. This resistance contributed to the significant solid solution strengthening, evident by the 5.02 ± 0.41 GPa strength, as well as sluggish twin boundary migration noted in the coupled simulations, Figure 1c. These results not only lend insights into compositional means to stunt cryogenic grain growth mechanisms but also the mechanical responses and microstructure stability higher solute additions can achieve in solid solution strengthening. This work will be submitted for publication shortly.

Future Plans

As noted, several topics of research are nearly ready for publication and should be submitted before the end of the year. Additionally, some exciting in situ cryogenic indentation has been carried out in partnership with Bruker-Hysitron Micromechanical Systems. Figure 3a-b are two-time lapse images that shown the pillar compression response in the highly twinned Cu-2Al alloy. Figure 3c is the ambient temperature response, with nearly elastic-to-plastic response for the same alloy. Figure 3d is Cu-2Al indented at 125 K. While shear bands were not noted in the postmortem, ex situ characterization, the clear ‘saw tooth’ response is indicative this alloy also experiences a shear reaction under compression, which was evident only through *in operando* environment test. The next series of tests planned will provide similar compression testing but with an electron transparent wedge allowing direct quantification of boundary motion in the cryogenic condition. Finally, a renewal proposal is being prepared to address longer term topics and goals.

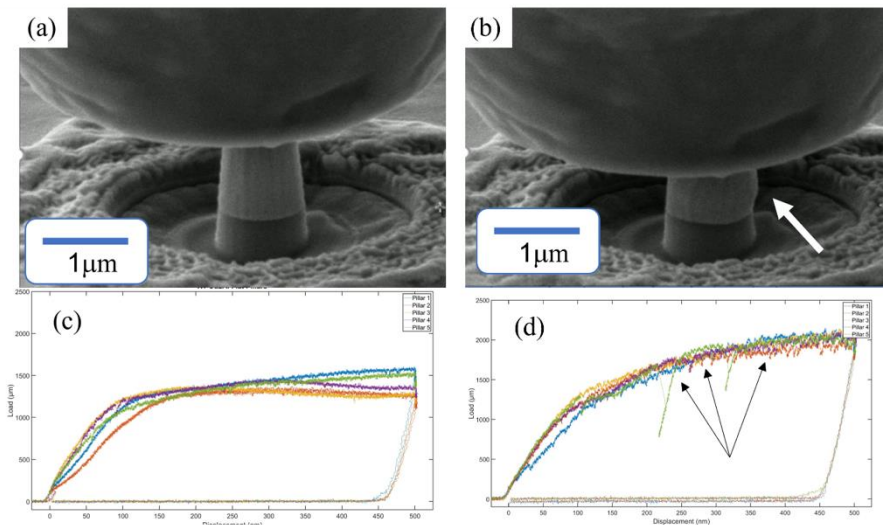


Figure 3: SEM time lapse images of a Cu-2Al sample compressed at 125 K (a) initial stage of loading (b) near the end of compression, note the bulge formation pointed to by the white arrow (c) near elastic-plastic response of the alloy at room temperature (d) work hardening and serrated response from shearing of the alloy at 125 K.

References

- Brons, J.G., Hardwick, J.A., Padilla, H.A., II, Hattar, K., Thompson, G.B., & Boyce, B.L., *The role of copper twin boundaries in cryogenic indentation-induced grain growth*. *Materials Science & Engineering A* **592**, 182–188 (2014).
- Zhang, K., Weertman, J.R., & Eastman, J.A., *Rapid stress-driven grain coarsening in nanocrystalline Cu at ambient and cryogenic temperatures*. *Applied Physics Letters* **87**, 061921 (2005).

Publications

1. Homer, E.R., Johnson, O.K., Britton, D., Patterson, J.E., Sevy, E.T., and Thompson, G.B., *A classical equation that accounts for observations of non-Arrhenius and cryogenic grain boundary migration*. npj Computational Materials **8**, 157 (2022a).
2. Homer, E.R., Verma, A., Britton, D., Johnson, O.K., Thompson, G.B., *Simulated migration behavior of metastable $\Sigma 3$ (11 8 5) incoherent twin grain boundaries*. IOP Conference Series: Materials Science and Engineering **1249**, 012019 (2022b).
3. Li, R., Homer, E.R., Hong, C., Zhang, Y., Jensen, D.J., *An experimentally-based molecular dynamics analysis of grain boundary migration during recrystallization in aluminum*. Scripta Materialia **211**, 114489 (2022)
4. Moore, R.D., Beecroft, T., Rohrer, G.S., Barr, C.M., Homer, E.R., Hattar, K., Boyce, B.L., and Abdeljawad, F., *The grain boundary stiffness and its impact on equilibrium shapes and boundary migration: Analysis of the $\Sigma 5$, 7, 9, and 11 boundaries in Ni*. Acta Materialia **218**, 117220 (2021).
5. Erickson, H.C., and Homer, E.R., *Insights into grain boundary energy structure-property relationships by examining computed [100] disorientation axis grain boundaries in Nickel*. Scripta Materialia **185**, 165–169 (2020).
6. Frazer, D., Bair, J.L., Homer, E.R., and Hosemann P., *Cryogenic Stress-Driven Grain Growth Observed via Microcompression with in situ Electron Backscatter Diffraction*. JOM **72**, 2051–2056 (2020).

Understanding the Role of Surface Energy in the Deformation of Metal Nanoparticles

Tevis D.B. Jacobs, University of Pittsburgh. Ashlie Martini, University of California, Merced.

Keywords: Nanoparticles, Deformation mechanisms, Dislocations, Surface diffusion,

1. Research Scope

Surfaces play a critical role in nanoscale deformation both due to surface-dislocation nucleation and surface diffusion; however, fundamental understanding of these mechanisms and their competitive or cooperative role in the mechanical behavior of nanoparticles is lacking. The long-term goal of this research program is to achieve fundamental understanding of how surface energy modifies (and is modified by) “bulk” deformation in nanoparticles. In service of that long-term goal, the current objective of this research is to understand how surface faceting and surface energy affect the deformation of small metal nanoparticles under compression. This research is carried out through a combination of *in situ* compression testing of nanoparticles inside of a transmission electron microscope (TEM) with complementary atomistic simulations using molecular dynamics (MD).

2. Recent Progress

2.1. Establishing the role of surface energy in the shape of undeformed nanoparticles.¹ While it is well established that nanoparticle shape can depend on equilibrium thermodynamics or growth kinetics, recent computational work has suggested the importance of thermal energy in controlling the distribution of shapes in populations of nanoparticles. Here, we used TEM to characterize the shapes of bare platinum nanoparticles and observed a strong dependence of shape distribution on particle size (Fig. 1).

Specifically, the smallest nanoparticles (<2.5 nm) had a truncated octahedral shape, bound by <111> and <100> facets, as predicted by lowest-energy thermodynamics.

However, as particle size increased, the higher-energy <110> facets increased in prevalence, leading to a large population of

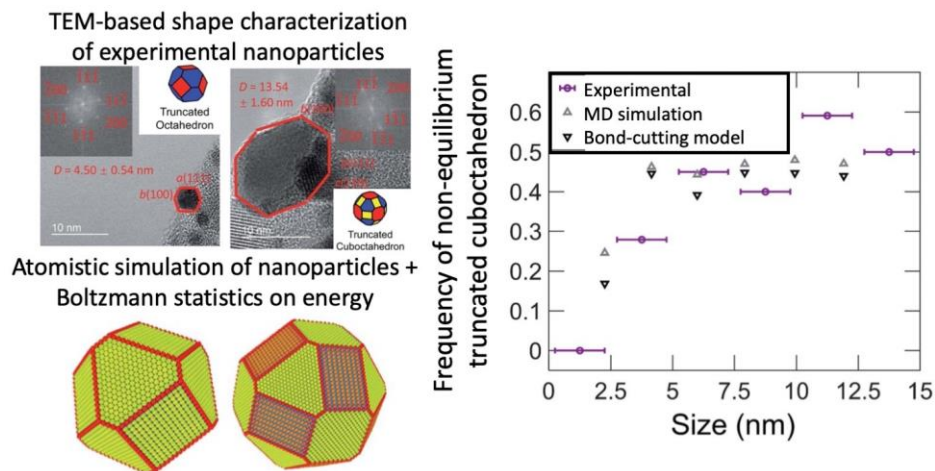


Figure 1: Experimental characterization of nanoparticle shape (top-left) and atomistic simulations combined with Boltzmann statistics (bottom-left) were consistent in predicting the fraction of a non-equilibrium shape present in populations of nanoparticles (right).

non-equilibrium truncated cuboctahedra. The observed trends were explained by combining atomistic simulations (both MD and an empirical square-root bond-cutting model) with Boltzmann statistics.¹ This study demonstrated the dependence of shape distributions on particle size, and showed how thermal energy leads to variation in the undeformed shape of metal nanoparticles.

2.2. Determining accurate potentials for small platinum nanoparticles.² To accurately model the platinum nanoparticles being studied experimentally, we evaluated nine different empirical

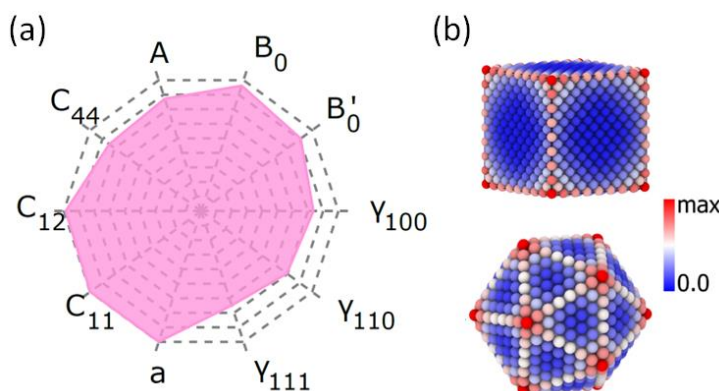


Figure 2: (a) A radar plot summarizes the accuracy of different MD potentials based on comparison to experiment and first-principles data. (b) Snapshots of cubic and icosahedral nanoparticles are shown with atoms colored based on displacement during energy minimization. Displacement and energy were used to evaluate stability.

potentials for molecular-dynamics simulations based on their ability to predict bulk and surface material properties (Fig. 2): lattice constant; stiffness constants, equations of state, and surface energies of {100}, {110}, and {111} facets. Model predictions were compared to previously reported experimental data and quantum-mechanics calculations. The potentials were further evaluated in terms of their ability to reproduce the stability of nanoparticles with experimentally observed shapes. Analysis of the simulation accuracy for bulk

properties, surface properties, and nanoparticle stability showed that, although none of the potentials could accurately model all properties, one of them performed best: the embedded atom method formalism with a specific parameter set.² This potential was recommended for future MD-based studies of platinum and was used subsequently for simulations in this project.

2.3. Characterizing the role of surfaces in the elastic deformation of platinum nanoparticles.³

We used MD simulations with the previously identified optimal potential to model compression of platinum nanoparticles with two different polyhedral shapes and a range of sizes from 4 to 20 nm, loaded in two different crystal orientations. We used conventional methods to compute elastic modulus

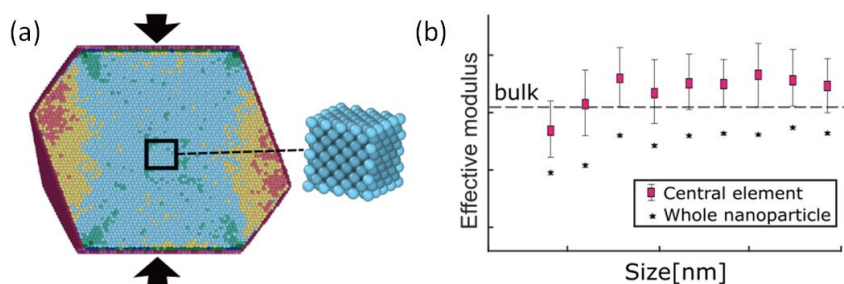


Figure 3: (a) A cross-section of a simulated stress distribution for 20-nm truncated octahedron nanoparticle is shown with atoms colored by stress. A representative volume unit element is used to calculate (b) consistent and physically meaningful measures of nanomaterial elasticity.

and evaluated their magnitude and particle-size dependence. The results depended on the calculation method and, even for larger nanoparticles where bulk-like behavior may be expected, the elastic modulus depended strongly on shape and didn't match bulk values for platinum. Analysis of per-atom stress distributions indicated that the shape- and orientation-dependence arose due to stress triaxiality and inhomogeneity across the particle. When the calculation was repeated using a representative volume element in the center of a large nanoparticle, the elastic modulus had the expected value for each orientation and was shape independent. Meaningful differences emerged only for few-nm-diameter nanoparticles, where even the very center of the particle had a lower modulus due to the presence of the surface.³ The findings disentangled geometric contributions that affect the calculated modulus (such as stress triaxiality and spatial inhomogeneity) from true changes in the elastic behavior of the nanoscale material.

2.4. Measuring strength and deformation mechanisms of a platinum nanoparticle.⁴

The mechanical behavior of nanoparticles governs their performance and stability in many applications. However, the small sizes of technologically relevant nanoparticles, with diameters in the range of 10 nm or less,

significantly complicate experimental examination. These small nanoparticles are difficult to manipulate onto commercial test platforms and deform at loads that are below the typical noise floor of the testing instruments. Here, we synthesized small platinum nanoparticles directly onto a mechanical tester and used a modified

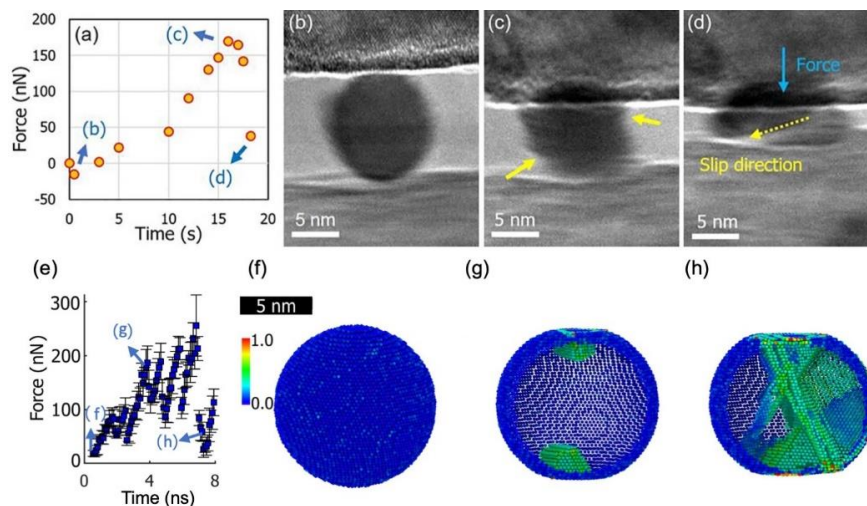


Figure 4. Experimental (top) and simulated (bottom) compression tests showed that an 11-nm-diameter platinum nanoparticle failed by dislocation slip at a critical resolved shear stress of 1.2 GPa.

nanomanipulator to enhance load resolution to the nanonewton scale. We demonstrated the *in situ* compression of an 11.5-nm platinum nanoparticle with simultaneous high-resolution measurements of load and particle morphology. MD simulations were performed on similarly sized particles to achieve complementary measurements of load and morphology, along with atomic resolution of dislocations. The experimental and simulation results revealed comparable values for the critical resolved shear stress for failure, 1.28 and 1.15 GPa, respectively. This investigation demonstrated the promise of, and some initial results from, the combination of atomistic simulations and *in situ* experiments with an unprecedented combination of high spatial resolution and high load resolution to understand the irreversible behavior of metal nanoparticles under compression.

3. Future Plans and Ongoing Work

3.1. Establishing the size-dependent strength of platinum nanoparticles. In platinum nanowires the smaller-is-stronger behavior was shown to persist down to few-nm diameters, with the explanation that surface diffusion in platinum is slow due to its high melting temperature. However, it is unclear how surface diffusion affects deformation mechanisms and strength of nanoparticles, which have higher curvature. Now, we are using *in situ* nanomechanical testing inside of a TEM to reveal the strength and deformation mechanisms of platinum nanoparticles ranging from 6 to 41 nm in diameter. Our results are revealing size-dependent trends in both strength and deformation mechanisms across this range.

3.2. Determining atomic-scale deformation mechanisms as a function of size, crystallographic orientation, and surface facets. We are using MD models to study the effects of surface energy and shape on deformation mechanisms of platinum nanoparticles under compression, specifically focusing on displacive and diffusive mechanisms. We hypothesize that the role of diffusion will vary with nanoparticle shape (different facets have different surface energies), nanoparticle size (small particles have a higher surface-to-volume ratio and also higher-energy surface atoms because of larger curvature), and temperature (high temperature facilitates atom mobility). To evaluate this, we are running compression simulations at a range of temperatures for nanoparticles with three different shapes and three different sizes. We are quantifying the average diffusion coefficient, which measures non-affine motion of atoms, while displacive deformation is quantified in terms of total dislocation length. We anticipate being able to correlate nanoparticle strength and deformation to size-, shape-, and temperature-dependent deformation mechanisms.

3.3. Establishing the effect of strain rate and surface coatings deformation mechanisms. Finally, we are performing *in situ* nanoparticle compression with varying surface chemistry (bare or coated with silica) and with varying strain rate. The addition of a surface coating modifies the rate of atomic migration on the surface, while a faster strain rate allows less time for thermally activated atomic hopping. Both of these effects are hypothesized to slow surface diffusion and thus increase the strength of the particle. In particular, we are testing 10-to-15-nm-diameter platinum nanoparticles, at a range of strain rates, with and without a silica surface coating, while measuring the real-time stress, strain, and structure of the particle. Taken together, these measurements will reveal and quantify the contributions of surface diffusion to deformation.

4. Publications

1. R. Ding, I. Padilla Espinosa, D. Loevlie, S. Azadehranjbar, A. J. Baker, G. Mpourmpakis, A. Martini, and T. D. B. Jacobs, *Size-dependent Shape Distributions of Platinum Nanoparticles*, *Nanoscale Advances*, **4**, 3978 (2022).
2. I. M. Padilla Espinosa, T. D. B. Jacobs, and A. Martini A, *Evaluation of Force Fields for Molecular Dynamics Simulations of Platinum in Bulk and Nanoparticle Forms*, *Journal of Chemical Theory and Computation* **17**, 7 (2021)

3. I. M. Padilla Espinosa, T. D. B. Jacobs, and A. Martini A, *Atomistic Simulations of the Elastic Compression of Platinum Nanoparticles*, *Nanoscale Research Letters* **17**, 96 (2022)
4. I. M. Padilla Espinosa, S. Azadehranjbar, R. Ding, A. J. Baker, T. D. B. Jacobs, and A. Martini *Platinum Nanoparticle Compression: Combining In situ TEM and Atomistic Modeling*, *Applied Physics Letters*, **120**, 013101 (2022).

Fundamental Study of Fatigue Crack Initiation at Grain and Twin Boundaries in Austenitic Stainless Steel

Josh Kacher, Georgia Institute of Technology

Keywords: Fatigue, electron backscatter diffraction, dislocations, grain boundaries, electron microscopy

Research Scope

The overarching goal of this project is to understand the dislocation-based mechanisms driving fatigue crack initiation at grain and twin boundaries. The hypothesis of the work is that dislocation structures equivalent to persistent slip bands (PSBs) form in the boundaries, leading to local stress concentrations and fatigue crack initiation. The sub-goals associated with this work include:

- Understanding the evolution of the dynamic stress state and dislocation density surrounding PSB/grain boundary interactions. This will require the development of new techniques that couple high resolution electron backscatter diffraction (HREBSD) with *in situ* scanning electron microscopy (SEM) deformation.
- Uncover the mechanisms by which dislocations are accommodated in grain and twin boundaries during fatigue. The proposed approach here is to couple transmission electron microscopy (TEM) analysis with site-specific sample preparation to directly correlate defect structures with the characterized stress state.
- Establish correlations between microstructure, deformation accommodation, and crack initiation across time and length scales.

This work primarily focuses on understanding fatigue crack initiation in austenitic stainless steels. During lab closures at the onset of the pandemic, we also investigated new direct electron detection capabilities for cross-correlation based EBSD analysis.

Recent Progress

Microstructural drivers for fatigue crack formation

The primary approach taken in this research has been to characterize deformation structures as a function of fatigue conditions in polished 316L stainless steel samples. The latest period of this project has focused on correlating crack formation locations with surrounding microstructural features. To this point, we have characterized several examples of nascent fatigue cracks under tension-tension loading conditions, with future work focused on collecting statistically relevant data sets. Figure 1 shows an example of the evolved damage layer in a fatigue loaded sample under load control after 10k cycles ($R=\infty$, $\sigma_{\max} = 300$ MPa). Three areas of interest are marked and

labeled in the inverse pole figure (IPF) map. The first, A, shows an example of significant dislocation accumulation, as evident by the geometrically necessary dislocation (GND) density map, at a random high angle grain boundary. The slip traces end at the grain boundary, suggesting that slip does not transmit through the boundary. Area C shows high GND levels of accumulation at a coherent twin boundary, again with slip traces terminating at the grain boundary. Both of these microstructure features are typically associated with fatigue crack initiation sites [1], with reports of crack formation at coherent twin boundaries being especially

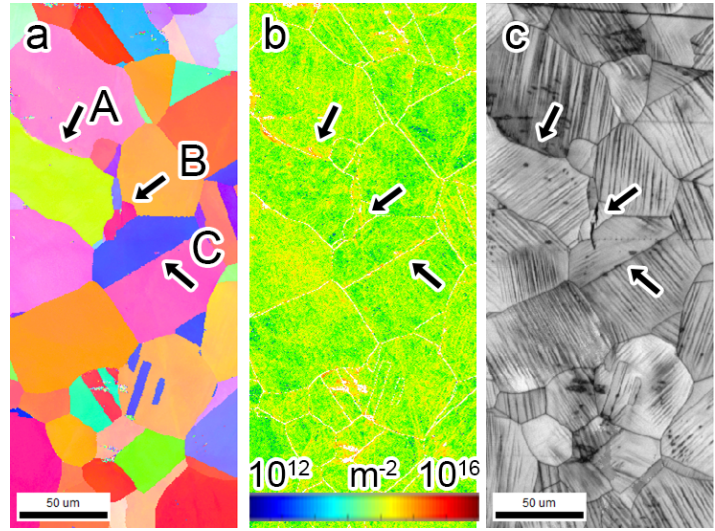


Figure 1. EBSD analysis of fatigue loaded 316L stainless steel (10k cycles, $R=\infty$, $\sigma_{\max} = 300$ MPa). a) IPF map. b) GND density map. c) IQ map. Arrows indicate areas of interest discussed in the text.

common in the literature [2]. However, only at site B is a crack visible in the image quality (IQ) map. At this location, there are multiple small grains surrounded by much larger grains. The crack appears to extend from a triple junction where two of the smaller grains meet. This configuration, the clustering of small grains within surrounding larger grains, was seen as the most common location for fatigue crack formation, though the range of conditions investigated is still small.

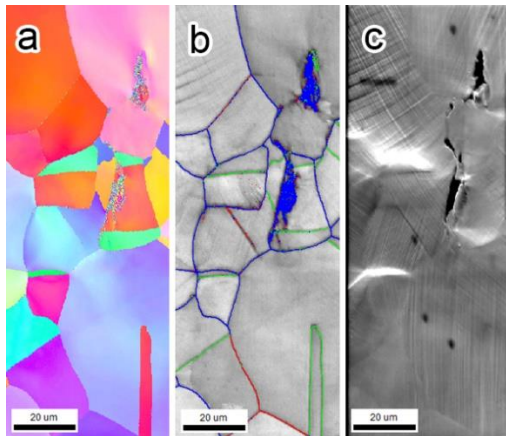
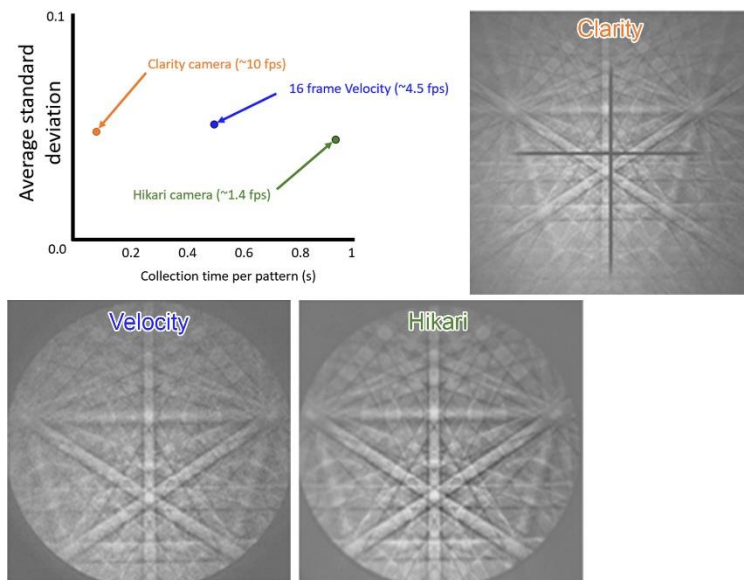


Figure 2. EBSD characterization of a fatigue crack. a) IPF map. b) IQ map with grain character labels (blue $> 15^\circ$ rotation, red $< 15^\circ$, green twin boundary). c) Secondary electron image of the same region.

Figure 2 shows a higher spatial resolution example showing evidence of the crack growth path after 10k cycles of fatigue loading, in this instance at $\sigma_{\max} = 250$ MPa. The crack again appears to form in a cluster of small grains surrounded by larger grains. Interestingly, the crack follows the path of a high angle grain boundary and cuts directly across a twin in the grain interior. Twins are often considered both strong barriers to crack propagation and, when considering adjacent planes, locations for crack formation. The evidence thus far suggests that grain clustering is a higher driver of crack formation, with twin boundaries not playing a central role.

Comparison of EBSD detectors for cross-correlation-based analysis

Cross-correlation-based EBSD has enabled high precision measurements of crystallographic rotations and elastic strain gradients at high spatial resolution [3]. The precision of the measurements relies on the accuracy of measured shifts in the EBSD patterns. Since the introduction of EBSD technology, there have been remarkable improvements in electron detector technology, including the advent of ultra-highspeed detectors and the widespread commercialization of direct electron detectors. Direct electron technology is especially notable as it reduces noise generation associated with scintillation. In order to assess the performance of different generations of EBSD detectors, we collected lines of EBSD patterns from single crystal Si samples. The shift as the beam scans across the samples is directly proportional to shifts in the collected EBSD patterns, providing a ‘ground truth’ measurement for comparing the cameras. We used two different metrics to assess the performance: The precision with which shifts in the EBSD



patterns could be measured and the speed at which high quality patterns could be collected.

Figure 3 Shows a visual and graphical comparison between the three most recently developed electron detectors from EDAX/TSL. The Hikari and Velocity cameras are both based on charge couple device (CCD) technology, though the velocity has been optimized for high speed pattern collection at the cost of lower signal to noise ratio. The Clarity camera is a direct

Figure 3. Comparison between different EBSD detector performance for cross-correlation EBSD. Graph shows comparison between detectors in terms of the collection time per per pattern and average standard deviation in the measured shifts from pattern to pattern.

electron detector and theoretically has the lowest noise level. The precision of the pattern shifts was measured by taking the standard deviation of the measured shifts, giving a measure of the scatter in the measured values. Initial analysis of the Velocity detector showed that it has very poor performance in comparison to the other detectors. However, by averaging sixteen frames of the collected patterns, the Velocity camera showed similar performance levels to the Hikari and Clarity detectors. Averaging frames from the Hikari and Clarity detectors did not show significant improvement, suggesting that there is a limit to how much frame averaging can improve performance. While the performance of the three detectors was comparable in terms of scatter in the measured shifts, collection time varied significantly between the detectors, with patterns

collected by the Hikari detector requiring almost an order of magnitude more time than when using the Clarity camera. Pattern collection time has significant impact on the science that is possible using the different detectors as long pattern collection time can lead to drift, sample contamination, and, for poorly conducting materials, sample charging.

Future Plans

Future plans will focus on correlating fatigue crack formation sites with microstructure features of interest via EBSD at interrupted stages of deformation and resolving the stress fields and mechanisms of crack formation using cross-correlation based EBSD. For microstructural correlations, we have now established fatigue loading regimes that lead to significant surface crack formation, allowing us to identify and characterize the environment associated with dozens to hundreds of fatigue cracks. We will generate libraries of surrounding microstructural features to identify those that are most commonly associated with crack formation. At higher spatial and angular resolution, we will use cross-correlation EBSD to identify how stresses are distributed around persistent slip bands, with a focus on slip band/grain boundary interactions. This will provide insight into features that cause stress concentrations and load shedding features, which will provide mechanistic insight into the microstructural correlations established by the statistical surveys. The cross-correlation EBSD analysis will be coupled with *in situ* scanning electron microscopy loading to discover how the stress state varies under loading conditions. Finally, focused ion beam (FIB) machining will be coupled with TEM analysis to correlate the characterized stress fields with the underlying defect structures.

References

1. V. Mazanova, M. Heczko, and J. Polak, *On the mechanism of fatigue crack initiation in high-angle grain boundaries*, International Journal of Fatigue **158**, 106721 (2022).
2. M. D. Sangid, *The physics of fatigue crack initiation*, International Journal of Fatigue **57**, 58-72 (2013).
3. J. Kacher, T. Ruggles, J. Key, M. Nowell, and S. Wright, *Characterizing defect structures in AM steel using direct electron detection EBSD*, Scripta Materialia **221**, 114952 (2022).
1. A. B. Author, C. D. Author, and E. F. Co-Author, *Title of the Publication*, Journal **Volume**, page (year).

Publications

1. J. Kacher, T. Ruggles, J. Key, M. Nowell, and S. Wright, *Characterizing defect structures in AM steel using direct electron detection EBSD*, *Scripta Materialia* **221**, 114952 (2022).

Fundamental Mechanisms of Newtonian Viscous Creep in Structural Alloys

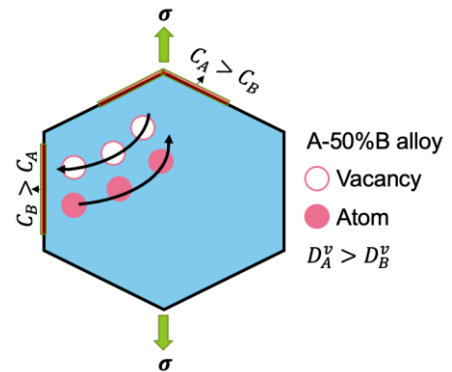
Boopathy Kombaiah, Idaho National Laboratory

Keywords: Diffusional creep, Chemical segregation, High entropy alloys, Hydrogen, Phase field modeling

Research Scope

Stress-driven diffusional mechanisms of atoms and point defects are critical to a wide range of materials phenomena such as creep deformation [1], self-assembly [3], thin-film growth [4], and embrittlement [5]. In the Newtonian diffusional creep process, the Nabarro-Herring (N-H) and Coble creep theories postulated that preferential flow of atoms toward the stress direction in exchange of vacancies governs the creep rate in materials. These diffusional creep theories provide a compelling picture for materials scientists to design microstructures that improve creep resistance. However, these theories remain vigorously debated due to a dearth of experimental evidence and poor prediction of creep rate.

To help address these issues, the overarching goal of this project is to understand Newtonian diffusional creep mechanisms in Ni-based structural alloys. We hypothesize that stress-assisted flow of vacancies to specific interfaces in multicomponent materials would cause elemental segregation based on the diffusivities of the constituents. Furthermore, the proposal describes a systematic approach to test the hypothesis under Newtonian diffusion creep. The proposal explores the Newtonian diffusional creep mechanisms by focusing on the following science questions that are relevant to materials serving in extreme environments: (1) How can we experimentally validate the occurrence of diffusional creep in materials? (2) What are the alloying effects on the diffusional creep in high entropy alloys? (3) How does soluble hydrogen in metallic systems influence the diffusional creep process? The project uses advanced research tools available at Idaho National Laboratory and Department of Energy user facilities to explore these questions. The research method will employ advanced testing and multiscale characterization techniques (i.e., in situ /ex-situ secondary ion mass spectrometry, transmission electron microscopy, and atom probe tomography) and mesoscale phase-field modeling tools to understand diffusional creep mechanisms. The mechanistic understanding of the diffusional creep mechanisms will enable new pathways for designing advanced creep-resistant materials for extreme environments of high temperature, stress, and corrosion medium.



Schematic diagram showing creep-induced elemental segregation at GBs due to the vacancy-exchange mechanisms

Future Plans

Ni-based binary alloys will be synthesized at the Materials Preparation Center of the Ames National Laboratory. Creep testing of the alloys will be conducted under diffusional creep conditions. Subsequently, advanced microstructural tools such as transmission electron microscopy and atom probe tomography will be employed on the crept samples to measure any resultant segregation induced by the diffusional creep processes. The dependence of segregation at the GBs on GB orientation relative to the stress axis, elemental diffusivities, creep strain, creep temperature, and the type of diffusional creep mechanism (N-H creep versus Coble creep) will be determined to test our hypotheses for validating diffusional creep. Phase-field modeling will be employed to understand the diffusional creep mechanisms in the model Ni-based alloys and for calibration and comparison with the experimental observations.

References

- [1] F.R.N. Nabarro, Creep at very low rates, *Metallurgical and Materials Transactions A* 33(2) (2002) 213-218.
- [3] C. Sun, C. Jiang, E. Jossou, M. Topsakal, S.K. Gill, L.E. Ecker, J. Gan, Self-assembly of solid nanoclusters in molybdenum under gas ion implantation, *Scripta Materialia* 194 (2021).
- [4] J.W. Shin, E. Chason, Compressive Stress Generation in Sn Thin Films and the Role of Grain Boundary Diffusion, *Physical Review Letters* 103(5) (2009) 056102.
- [5] S.Y. Persaud, K. Arioka, K. Farquharson, C. Dixon, C.D. Judge, A Mechanistic Study of Carbon Steel Cracking in 360°C Air and Hydrogen Environments, *Corrosion* 75(11) (2019) 1354-1370.

Publications

New project

Elucidating Grain Growth in Thermo-Magnetic Processed Materials by Transfer Learning and Reinforcement Learning

PI: Amanda R. Krause, Carnegie Mellon University

Co-PIs: Michael R. Tonks, University of Florida (UF); Joel P. Harley (UF); Michael S. Kesler, Oak Ridge National Laboratory (ORNL)

Keywords: microstructure, grain growth, magnetic processing, deep learning, transfer learning

Research Scope

The overall goal of this project is to develop a physics-regulated interpretable machine learning model to elucidate one of the most fundamental, yet poorly understood, mechanisms in materials science: abnormal grain growth. We propose that abnormal grain growth represents an extreme case that can serve as a convenient guide to identifying the impact of grain boundary (GB) anisotropy on microstructure evolution. The hypothesis driving this work is that grains exhibiting abnormal grain growth are those grains that have a sufficient number of asymmetric triple junctions to sustain a growth advantage.

Our approach to elucidate abnormal grain growth is to build a machine learning model that captures GB motion observed in real polycrystalline materials captured with non-destructive x-ray diffraction microscopy (3D-XRM). The benefit of this approach is that such a model does not rely on physical assumptions and can create higher order representations to address the complexity of the GB network. Towards this goal, our team has built a deep learning Physics-Regulated Interpretable Machine Learning Microstructure Evolution (PRIMME) model that can simulate isotropic grain growth. This model is based on a new architecture that we developed by incorporating the dynamic process of Monte Carlo Potts (MCP) models with concepts from deep reinforcement learning. Additionally, we have used deep learning to extract high-order descriptors of microstructures associated with anisomorphic grain growth behavior. With these machine learning tools, we will be able to emulate anisotropic grain growth behavior and extract the critical descriptors associated with abnormal grain growth to guide processing pathways for microstructures with engineered properties.

Recent Progress

Extending PRIMME from Isotropic to Anisotropic Grain Growth Predictions

We first developed and trained a deep neural network model to predict isotropic grain growth (i.e., assuming all GBs have the same energy and mobility) using simulated grain growth data produced by a Monte Carlo Potts (MCPs). The developed architecture uses microstructural images (both simulated or experimentally collected are possible) as the input data, where each pixel is labeled by the grain identification number it is associated with. The microstructure evolves by a series of actions, in which each of the pixel can “flip” to the identification of another grain or remain the same. The neural network’s architecture is designed to learn the likelihood of each

possible action and then proceeds to take the action that has the highest probability of occurring. This approach provides flexibility because particular actions can be constrained by known physics. Furthermore, this introduces the ability to interpret the model because we can map the likely actions for each site.

Our PRIMME model was validated by comparing the predicted growth behavior with analytical models of normal grain growth. It is important to note that these analytical models have been used to verify the MCP simulations, which were used as the training data for PRIMME. Therefore, this validation ensures that PRIMME captures the underlying physics represented in the training data and can be applied to scenarios (microstructures) not present in the training set. We carried out four sets of simulations where we compared the PRIMME predictions against analytical theory and results from the Monte Carlo Potts (MCP) and phase-field (PF) models. We highlight one comparison here. We carried out a quantitative comparison for a 2400×2400 pixel domain with 20,000 initial grains. The machine learning model predicted all aspects of the growth consistent with the other models and normal grain growth theory, including the change in the average grain size with time, steady-state grain size distribution, average number of sides with time, and the steady-state distribution of the number of sides per grain (Fig. 1). These comparisons demonstrate that the machine learning model has learned to predict 2D isotropic grain growth.

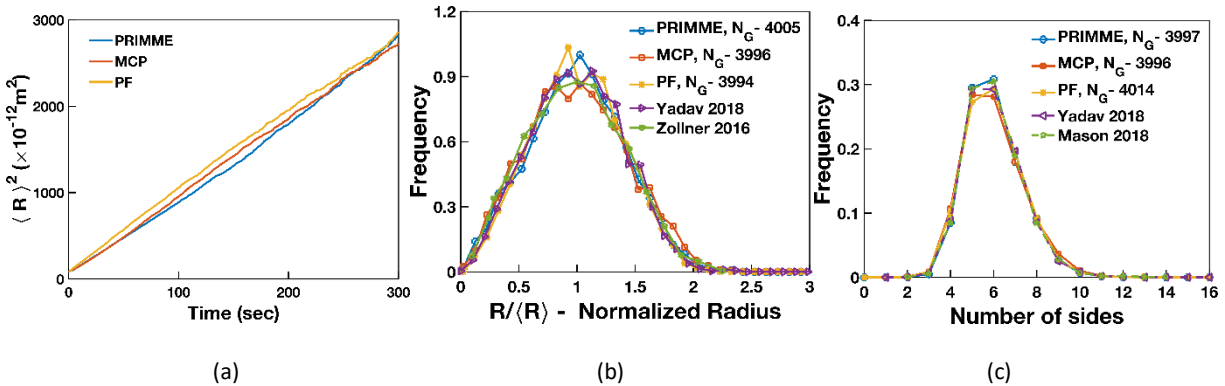


Figure 1: (a) Evolution of the square of the mean grain size with time. The PRIMME and MCP results were scaled to real time by fitting their slope to the slope of the PF results. Comparison of the (b) grain size distribution and (c) number of sides distribution for 4000 grains from PRIMME, MCP, and PF.

For PRIMME to predict abnormal grain growth, the MCP model was modified to produce anisotropic grain growth based on a function of the full GB character. While misorientation can be easily calculated from the crystal orientations of neighboring grains, extracting the plane inclination from a pixelated image is non-trivial. We compared several different methods and created a workflow that optimizes the smoothing algorithm for different geometries. The current training data is anisotropic MCP simulations where the GB energy is a function of misorientation.

Preliminary results indicate that PRIMME is replicating the anisotropic behavior. Despite being trained only on polycrystalline data, a model validation study with only 3 grains shows the expected behavior: the grain terminated by the GB with higher misorientation angles shrinks away faster than the other grain. Further work is needed to validate the anisotropic model for a polycrystalline matrix.

Interpretability of High Order Descriptors of Microstructure

PRIMME is designed to replicate anisotropic growth, which it can learn from simulated or experimental training data. The simulated data has built in assumptions regarding the relationship between GB energy and GB character (misorientation and plane inclination). While this is useful for validating PRIMME, the goal is to be able to learn from experimental data the true relationship between GB character and grain growth. As such, we want to be able to interpret the model to identify which particular GBs and, perhaps more significantly, their neighborhoods that lead to abnormal grain growth. We are using two different methods to identify what microstructural features are critical for abnormal grain growth. The first attempt is to analyze the action likelihoods that are produced by the unique architecture of PRIMME. The second approach uses a different machine learning approach where a convolutional neural network is trained to delineate microstructures by high order descriptors.

In this second approach, we developed a convolutional neural network (CNN) to classify microstructures of different texture without information about the crystal orientations. Over time, the textured grains elongate in a specific direction with respect to

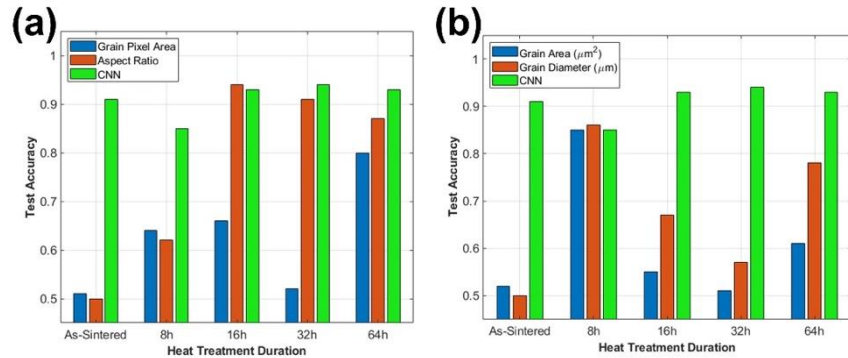


Figure 2: Classification accuracy by CNN and by Kolmogorov-Smirnov statistical tests using (a) uncalibrated and (b) calibrated grain descriptors.

the magnetic-field direction. However, the as-sintered microstructures of the textured and untextured alumina show no statistical difference in grain size or aspect ratio. Hence, if we do not consider the crystallographic orientations of the grains, we are not able to distinguish a textured microstructure and an untextured microstructure apart using conventional metrics (see Fig. 2). To test the possibility of a high order descriptor reflecting the GB network, we evaluated whether a trained CNN model could correctly classify the binary images of the textured and untextured microstructures.

Figure 2 shows the accuracy of the CNN compared to statistical tests evaluated from conventional metrics. For almost all of the microstructures, CNN classification has a higher accuracy than the traditional metrics. Furthermore, it provides higher accuracy for all microstructures with less data (fewer grains) than needed for the statistics. This finding suggests a possible higher order descriptor can be used to delineate microstructures with relatively the same grain size and shape but unique GB structures. Furthermore, the filters in the CNN can be used to interpret what microstructural features are associated with this higher-order descriptor. The interpretation of this work is still on-going.

Future Plans

Developing 3D PRIMME Architecture to Learn Grain Boundary Plane Inclination

PRIMME will be modified to do 3D simulations and incorporate GB plane inclination to account for the full GB character. First, simulated data will be used to train the new anisotropic 3D PRIMME because the “correct” growth behavior is known. Hence, we can easily validate that PRIMME has been trained to accurately predict the GB migration. The MCP model needs to be modified to include GB energies that are a function of both the GB misorientation and inclination. However, anisotropic grain growth models using MCP have only been developed with misorientation dependence, due to the difficulty in determining the GB inclination from the voxelated data generated by the MCP model. We have implemented our approach for determining the GB inclination of voxelated data and we will use it to develop a MCP grain growth model in which the GB energy is a full five-dimensional function of the GB misorientation and inclination. This revolutionary new model will then be used to generate training data to determine how best to train PRIMME for predicting abnormal grain growth.

Train PRIMME with Microstructures Measured by X-ray Diffraction Microscopy

The current PRIMME model is trained by contiguous microstructural data extracted from MCP simulations. Contiguous data is necessary because attempts to use static micrographs (i.e., random grain configurations at different time steps) from both experimental and computational studies have proven to be insufficient to train PRIMME. Therefore, a new characterization technique, laboratory-based x-ray diffraction contrast tomography (LabDCT), will be employed to capture the contiguous experimental training set. LabDCT is a type of 3D x-ray diffraction microscopy technique that characterizes the full 3D microstructure (i.e., size, orientation, and shape of each grain). Recently, the PI has used this technique to explore grain growth in real anisotropic systems, where deviations from ideal grain growth behavior have been observed [1]. CMU and UF’s recent acquisition of the LabDCT (NSF MRI: 2017977) makes such grain growth experiments possible. 3D microstructures at different time steps will be captured in calcia-doped alumina and iron using the non-destructive LabDCT technique. Furthermore, textured and untextured microstructures will be used in this study to vary the spatial distribution of particular GB types and, thus, asymmetric triple junctions. PRIMME will be trained using LabDCT datasets collected from randomly oriented microstructures to create an anisotropic grain growth model. Then, LabDCT observations and PRIMME predictions for *textured* microstructures created using thermomagnetic processing will be compared to test the hypothesis that the spatial distribution of the asymmetric triple junctions is a good predictor for abnormal grain growth.

References

1. V. Muralikrishnan, H. Liu, L. Yang, B. Conry, C.J. Marvel, M.P. Harmer, G.S. Rohrer, M.R. Tonks, R. M. Suter, C.E. Krill III, and A.R. Krause, *Observations of unexpected grain boundary migration in SrTiO₃*, Scripta Mater. **222**, 115055 (2023).

Publications

1. W. Yan, J. Melville, V. Yadav, K. Everett, M.S. Kesler, A.R. Krause, M.R. Tonks, J.B. Harley, *A novel physics-regularized interpretable machine learning model for grain growth*, *Materials & Design* **222**, 111032 (2022).
2. B. Conry, J.B. Harley, M.R. Tonks, M.S. Kesler, A.R. Krause, *Engineering grain boundary anisotropy to elucidate grain growth behavior in alumina*, *Journal of the European Ceramic Society* **42**, 5864-5873 (2022).
3. L. Yang, F. Hilty, V. Muralikrishnan, K. Silva-Reyes, J.B. Harley, A.R. Krause, M.R. Tonks, *Calculating the grain boundary inclination of voxelated grain structures using a smoothing algorithm*, *Scripta Materialia* **218**, 114796 (2022).

Far-From-Equilibrium Processing of Materials under Extreme Conditions

Maik Kurt Lang (Principal Investigator)

Department of Nuclear Engineering, University of Tennessee, Knoxville, Tennessee 37902

Keywords: short-range order, ion irradiation, milling, disorder, neutron total scattering

Research Scope

This research project aims to generate fundamental insight into the formation of material phases that are formed under far-from-equilibrium conditions. High energy ball milling and exposure to energetic heavy ion beams (Fig. 1) are two material processing methods that rapidly impart massive amounts of energy into small volumes, yielding material states that are otherwise not accessible (1). The strategy of this project involves the application of neutron total scattering experiments, coupled with advanced modeling, to investigate the nature of structural disorder in far-from-equilibrium processed complex oxides over a wide range of length-scales. This approach presents a significant improvement over conventional long-range characterization techniques, utilizing X-ray and electron probes, that are less sensitive to anion sublattices and the unique aperiodic, short-range structural features produced by extreme processing conditions.

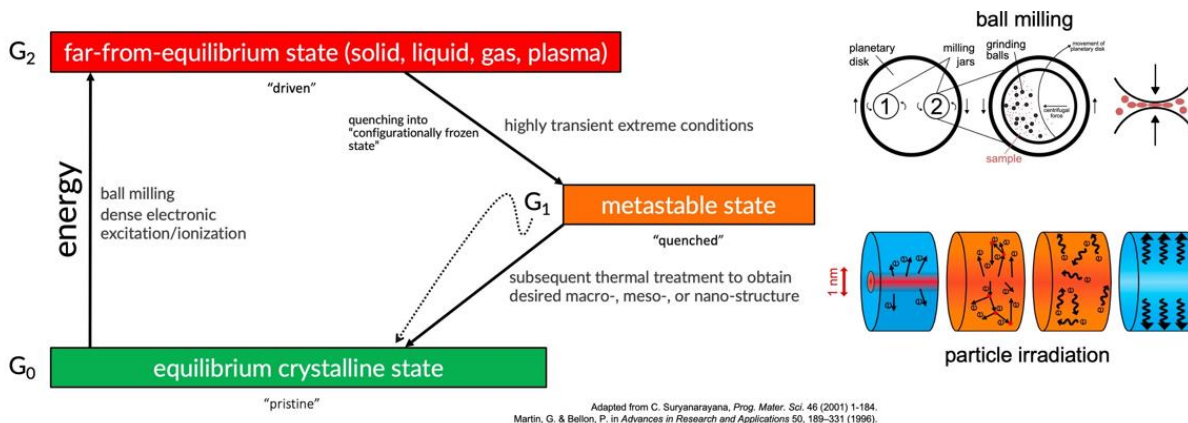


Figure 1: Schematic representation of the energy states accessible by far-from-equilibrium processing techniques. The central hypothesis of this project is that the highly transient temperature and pressure conditions induced by mechanical milling and energetic ion irradiation lead to unique material states with a high degree of structural heterogeneity and disorder not accessible otherwise. Figure adapted from Reference (1).

Structural heterogeneity appears to be a more general phenomenon observed in many disordered materials (2) and is responsible for many interesting properties (3). This project will explore the fundamental nature of defects, disorder and structural heterogeneity characteristic for highly transient energy depositions and utilize energetic ion irradiation and mechanical milling to synthesize and process several oxides model systems (e.g., pyrochlore, bixbyite, weberite-type). We will adjust ion-beam and milling parameters over a range of conditions and include additional thermal treatment to study material states that are accessible through different energetic pathways (Fig. 1). The induced modifications will be compared in the same materials that are disordered by

other means (*e.g.*, high-temperature, changes in stoichiometry and chemical composition) to identify structural features that are uniquely induced by far-from-equilibrium processing. Our aim is to understand how intricate defects and disorder form across all length scales, and how underlying processes can be used to enhance materials performance under extremes or tailor material properties by specific structural changes.

Recent Progress

During the past two years, we have mainly focused on examining the short-range order and local atomic arrangement that is induced in complex oxides by equilibrium and far-from-equilibrium processing techniques. Our recent results from neutron total scattering experiments have shown that the atomic arrangements of many disordered complex oxides are not random, nor is their local symmetry represented by the long-range structure observed from diffraction experiments. We found that this heterogeneous disordering, and the existence of unexpected short-range order, within disordered $A_2B_2O_7$ pyrochlore and AB_2O_4 spinel can be understood by the straightforward application of a set of fundamental chemical rules. Once disorder is induced *via* some internal (*e.g.*, doping) or external (*e.g.*, irradiation and mechanical action) mechanisms, the atomic structure will rearrange itself to a specific configuration (Fig. 2a) that is a direct consequence of Pauling’s rules (O’Quinn *et al.*, Science Advances 2020). For example, inversion in spinel or cation antisite defects in pyrochlore are not merely the exchange of atomic sites, which would violate these rules, but instead involve the creation of new sites that accommodate the sizes and charges of the different cations. This process can be described by a transformation of atomic building blocks (geometrically and electrostatically stable groups of coordination polyhedra) characteristic of the ordered phase to new building blocks that accommodate atomic defects (Fig. 2a).

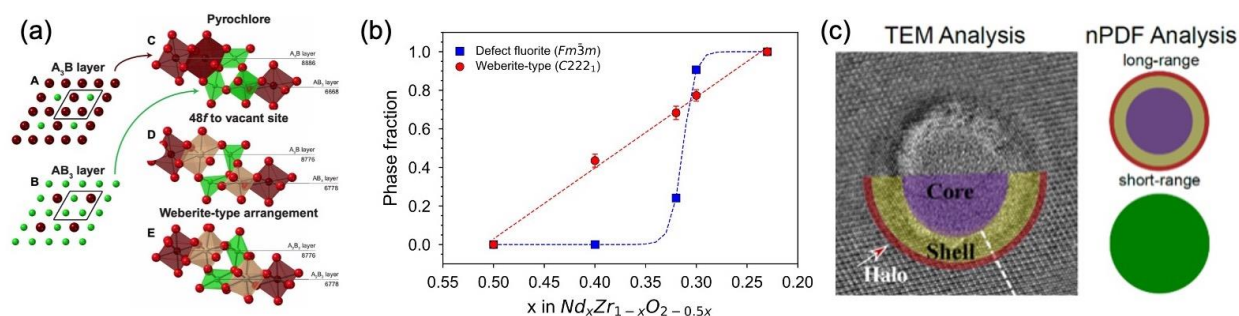


Figure 2: (a) Two cation layers comprise the layer stacking model that describes the ordered pyrochlore structure. During disordering, the fundamental building blocks which form these two layers is modified from a pyrochlore-type building block to a weberite-type building block by an anion Frenkel defect. (b) Accumulation of disorder in $Nd_xZr_{1-x}O_{2-0.5x}$ with increasing Nd-content proceeds at different rates across length scales, suggesting a decoupling of short-range and long-range structural regimes.

Accumulation of modified local building blocks leads to a fully disordered, long-range structure. Based on group theory and crystallographic relationships, we found that averaging of

the local symmetry must yield the long-range symmetry. However, we discovered that disorder accumulates differently across length scales (Fig. 2b), implying that short-range order is decoupled from the long-range structure; furthermore, the specific disordering pathway and relationship between short- and long-range behaviors depends on chemical composition and stoichiometry (Drey *et al.*, RSC Advances 2020 and Acta Materialia 2022).

We found that for some materials, ordered and disordered phases consist of the same atomic building blocks, but have different long-range structures. Variations in the stacking or arrangement of short-range order is even apparent within individual swift heavy ions tracks. Irradiated $\text{Er}_2\text{Sn}_2\text{O}_7$ stannate pyrochlore displays a heterogeneous track morphology, consisting of three distinct damage zones: an amorphous core, a disordered shell, and an ordered but defective halo. In contrast to this longer-range view, neutron PDF data show a very different picture of fully homogeneous tracks characterized by only weberite-type atomic arrangements from the inner core to the outer halo region (Fig. 2c) (O'Quinn *et al.*, Journal of Materials Chemistry A 2021). This research on ion irradiated complex oxides demonstrates that analysis of all length scales must be included for a complete assessment of radiation behavior of nuclear ceramics. This was also evident when comparing radiation resistance of orthorhombic Dy_2TiO_5 with cubic $\text{Dy}_2\text{Ti}_2\text{O}_7$. The former amorphizes under ion irradiation more readily, but has superior stability at the atomic-scale by retaining its local bonding environment. This demonstrates that analysis of all length scales must be included and that radiation resistance depends on the length scale of interest. In this specific case, $\text{Dy}_2\text{Ti}_2\text{O}_7$ would be the material of choice to retain crystallinity to much higher ion fluences, while Dy_2TiO_5 is superior in maintaining a more homogenous atomic-bonding environment with less atomic rearrangements through the entire amorphization process (Sherrod *et al.*, npj Materials Degradation 2021).

Future Plans

Within the last year of our funding, we will complete all publications that are currently in preparation. As a last step, we plan to use Reverse Monte Carlo (RMC) modeling to gain further insight into the structural arrangement of a pyrochlore ceramic that was completely amorphized by ion irradiation. We are able to describe the local atomic arrangement and short-range order in such a non-crystalline material, but we have no information on how these local atomic building blocks are connected with each other across the mesoscale. By using RMC, we will be able obtain an atomic supercell (>16,000 atoms) that is representative of the underlying structure. This supercell will then be evaluated and the connectivity of local building blocks established. This approach may help to shed more light into the irradiation-induced amorphization process as it identifies at which structural length scale the structure loses its coherency.

References

1. C. Suryanarayana, Mechanical alloying and milling. *Prog. Mater. Sci.* **46**, 1–184 (2001).
2. J. Shamblin, M. Feygenson, J. Neuefeind, C. L. Tracy, F. Zhang, S. Finkeldei, D. Bosbach, H. Zhou, R. C. Ewing, M. Lang, Probing disorder in isometric pyrochlore and related complex oxides. *Nat. Mater.* **15**, 507–511 (2016).
3. D. A. Keen, A. L. Goodwin, The crystallography of correlated disorder. *Nature.* **521**, 303–309 (2015).

Publications

1. Overstreet, C. Structural stability of REE-PO₄ (REE=Sm,Tb) under swift heavy ion irradiation. *Nucl. Inst. Methods Phys. Res. B*
2. Drey, D. *et al.* Composition dependent order-disorder transition in Nd_xZr_{1-x}O_{2-0.5x} pyrochlores: A combined structural, calorimetric and ab initio modeling study. *Acta Mater.* **125**, 166–176 (2017).
3. O’Quinn, E. C., Drey, D. L. & Lang, M. K. Defining the Structural Stability Field of Disordered Fluorite Oxides. *Frontiers in Chemistry* **9**, 673 (2021).
4. O’Quinn, E. C. *et al.* Multi-scale investigation of heterogeneous swift heavy ion tracks in stannate pyrochlore. *J. Mater. Chem. A* **9**, 16982–16997 (2021).
5. Solomon, A. P. *et al.* Transformations to amorphous and X-type phases in swift heavy ion-irradiated Ln₂O₃ and Mn₂O₃. *J. Appl. Phys.* **129**, 225903 (2021).
6. Sherrod, R. *et al.* Comparison of short-range order in irradiated dysprosium titanates. *npj Mater. Degrad.* **5**, 19 (2021).
7. Drey, D.L. *et al.* Disorder in Ho₂Ti_{2-x}Zr_xO₇: pyrochlore to defect fluorite solid solution series, *RSC Advances* **10**, 34632 (2020).
8. Gussev, I.M. *et al.* Local order of orthorhombic weberite type Y₃TaO₇ as determined by neutron total scattering and density functional theory calculations. *Acta Materialia* **196**, 704-709 (2020).
9. O’Quinn, E.C. *et al.* Predicting short-range order and correlated phenomena in disordered crystalline materials. *Science Advances* **6**, 1–8 (2020).

Mechanical Properties of Metals at the Micrometer Scale in Different Environments

Seok-Woo Lee, University of Connecticut

Keywords: Plasticity, Micro-Mechanical Testing, Body-Centered-Cubic Metals, Cryogenic Temperature, Tensile Deformation

Program Scope

Mechanical behavior of metals at the micrometer scale is often different from that of bulk metals because the plasticity at the micrometer scale is controlled by the intermittent operation of dislocation sources while the plasticity in bulk scale is controlled by continuous and collective evolution of dislocation structures. Temperature is an important factor that affects the motion of dislocation, but the effect of temperature on the source-controlled plasticity at the micrometer scale has not been understood well, particularly for tensile deformation. For the past decade, the combined effect of temperature and sample dimension on compressive flow strength has been widely investigated. These efforts revealed that the temperature-dependent lattice resistance controls the size dependence of compressive flow strength. However, the combined effect of temperature and sample dimension on tensile plasticity and fracture has not been explored yet. In this project, therefore, we proposed the experimental and computational studies on tensile plasticity of body-centered-cubic (BCC) metals at the micrometer scale using *in-situ* cryogenic mechanical testing, molecular dynamics (MD) simulation, and dislocation dynamics (DD) simulation. *This project aims to understand how the interplay between temperature and sample dimension affects tensile plasticity and fracture of BCC metals at the micrometer scale.* The plasticity of most BCC metals is temperature-dependent because the mobility and cross-slip of screw dislocation is affected by temperature. Sample dimension brings additional complexity in dynamics of screw dislocation due to the strong image stress, which affects the mobility and cross-slip of screw dislocation. Therefore, it is critical to understand how the interplay between temperature and sample dimension influences dislocation dynamics in BCC metals and how dislocation plasticity affects the tensile ductility and fracture. Research outcomes of this project will give a deep insight into micro-mechanical behavior of BCC metals at low temperature and will advance our scientific knowledge in dislocation plasticity.

Recent Progress

(a) The effect of temperature on micro-tensile behavior of niobium and molybdenum single crystals:

In-situ cryogenic micro-tensile test has been done on [001] niobium (Nb) [1] and molybdenum (Mo) single crystals with 2 μ m in width. The yield strength of Nb showed the strong temperature dependence in yield strength (~300MPa at 298K and ~600MPa at 100K), but Mo shows the weak temperature dependence of yield strength (~1.1GPa at 298K and ~1.3GPa at 100K). Both Nb and Mo showed the similar characteristics of plastic flow; the continuous plastic flow was observed at 298K, but the intermittent plastic flow was observed at 100K. Ductility measurement from stress-strain data could be misleading because it is difficult to distinguish between plastic displacement and tip displacement after fracture. Scanning electron microscopy

(SEM) revealed that both Nb and Mo underwent nearly perfect plasticity at 298K, which ends up with a pointy fracture surface, but they showed the limited ductility at 100K.

Weaker temperature dependence of flow strength of Mo micropillars, but it could be related to the source-controlled plasticity. Due to the high shear modulus of Mo, the operation stress of dislocation source, which is proportional to the shear modulus, would dominate the flow strength over the intrinsic lattice resistance. Nb has four times lower shear modulus than Mo. Thus, the intrinsic lattice resistance may still play an important role in determining flow strength, so the effect of temperature on flow strength is more significant in Nb.

Transition from smooth to discrete plasticity could be understood in terms of temperature-dependent cross-slip and rapid dislocation annihilation. At low temperature, cross-slip of screw dislocation is suppressed. At the micrometer scale, mobile dislocations could be annihilated rapidly at the free surface before they interact with each other. Then, the dislocation multiplication could be significantly limited, and it is difficult to store enough mobile dislocations that can produce the continuous plastic flow. Therefore, the plasticity could be controlled by the intermittent operation of dislocation source until fracture occurs. Intermittent plasticity at low temperature appears to be beneficial for the mechanical stability because unstable continuous plastic flow leads fracture rapidly.

Limited ductility at low temperature could be understood in terms of high flow stress and stress concentration at a slip step. Due to the combined effect of sample dimension and temperature, flow strength of micropillar at low temperature is much higher than the bulk value. Once slip steps form under a high stress state, the significantly high stress is developed at slip steps due to stress concentration, leading to microcracking at slip steps followed by fracture. SEM images confirm that most micro-cracks were initiated at a slip step.

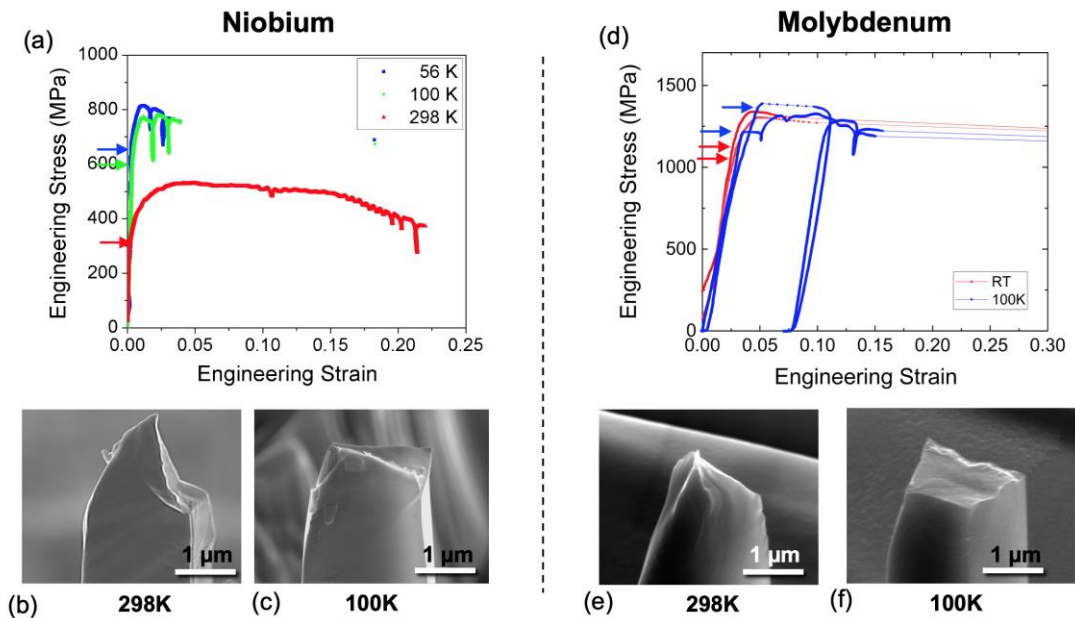


Figure 1. (a) Stress-strain curve of Nb at 56, 100, and 298K, SEM images of fractured Nb micropillar at (b) 298K and (c) 100K [1]; (d) Stress-strain curve of Mo at 56, 100, and 298K, SEM images of fractured Mo micropillar at (e) 298K and (f) 100K. Arrows indicate the yield strength.

(b) The effect of dislocation density and temperature on micro-tensile behavior of niobium

We also investigated the effect of dislocation density on micro-tensile behavior of Nb. The plastic strain of 15% was applied, and the stress-strain data were obtained at different temperatures. We found the increase in yield strength and the reduction of ductility, compared to a pristine Nb sample. The increase in yield strength at 298K can be understood in terms of work hardening. Plastic flow of high dislocation density structure is more difficult. In addition, unlike a pristine sample, stress-strain curves at low temperature do not exhibit the strain bursts, and fracture occurs right after the small plastic strain. Low temperature sample showed almost no slip bands, so fracture occurs almost immediately after the limited plastic strain.

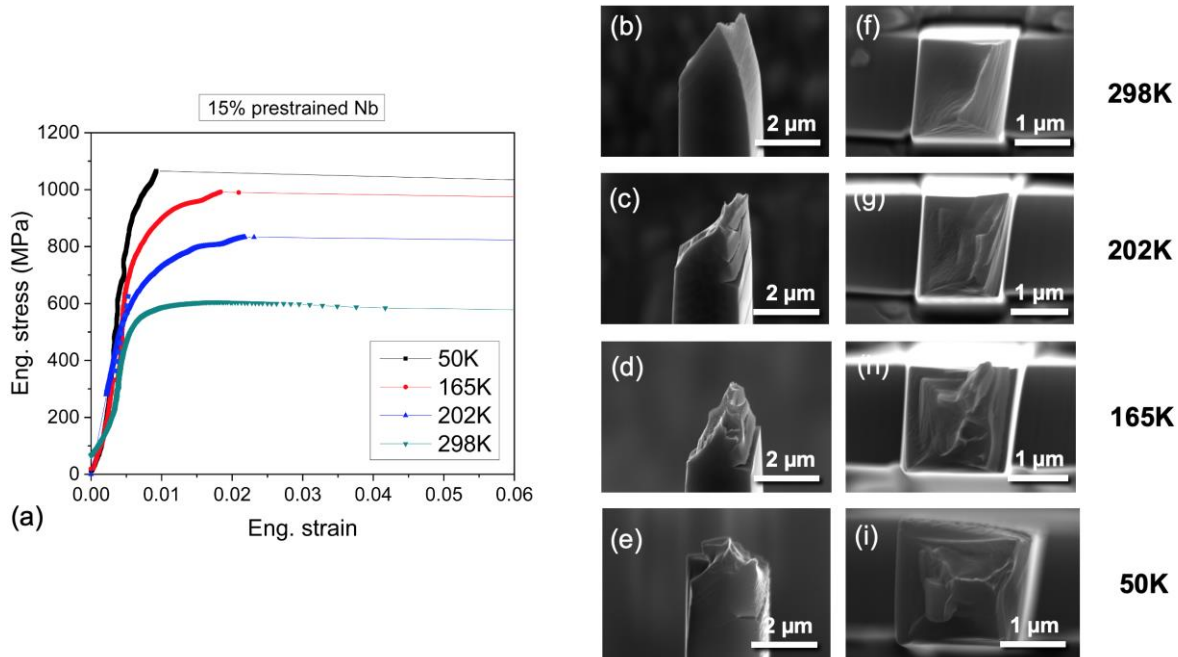


Figure 2. (a) Stress-strain curve of Nb at 50, 165, 202, and 298K; SEM image of fractured Nb samples tested at (b) 298K, (c) 202K, (d) 165K, and (e) 50K; SEM images of fracture surface of Nb sample tested at (b) 298K, (c) 202K, (d) 165K, and (e) 50K

(C) The effect of temperature and applied stress on the dynamics of a single screw dislocation in niobium and molybdenum (Molecular Dynamics Study)

The dynamics of a single screw dislocation is important in the plasticity of BCC metals. In this project, we study the dynamics of a single screw dislocation in Nb and Mo nanopillars under the constant compression and tension stresses at different temperatures. Interestingly, we found the tension-compression asymmetry in the behavior of a single screw dislocation. Under compression, both Nb and Mo show the surface-controlled dislocation multiplication with three different regimes (I, II, and III) [2]. However, under tension, we found that the surface-controlled dislocation multiplication does not occur, and a screw dislocation just glides out of the free surface. At a significantly high stress, deformation twinning occurs. Our result implies that in a confined volume, it is more difficult for a screw dislocation to be multiplied under tension.

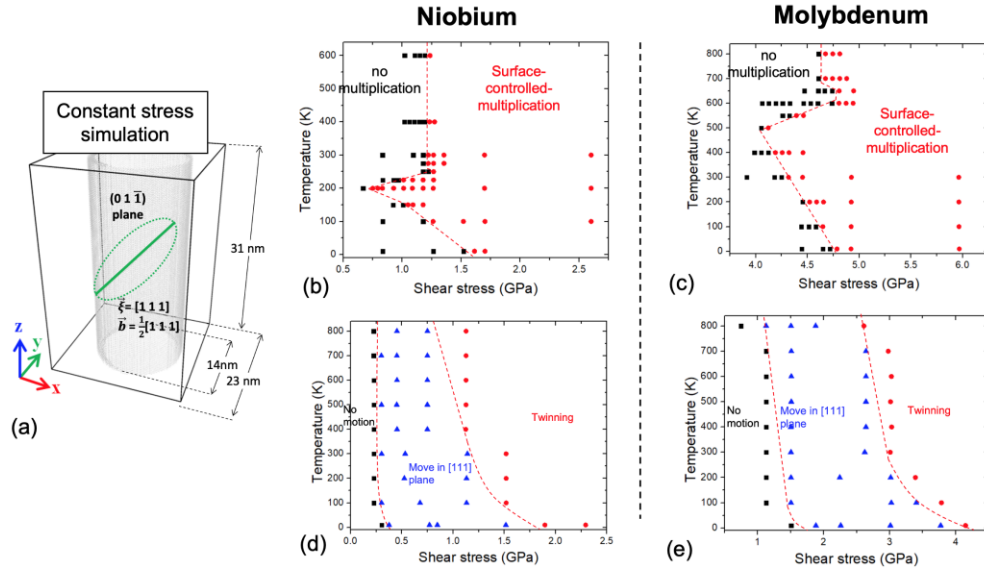


Figure 3. (a) Schematic diagram of nanopillar geometry; Mechanism map of (b) Nb and (c) Mo under the constant compression stress [2]; Mechanism map of (d) Nb and (e) Mo under the constant tension stress.

Future Plans

(1) Effect of dislocation density on tensile behavior of Nb and Mo at low temperature: Different pre-strains smaller than 15% will be applied and micro-tensile test will be performed at low temperature. The role of dislocation density in micro-tensile behavior of Nb and Mo will be investigated.

(2) Micro-tensile testing of large size micropillar at low temperature: We will test 6~8 μm thick micropillars and compare with 2 μm thick micropillars that we have tested. All results will allow us to see the combined effect of sample dimension, dislocation density, and temperature on micro-mechanical behavior of BCC metals under uniaxial tension.

(3) Theoretical investigation on tension-compression asymmetry in the behavior of screw dislocation in BCC metals: Atomistic details in tension-compression asymmetry has not been understood. Simulation data will be analyzed in the context of the dislocation core splitting.

References

1. Gyuho Song, Nicole K. Aragon, Ill Ryu, Seok-Woo Lee, "Low Temperature Failure Mechanism of [001] Niobium Micropillars Revealed by in-situ Cryogenic Micro-Tensile Tests and Dislocation Dynamics Simulations," *Journal of Materials Research (Invited Paper)*, 36, 2371–2382 (2021)
2. Gyuho Song, Seok-Woo Lee, "Effect of temperature on surface-controlled dislocation multiplication in body-centered-cubic metal nanowire," *Computational Materials Science* **168**, 172-179 (2019)

Publications

1. Gyuho Song, Nicole K. Aragon, Ill Ryu, Seok-Woo Lee, "Low Temperature Failure Mechanism of [001] Niobium Micropillars Revealed by in-situ Cryogenic Micro-Tensile Tests and Dislocation Dynamics Simulations," *Journal of Materials Research (Invited Paper)*, 36, 2371–2382 (2021)

The Role of Strain Localization at Interfaces on Fatigue Crack Initiation in Highly Textured Magnesium Alloys

Dr. Aerial D.M. Leonard, The Ohio State University

Keywords: Plasticity, Micro-Mechanical Testing, Body-Centered-Cubic Metals, Cryogenic Temperature, Tensile Deformation

Keywords: Plasticity, Fatigue, Synchrotron, Electron Microscopy, Hexagonal-Close-Packed Metals

Program Scope

New and novel materials with extraordinary properties, from superior fatigue resistance to excellent high temperature performance, enable a shift from energy-expensive materials to sustainable materials with a positive impact on communities and the environment. Though these material systems provide many advantages, the underlying meso- and micro-scale structures are complex and as a result, the mechanical behavior is very different than that of traditional metallic alloys. Of the properties, fatigue – the repeated cycling of stress on a material – is the most critical form of damage in load bearing structures. In fact, fatigue accounts for 80 to 90% of failures in structural components and is still a major problem in many industries. Though fatigue has been studied for over 180 years there are still gaps in our understanding of the processes controlling fatigue crack initiation and growth. This project will directly address these challenges using a specifically designed and multimodal systematic study that combines electron microscopy, digital image correlation, and high energy X-ray based techniques to understand the mechanisms of damage accumulation at interfaces in complex microstructures leading to crack initiation and growth. A fundamental understanding of the complex interactions at the meso- and micro scale that influence fatigue behavior and crack initiation will provide the underpinning knowledge needed to: 1). inform physically based models that accurately predict fatigue lifetime in complex systems and 2). develop fatigue resistant, microstructurally, and compositionally complex alloy systems.

Fatigue Crack Initiation and Growth in Ultrafine-Grained Magnesium Deformed at Subfreezing Environmental Temperatures

Qizhen Li, Washington State University

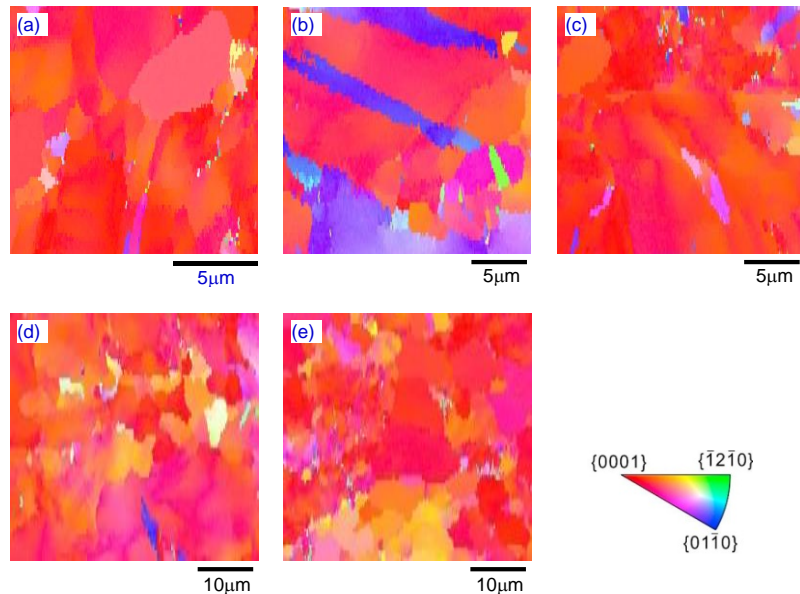
Keywords: Magnesium, Fatigue, Deformation mechanism, Crack initiation and growth, Testing temperature

Research Scope

Limited research efforts were devoted to study fatigue properties of metals under very low temperatures [1-5]. McCammon and Rosenberg measured the fatigue lives of pure metals such as copper, silver, gold, aluminum, magnesium, zinc, iron and cadmium between room temperature and 4.2 K [5]. These studied materials did not have ultrafine grain structure. The major research goal of this project is to understand cyclic mechanical properties, fatigue deformation mechanisms, and fatigue crack behaviors of ultrafine grained magnesium at sub-freezing temperatures through investigating endurance limit and fatigue life, and through exploring grain boundary activities, twinning/detwinning, and dislocation operations.

Recent Progress

EBSD inverse pole figure maps as shown in Figure 1 were obtained for the samples before testing and after mechanical testing under different temperatures, and the data were analyzed to understand the variation of deformation mechanisms with the change of testing temperature. Figure 1(a) is for the untested samples and shows that the magnesium samples had fine and equiaxed grains with an average grain size of about 6 μm and a strong basal texture. Figure 1(b) shows the microstructure of the sample tested at room temperature, indicating extensively activated tensile twinning. When the testing temperature decreased to 0°C, the sample still experienced considerable deformation.



However, the tensile twinning activity was drastically reduced, and the deformation was primarily accommodated by dislocations with the increase of GB₃^o. The further decrease of testing

temperature to -60°C indicates that tensile twinning was barely activated, and the deformation was primarily accommodated by dislocation activities.

Figure 2 presents the variation of the percentages of TTB (tensile twin boundaries), HAGB (high angle grain boundaries), and $\text{GB}_{3^{\circ}}$ (the boundaries with $\sim 3^{\circ}$ misorientation) with the change of the employed testing temperature. Compared to the data for the untested sample, the overall variation of the percentages for all these boundaries decreased with the decrease of testing temperature, since the sample became less ductile and experienced less deformation before fracture. For TTB, there was a tremendous increase in its percentage after the sample was tested at room temperature, and its percentage decreased sharply with the decrease of testing temperature and reached a plateau value that is about the TTB percentage for the untested sample. For $\text{GB}_{3^{\circ}}$, its percentage increased when the testing temperature decreased from room temperature to 0°C and then decreased with the further decrease of testing temperature from 0°C to -60°C , and the percentage of $\text{GB}_{3^{\circ}}$ for the lowest temperature of -60°C is slightly higher than that of the untested sample. The percentage of HAGB decreased at a low rate when the testing temperature decreased from room temperature to -30°C and increased considerably for the testing temperature of -60°C . Dislocation activities were related to the absolute value of the change of HAGB from the untested condition to the tested state. For the fine-grained magnesium samples, profuse grain boundaries existed in the untested condition and these boundaries can serve as dislocation sources and sinks during deformation. When the applied stress was low, most dislocations may stop inside the grains and align to form the low angle boundaries to increase the percentage of $\text{GB}_{3^{\circ}}$, but some dislocations passed through the grains that can either reduce or increase slightly the percentage of HAGB. With the decrease of testing temperature, the observations are: (i) the samples exhibited higher strength and higher applied stresses were required during tensile testing, (ii) the ductility and plastic deformation decreased, (iii) the counterbalancing effect of increased stress and reduced deformation resulted in the decrease of $\text{GB}_{3^{\circ}}$ from 0°C to -60°C , and (iv) the increased stress led to the increase of the variation of HAGB since more dislocations passed through the grains.

Fatigue testing was performed at 0°C for different stress levels. Figure 3 shows a typical stress-strain relation. Smith Watson and Topper (SWT) model was utilized to analyze and predict fatigue life of fine-grained magnesium tested at 0°C :

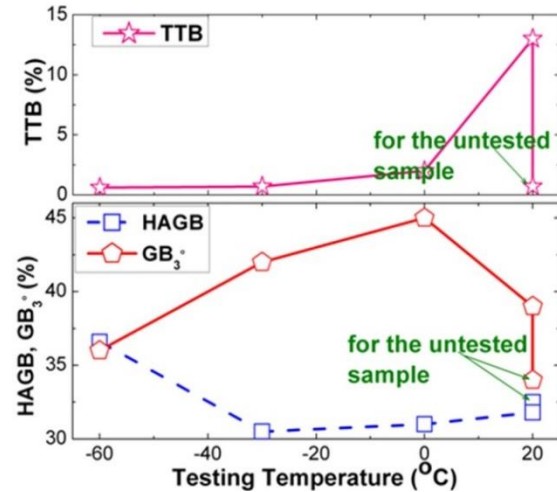


Figure 2. Variation of the fractions of TTB, HAGB, and $\text{GB}_{3^{\circ}}$ with the testing temperature. HAGB, TTB, and $\text{GB}_{3^{\circ}}$ represent high angle grain boundaries, tensile twin boundaries, and the boundaries with $\sim 3^{\circ}$ misorientation respectively.

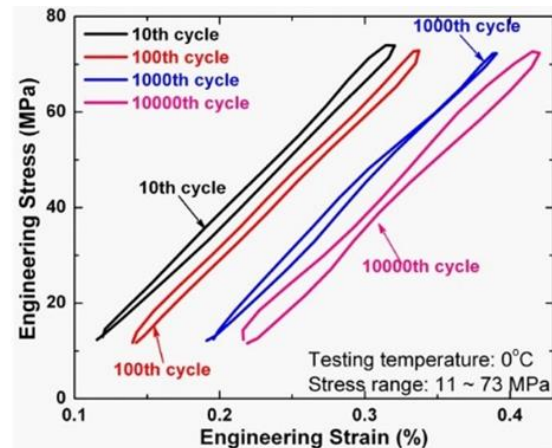


Figure 3. Engineering stress-engineering strain curves for the hysteresis loops.

$$\Delta\varepsilon\Delta\sigma = \frac{(\sigma'_f)^2}{E} (2N_f)^{2b} + \sigma'_f \varepsilon'_f (2N_f)^{b+c}$$

where $\Delta\varepsilon$ is the strain range, $\Delta\sigma$ is the stress range, E is the elastic modulus, N_f is the fatigue life, σ'_f and b are high-cycle fatigue constants, and ε'_f and c are low-cycle fatigue constants. The predicted fatigue life was obtained for each experimental fatigue life and presented in Figure 4. This figure shows that the SWT model provides reasonable fatigue life predictions since the data points are within the two times of error bands.

The Jahed-Varvani energy-based (JV) model is also utilized for the prediction of fatigue life of fine-grained magnesium. Since the sample volume can be varied, the model utilized energy density (i.e., energy per unit volume). In this energy-based model, the total strain energy density ΔE_t has the following relationship with fatigue life using four parameters:

$$\Delta E_t = E'_e (2N_f)^\gamma + E'_f (2N_f)^\delta$$

Where E'_e is the fatigue strength coefficient, E'_f is the fatigue toughness coefficient, γ is the fatigue strength exponent, and δ is the fatigue toughness exponent. ΔE_t is consisted of the elastic portion ΔE_e and the plastic portion ΔE_p . Figure 5 shows that the JV model is conservative for the cases with high applied stress range and short experimental fatigue lives, while it is non-conservative for the cases with low applied stress range and long experimental fatigue lives. The data for all tested cases fall within the boundary of a factor of 2. R^2 for the JV model equals to 0.9925, which is slightly higher than the value for the SWT model. Thus, the JV model provides a slightly better prediction of fatigue life for fine-grained magnesium than the SWT model.

To explore the deformation mechanisms for fine-grained magnesium under tension-tension fatigue testing at 0°C, EBSD observations were performed for three fatigue tested cases with low, medium, and high σ_{\max} respectively. The relations between σ_{\max} and σ_y for the

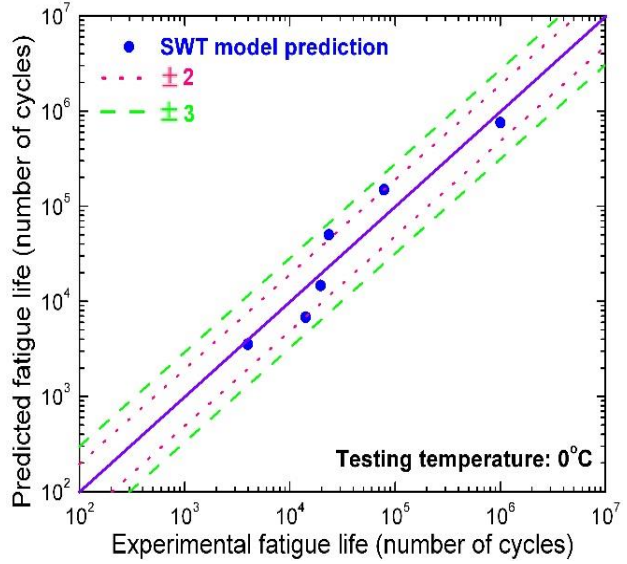


Figure 4. Relation between experimental fatigue life and predicted fatigue life by SWT model.

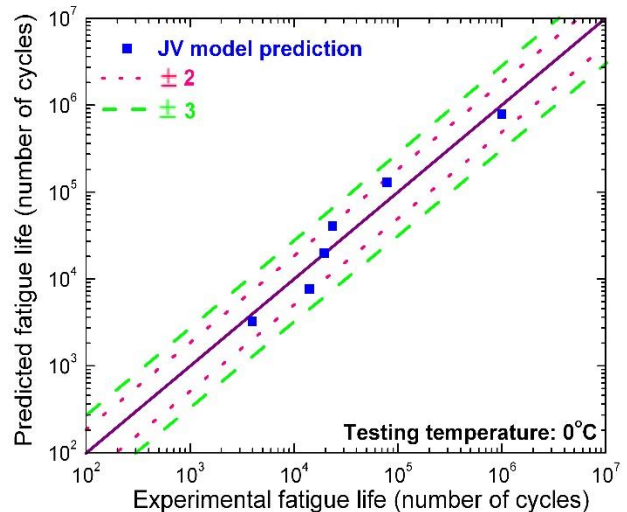


Figure 5. Relation between experimental fatigue life and predicted fatigue life by JV model.

three fatigue tested cases are $\sigma_{\max} < \sigma_y$, $\sigma_{\max} \approx \sigma_y$, and $\sigma_{\max} > \sigma_y$ respectively. Figure 6 provides a schematic sketch of grain rotation. Each hexagon represents a grain, and the edges of hexagons are grain boundaries. The parallel lines in each grain denote the atomic planes. Grain rotation can lead to the alignment of the atomic planes for the neighboring grains, the elimination of some grain boundary and the grain growth, and thus the increase of grain size. Small grains rotated to merge with the neighboring small grains, resulting in the disappearance of some blocks of small grains. When σ_{\max} was much higher than the yield strength (i.e., the fatigue tested sample with high σ_{\max} and the quasi-static tested sample), small grains also merged with the neighboring large grains in addition to the merging among small grains, and thus resulting in the further disappearance of blocks of small grains and the increase of the maximum grain size.

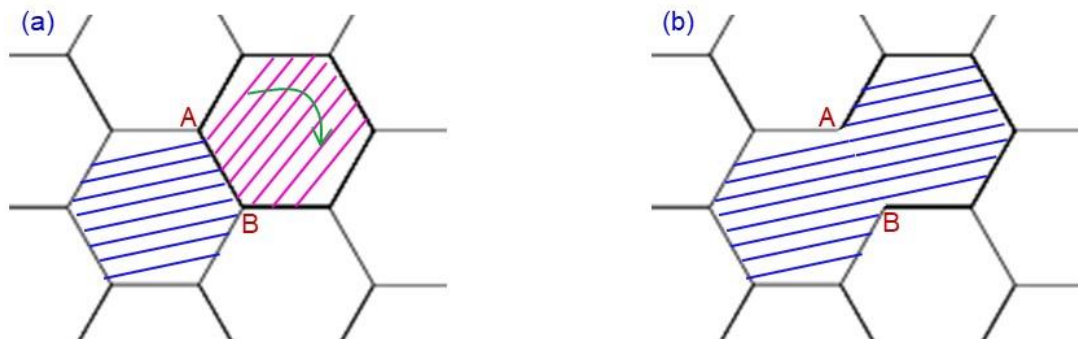


Figure 6: Schematic drawing shown the elimination of the grain boundary AB through grain rotation mechanism. (a) Before rotation and (b) after rotation. (Note: the curved arrow in (a) indicates the rotation of a grain. The parallel lines in each grain denote the atomic planes.)

Future Plans

The project will continue exploring the fatigue crack initiation and growth mechanisms and fatigue properties through further microstructural and mechanical characterizations of the UFG magnesium samples at sub-freezing testing temperatures. The coarse-grained magnesium samples are also to be investigated for comparison.

References

1. O.P. Ostash, I.M. Andreiko, V.V. Kulyk, I.H. Uzlov, K.I. Uzlov, O.I. Babachenko, Low-Temperature Cyclic Crack Resistance Of Steels Of Railroad Wheels, *Materials Science* 44, 2008, pp. 524
2. D. Jeong, S. Lee, J. Yoo, J. Lee, S. Kim, Comparative studies on near-threshold fatigue crack propagation behavior of high manganese steels at room and cryogenic temperatures, *Materials Characterization* 103, 2015, pp. 28
3. D. Jeong, T. Park, J. Lee, S. Kim, Ambient and Cryogenic S-N Fatigue Behavior of Fe15Mn Steel and Its Weld, *Met. Mater. Int.* 21, 2015, pp. 453
4. D. Jung, J. Kwon, N. Woo, Y. Kim, M. Goto, S. Kim, S-N Fatigue and Fatigue Crack Propagation Behaviors of X80 Steel at Room and Low Temperatures, *Metallurgical and Materials Transactions A* 45, 2014, pp. 654
5. R.D. McCammon, H.M. Rosenberg, *Proc. R. Soc. London, Ser. A* 242, 1957, pp. 203.

Publications

1. Y. Zhu, D. Hou, Q. Li, Quasi in-situ EBSD analysis of twinning-detwinning and slip behaviors in textured AZ31 magnesium alloy subjected to compressive-tensile loading, *Journal of Magnesium and Alloys* 10 (2022) 956-964.
2. Q. Li, Microstructural Analysis of Fine-grained Magnesium after Cyclic Tension-Tension Fatigue Testing at 0°C, *Journal of Materials Research and Technology* 20 (2022) 4306-4317.
3. Q. Li, Study of Growth Twins Produced through Heat Treatment of Fine-Grained Magnesium, *Materials Science and Engineering A* 841 (2022) 143047.
4. Q. Li, Fatigue Behavior of Fine-grained Magnesium under Tension-Tension Loading at 0°C, *International Journal of Fatigue* 153 (2021) 106506.
5. J. Wang, Q. Li, Grain Size and Mechanical Property of Magnesium Experienced Rolling and Post Heat Treatment, *Thermomechanics & Infrared Imaging, Inverse Problem Methodologies and Mechanics of Additive & Advanced Manufactured Materials*, Volume 7, pp. 13-19 (2021).
6. Q. Li, Effect of Subfreezing Testing Temperature on Tensile Mechanical Behavior of Fine-grained Magnesium, *Materials Science and Engineering A* (2021) 140457.
7. X. Li, Q. Li, Effect of pre-compression on microstructural evolution, mechanical property and strengthening mechanism of AZ31 alloy, *Journal of Materials Science* 55 (2020) 11637-11649.
8. Y. Zhu, PhD thesis, Activity of twinning, basal slip and pyramidal slip systems in textured AZ31 magnesium alloy (2020) (Advisor: Q. Li).

Influence of 3D heterophase interface structure on deformation physics

Prof. Nathan A. Mara, University of Minnesota-Twin Cities

Prof. Irene J. Beyerlein, University of California, Santa Barbara

Keywords: Dislocation-interface interactions; Phase Field Dislocation Dynamics; Nanolayered Composites; Electron Microscopy; Enhanced Strength and Ductility

Research Scope

Detailed work into the defect-interface interactions enabling the enhanced mechanical behavior of two-phase or multiphase materials have only begun to investigate the rich parameter space of heterophase interface character, morphology, and chemistry. To date, heterophase interfaces are generally regarded as two dimensional (2D), and chemically and structurally abrupt. Yet for decades, studies have pointed to the enormous influence that the properties of the interface in the out-of-plane dimension can have on strength and mechanical behavior.

In this project, we aim to understand defect-interface interactions by pioneering basic research on *3D interfaces*. 3D interfaces are heterophase interfaces that extend out of plane into the two crystals on either side and are chemically, crystallographically, and/or topologically divergent, in up to three dimensions, from both crystals they join. Such interfaces influence not only the unit processes of single dislocations that can be understood at the atomic scale, but also mechanical behavior at the scales of a few to tens of dislocations and the resulting bulk behavior. Very rarely are interfaces found in nature to be 2D, that is spanning no more than a nanometer or two. The goal of this program is to systematically develop an understanding on how 3D interfaces can affect mechanical response. The types of 3D interfaces studied will encompass those containing chemical gradients and/or boundary curvature (of relevance to particle-strengthened materials, irradiated materials, lamellar composites, and more).

For 3D interface effects, the scientific issues that need to be addressed concern attaining a multiscale understanding of defect physics from the unit process encompassing the alterations in the dislocation core as it reacts with an interface to the collective process of impinging dislocation arrays that transform the interface structure to collective processes of multiple slip interactions. Each process is expected to be profoundly altered by varying the chemical composition and structure of the 3D interface. In this program, we converge synthesis, measurement, and modeling efforts to elucidate basic, controllable structural variables of the 3D interface that affect structural material performance. The materials containing interfaces are synthesized via physical vapor deposition, a process by which the composition and/or structure may be systematically varied in the out-of-plane direction. Microstructural characterization will consist of a suite of techniques that addresses structure at the atomic level (TEM, Atom Probe), as well as mesoscales (X-ray). Mechanical behavior is investigated at length scales ranging from atomic-level dislocation-interface interactions (in-situ TEM) to micro scales (in-situ SEM and ex-situ nanomechanical

testing). A combination of atomic-scale simulation and mesoscale phase field modeling is employed to simulate dislocation interactions with the 3D interfaces we synthesize. The calculations together aim to uncover fundamental mechanistic details underlying the dislocation reactions, to extract the energies and critical stresses associated with them, and to relate them to the morphology and chemistry of the 3D interfaces.

Recent Progress

Recently, we discovered that Cu-Nb nanocomposites containing 3D interfaces with layer thickness $h=10$ nm and 3D interfacial thickness of $h'=10$ nm possess enhanced compressive strength and deformability as compared to similar material with 40 nm pure layer thickness [1]. (See **Figure 1**) In conventional (2D interface) nanolaminate materials, such a decrease in layer thickness has historically been associated with an increase in strength, but a decrease in deformability [3]. Moreover, we investigated the anisotropy of these same materials using micropillar compression parallel, perpendicular, and at a 45° angle with respect to the interface. When loaded in shear, $h=10$ nm $h'=10$ nm Cu/Nb exhibits enhanced work hardening, and homogeneous deformation without shear banding to large strains (manuscript in preparation).

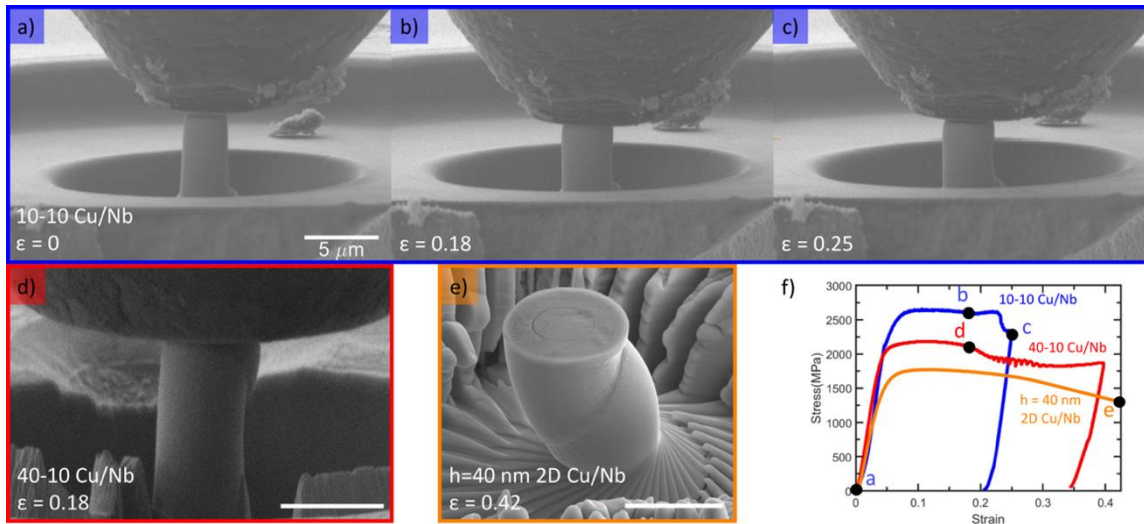


Figure 1. Snapshots of the compressed $h=10$ - $h'=10$ Cu/Nb micropillar: (a) before compression, (b) during homogeneous deformation, and (c) after shear localization. For comparison, we have included a snapshot of $h=40$ - $h'=10$ Cu/Nb at a comparable strain to (b) in (d), as well as a micrograph of $h=40$ nm 2D Cu/Nb in (e) after ex-situ compression. It can be seen in (d) and (f) that 40-10 Cu/Nb shear localizes prior to the strains indicated in (b) and (d), and it does so very severely. Strains presented are engineering. All scale bars represent equal lengths. [1]

During the above experiments, we observed that the interfacial structure consisted of a mixture of ordered and disordered regions, varying in their composition in all 3 dimensions, as confirmed by Atom Probe Tomography (not shown, but can be found in [4]). Dislocation interactions with such complex microstructural variability is not easily addressed by conventional modeling approaches, so we further developed our Phase Field Dislocation Dynamics (PFDD) model to accommodate multiple material phases, firstly as particulate phases within a FCC or BCC matrix [2]. Here, the

chemical composition of the phases was altered to produce a thermodynamically amorphous phase ($\text{Cu}_{0.5}\text{Nb}_{0.5}$), or a phase of similar crystallographic phase, but different composition than the surrounding matrix. From such simulations in an FCC matrix, the behavior of leading and trailing Shockley partials with an amorphous particle, as well as crystalline particles of similar phase and different stacking fault energy, were simulated, with their ability to either shear the particles as in the case of an FCC particle in an FCC matrix, or to bow around non-shearable amorphous obstacles clearly revealed. These simulations set the stage for our future work, outlined below.

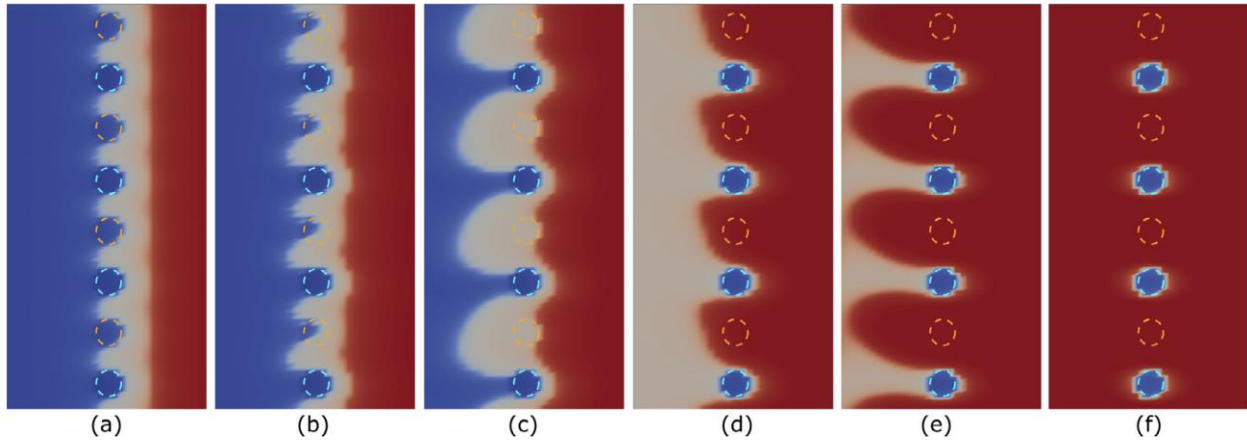


Figure 2. Snapshots of selected configurations for an edge dislocation bypassing four FCC $\text{Cu}_{0.8}\text{Nb}_{0.2}$ precipitates (cyan circles) and four amorphous precipitates (orange circles) in a Cu matrix. The applied stress is constant and is slightly higher than the critical stress for a dislocation to overcome the array of obstacles. Snapshots are colored by the disregistry field along the x direction, ξ_x , where blue and red correspond to $\xi_x = 0$ and b , respectively. The light brown region is the intrinsic stacking fault between two Shockley partial dislocations. [2]

Future Plans

In the next cycle, we plan to focus on 3D interfaces within HCP/BCC systems, composed specifically of alternating phases created by co-deposition of Ti and phase X, where X is Nb, V, or Ta (**See figure 3**). For these systems, we will aim to understand the 3D interface structure, such as thickness and crystallinity, and its evolution under heating, with the anticipation that a range of interesting 3D structures may emerge. The effort entails mapping their morphology and chemistry with Atom Probe Tomography (APT) and transmission electron microscopy.

For these materials systems, another future plan is to understand the thermo-mechanical stability of the 3D interface in deformation and how stress-driven dislocation transmission is accomplished. We will build upon the multi-phase phase field dislocation dynamics model advanced in the last cycle of the program. Previously, the model was extended to account for three or more phases, their energies and anisotropies, and structure, including combinations of amorphous and fcc or bcc crystal structures. The current modeling goal is to consider the simultaneous effects of temperature on dislocation glide, the hexagonal close packed structure, and 3D interface evolution and to track the motion of the 3D interface boundaries in addition to the motion of the dislocations.

With the combined experimental and modeling effort, we will seek to identify the role of composition and structure of the 3D interface on the interaction with a series of impinging dislocations. This involves the study of active dislocations impinging dislocations on a 3D interface and analyzing changes in the interface properties and the ability of subsequent dislocations to transmit across it.

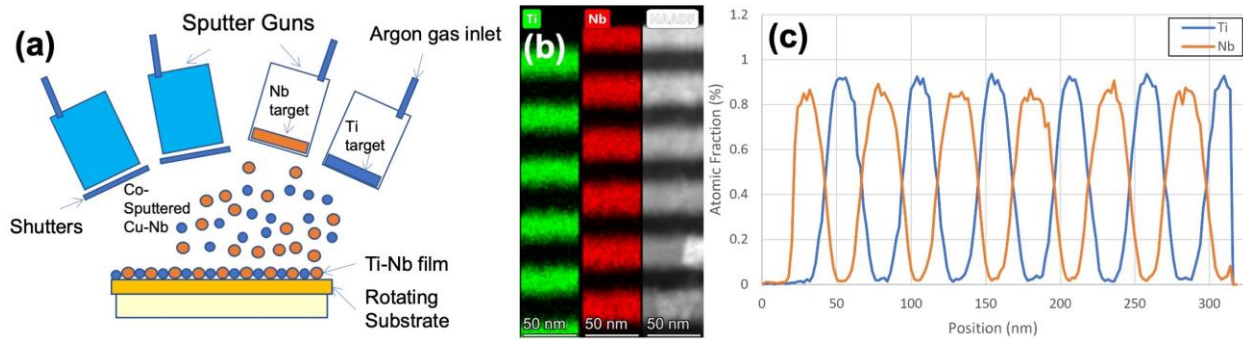


Figure 3. (a) Alternating layers with diffuse interfaces are created by varying the deposition power of the Ti and Nb targets. Increasing the power on one target while simultaneously decreasing the power on the other allows for tailoring of the compositional gradient. (b) Cross-sectional STEM/EDS micrograph of Ti/Nb multilayers where pure hcp Ti and bcc Nb alloy layers are separated by interfaces that are chemically diffuse over distances of ~ 15 nm. (c) EDS line scan showing the variation in chemical composition as a function of position in (b).

References

1. Cheng, J.Y., S. Xu, Y. Chen, Z. Li, J.K. Baldwin, I.J. Beyerlein, and N.A. Mara, *Simultaneous High-Strength and Deformable Nanolaminates With Thick Biphasic Interfaces*. *Nano Letters*, 2022. **22**(5): p. 1897-1904. DOI:10.1021/acs.nanolett.1c04144
2. Xu, S., J.Y. Cheng, N.A. Mara, and I.J. Beyerlein, *Dislocation dynamics in heterogeneous nanostructured materials*. *Journal of the Mechanics and Physics of Solids*, 2022. **168**: p. 105031. DOI:<https://doi.org/10.1016/j.jmps.2022.105031>
3. Beyerlein, I.J., Z. Li, and N.A. Mara, *Mechanical Properties of Metal Nanolaminates*. *Annual Review of Materials Research*, 2022. **52**(1): p. 281-304. DOI:10.1146/annurev-matsci-081320-031236
4. Li, Z., J.Y. Cheng, J.D. Poplawsky, S. Xu, J.K. Baldwin, I.J. Beyerlein, and N.A. Mara, *Critical length scales for chemical segregation at Cu/Nb 3-D interfaces by atom probe tomography*. *Scripta Materialia*, 2022. in press.

Publications

1. Y. Chen, N. Li, R.G. Hoagland, X.Y. Liu, J.K. Baldwin, I.J. Beyerlein, J.Y. Cheng, N.A. Mara, *Effects of three-dimensional Cu/Nb interfaces on strengthening and shear banding in nanoscale metallic multilayers*, *Acta Materialia* **199**, 593-601 (2020).
2. A. Misra, M. Goken, N.A. Mara, I.J. Beyerlein, *Hierarchical and heterogeneous multiphase metallic nanomaterials and laminates*, *MRS Bulletin* **46**, 236-243 (2021).
3. S. Xu, J.Y. Cheng, N.A. Mara, I.J. Beyerlein, *Phase-field modeling of the interactions between an edge dislocation and an array of obstacles*, *Computer Methods in Applied Mechanics and Engineering* **389**, 114426 (2021).
4. J.M. Wheeler, C. Harvey, A. Misra, N.A. Mara, X. Maeder, J. Michler, S. Pathak, *High temperature nanoindentation of Cu-TiN nanolaminates*, *Materials Science and Engineering A* **804**, 140522, (2021).
5. J.Y. Cheng, S. Xu, Z. Li, I.J. Beyerlein, N.A. Mara, *Simultaneous High-Strength and Deformable Nanolaminates With Thick Biphase Interfaces*, *Nano Letters* **22**, Issue 5, 1897-1904 (2022).
6. I.J. Beyerlein, Z. Li, N.A. Mara, *Mechanical Properties of Metal Nanolaminates*, *Annual Review of Materials Research* **52**, 281-304 (2022).
7. Z.Li, J.Y. Cheng, J.D. Poplawsky, S. Xu, J.K. Baldwin, I.J. Beyerlein, N.A. Mara, *Critical length scales for chemical segregation at Cu/Nb 3-D interfaces by atom probe tomography*, *Scripta Materialia*, in press.
8. S. Xu, J.Y. Cheng, N.A. Mara, I.J. Beyerlein, *Dislocation dynamics in heterogeneous nanostructured materials*, *Journal of the Mechanics and Physics of Solids* **168**, 105031 (2022).
9. S. Xu, J.Y. Cheng, N.A. Mara, I.J. Beyerlein, *Thick interface size effect on dislocation transmission in nanolaminates*, *IOP Conference Series: Materials Science and Engineering* **1249**, 012005 (2022).

Chemical partitioning and radiation damage in concentrated alloys

Emmanuelle Marquis (University of Michigan), Fadi Abdeljawad (Clemson University), Enrique Martinez (Clemson University), Suveen Mathaudhu (Colorado School of Mines)

Keywords: Irradiation-induced segregation, concentrated alloys, grain boundary, defects

Research Scope

Critical to the development of clean, reliable nuclear energy is the discovery of fundamental knowledge about materials behavior under irradiation. In response, the proposed program seeks to uncover, understand, and model the synergies between chemistry and structural defects controlling the development and evolution of chemical partitioning via radiation-induced segregation (RIS) at defect sinks in alloys during irradiation.

Microstructural features that develop during irradiation, i.e. dislocation loops, cavities, and RIS, are typically studied in isolation in an effort to reduce the complexity of the problem. However, such an approach masks their inherent interactions. Instead, we contend that RIS is highly sensitive to, and interacts with the microstructure developing in the vicinity of grain boundaries due to the synergies and competition for point defects. Therefore, through integrated ex-situ and in-situ experimental, computational, and data analytics approaches, the proposed program will address fundamental questions linking the temporal and spatial evolution of RIS at grain boundaries and dislocations and the development of alloy microstructures in the proximity of such defect sinks.

While these scientific questions are universal and the findings will generally be extendable to any alloy system, the work will focus on concentrated multicomponent alloys which have not yet been widely investigated. The proposed methodology will vastly expand the range of experimental conditions to enable extrapolation of materials behavior to modern reactor conditions, push existing models that are unable to account for untapped synergies and multiple length and time scales, and will resolve conflicting literature data.

Recent Progress

Since the recent project start mid-August, the PIs have hired graduate students in their respective groups: Daniele Offidani (Michigan), Marie Thomas (Mines), and Jacob Jeffries and Yasir Mahmood (Clemson), initiated weekly project meetings, and are discussing possible collaborative interactions with other groups and institutions. Initial experiments and computations are under way.

Future Plans

Experimental work will focus on understanding thermal stability and chemistry of grain boundaries under thermal conditions at intermediate temperature to establish a baseline for comparison with irradiation behavior (Mines). Once the high pressure torsion instrument is operational at Mines (expected January 2023), we will start on processing materials of varying grain sizes. In parallel, ion irradiations and microstructure characterization will continue to quantify the role of Mn and Co on the RIS behavior of CrFeNi alloys (Michigan). On the modeling side, the groups at Clemson University have started a literature review to understand different approaches to compute transport coefficients for multicomponent concentrated alloys and phase field methods to model materials under irradiation. The goal is to develop a methodology to compute such transport coefficients in a systematic way. Purely analytical approaches will be explored along with computational algorithms based on Monte Carlo sampling. Phase field methods will be also implemented in the context of RIS to analyze the long-term chemical redistribution induced by irradiation.

References

N.A.

Publications

N.A.

Taming Martensitic Transformations by Defect Engineering

**Principal Investigators: Profs. Michael J. Mills, Yunzhi Wang, and Peter M. Anderson
The Ohio State University, Department of Materials Science and Engineering**

Keywords: Ion implantation, shape memory alloy, nanoindentation, pseudoelastic, phase field

Research Scope

Shape memory alloys (SMAs) are class of alloys that can undergo a reversible martensitic transformation (MT) giving rise to their functional properties (pseudoelasticity & shape memory effect). Phase transformations are elicited via a change in temperature or stress state, resulting in a dimensional change that can be utilized for actuation. Such characteristics would be better exploited in biomedical and aerospace applications if strain accumulation during cycling (i.e. transformation-induced plasticity/walking), hysteresis, and nonlinear response could be efficiently mitigated without extensive training. Conventional routes to stabilize transformation-induced plasticity/walking usually rely on thermomechanical processing and alloying to generate dislocation substructures and precipitates to modulate the martensitic transformation. The primary goal of this program is to manipulate the pseudoelastic properties of Nitinol (NiTi) using novel defect structures to achieve dimensional stability, reduced hysteresis, and linearized response. Our most recent work has focused on high energy ion implantation to create unique defect microstructures to modulate and tame the temperature and stress-induced phase transformation in novel ways.

Experimental testing and characterization, theoretical analysis, and computer simulations are used at multiple scales to study the potency of various extended defects that induce distortions and spatially nonuniform chemistry. Implantation of Ni-rich NiTi in pristine, thermally-cycled and cold rolled forms are chosen to explore varied processing routes. High-energy implantation has been performed at the Center for Integrated Nanotechnologies (CINT)-Sandia National Laboratories through a User-Facilities Grant. The resulting material has been characterized through nanoindentation at CINT-Los Alamos National Labs, scanning electron microscopy and high-resolution transmission electron microscopy, and an array of simulation techniques to estimate defect densities (SRIM), interpret nanoindentation results (finite element method), and study how nm-scale (phase field method) and atomic-scale (molecular dynamics, through a collaboration with J Wharry, Purdue) defects can modulate the austenite to martensite phase transformation. The experimental and computational results demonstrate the ability to create nm-scale clusters of amorphous, non-transforming defects that tame the martensitic transformation, achieving stable, ultra-low hysteretic response.

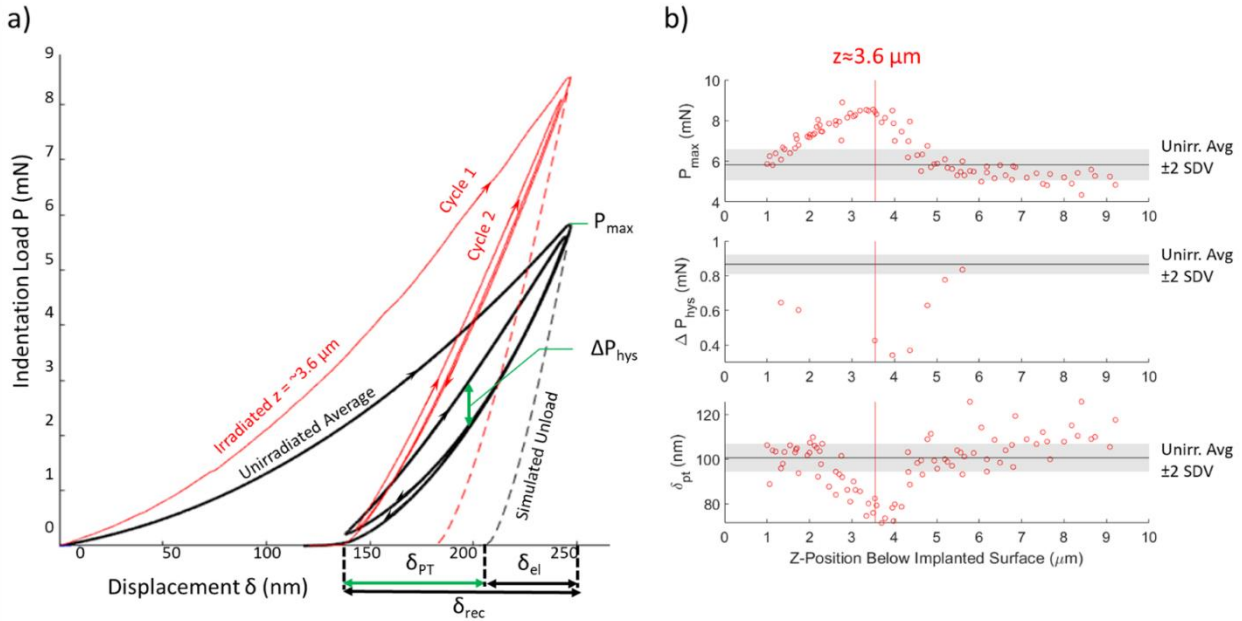


Figure 1 (a) shows dual cycle nanoindentation curves for peak implanted (red) and pristine Ni-rich NiTi. (b) shows the variation in the hardness (P), effective hysteresis (ΔP_{hys}), and displacement from phase transformation (δ_{PT}), as a function of implantation depth.

Recent Progress

Post-implantation nanoindentation revealed that the treated NiTi had not only a 50% increase in hardness and a retention of the ability to undergo the MT, but also had a reduced hysteresis within the proximity of the highest damaged region of NiTi. A two-cycle nanoindentation testing process with a Berkovich indenter tip had been developed to by loading to a fixed depth (250nm), then partial unloading (130nm, $\sim 50\%$ of the peak depth), followed by full loading and unload. This test method allows one to differentiate the displacement attributed from elasticity (δ_{el}), plasticity (δ_P), and phase transformation (δ_{PT}). Additionally, through this indentation process the cycling allows one to assess the difference in applied load (ΔP_{hys}). These key measurements, illustrated in Figure 1a, are plotted against their depth relative to the irradiated surface in Figure 1b, showing a non-monotonic trend about the peak implanted response $\sim 3.6 \mu\text{m}$ just before the visible damage band $\sim 4.2 \mu\text{m}$ shown in Figure 2.

Characterization with electron microscopy, Figure 2, reveals a B2 matrix with disparate amorphous clusters (with no signs of other defects) in the region where extrema in nanoindentation properties are observed. Scanning transmission electron microscopy (STEM) revealed a structural change in the implanted region around $z \sim 3.1$ to $4.2 \mu\text{m}$. The selected area electron diffraction patterns (SAEDPs) confirm the B2 structure at more shallow positions (aqua inset) while near peak damage an amorphous ring about the $\{011\}$ spacing (pink inset), consistent with amorphization at $z \sim 3.5$ to $4.2 \mu\text{m}$. High resolution STEM-HAADF imaging (yellow inset), taken from the yellow

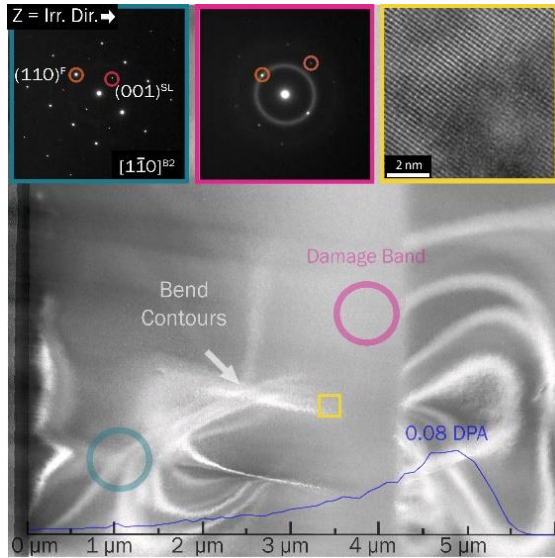


Figure 2 HAADF STEM micrograph of implantation cross section with SAED patterns and high resolution HAADF image from implanted regions.

shown in Figure 3(a). Figure 3(b) shows a two-dimensional cross-section of the microstructure and Figure 3(c) shows the three-dimensional simulation cell after the application of a compressive load, where the nonuniform distributions of martensite underscore the constraint imposed by the non-transforming amorphous phase. The results signify a more protracted evolution, equivalent to linearization of the stress-strain response. The unequal distribution of variants in Figure 3 arises from random nucleation and thus the same result with counterpart martensite variants is equally likely.

Results supporting the phase field simulations obtained from the molecular dynamics simulations show that the presence of implantation like defects hinders the B2-B19' martensitic transformation and produces fewer B19' transformed lattice sites. This suppressive effect is more pronounced for vacancy clusters than for point defects (i.e., interstitials, vacancies, antisite defects). The suppression mechanism appears to be the pinning of B19' phase boundaries by vacancy clusters. The vacancy cluster simulation requires $\sim 40\%$ higher strain to reach any given B19' phase fraction than in the pristine simulation. All MD simulations show full recovery of the B2 phase upon

square inside the damage band in Figure 2, reveals ordered B2-crystalline and amorphous regions. The SRIM predictions, blue curve overlaid on Figure 2, indicates a peak in damage at $z \sim 4.9 \mu\text{m}$. This discrepancy is likely due to the inability of the SRIM code to capture displacements of atoms with tight bonding as in B2 ordered structures.

Phase field (PF) simulations predict that a co-continuous B2-amorphous composite exhibits incomplete martensitic transformation of B2 regions, even at 20% larger applied stress than that to fully transform the pure B2 (pristine) case. A representative B2+amorphous periodic cell used in the phase field simulations, where the B2 and amorphous phases are assumed to be co-continuous with equal volume fraction and elastic moduli, is

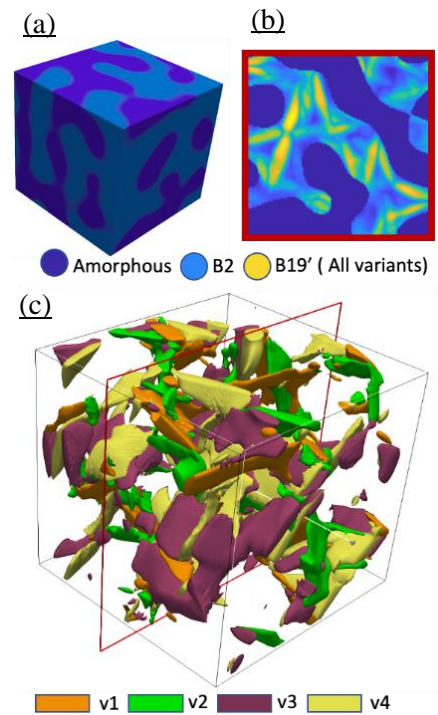


Figure 3 (a) B2+amorphous co-continuous simulation cell used for the study. (b) Shows the distribution of B2 and B19' in 2D slices. (c) 3D simulation box showing the distribution 4 variants of martensite labelled v1 to v4.

unloading since the physical phenomena typically responsible for hysteresis are not considered within the simulations.

Future Plans

Recent indentation experiments have characterized the effect of ion implantation on thermally cycled and cold rolled NiTi. The same 2 load cycle indentation method is applied to examine whether the shape memory effect is retained and evaluate the amount of hysteresis. This effort seeks to determine how the amorphous clusters induced by ion implantation interact with prior dislocation substructures produced by standard thermomechanical methods. This investigation will examine mechanistically the impact of amorphous clusters on material properties. In conjunction with indentation testing, FE modeling of indentation is implemented to extract stress strain curve material parameters. This second effort will be combined with machine learning, namely Bayesian inference, to infer key NiTi properties from indentation testing.

Characterization of the change in local structure as a result of implantation, and the local stress fields in the B2 matrix adjacent to amorphous regions and precipitates is highly challenging. The 4D-STEM technique is being applied as a complement to the diffraction contrast and HAADF-STEM methods applied thus far in the program. A Molecular Foundry proposal has been approved and work with Colin Ophus and the National Center for Electron Microscopy (NCEM) has initiated to measure the local strain fields determined from coherent H-phase precipitates embedded in a B2 matrix. Simulation of the strain fields for various precipitate/matrix configurations is being simulated using dynamical electron diffraction theory and compared with 4D-STEM experiments. This investigation will allow us to quantitatively interpret the 4D-STEM data for embedded precipitates and amorphous regions.

The phase field framework developed thus far will be used to perform a systematic parametric study to understand the effects of size and distribution of amorphous clusters on martensitic transformation. Insights gained from experimental characterization will be used to capture the local field effect induced by the amorphous clusters and model the pseudo elastic response of B2-amorphous composite microstructures more accurately. The ability of amorphous clusters to reduce the inherent elastic anisotropy will also be explored. Finally, the phase field framework will be used to analyze the hard confinement effect of non-transforming precipitates and the soft confinement effect imposed by pockets of high and low M_s regions through dissolution of precipitates.

Publications

Gao, X., Hong, D., Paranjape H., Zhang, W., Anderson, P.M., The Oliver-Pharr Method: A Guide for Shape Memory Alloys. Manuscript in preparation.

Hinojos. A., Hong. D., Feng L., Yang, C., Wharry, J.P., Gao, X., Hattar, K., Li, N., Schaffer, J.E., Wang, Y., Mills, M.J., Anderson, P.M. 2022. Taming the Pseudoelastic Response of Nitinol Using Ion Implantation. Submitted to Scripta Materialia.

Hinojos, A., Hong, D., Feng, L., Yang, C., Wharry, J.P., Gao, X., Hattar, K., Li, N., Schaffer, J.E., Wang, Y., Mills, M.J., Anderson, P.M. 2022. Modulating the Pseudoelastic Response of Nitinol Using Ion Implantation. *Journal of Advanced Manufacturing and Processes*.

Yu, T., Gao, Y., Casalena, L., Anderson, P., Mills, M., Wang, Y., 2021. H-phase precipitation and its effects on martensitic transformation in NiTi-Hf high-temperature shape memory alloys. *Acta Materialia* 208, 116651–116651. <https://doi.org/10.1016/j.actamat.2021.116651>

Zhu, Y., Ameyama, K., Anderson, P.M., Beyerlein, I.J., Gao, H., Kim, H.S., Lavernia, E., Mathaudhu, S., Mughrabi, H., Ritchie, R.O., Tsuji, N., Zhang, X., Wu, X., 2021. Heterostructured materials: superior properties from hetero-zone interaction. *Materials Research Letters* 9, 1–31. <https://doi.org/10.1080/21663831.2020.1796836>

Gao, Y., Yu, T., and Wang, Y., “Phase Transformation Graph and Transformation Pathway Engineering for Shape Memory Alloys.” *Shap. Mem. Superelasticity* 6 (2020) 115-130. <https://doi.org/10.1007/s40830-020-00271-5>.

Gao, Y., Zhang, Y.F., Aagesen, L.G., Yu, J.G., Long, M., Wang, Y., “Defect-free plastic deformation through dimensionality reduction and self-annihilation of topological defects in crystalline solids,” *Phys. Rev. Research* 2 (2020) 013146-1 – 10.

Metal-ceramic interfaces at high temperatures

Yuri Mishin, George Mason University, Virginia

Keywords: Interfaces, metals, ceramics, modeling, simulation

Research Scope

This research program aims to improve the fundamental understanding of metal-ceramic interfaces at high temperatures and develop new methods for computational prediction of their structure, thermodynamics, kinetics, and mechanical responses. This goal will be achieved by atomistic computer simulations of interfacial creep and interface diffusion in several model systems representing metal-nonmetal contacts. One of the key components of the methodology is the development of physically informed machine-learning interatomic potentials based on massive databases of first-principles calculations. Such potentials will enable reliable energy and atomic force predictions in mixed-bonding systems. The initial stage of the program will focus on Al-Si alloys as prototypical composite materials. However, our long-term goal is to expand this program to other classes of metal-matrix composites. The project can significantly impact the fundamental knowledge of metal-ceramic interfaces at high temperatures. It can also create a theoretical foundation for the design of new creep-resistant composite materials in the future.

Recent Progress

This is a new project that only started about two months ago. Thus, only preliminary results are discussed below. Initial progress has been made in three directions:

1. Development of a machine-learning interatomic potential for the Al-Si system.

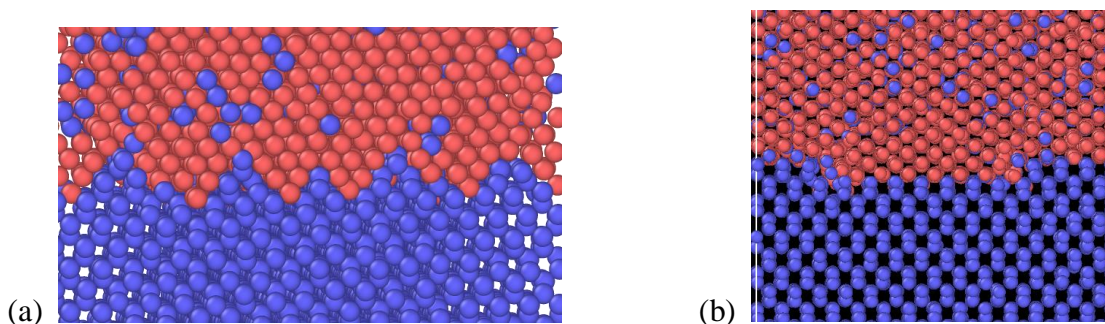
The first step in the development of the physically informed neural network (PINN) [1,2] interatomic potential for the Al-Si system is to create an extensive database of energies and forces for diverse atomic configurations computed by density-functional theory (DFT) calculations. This database will include tens of thousands of supercells representing the solid and liquid phases of Al, Si and Al-Si ordered and disordered structures. The solid-state supercells will represent a set of different crystalline structures, including different point, linear and 2D defects. The construction of this database is now about 50% complete. Furthermore, we have already started training the PINN potential on the present database and have very encouraging results. The potential will be trained to the root-mean-square error of 3-4 eV/atom relative to the DFT energies and will accurately reproduce many properties of Al and Si and Al-Si liquid solutions.

2. Atomistic modeling of Al-Si interfaces at high temperatures

While the PINN potential is under construction, we have made a head start by launching Al-Si interface simulations using an existing semi-empirical interatomic potential [3]. Although it is less

accurate than the future PINN potential, it is fast and suitable for exploratory simulations. We will later verify the main results by the slower but more accurate PINN simulations.

We have studied a series of Al-Si interfaces with different orientation relationships and examined their structural stability at relatively high temperatures up to the eutectic point. Some of the interfaces were found to be unstable and split into a more stable interface and a grain boundary in Al. Some of the stable interfaces spontaneously develop thermal disconnections pairs and other defects. Diffusion of Al and Si along the most stable interfaces has been computed and compared with the diffusivities along Al grain boundaries, dislocation lines, and perfect lattice. The phase boundary diffusion coefficients were found to be significantly lower than the grain boundary and dislocation pipe diffusivities. This finding is consistent with the recent experimental results for Ni/sapphire interfaces [4] and points to the greater thermodynamic stability of metal-ceramic interfaces compared to metallic grain boundaries.



Representative structures of phase boundaries between Al (red) and Si (blue) in atomistic computer simulations at the temperature of 650 K. (a) Al (100) || Si (100) cube orientation relationship. Note the spontaneous formation of Al (110) || Si (110) nano-facets. (b) Al (110) || Si (110) interface containing a disconnection dipole (looking like two steps). Al and Si atoms display accelerated diffusion along the disconnection lines with rates that are similar to those in dislocation pipe diffusion.

3. Collaboration with experimentalists

Recognizing the importance of validating the computer simulations through experiments, we have reached out to two experimental groups and are now working on a detailed three-side collaboration plan. According to our preliminary plan, Dr. Gunther Richter (Max Planck Institute, Stuttgart, Germany) will create a series of Al-Si interfaces by MBE deposition of Al on precisely oriented Si substrates in ultrahigh vacuum. The bilayers will be annealed at different temperatures, including high temperatures resulting in solid-state dewetting and the formation of defect-free Al nano-islands and nano-particles supported by the Si substrate. The structures obtained will be covered by a Pt layer to prevent oxidation and transported to Technion (Israel Institute of Technology), where Prof. E. Rabkin will study the interface structures by a set of characterization

methods, including HRTEM. The experimental work will be organized in a way that ensures synergy with the concurrent simulation work performed in our group. Both Dr. Richter and Prof. Rabkin are experts in synthesis, processing, and characterization of nano-particles, nano-layers, and metal-ceramic interfaces.

Future Plans

Our plans for the remainder of the first year include:

1. Finish the development of the Al-Si PINN potential and test it for a broad spectrum of properties, including the ability to correctly reproduce the Al-Si phase diagram.
2. Continue the atomistic modeling of Al-Si interfaces, including the mass transport of Al and Si atoms as a function of the interface structure and temperature. Preparing the methodology for testing the interfaces for shear and high-temperature interfacial creep.
3. Collaborate with the experimental groups mentioned above by suggesting interface orientation relationships and implementing the experimentally observed interface structures in the simulations.

References

1. Y. Mishin, *Machine-learning interatomic potentials for materials science*, Acta Materialia **214**, 116980 (2020).
2. G. P. Purja Pun, R. Batra, R. Ramprasad and Y. Mishin, *Physically informed artificial neural networks for atomistic modeling of materials*, Nature Communications **10**, 2339 (2019).
3. P. Saidi, T. Frolov, J. J. Hoyt, and M. Asta, *An angular embedded atom method interatomic potential for the aluminum–silicon system*, Modelling and Simulation in Materials Science and Engineering **22**, 055010 (2014).
4. H. Barda and E. Rabkin, *Metal hetero-diffusion along the metal-ceramic interfaces: A case study of Au diffusion along the Ni-sapphire interface*, Acta Materialia **186**, 242-249 (2020).

Publications

None so far.

Plasticity of High-Strength Multiphase Metallic Composites

Amit Misra¹ (PI), Jian Wang² (co-PI)

¹University of Michigan, Ann Arbor; ²University of Nebraska, Lincoln.

Keywords: slip transmission, interfaces, nanoscale eutectics, nanomechanics, atomistic modeling.

Research Scope

The interactions of glide dislocations with planar interfaces such as grain or interphase boundaries determine the overall strength, strain hardening, and ductility of metallic microstructures. Dislocations can be effectively blocked at, transmitted across, deflected along, or reflected from interfaces. For grain boundaries or interphase boundaries involving soft metals, the efficiency of slip transmission can be predicted in terms of geometry of incoming and outgoing slip systems. However, in the case of metal-hard phase (intermetallic or covalent) composite microstructures, the slip system geometry, although necessary, is not sufficient to predict active slip systems since the high Peierls stress of the hard phase [1] may suppress slip transmission in favor of fracture or slip deflection/reflection from interface. In general, many metal-hard phase systems show unique mechanical behavior of simultaneous enhancement in strength and ductility due to uniform plastic flow (suppression of localized shear bands) as the microstructure is refined to nanoscale. But there is a critical gap in knowledge of predicting the active dislocation mechanisms and relating it to the strength-strain hardening-plastic co-deformability relationship of a given composite microstructure. The goal of this research program is to develop fundamental understanding of the complex dislocation-dislocation and dislocation-interface interactions in *nanocomposite* microstructures that depend on a combination of factors such as Peierls stress of the hard phase, shape of the hard phase (fibrous, lamellae), crystallographic orientation relationships, and the thermodynamic and mechanical properties of the interphase boundary.

Recent Progress

Recent work in the current grant focused on testing the following hypotheses:

- (i) In metallic soft/hard composites, plastic co-deformability is favored at reduced dimensions of the hard phase, independent of the phase morphology (lamellar or fibrous or bicontinuous).
- (ii) A bimodal morphology of coarse/fine phase constituents is not required for plastic co-deformability in nano-composites where the slip can be transmitted across interfaces.

The range of microstructure morphologies, interface properties, crystal structures and crystallographic orientation relationships of constituent phases in the model Al-Cu-Si eutectic alloys refined using laser rapid solidification (LRS) enabled testing of stated hypotheses through integration of atomistic modeling and experimental characterization.

The microstructures and stress-strain response in compression and tension for Al-Si are shown in Figures 1 and 2, respectively. For a nominal composition of Al-16 wt.% Si in the laser melt pool, two distinct microstructure morphologies were observed (Figure 1a). First, nanoscale fully eutectic Al-Si, and second, a heterogeneous structure of nanoscale eutectic surrounded by primary Al phase, ≈ 900 nm diameter. The primary Al grains sometimes contained Si precipitates that tended to be faceted polyhedral with dimension < 100 nm. The Si fiber diameter ranged from ≈ 45 -65 nm, and the inter-fiber spacing was ≈ 100 nm. The Si flakes in the as-cast eutectic, underneath the laser

melt pool, had width of $1.3 \pm 0.4 \mu\text{m}$. The transition in Si morphology from flake in as-cast to fibrous in LRS (high cooling rate) eutectic is consistent with earlier literature [2].

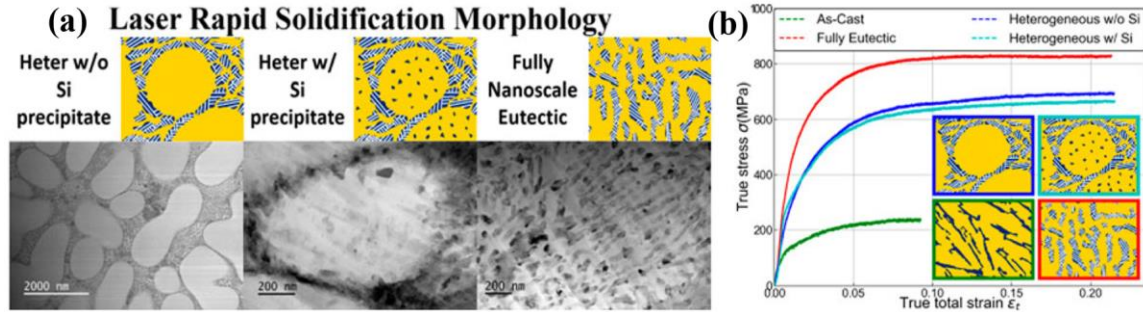


Figure 1(a) A range of nanoscale eutectic morphologies in laser processed Al-16Si, and (b) corresponding compression stress-strain response.

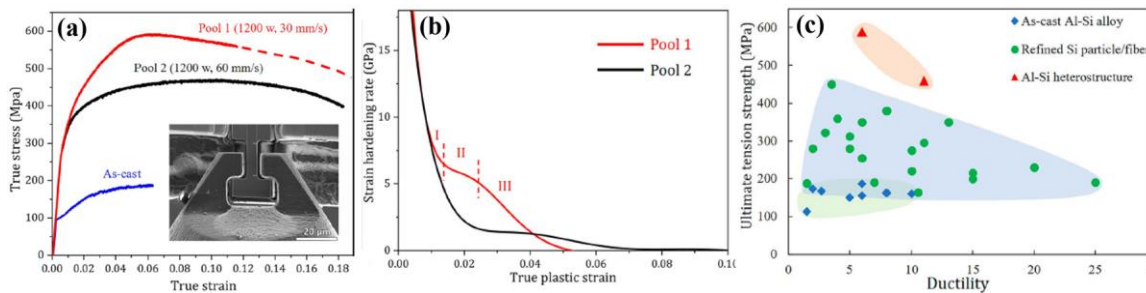


Figure 2. (a) Tensile stress–strain curves of Al-16Si laser refined at different scan rates, with primary Al + eutectic Al-Si phases; (b) Strain hardening rates as a function of true plastic strain calculated from stress–strain curves shown in (a). (c) Tensile strength and ductility of Al–Si alloys reported in literature compared to the current study.

Even in compression (Figure 1b), the as-cast hypereutectic Al-Si alloys ($\approx 16\text{-}20 \text{ at.}\% \text{ Si}$) fractured at a relatively low flow stress of $\approx 235 \text{ MPa}$ at $\leq 8 \%$ plastic strain. The LRS heterogeneous (primary Al + nanoscale eutectic) and fully eutectic morphologies both exhibited uniform plastic flow to $>20\%$ strain and maximum flow strength of ≈ 650 and $\approx 800 \text{ MPa}$, respectively, with comparable strain hardening rates that were significantly higher than the as-cast alloy. Compressive strengths for heterogeneous Al-Si with and without Si nano-precipitates were similar, due to the relatively coarse nature of these precipitates. The LRS Al-Si alloys exhibited enhanced strength and ductility in tension, as compared to the as-cast alloy (Figure 2a) that fractured at stress $< 200 \text{ MPa}$ and ductility $< 6\%$. The ultimate tensile strengths, UTS, ranged from 450 to 600 MPa, for the LRS samples with the difference attributed to the higher volume fraction of the primary Al phase in the lower strength alloy, as measured in the fractured or necked region. For UTS of 600 MPa, the test was stopped after $\approx 12\%$ strain without fracture for microscopy examination. In the sample with lower UTS of 450 MPa, gradual load drop was observed above 12% strain and surface cracks appeared at $\approx 18\%$ strain. The strain hardening rate of up to 7 GPa was measured at a true strain of $\approx 2\%$ (Figure 2b). The overall strength-ductility combination (Figure 2c) measured for LRS Al-Si eutectic was found to be superior to Al-Si eutectic alloys reported in the literature [3].

Al-Al₂Cu nano-lamellar eutectics exhibited maximum compressive flow stress of $\approx 2 \text{ GPa}$ and strain to failure $\approx 26\%$, while the ternary Al-Al₂Cu-Si bimodal eutectic exhibited lower strength of $\approx 1.6 \text{ GPa}$ and comparable plasticity with strain to failure $\approx 28\%$. The bimodal eutectics had

interface spacings of $\approx 40\text{-}50$ nm in the finer zones (Al-Al₂Cu-Si ternary eutectic) and $\approx 100\text{-}400$ nm in the coarser zones (Al-Al₂Cu binary eutectic). Based on a variety of tests that included micropillar compression, plane-strain compression via rolling, nanoindentation hardness and tensile testing on these three systems (binary lamellar Al-Al₂Cu, binary fibrous Al-Si, ternary bimodal Al-Al₂Cu-Si), the key hypothesis was tested that refinement of interface spacing to nanoscale (typically, $< \approx 100$ nm) simultaneously increased both flow strength and plastic co-deformability. The second hypothesis was also tested that a bimodal morphology does not produce higher plastic deformability when the microstructure has been refined to $< \approx 100$ nm. This was observed for both fibrous Al-Si as well as ternary bimodal Al-Al₂Cu-Si.

Dislocation mechanisms were studied using TEM, Figure 3, and atomistic modelling, Figure 4. Geometrically necessary dislocation (GND) accumulation in the interface region between Al dendrites and Al-Si eutectic was prevalent in the tensile tested sample, Figure 3. With increasing strain, dislocation plasticity was observed in the nanoscale eutectic domains, confined to the Al nano-channels between the elastically deforming Si nano-fibers that eventually fracture to discretize the accumulated dislocations. However, the cracks in Si nanofibers are arrested by the strain hardening Al matrix, thereby enabling continued plastic deformation of Al-Si eutectic domains.

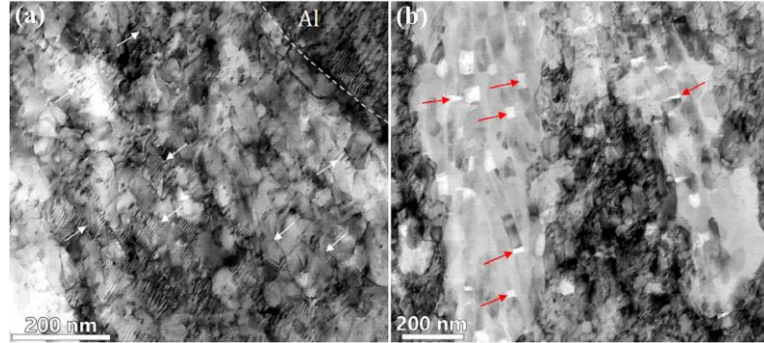


Figure 3. BF-STEM images showing (a) dislocation activity in the nano-Al channels inside the Al/Si eutectic domains; (b) cracks in Si nanofibers arrested by the surrounding strain hardening Al.

MD simulations using interatomic potentials [4] of the interaction of glide dislocations in Al with planar Al-Si interface as well as computation of interface shear strength were used to provide insights on the unit mechanisms. Figure 4 shows the interaction of Al glide dislocations with Al-Si interface where an edge dislocation is observed to climb and screw dislocation is observed to cross-slip along the interface and reflected back into the Al phase. Direct dislocation transmission from Al matrix to Si fibers was not observed. Alternately, dislocations in Al matrix tend to accumulate around Si fibers. These unit mechanisms of dislocation-interface interactions can be interpreted using the thermodynamic and mechanical properties of the interface. A generalized stacking fault energy surface (γ -surface) was calculated for the Al-Si interface using a quasi-coincident site lattice (Q-CSL) as the unit supercell with 4 periodic units for Al and 3 for Si (Figure 5a) that revealed three coherent Q-CSL structures (Figure 5b). Shear of this $\{111\}\text{Al}/\{111\}\text{Si}$ semi-coherent interface along a $\langle 112 \rangle$ direction shows shear yield strength of only 20 MPa due to easy glide of interface dislocations (Figure 5c). The easy climb of mixed dislocations along the interface plane is ascribed to the low formation (0.65 eV/atom) and migration (0.40 eV/atom) energies of vacancies within the interface (Figure 5d-e). More importantly, dislocation climb enables the discreteness of planar dislocation arrays along the interface, which will blunt the stress concentration of the pileup.

Although both (Al-Al₂Cu and Al-Si) systems demonstrated increased strength and ductility, the mechanisms of plasticity enhancement were fundamentally different and unexpected. i) The nano-lamellar Al-Al₂Cu structures exhibited unit defect mechanisms not reported in monolithic

Al₂Cu intermetallic: localized shear on $\{011\}_{\text{Al}_2\text{Cu}}$ and shear-induced faults on $\{121\}_{\text{Al}_2\text{Cu}}$ planes, enabled by slip continuity in nanoscale Al-Al₂Cu eutectics associated with the orientation relationship and interface habit planes. Thus, slip transmission was the key reason for enhanced plasticity at nanoscale, although the shear planes activated in the hard phase were different from those reported in monolithic alloy. ii) In nano-fibrous Al-Si eutectic, however, enhanced tensile ductility and strength were observed even though there was no evidence of direct slip transmission. Dislocation plasticity in the Al was confined to nano-channels between fibers resulting in high strain hardening that suppresses the propagation of nano-cracks in Si.

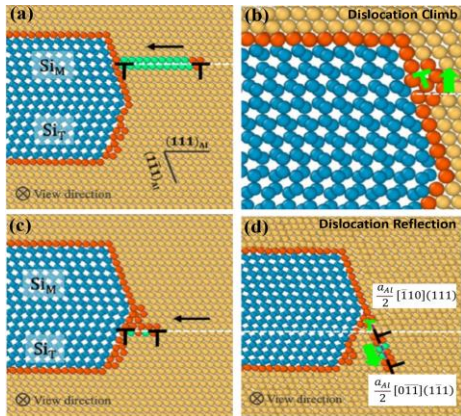


Figure 4. Interaction of (a) an edge dislocation that is observed to (b) climb along the Al-Si interface, and (c) mixed dislocation where the screw segment cross-slips along the interface and emitted back into the Al.

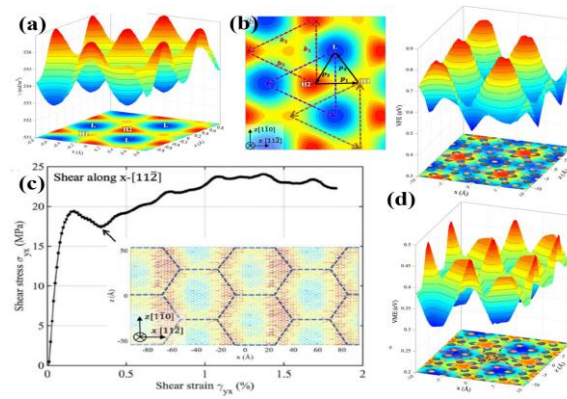


Figure 5. (a) γ -surface of Q-CSL Al-Si interface showing (b) three Q-CSL structures labeled L, H1, H2. (c) Shear stress-strain curve for a bilayer model sheared along $\langle 112 \rangle$. Disregistry plot (inset) shows the interface displacements at strain of 0.4 %. (d) formation and (e) migration energies of vacancies in the Q-CSL interface.

Future Plans

Energy barriers associated with unit mechanisms of dislocation-interface interactions such as transmission across and reflection from soft/hard interphase boundaries will be quantified from first-principles on model eutectic systems. Dislocation mechanisms of high strain hardening rate in metals, including high stacking fault energy metals such as Al that can easily cross-slip, confined by nano-scale hard phases will be elucidated from large-scale atomistic simulations. Experimental characterization of stress-strain response and dislocation mechanisms on a broad range of laser-refined eutectic systems will be integrated with computational modeling. Fundamental understanding of dislocation mechanisms will be used to construct maps of plastic deformation compatibility in terms of relative energy barriers for slip transmission or reflection.

References

1. J.J. Gilman, *Why Silicon is hard*, Science **261** (1993) 1436.
2. M. Pierantoni, M. Gremaud, P. Magnin, D. Stoll, W. Kurz, *The coupled zone of rapidly solidified Al-Si alloys in laser treatment*, Acta Metall. Mater. **40** 1637–1644 (1992).
3. T. Hosch, R.E. Napolitano, *The effect of the flake to fiber transition in silicon morphology on the tensile properties of Al-Si eutectic alloys*, Materials Science and Engineering A **528**, 226–232 (2010).
4. A. Noreyan, Y. Qi, V. Stoilov, *Critical shear stresses at aluminum-silicon interfaces*, Acta Materialia, **56** (2008) 3461–3469.

Publications from this grant (2020-2022)

1. H.H. Lien, J. Mazumder, J. Wang, A. Misra, *Microstructure of hypereutectic Al-Si alloy and high density of nanotwinned ultrafine Si by laser surface remelting*, *Materials Characterization*, **161**, 110147 (2020).
2. H.H. Lien, J. Mazumder, J. Wang, A. Misra, *Ultra-high strength and plasticity in laser rapid solidified Al-Si nanoscale eutectics*, *Materials Research Letters* **8** (8), 291-298 (2020).
3. G. Liu, S. Wang, A. Misra, J. Wang, *Plastic deformation behavior of laser-processed nanoscale Al-Al₂Cu eutectic alloy*, *Acta Materialia*, **186**, 443-453 (2020).
4. S.J. Wang, D.Y. Xie, J. Wang, A. Misra, *Deformation behavior of nanoscale Al-Al₂Cu eutectics studied by in situ micropillar compression*, *Materials Science and Engineering: A* **800**, 140311 (2021).
5. Q. Lei, J. Wang, A. Misra, *Mechanical Behavior of Al-Al₂Cu-Si and Al-Al₂Cu Eutectic Alloys*, *Crystals*, **11** (2), 194 (2021).
6. B.Q. Wei, W.Q. Wu, D. Xie, H.-H. Lien, M. Kayitmazbatir, A. Misra, J. Wang, *In Situ characterization of tensile behaviour of laser rapid solidified Al-Si heterogeneous microstructures*, *Materials Research Letters*, **9**(12), 507-515, (2021).
7. W.Q. Wu, M. Gong, B.Q. Wei, A. Misra, J. Wang, *Atomistic Modeling of Interface Strengthening in Al-Si Eutectic Alloys*, *Acta Materialia*, **225**, 117586 (2022).
8. H.-H. Lien, J. Wang, A. Misra, *Plastic deformation induced microstructure transition in nano-fibrous Al-Si eutectics*, *Materials & Design*, **218**, 110701 (2022).
9. M. Kayitmazbatir, H.H. Lien, J. Mazumder, J. Wang, A. Misra, *Effect of Cooling Rate on Nano-Eutectic Formation in Laser Surface Remelted and Rare Earth Modified Hypereutectic Al-20Si Alloys*. *Crystals*, **12**, 750 (2022).
10. B.P. Sahu, J. Wang, A. Misra, *A comparative study of deformation behavior of the crystalline/amorphous nanocomposite having nanolaminate and fibrous morphology*, *Physical Review Materials*, **6**(9), 094002 (2022).

Determining the rate-controlling, grain-boundary-mediated mechanisms in ultrafine grained Au films

Olivier Pierron, Josh Kacher and Ting Zhu, Georgia Tech

Keywords: In situ TEM, activation volume, grain boundary, dislocation, disconnection

Research Scope

The main goal of this research project is to acquire a fundamental understanding of grain boundary (GB) mediated mechanisms active in ultrafine grained (ufg) metallic films, and the extent to which they dictate plastic flow kinetics. Our approach consists of a synergistic integration of *in situ* transmission electron microscopy (TEM) deformation experiments, nanomechanical testing, and transition state theory based atomistic modeling, in order to provide a linkage between GB-mediated dislocation processes and their deformation kinetics. The *in situ* TEM nanomechanical testing experiments are employed to simultaneously identify plastic deformation mechanisms, obtain key details (such as character of the GBs where dislocation processes are observed, characteristics of meso-scale microstructure where GB and triple junction migration occurs), and measure the sample-level true activation volume in ufg thin films. The activation of relevant GB mediated dislocation mechanisms is modeled using the atomistic free-end nudged elastic band (FENEB) method (overcoming the timescale limitation of molecular dynamics simulations) as a function of representative, experimentally observed GB characters and local stress. Proper integration of experiments (sample-level true activation volume) and atomistic simulations (activation volumes of dislocation processes) to determine strength/rate-controlling mechanisms requires linking the applied stress to the local stress. To that end, a model of grain-size-dependent activation volume previously developed by Conrad is extended to account for the competition between various GB mediated mechanisms.

Recent Progress

Figure 1A shows the microstructure of our 100 nm thick Au films, having an average grain size of 150 nm and a [111] out-of-plane texture. These specimens were tested in the TEM to measure the sample-level activation volume (V_{exp}^*) as a function of applied stress, with and without e-beam (we used our quantitative *in situ* TEM technique to quantify the e beam effects on the measured mechanical properties, and found that the effects were negligible for Au [1]), whose results are summarized in Figure 1B. The average experimental value is $10 b^3$ for our Au thin films [2]. The *in situ* TEM observations include isolated dislocation nucleation from GBs and interaction of both perfect and partial dislocations. Figure 1C shows an example of a dislocation cross-slip event leading to a transition between intra- and intergranular glide.

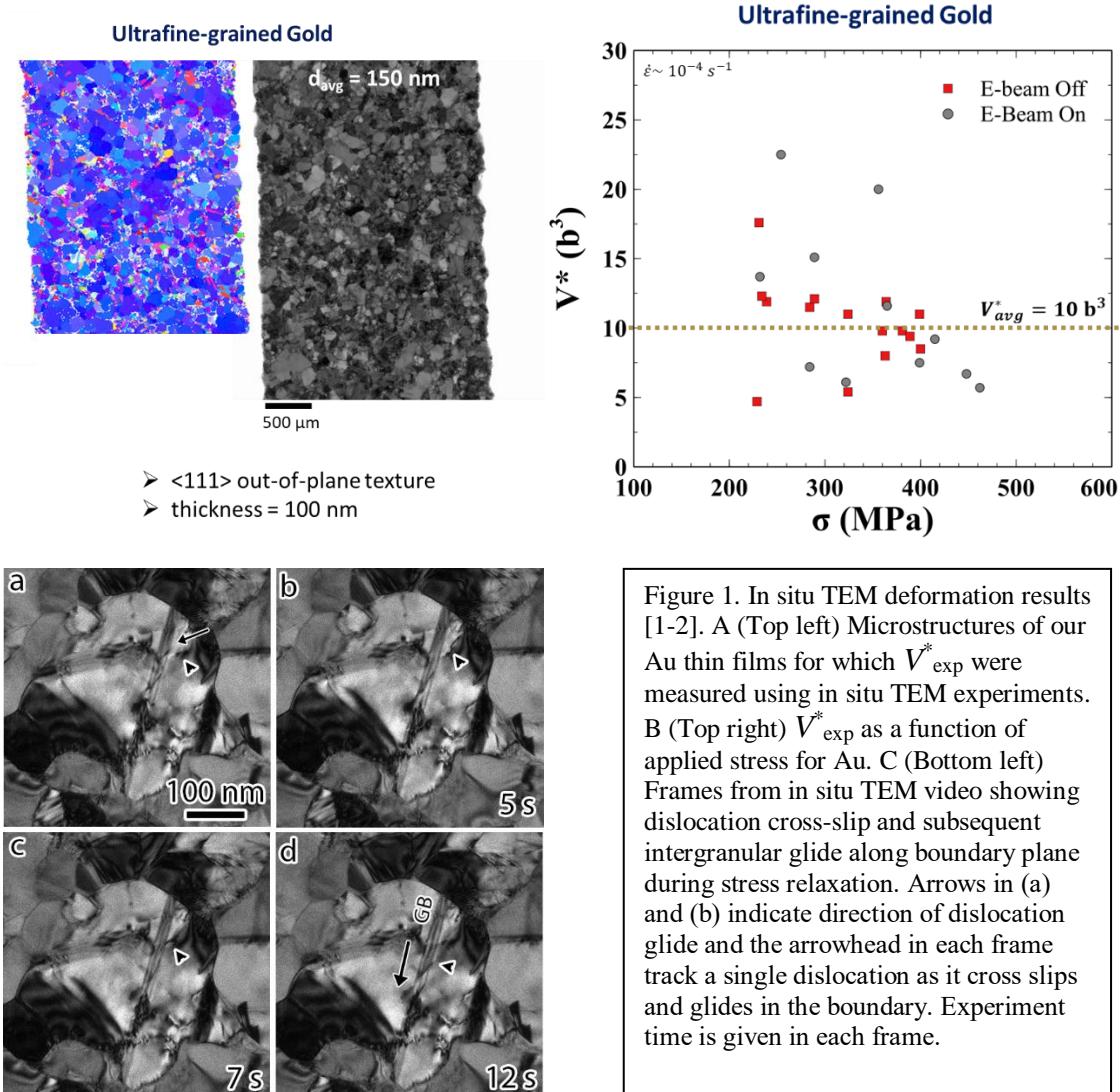


Figure 1. In situ TEM deformation results [1-2]. A (Top left) Microstructures of our Au thin films for which V_{exp}^* were measured using in situ TEM experiments. B (Top right) V_{exp}^* as a function of applied stress for Au. C (Bottom left) Frames from in situ TEM video showing dislocation cross-slip and subsequent intergranular glide along boundary plane during stress relaxation. Arrows in (a) and (b) indicate direction of dislocation glide and the arrowhead in each frame track a single dislocation as it cross slips and glides in the boundary. Experiment time is given in each frame.

Our FENEB calculations with Au have so far been focused on the nucleation of both surface dislocation and GB dislocation [3]. Surface dislocation nucleation was modeled from the corner of a single-crystal Au nanowire with the axial loading direction of $[\bar{4}\bar{1}5]$. GB dislocation nucleation was modeled by setting up a bi-crystal nanowire containing a symmetrical tilt GB with the tilt axis of $[111]$, the GB plane of $(\bar{2}\bar{3}1)$ and the grain misorientation of 21.8° . This $[111]$ -tilt GB is selected as a representative GB of our $[111]$ -textured Au thin films. One of the grains in the bi-crystal nanowire has the same orientation and geometry as the single-crystal nanowire for surface dislocation nucleation, for proper comparison of both events. The FENEB calculations provide the minimum energy paths (MEPs) for the nucleation events, from which activation volume (V_{mod} , the slope of the activation energy, E_{act} , versus local resolved shear stress) can be obtained. Figure 2 shows the V_{mod} vs. E_{act} curves for four studied metals (Au, Al, Cu, Ni), for both surface dislocation nucleation (Figure 2A) and GB dislocation nucleation (Figure 2B). Both figures show that for the same activation energy, the corresponding activation volume decreases with

increasing shear modulus in Au, Cu, and Ni. To compare these atomistic results with our experimental results obtained under typical laboratory strain rate of 10^{-3}s^{-1} at room temperature, we need to look at the activation volumes corresponding to an activation energy of 0.7 eV (see dotted lines in Figure 2). For example, corresponding to $E_{\text{act}} = 0.7\text{eV}$, the activation volume V_{mod} increases from $20b^3$ for surface dislocation nucleation to $40b^3$ for GB dislocation nucleation in Au. Overall, a key finding from these FENEb results is that both surface and GB dislocation nucleation are associated with activation volumes larger than $20b^3$ for Au (corresponding to an activation energy of 0.7 eV).

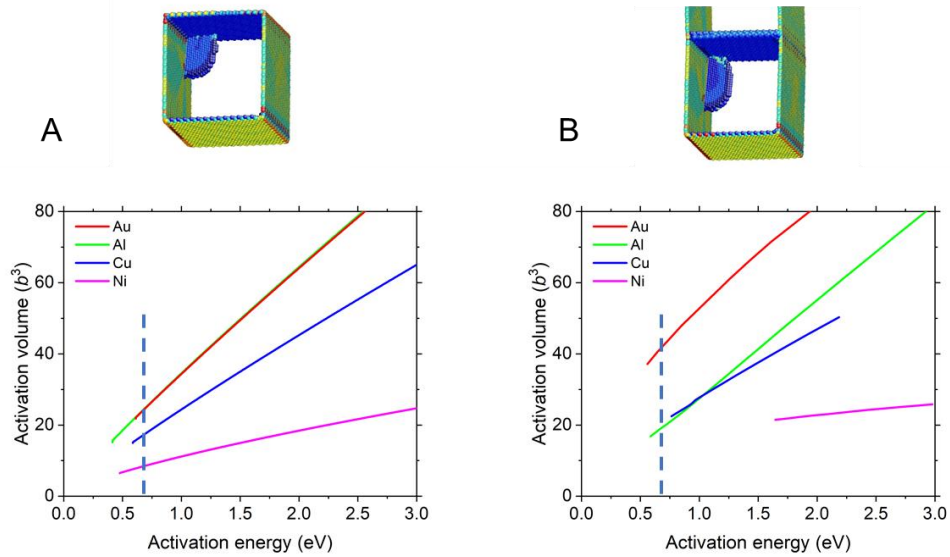


Figure 2. Comparison of activation volume vs activation energy in Au, Al, Cu and Ni based on our FENEb results [3]: (A) surface dislocation nucleation, and (B) GB dislocation nucleation. An activation energy of 0.7 eV (indicated by a blue dashed line) is used to determine the activation volumes to compare with our experimental values.

To compare our atomistically determined activation volumes with our experimentally measured values from polycrystalline specimens, it is necessary to account for the amplification of local stress at a GB (where the rate-controlling dislocation process is activated) relative to the applied stress on a polycrystal. To this end, we invoke the Conrad model giving a Hall-Petch-like relation of grain size dependent activation volumes [4,5]. This model evaluates the amplified local stress at the GB by considering the pileup of a dislocation array against this GB. Since the number of dislocations in the pileup is proportional to grain size, Conrad showed that the activation volume for a polycrystal exhibits a Hall-Petch like relation:

$$\frac{1}{V} = \frac{1}{V_i} + \frac{M^2 \mu b}{2\pi\alpha K_{\text{HP}} \sqrt{d}} \frac{1}{V_c} \quad (1)$$

where V_i is the activation volume of a rate-controlling process inside grains such as cutting of forest dislocations by glide dislocations, V_c is the activation volume of a rate-controlling process at GBs, $K_{\text{H-P}}$ is the Hall-Petch coefficient for characterizing the grain size dependence of yield stress, M is the Taylor factor, and α is the dimensionless parameter in the dislocation pileup model. Inside grains, V_i usually scales with lb^2 , where l is the average spacing between forest junctions obstructing glide dislocations. For a typical dislocation density of 10^{14} m^{-2} , $V_i = 500 b^3$. Based on this model, if GB dislocation nucleation is the rate limiting process, we expect V_c to be equal to V_{mod} from our FENEB calculations as shown earlier. For our Au specimens with an average grain size of 150 nm, Eq. (1) implies that the sample level V_{exp}^* should be significantly larger than $V_c = V_{\text{mod}}$ (obtained for the grain size of ~ 10 nm), given that $1/V_i$ is negligible. However, our experimental values (average $V_{\text{exp}}^* \sim 10b^3$; see Figure 1(b)) are lower than V_{mod} under experimental loading conditions ($20b^3$ for surface dislocation nucleation, $40b^3$ for GB dislocation nucleation; see Figure 2) even though the grain size is much larger than 10 nm. Hence, we conclude that the operation of other rate-controlling mechanisms with small activation volumes less than $10b^3$ is necessary to reconcile this discrepancy. We currently hypothesize that the operation of rate-controlling diffusive processes associated with GB disconnections would likely give small V_{mod} less than $10b^3$.

Future Plans

We plan to further investigate the activation energies and activation volumes associated with dislocation nucleation and slip transmission processes at different types of grain boundaries. We will select a few more representative types of general grain boundaries based on our experimental characterization results. These general grain boundaries can be the asymmetric tilt type (present in our Au thin films), and contain pre-existing intrinsic grain boundary dislocations, among others. We will perform atomistic FENEB calculations to understand the effects of these grain boundary structures and intrinsic grain boundary dislocations on E_{act} and V_{mod} of corresponding grain boundary dislocation processes. In addition, we plan to investigate the effects of grain size through dislocation pile-up on the modeled activation volume, so as to provide a direct assessment of the Conrad model of grain size-dependent activation volume.

We also plan on further investigating an expected transition between displacive GB mechanisms and diffusive ones, by exploring the deformation of the ufg Au films over a range of flow stress conditions. The flow stress will be experimentally controlled using three methods: varying the strain rates, varying the grain size, and introducing irradiation damage to harden the matrix. The measured V_{exp}^* will be compared to the atomistic results (V_{mod}) using Conrad's model. These results are expected to give a more unified view of the factors that govern transitions in deformation mechanisms at the micro and nanoscales.

References

1. S. Gupta, S. Stangebye, K. Jungjohann, B. Boyce, T. Zhu, J. Kacher, O.N. Pierron, *In situ TEM measurement of activation volume in ultrafine grained gold*, *Nanoscale* **12**(13) 7146-7158 (2020).
2. S. Stangebye, Y. Zhang, S. Gupta, T. Zhu, O. Pierron, and J. Kacher, *Understanding and quantifying electron beam effects during in situ TEM nanomechanical tensile testing on metal thin films*, *Acta Materialia*, **222**, 117441 (2022)
3. Y. Zhang, K. Ding, S. Stangebye, D. Chen, J. Kacher, O. Pierron, T. Zhu, *Atomistic modeling of surface and grain boundary dislocation nucleation in FCC metals*, *Acta Materialia*, **237**, 118155 (2022)
4. H. Conrad, *Grain size dependence of the plastic deformation kinetics in Cu*, *Materials Science and Engineering* **341**(1-2) 216-228 (2003)
5. H. Conrad, *Plastic deformation kinetics in nanocrystalline FCC metals based on the pile-up of dislocations*, *Nanotechnology* **18**(32) 325701 (2007)

Publications from past two years

1. S. Stangebye, Y. Zhang, S. Gupta, E. Hosseinian, C. Barr, K. Hattar, O. Pierron, T. Zhu, and J. Kacher, *Grain growth of nanocrystalline aluminum under tensile deformation: a combined in situ TEM and atomistic study*, *Materialia* **16**, 101068 (2021)
2. S. Stangebye, Y. Zhang, S. Gupta, T. Zhu, O. Pierron, and J. Kacher, *Understanding and quantifying electron beam effects during in situ TEM nanomechanical tensile testing on metal thin films*, *Acta Materialia*, **222**, 117441 (2022)
3. A. Barrios, Y. Zhang, E. Kakandar, X. Maeder, G. Castelluccio, O. Pierron, T. Zhu, *Abnormal grain growth in ultrafine grained Ni under cyclic loading*, *Scripta Materialia*, **209**, 114372 (2022)
4. Y. Zhang, K. Ding, S. Stangebye, D. Chen, J. Kacher, O. Pierron, T. Zhu, *Atomistic modeling of surface and grain boundary dislocation nucleation in FCC metals*, *Acta Materialia*, **237**, 118155 (2022)

NanoMechanics: Elasticity and Friction in Nano-Objects

Elisa Riedo, NYU Tandon School of Engineering

Keywords: nanomechanics, 2D Materials, graphene, 2D diamond, friction

Research Scope

A large scientific and technological effort is underway to investigate the properties of two-dimensional (2D) materials to become building blocks in integrated nano-electronic and photonic circuits, composites, coatings, energy harvesting nano-systems, nano-sensors, and nano-electro-mechanical systems (NEMS). While several experiments and calculations have revealed exciting novel phenomena in these nanostructures, many scientific and technological questions remain open. In particular, understanding and controlling the structure and mechanical properties of 2D materials at the interface with a solid surface is of key importance to enable the aforementioned nanotechnologies, as well as to fulfill the potential of strain engineering to tailor their properties. The vision of this DoE research program is to investigate novel mechanical properties and phenomena in 2D materials with the overarching goal of defining a new basic understanding of mechanical behavior in nano and quantum systems.

Recently, several experimental and theoretical scientists have started to study phase changing 2D materials, with a focus on the transformation of multi-layer graphene into a diamond-like structure induced by chemical functionalization of the graphene layers. In 2018, the PI's group and theoretical collaborators reported for the first time that under localized pressure, an atomically-thin (buffer layer plus one layer) graphene film grown on SiC(0001) behaves as a diamond-hard coating, exhibiting mechanical responses to nano-indentation similar or superior to those of bulk diamond [1-4]. Here, we propose a research program aimed at developing a new basic understanding of the mechanical properties of 2D materials at the interface with solid substrates, with a focus on pressure induced phase-changing 2D materials, and 2D material-substrate interfaces. Ultimately, we aim at developing the basic knowledge and experimental tools for manipulating 2D materials' structure, stacking, substrate interaction, defects, and number of layers to realize an entirely new class of ultra-hard, ultra-thin, and ultra-light active protective coatings with *ad-hoc* mechanical properties for a variety of applications.

Recent Progress

1. Interfacial Shear at the Atomic Scale in 2D Materials

Understanding the interfacial properties between an atomic layer and its substrate is of key interest at both the fundamental and technological level. From Fermi level pinning to strain engineering and superlubricity, the interaction between a single atomic layer and its substrate governs electronic, mechanical, and chemical properties. Here, we measure the hardly accessible interfacial transverse shear modulus of an atomic layer on a substrate (Figure 1). By performing measurements on bulk graphite, and epitaxial graphene films on SiC with different stacking order

and twisting, as well as in presence of intercalated hydrogen, we find that the interfacial transverse shear modulus is critically controlled by the stacking order and the atomic layer-substrate interaction. Importantly, we demonstrate that this modulus is a pivotal measurable property to control and predict sliding friction in supported two-dimensional materials. The experiments demonstrate a general universal reciprocal relationship between friction force per unit contact area and interfacial shear modulus (Figure 1b). The same relationship emerges from simulations with simple friction models (Figure 1c), where the atomic layer-substrate interaction controls the shear stiffness and therefore the resulting friction dissipation. These results can be generalized to other 2D materials and represent a new way to control atomic sliding friction, as well as to manipulate strain fields for band-structure engineering and photonics applications.

This work is in press in *Nature Nanotechnology* 2022.

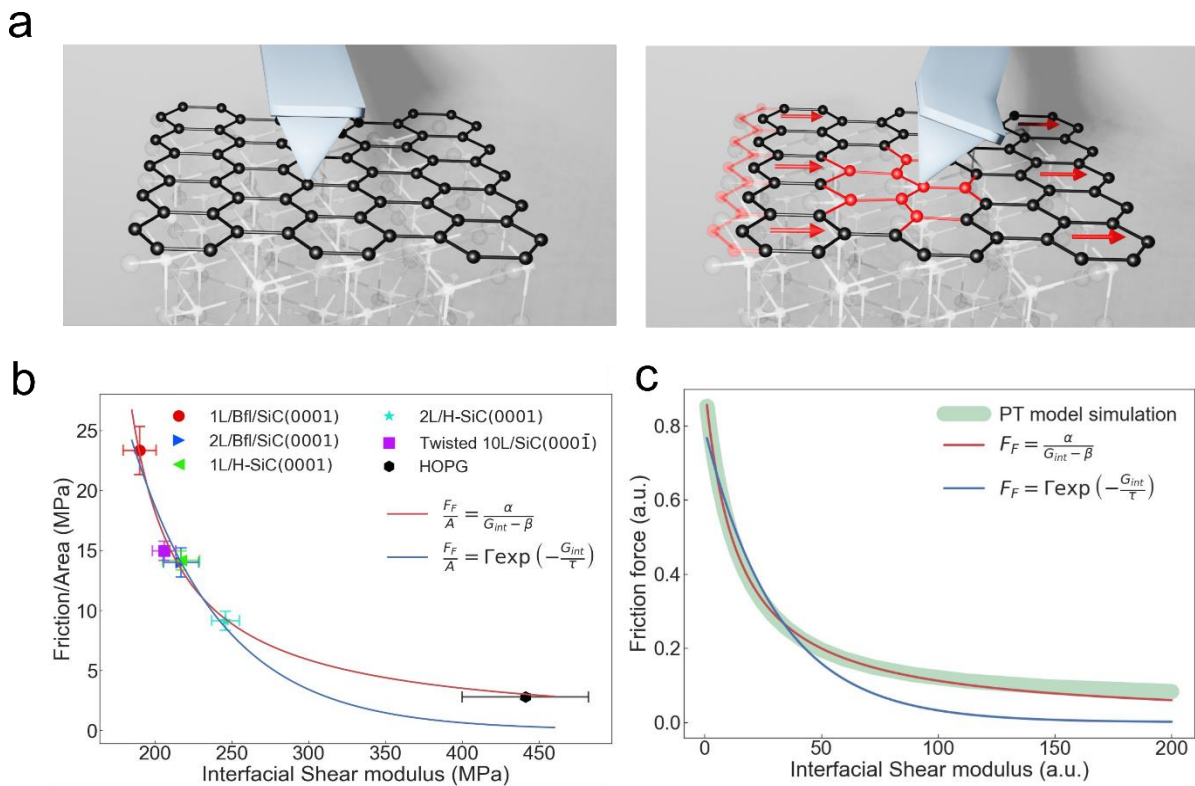


Figure 1: Relation between interfacial shear and friction force in 2D materials. **a)** Scheme of the interfacial shear modulus experiments. Initially, an AFM tip is brought into contact with a graphene layer sitting on a substrate. The AFM tip is then oscillated in-plane while in contact with the graphene surface, causing rigid moving of the graphene atomic layer in an elastic regime (no slipping). **b)** Experimentally measured friction force per unit contact area as a function of the measured interfacial transverse shear modulus for the different samples. The red solid line represents a two-parameter reciprocal function, while the blue solid line represents a two-parameter exponential decay function. **c)** Prandtl-Tomlinson simulations of friction force as a function of the interfacial shear modulus, and fitting functions. The red solid line represents a two-parameter reciprocal function, while the blue solid line represents a two-parameter exponential decay function.

3. Giant increase of hardness in silicon carbide by metastable single layer diamond

Silicon carbide (SiC) is one of the hardest known materials. Its exceptional mechanical properties combined with its high thermal conductivity make it a very attractive material for a variety of technological applications. Recently, it was discovered that two-layer epitaxial graphene films on SiC can undergo at room temperature a pressure activated phase transition into a sp^3 diamene structure. By using a Berkovich diamond indenter and nanoindentation experiments (Figure 2a), we show that epitaxial graphene films grown on SiC can increase the hardness of SiC up to 100% for low loads (up to 900 μN), and up to 30% for high loads (10 mN) (Figure 2b and 2c). We also demonstrate that the 30% increase in hardness is present even for indentations depths of 175 nm, almost three hundred times larger than the graphene film thickness. The experiments also show that the yield point of SiC increases up to 77% when the SiC surface is coated with epitaxial graphene (Figure 2d). These improved mechanical properties are explained with the formation of diamene under the indenter's pressure.

This work is under the second round of review in *Advanced Science*.

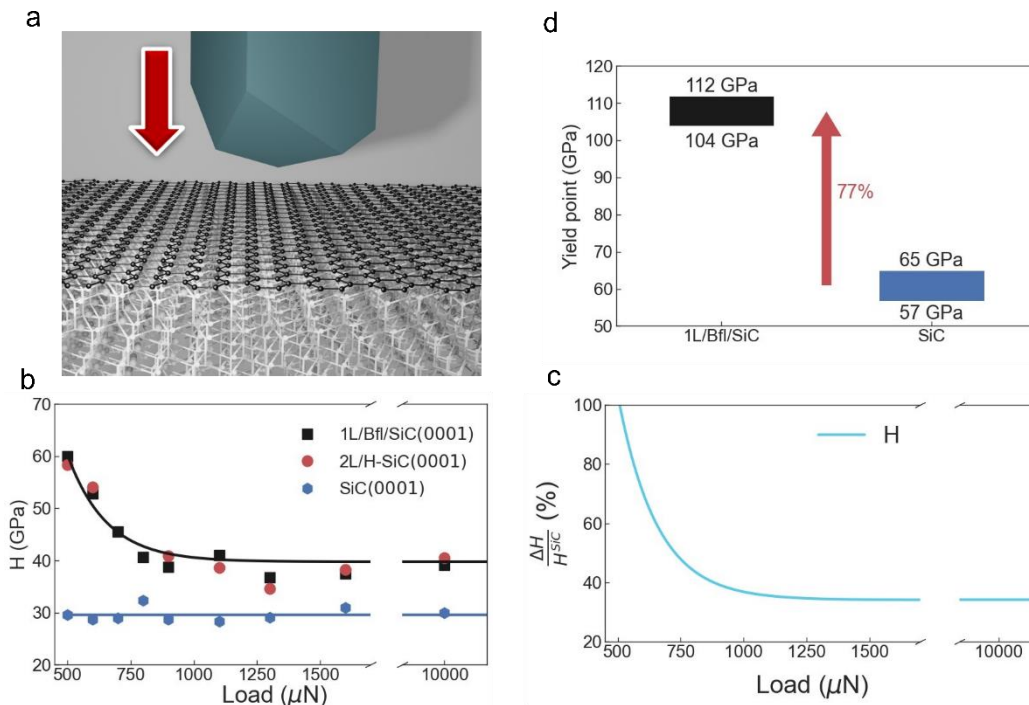


Figure 2: Giant increase of hardness in silicon carbide by metastable single layer diamond. a) Scheme of the nanoindentation experiments with a diamond Berkovich tip. **b)** Hardness dependency on the applied load for different samples. Experimental data are shown as markers and solid lines represent fit with an exponential decay function as a guide for the eye. **c)** The percentage change in hardness between graphene coated and bare SiC. **d)** Calculated yield point showing an increase of about 77% for 1L/Bfl/SiC sample compared to bare SiC.

3. Pressure-induced Formation and Mechanical Properties of 2D Diamond Boron Nitride

Understanding phase transformations in two dimensional (2D) materials can unlock unprecedented developments in nanotechnology, since their unique properties can be dramatically modified by external fields that control the phase change. Here, experiments and simulations are used to investigate the mechanical properties of a 2D diamond BN phase induced by applying local pressure on atomically thin h-BN on a SiO₂ substrate, at room temperature, and without chemical functionalization. Molecular dynamics (MD) simulations, performed by our collaborators at Sandia Labs, show a metastable local rearrangement of the h-BN atoms into diamond crystal clusters when increasing the indentation pressure. Raman spectroscopy experiments confirm the presence of a pressure-induced cubic BN phase, and its metastability upon release of pressure. Å-indentation experiments and simulations show that at pressures of 2 - 4 GPa, the indentation stiffness of monolayer h-BN on SiO₂ is the same of bare SiO₂, whereas for 2- and 3-layer-thick h-BN on SiO₂ the stiffness increases of up to 50% compared to bare SiO₂, and then it decreases when increasing the number of layers. Up to 4 GPa, the reduced strain in the layers closer to the substrate decreases the probability of the sp^2 -to- sp^3 phase transition, explaining the lower stiffness observed in thicker h-BN.

This research has been published as Cover Article in *Advanced Science* 2021.

Future Plans

(1) Quenching of Diamene Phase: FETs device fabrication and electrical experiments after large-area scan pressurization and stabilization of the diamene phase in 1LG and 2LG. Raman spectroscopy to investigate the quenched phase. Local rapid heating/cooling cycles to study the effect of local heating on the stabilization of the diamene phase, using in-situ thermal scanning probe lithography (tSPL) with 10-nm spatial resolution. Using pressure and heat, patterning of stabilized diamene regions within the surface of graphene films.

(2) Complete the experiments and simulations about the negative compressibility of diamene.

References

1. Y. Gao, T. Cao, F. Cellini, C. Berger, W. Heer, E. Tosatti, E. Riedo, A. Bongiorno "Ultra-hard carbon film from epitaxial two-layer graphene" *Nature Nanotechnology* 13, 133–138 (2018), doi:10.1038/s41565-017-0023-9
2. F. Cellini, Y. Gao, E Riedo, "Å-Indentation for non-destructive elastic moduli measurements of supported ultra-hard ultra-thin films and nanostructures", *Scientific Reports* 9, Article number: 4075 (2019) <https://doi.org/10.1038/s41598-019-40636-0>
3. F. Cellini, F. Lavini, C. Berger, W.d. Heer, E. Riedo, Layer dependence of graphene-diamene phase transition in epitaxial and exfoliated few-layer graphene using machine learning, *2D Materials*, doi:10.1088/2053-1583/ab1b9f, (2019).
4. Filippo Cellini, Francesco Lavini, Tengfei Cao, Walt de Heer, Claire Berger, Angelo Bongiorno, Elisa Riedo, "Epitaxial two-layer graphene under pressure: Diamene stiffer than Diamond" *FlatChem*, 10 8-13 (2018) doi.org/10.1016/j.flatc.2018.08.001

Publications

* indicates Riedo Contact Author

1. Martin Rejhon, Xinliu Zhou, Francesco Lavini, Alessandra Zanut, Filip Popovich, Lorenzo Schellack, Lukasz Witek, Paulo Coelho, Jan Kunc, and Elisa Riedo* “*Giant increase of hardness in silicon carbide by metastable single layer diamond*”, **Advanced Science** (2022), second round of review.
2. A. Zanut, M. Rejhon, G. de Peppo, E. Riedo*, "A polymer canvas with the stiffness of the bone matrix to study and control mesenchymal stem cell response" **Advanced Healthcare Materials** (2022), second round of review.
3. Martin Rejhon, Francesco Lavini, Ali Khosravi, Mykhailo Shestopalov, Jan Kunc, Erio Tosatti, Elisa Riedo*, “*Interfacial Shear at the Atomic Scale in 2D Materials*” **Nature Nanotechnology** (2022), in press.
4. F. Lavini, M. Rejhon, E. Riedo*, “*Two-dimensional diamonds from sp^2 -to- sp^3 phase transitions*”, **Nature Reviews Materials** (2022) doi.org/10.1038/s41578-022-00451-y
5. E. Albisetti, A. Calò, A. Zanut, E. Riedo* “*Thermal scanning probe lithography*”. **Nature Reviews Methods Primers** 2, 32 (2022). doi.org/10.1038/s43586-022-00110-0
6. F. Lavini, F. Cellini, E. Chen, A. Bongiorno, F. Popovic, R. Hartman, R. Dingreville, and E. Riedo*, “*Pressure-induced formation and mechanical properties of 2D diamond boron nitride*”, **Advanced Science** (2021) 8, 2002541, doi.org/10.1002/advs.202002541. (Cover Article)
7. Xiangyu Liu, Alessandra Zanut, Martina Sladkova-Faure, Liyuan Xie, Marcus Weck, Xiaorui Zheng, Elisa Riedo* and Giuseppe Maria de Peppo, “*Cost and Time Effective Lithography of Reusable Millimeter Size Bone Tissue Replicas With Sub-15 nm Feature Size on A Biocompatible Polymer*”, **Advanced Functional Materials** (2021) doi.org/10.1002/adfm.202008662 (Cover Article)
8. X. Liu, Z. Huang, X. Zheng, D. Shahrjerdi, and E. Riedo*, “*Nanofabrication of graphene field-effect transistors by thermal scanning probe lithography*”, **Applied Physics Letters Materials** 9 (1), 011107, (2021) doi.org/10.1063/5.0026159
9. X. Zheng, A. Calo, T. Cao, X. Liu, Z. Huang, P. M. Das, M. Drndic, C. Aruta, E. Albisetti, F. Lavini, T.-D. Li, V. Narang, W. King, J. Harrold, M. Vittadello, D. Shahrjerdi, E. Riedo*, “*Spatial Defects Nanoengineering for Bipolar Conductivity in MoS_2* ”, **Nature Communications** 11, 3463 (2020) <https://doi.org/10.1038/s41467-020-17241-1>
10. Francesco Lavini, Filippo Cellini, Martin Rejhon M, Jan Kunc, Claire Berger, Walt de Heer, and Elisa Riedo*, "Atomic Force Microscopy Phase Imaging of Epitaxial Graphene films", **Journal of Physics: Materials**. (2020) 3 024005. doi.org/10.1088/2515-7639/ab7a02

Damage-Tolerance in Structural Materials

Robert O. Ritchie, Mark Asta and Andrew M. Minor
Lawrence Berkeley National Laboratory

Keywords: High-entropy alloys, Deformation, Fracture, Toughness, Short-range order

Research Scope

The attainment of strength and toughness is a vital requirement for structural materials; unfortunately, these properties are often mutually exclusive. Indeed, the development of damage-tolerant materials has traditionally been a compromise between hardness *vs.* ductility. Using coupled theoretical and experimental approaches, we are examining strategies to solve this “conflict” in advanced metallic alloys by focusing on the interplay between the individual mechanisms that contribute to strength and toughness, that of plasticity and crack-tip shielding, noting that these phenomena may originate at different structural length-scales. Our central objective is to seek a fundamental understanding, at atomistic to near-macroscopic length-scales, of the scientific origins of damage-tolerance in multi-element metallic alloys. Our focus is currently on medium- and high-entropy alloys (M/HEAs), which can display excellent mechanical properties due to novel mechanisms arising from their disordered structures. With respect to damage-tolerance in face-centered cubic (*fcc*) CrCoNi-based high-entropy alloys, we have coupled fracture mechanics measurements with *in situ* SEM and TEM testing to discern the sequence of their deformation mechanisms that is responsible for their exceptional fracture resistance. We are also actively examining the existence, kinetics and role of local order in these alloys to confirm our first-principles simulations. We are also focusing on body-centered cubic (*bcc*) refractory high-entropy alloys (RHEAs) which are intended for ultrahigh-temperature applications but are often plagued by severe brittleness. Our ultimate aim is to uncover the relationships between atomic-scale phenomena and the macroscopic mechanical behavior of these structural materials.

Recent Progress

The two major highlights of our most recent work on the *fcc* M/HEAs pertain to their deformation and fracture behavior in extreme environments - at liquid He temperatures and at high strain rates, and the nature of local chemical ordering in these non-dilute solid solutions.

CrCoNi-based alloys are known to display outstanding tensile strength and ductility with exceptional fracture toughness,¹ properties which we have shown to be progressively enhanced at cryogenic temperatures due to the activation of multiple plastic deformation mechanisms. To examine this further, we measured their mechanical properties, in particular their fracture toughness and crack-resistance curve (R-curve) behavior, under quasi-static strain rates in a liquid helium environment. Specifically, we performed *J*-based fracture-mechanics R-curve measurements on the *fcc* equiatomic CrCoNi and CrMnFeCoNi alloys at temperatures of 20K.

At tensile strengths of ~ 1.5 GPa, crack-initiation K_{JIC} fracture toughnesses were found to be exceptionally high, respectively 262 and 459 $\text{MPa}\sqrt{\text{m}}$ for CrMnFeCoNi and CrCoNi, with the latter alloy displaying a crack-growth toughness $K_{SS} > 540 \text{ MPa}\sqrt{\text{m}}$ after ~ 2.25 mm of stable cracking (Fig. 1). Indeed, we believe that the CrCoNi alloy possesses the highest fracture toughness on record. 4D-STEM electron microscopy characterization of the crack-tip regions showed deformation structures quite distinct from that at higher temperatures, involving heterogeneous nucleation, but restricted growth, of stacking faults and very fine nano-twins, together with relatively limited transformation to hexagonal closed-packed (*hcp*) ϵ -martensite – the restriction in growth of these features was suggested to be due to known effects of short-range order on limiting interface motion. Combined with the lower dislocation density and suppressed dynamic recovery at these low temperatures, a synergy of deformation mechanisms, including glide, nano-twinning, stacking fault formation and transformation-induced plasticity, is created at increasing strain levels, which presents a highly efficient process for developing and prolonging strain hardening to restrict the localization of deformation in the crack-tip region, all of which results in exceptional toughness.

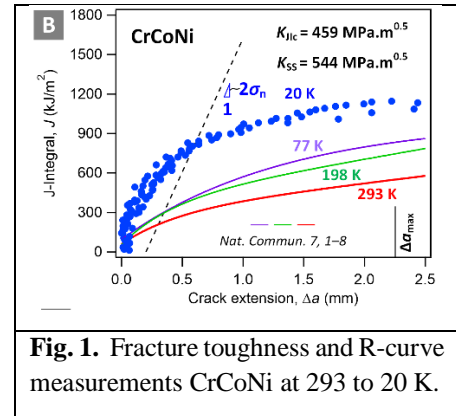


Fig. 1. Fracture toughness and R-curve measurements CrCoNi at 293 to 20 K.

We also found a dramatic enhancement in strength and toughness in the CrMnFeCoNi HEA with severe plastic deformation using dynamic shear testing at very high strain rates, *i.e.*, at $6 \times 10^5 \text{ s}^{-1}$, some 8 orders of magnitude higher than quasi-static.² Under these conditions, we observed a dense structure comprising stacking faults, twins, transformation to the *hcp* phase, and most notably amorphous regions. The coordinated propagation of stacking faults and twins along $\{111\}$ planes engender high-deformation regions which can reorganize into *hcp* packets, and at high defect densities generate islands of amorphous material. The result was tensile strengths in this HEA as high as 4 GPa and toughnesses (absorbed deviatoric strain energies) higher than all comparable traditional alloys.

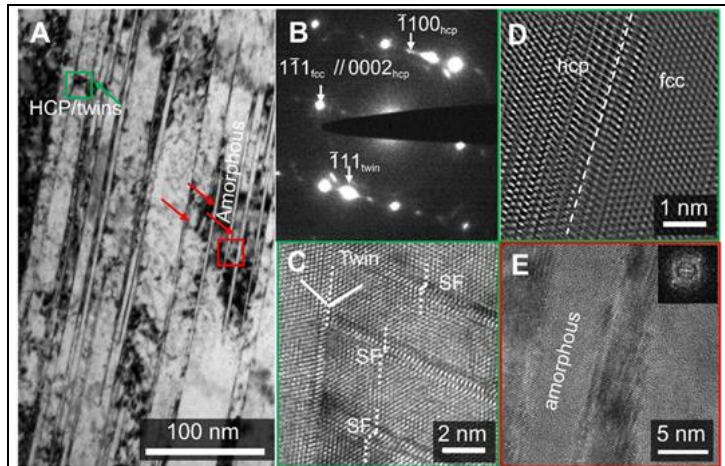


Fig. 2. Deformation microstructure of CrMnFeCoNi subjected to dynamic compression/shear: (a) Bright-field image of the twins, stacking faults, *hcp* phase and amorphous bands; (b) selected area electron diffraction pattern shows the existence of the *fcc* matrix, twinning and *hcp* reflections. (c) Co-existence of nanoscale twins and stacking faults; (d) Fourier-filtered lattice image of the *hcp/fcc*; (e) amorphous bands (red square in a) and corresponding Fast Fourier Transformed (FFT) diffractograph.

One particularly fascinating aspect of these presumed random solid-solution alloys is the presence of local short-range order (SRO). Following predictions from density functional theory (DFT)-

based Monte Carlo simulations,³ we provided direct experimental evidence for the existence of SRO in CrCoNi using energy-filtered transmission electron microscopy (TEM), where its occurrence was concomitant with an increase in the stacking-fault energy, a transition in slip mode from wavy to planar slip, and changes in mechanical properties.⁴ To further examine the latter issue, we subsequently investigated the role of SRO in influencing mechanical properties in CrCoNi by bulk tensile tests and nanoindentation after different annealing treatments.⁵ While bulk mechanical properties were unaffected, nanoindentation tests revealed notable differences, as indicated by an increase in the load at first pop-in associated with the onset of plasticity from the homogeneous nucleation of dislocations. Energy-filtered TEM revealed the presence of diffuse intensity in electron diffraction patterns, even in splat-quenched samples, although a much higher diffuse intensity was detected after aging, peaking in the 900°C aged sample. Although we are still uncertain as to the exact atomistic structural origin of this diffuse intensity, and what it implies for the nature of the SRO in these alloys, our studies suggest that it is ubiquitous and indicates local structural ordering or distortions that may play a critical role in “catalyzing” the synergist sequence of deformation mechanisms that creates prolonged strain hardening in CrCoNi-based M/HEAs, which is the basis of their exceptional toughness.

Future Plans

In addition to our continuing studies on the nature, kinetics and mechanistic role of SRO in the *fcc* HEAs, we are currently focusing on the *bcc* refractory HEAs which present exciting possibilities for the development of ultrahigh-temperature structural materials. However, they often suffer from low *tensile* ductility and poor oxidation resistance. We are currently investigating two RHEAs, MoNbTaW and NbTaTiHf(Zr), which represent extremes of behavior – the former alloy displays very high strength at high temperature but is very brittle, while the latter is a somewhat lower strength alloy but can display remarkable ductility and even toughness.

Our approach to the technological ductility/toughness challenge is to gain a fundamental understanding of the ductile-to-brittle transition in these alloys through atomistic simulations and a comprehensive assessment of their deformation and fracture mechanisms *under tensile loading* at nano- to macro-scales (the community has largely focused on compression testing to date which can mask the extreme lack of damage-tolerance in these RHEAs). As these alloys invariably fail by intergranular fracture at high temperatures, grain boundaries are clearly critical as they can lead to a dramatic reduction in fracture toughness due to segregation of multiple alloying elements, the resulting formation of new grain-boundary structures or complexions, the precipitation of intergranular nitrides and carbides, and consequent high-temperature stress-corrosion/creep mechanisms.

Our objective is to mechanically characterize the mechanical behavior of these RHEAs at multiple length-scales coupled with TEM and 4D-STEM structural characterization to provide input to atomistic simulations of fracture, segregation and grain-boundary structure in an attempt to identify and model the salient phenomena underlying their damage-tolerance at both low and high

temperatures. The latter will build upon our previous work^{6,7} employing DFT and molecular dynamics calculations, including in the development of machine-learning potentials, to investigate the energetic landscape underlying dislocation motion and how it is affected by SRO in the *bcc* alloys (Fig. 3). Through this combined experimental and computational approach, we plan to identify the prime origins of the lack of tensile ductility and toughness in most RHEAs, yet at the same time discern why certain compositions, such as NbTaTiHf(Zr), can exhibit unusual ductility and toughness even at cryogenic temperatures.

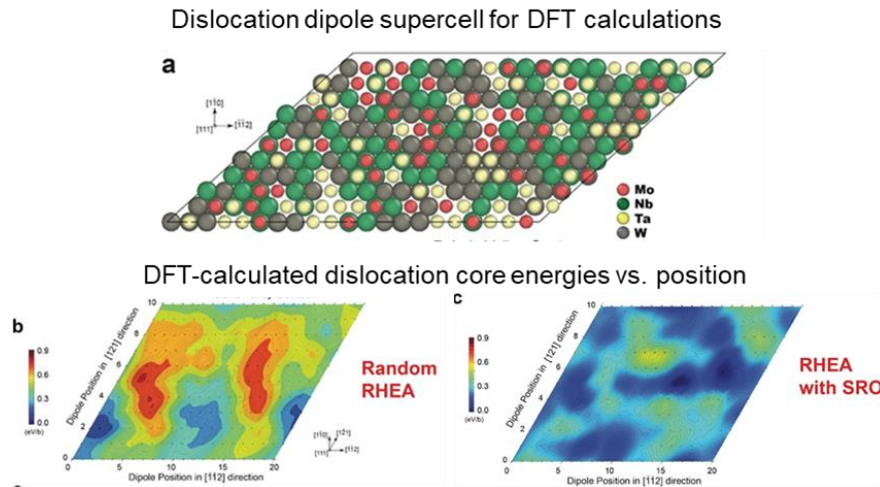


Fig. 3. DFT calculations of the energy landscape for a screw dislocation dipole in a MoNbTaW alloy. (a) A representative 462 atom supercell used to compute the energy of screw dislocation dipoles by DFT. Energy landscapes derived by moving the center of the dislocation dipole to all possible locations within the supercell for an alloy with (b) random configurational disorder and with (c) short-range order derived from DFT-Monte-Carlo simulations.⁶

References

1. B. Gludovatz, A. Hohenwarter, D. Catoor, E. H. Chang, E. P. George, R. O. Ritchie, *A fracture resistant high-entropy alloy for cryogenic applications*, *Science*, **345**, 1153 (2014).
2. S. T. Zhao, Z. Z. Li, C. Y. Zhu, W. Yang, Z. R. Zhang, D. E. J. Armstrong, P. S. Grant, R. O. Ritchie, M. A. Meyers, *Amorphization in extreme deformation of the CrMnFeCoNi high-entropy alloy*, *Science Advances* **7**, eabb3108 (2021).
3. J. Ding, Q. Yu, M. Asta, R. O. Ritchie, *Tunable stacking fault energies by tailoring local chemical order in CrCoNi medium-entropy alloys*, *PNAS* **115**, 8919 (2018).
4. R. P. Zhang, S. T. Zhao, J. Ding, Y. Chong, T. Jia, C. Ophus, M. Asta, R. O. Ritchie, A. M. Minor, *Short-range order and its impact on the CrCoNi medium-entropy alloy*, *Nature* **581**, 283 (2020).
5. M. Zhang, Q. Yu, C. Frey, F. Walsh, M. I. Payne, P. Kumar, D. Liu, T. M. Pollock, M. Asta, R. O. Ritchie, A. M. Minor, *Determination of peak ordering in the CrCoNi medium-entropy alloy via nanoindentation*, *Acta Materialia*, **241**, 118380 (2022).
6. S. Yin, J. Ding, M. Asta, R. O. Ritchie, *Ab initio modeling of the energy landscape for screw dislocations in body-centered cubic high-entropy alloys*, *npj Computational Materials* **6**, 110 (2020).
7. S. Yin, Y. Zuo, A. Abu-Odeh, H. Zheng, X.-G. Li, J. Ding, S. P. Ong, M. Asta, R. O. Ritchie, *Atomistic simulations of dislocation mobility in refractory high-entropy alloys and the effect of chemical short-range order*, *Nature Communications* **12**, 4873 (2021).

Publications

1. S. Yin, J. Ding, M. Asta, R. O. Ritchie, *Ab initio modeling of the energy landscape for screw dislocations in body-centered cubic high-entropy alloys*, npj Computational Materials **6**, 110 (2020). doi.org/10.1038/s41524-020-00377-5.
2. J. Rackwitz, Q. Yu, Y. Yang, G. Laplanche, E. P. George, A. M. Minor, R. O. Ritchie, *Effects of cryogenic temperature and grain size on fatigue-crack propagation in the medium-entropy CrCoNi alloy*, Acta Materialia **200**, 351 (2020). doi.org/10.1016/j.actamat.2020.09.021
3. R. P. Zhang, S. T. Zhao, J. Ding, Y. Chong, T. Jia, C. Ophus, M. Asta, R. O. Ritchie, A. M. Minor, *Short-range order and its impact on the CrCoNi medium-entropy alloy*, Nature **581**, 283 (2020). doi.org/10.1038/s41586-020-2275-z
4. R. O. Ritchie, *Toughening materials: Enhancing resistance to fracture*, Philosophical Transactions of the Royal Society A-Mathematical Physical and Engineering Sciences **379**, 20200437 (2021). doi.org/10.1098/rsta.2020.0437.
5. S. Yin, Y. X. Zuo, A. Abu-Odeh, H. Zheng, X. G. Li, J. Ding, S. P. Ong, M. Asta, R. O. Ritchie, *Atomistic simulations of dislocation mobility in refractory high-entropy alloys and the effect of chemical short-range order*, Nature Communications **12**, 4873 (2021). doi.org/10.1038/s41467-021-25134-0
6. S. T. Zhao, Z. Z. Li, C. Y. Zhu, W. Yang, Z. R. Zhang, D. E. J. Armstrong, P. S. Grant, R. O. Ritchie, M. A. Meyers, *Amorphization in extreme deformation of the CrMnFeCoNi high-entropy alloy*, Science Advances **7**, eabb3108 (2021). doi.org/10.1126/sciadv.abb3108
7. J. Ding, L. Li, N. Wang, L. Tian, M. Asta, R. O. Ritchie, T. Egami, *Universal nature of the saddle states of structural excitations in metallic glasses*, Materials Today Physics **17**, 1000359 (2021). doi.org/10.1016/j.mtphys.2021.100359.
8. F. Walsh, M. Asta, R. O. Ritchie, *Magnetically driven short-range order can explain anomalous measurements in CrCoNi*, Proceedings of the National Academy of Sciences of the United States of America **118**, e2020540118 (2021). doi.org/10.1073/pnas.2020540118
9. M. Zhang, Q. Yu, C. Frey, F. Walsh; M. I. Payne, P. Kumar, D. Liu, T. M. Pollock, M. Asta, R. O. Ritchie, A. M. Minor, *Determination of peak ordering in the CrCoNi medium-entropy alloy via nanoindentation*, Acta Materialia, 241, 118380 (2022). doi.org/10.1016/j.actamat.2022.118380.
10. D. Liu, Q. Yu, S. Kabra, M. Jiang, P. Forna-Kreutzer, R. Zhang, M. Payne, F. Walsh, B. Gludovatz, M. Asta, A. M. Minor, E. P. George, R. O. Ritchie, *Exceptional fracture toughness of CrCoNi-based medium- and high-entropy alloys at 20 K*, Science (2022) accepted for publication. <http://arxiv.org/abs/2204.01635>.
11. P. Kumar, S. J. Kim, Q. Yu, J. Ell, M. Zhang, Y. Yang, J. Young Kim, H.-K. Park, A. M. Minor, E. S. Park, R. O. Ritchie. *Compressive vs. tensile yield and fracture toughness behavior of a body-centered cubic refractory high-entropy superalloy Al_{0.5}Nb_{1.25}Ta_{1.25}TiZr at temperatures from ambient to 1200°C*, Acta Materialia, resubmitted after favorable review, Oct. 2022.

Improving Interfacial Damage Tolerance with Amorphous Complexion Transitions

Timothy J. Rupert - University of California, Irvine

Keywords: complexions, grain boundaries, nanocrystalline, interfacial engineering

Research Scope

Grain boundaries are ubiquitous microstructural features which often act as failure nucleation sites during plastic deformation. This project aims to understand how dopant-induced transitions to thermodynamically-distinct grain boundary states, known as *complexions*, can be used to toughen these critical weak points. Specifically, we focus on nanocrystalline metals, as these materials are notorious for failing prematurely, which contain amorphous grain boundary complexions, as these features are hypothesized to be particularly damage-tolerant. Our primary focus is on mechanical damage due to dislocation-based plasticity, although we pursue some limited avenues of investigating the ability of amorphous complexions to act as point defect sinks as well. The objective of this research is to understand how fundamental descriptors of individual complexions and the network they form within the microstructure determine damage tolerance.

Recent Progress

The description of our progress is organized based on three core hypotheses: (1) Amorphous complexions can increase the ductility of a range of nanostructured alloys. (2) Amorphous complexion thickness and number fraction can be increased, leading to improvements in damage tolerance. (3) Local structural order and chemical composition act as internal descriptors that can be used to tailor the damage tolerance of individual complexions.

Amorphous complexions improve nanocrystalline plasticity

The need for clear evidence of amorphous complexions leading to increased ductility led us to perform in situ scanning electron microscopy tensile testing, with results from samples with and without amorphous complexions shown in Fig. 1. Testing in situ allowed local strains to be mapped to understand the exact failure modes. The ordered grain boundary specimens exhibit failure that is typical of “normal” nanocrystalline metals, with small cross-sectional area reductions and intense localization of plastic strain. In contrast, the sample with amorphous complexions demonstrates roughly twice the ductility in terms of area reduction and also experienced a homogeneous strain distribution along the gauge length, providing definitive proof that amorphous complexions can significantly increase the ductility of nanocrystalline metals.

To demonstrate that a wide range of material systems can be toughened with amorphous complexions, we have been investigating nanocrystalline Al- and Fe- alloys. Fig. 2(a) shows three binary Al-rich alloys that demonstrate varying abilities to host amorphous complexions. Al-Ni is similar to Cu-Zr, in that amorphous complexions are found when the alloy is rapidly quenched but not if the sample is slowly cooled. In contrast, Al-Y can host amorphous complexions even if slowly cooled, with faster quenching freezing in thicker complexions, while no amorphous

complexions are found in Al-Mg. Preliminary data for Fe-Zr also suggests that amorphous complexions are present. The stabilization of grain size by these complexions also means that bulk specimens can be made from the alloys, with examples of Al-, Cu-, and Fe-rich samples shown in Fig. 1(b), enabling the testing of bulk properties. Fig. 1(c) shows bulk compression tests of Cu-Zr and Al-Ni-Y, where very high strengths and good plasticity are evident.

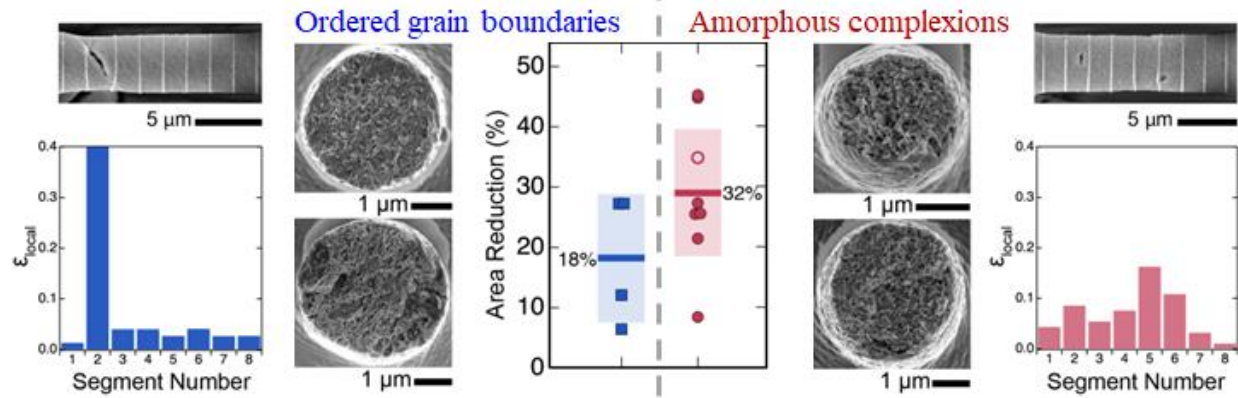


Figure 1. Tensile testing results for nanocrystalline Cu-Zr with only ordered grain boundaries (left) and samples containing amorphous complexions (right). A large increase in ductility and decrease in strain localization is observed when amorphous complexions are present.

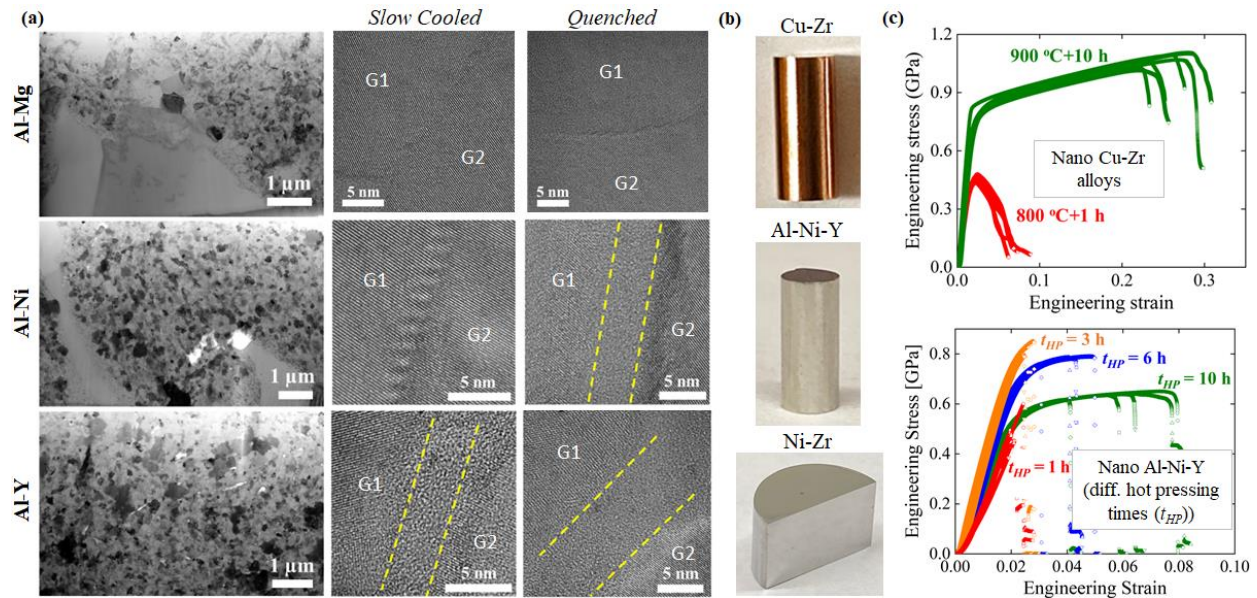


Figure 2. (a) Three binary Al-rich alloys demonstrate how amorphous complexions can be stabilized to different degrees in a new base metal system. (b) Bulk samples with nanocrystalline grains between 20-50 nm can be fabricated due to amorphous complexion stabilization of the grain structure. (c) Preliminary bulk compression tests show that high strength and good plasticity can be achieved in Cu- and Al-rich nanocrystalline alloys.

Network descriptors: Complexion thickness and transformed fraction

Complexion thickness distribution and the fraction of boundaries which have transformed to amorphous complexions refer to the complexion population present in the material, serving as descriptors of the overall interfacial network. Controlled cooling experiments on bulk samples with a heat sink on one side were used to induce a gradient in quenching rates, with faster cooling

resulting in thicker complexion distributions (Figs. 3(a) and (b)). Slow cooling allows some of the interfaces which are amorphous at high temperature to revert back into ordered grain boundaries. Alloy complexity was also investigated, with the complexion thickness distributions in Fig. 3(c) showing that having more elemental variety in the grain boundary region results in thicker amorphous complexions. The fraction of boundaries that are a given complexion type is often an intractable experimental problem, yet atomistic models of polycrystalline grain structures can provide a bridge to understand this descriptor. Fig. 3(d) shows that the measurement of a thicker amorphous complexion distribution also means that a higher fraction of interfaces are amorphous. Hence, the two metrics of complexion thickness and fraction are intimately coupled, with faster cooling and increased grain boundary compositional complexity resulting in increases to both.

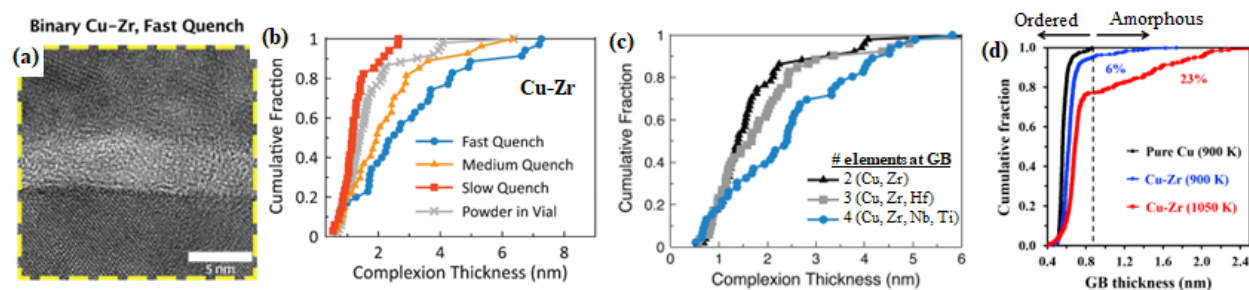


Figure 3. (a, b) Faster quenching results in the complexion thickness distribution shifting further to the right, toward thicker values. (c) Comparison of different alloys shows that increased grain boundary chemical complexity leads to a thicker amorphous complexion distribution. (d) Atomistic modeling shows that an increase in complexion thickness distribution also means an increase in the fraction of transformed boundaries, linking these two critical descriptors.

Armed with ways of altering the complexion network, we have subsequently moved to testing that increases in complexion thickness and/or fraction will increase an interface's damage tolerance. We have been studying the ability of a complexion to absorb point defects as part of a new collaboration with Prof. Janelle Wharry, also a PI in this program. Atomistic simulations of collision cascades near different interface types confirm that amorphous complexions are efficient point defect sinks, whether at a Cu-Cu grain boundary or at a Cu-Ta phase boundary, with a stronger effect observed as complexion thickness is increased.

Internal descriptors: Local structure and chemistry

An individual amorphous complexion can be characterized in terms of its local structure and chemistry, marking another set of important descriptors that are hypothesized to impact damage tolerance. We began our study of this topic by looking at structural SRO, generally defined in terms of local atomic packing motifs. Metallic glasses serve as an important comparison, where disordered Voronoi polyhedra are the most common motif (Fig. 4(a)). The interior of an amorphous complexion has a similar structure, but there are importance deviations where the complexion meets the grains in a region that can be called the amorphous-crystalline transition region (ACTR). In these regions, the most common atomic packing motifs are ordered Voronoi polyhedra that are only slightly different than the perfect face-centered cubic structure. Atomistic modeling shows us that ACTR structure can vary a great deal between different complexions and even between the two sides of an individual complexion. While it would seem logical that this

structure was determined by the constraint nearest grain, more detailed analysis shows that the entire grain-film-grain system must be considered to understand asymmetries in the SRO. The grain boundary strain, here quantified as the percentage of atoms in the nearby crystal with free volume and serving as a measure of the incompatibility between the grains prior to the complexion transition, is found to determine the ordered SRO density difference between the two ACTRs (Fig. 4(b)). Preliminary simulations (Fig. 4(c)) show that these spatial patterns in SRO determine a complexion's ability to absorb dislocations without nucleating cracks/voids, as it is beneficial to have the material through the entire complexion deforming to accommodate the plastic strain over a larger volume of material. Another important effect is that plasticity can be activated in the neighboring grain under certain conditions, reducing strain localization within the complexion.

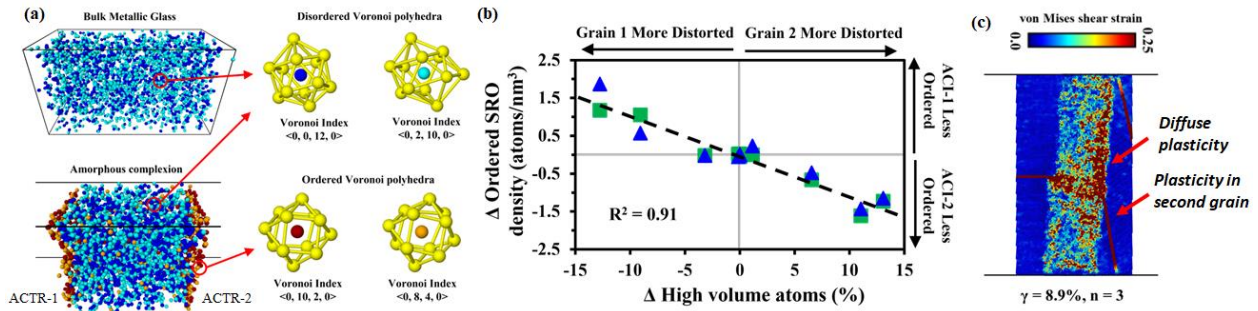


Figure 4. (a) Ordered SRO motifs decorate the ACTRs, while disordered SRO motifs are more common in the complexion interior. (b) The difference between ACTR SRO can be predicted by looking at the grain boundary strain, or incompatibility of the initial bicrystal prior to transition, showing that the entire grain-film-grain system must be considered. (c) SRO distribution within the complexion can cause diffuse plasticity and flow transfer into neighboring grains.

Preliminary high resolution transmission electron microscopy results have shown that Nb and Ti in a Cu-Zr-Nb-Ti alloy have their highest concentrations at the ACTRs. These elements prefer to form ordered grain boundaries when studied by themselves in Cu-rich binary alloys, leading to the conclusion that they prefer ordered structural motifs such as those found in the ACTRs. We find a similar maximum local enrichment of Ni at the ACTRs in nanocrystalline Al-Ni and Al-Ni-Y. It is becoming clear that local chemical composition is coupled to complexion structure.

Future Plans

In the next year, we will investigate the mechanical damage tolerance of Cu-rich alloys as a function of complexion thickness/fraction by probing the interfacial populations shown in Fig. 3 with micropillar compression experiments. In addition, we will study bulk plasticity in Al, Fe, and Cu alloys, to understand if differences in crystal structure and second phase precipitation can modify the beneficial effects of amorphous complexions. We will work to characterize SRO distributions in our real world alloys using 4D-STEM nanodiffraction. Specific challenges in this area include complications from overlapping grains in a nanocrystalline grain structure and difficulties in interpreting the local diffraction patterns. Novel sample geometries will be created for the prior, while atomistic models and pattern matching algorithms will allow us to address the latter. In addition, we will complete a study of local composition in amorphous complexions, building on our preliminary results to obtain statistically significant collections of data.

Publications (July 2020 - July 2022)

PUBLISHED:

1. M.J. McCarthy and T.J. Rupert, *Alloying induces directionally-dependent mobility and alters migration mechanisms of faceted grain boundaries,* Scripta Materialia, **194**, 113643, (2021).
2. C.M. Grigorian and T.J. Rupert, *Critical cooling rates for amorphous-to-ordered complexion transitions in Cu-rich nanocrystalline alloys,* Acta Materialia, **206**, 116650, (2021).
3. G.H. Balbus, J. Kappacher, D.J. Sprouster, F. Wang, J. Shin, Y.M. Eggeler, T.J. Rupert, J.R. Trelewicz, D. Kiener, V. Maier-Kiener, and D.S. Gianola, *Disordered interfaces enable high temperature thermal stability and strength in a nanocrystalline aluminum alloy,* Acta Materialia, **215**, 116973, (2021).
4. J.L. Wardini, C.M. Grigorian, and T.J. Rupert, *Amorphous complexions alter the tensile failure of nanocrystalline Cu-Zr,* Materialia, **17**, 101134, (2021).
5. P. Garg, Z. Pan, V. Turlo, and T.J. Rupert, *Segregation competition and complexion coexistence within a polycrystalline grain boundary network,* Acta Materialia, **218**, 117213, (2021).
6. C.M. Grigorian and T.J. Rupert, *Multi-principal element grain boundaries: Stabilizing nanocrystalline grains with thick amorphous complexions,* Journal of Materials Research, **37**, 554, (2022).

UNDER REVIEW:

1. Garg P, Rupert TJ, *Grain incompatibility determines the local structure of amorphous grain boundary complexions,* Acta Materialia, (reviews received, under revision).

Segregation and Shear Localization in Nanocrystalline Alloys

Frederic Sansoz

Department of Mechanical Engineering, The University of Vermont, Burlington VT (USA)

Keywords: Nanocrystalline alloys, GB segregation, strain localization, atomistic simulation, in-situ tensile SEM

Research Scope

Over the past decade, considerable research effort has been focused on the role of solute segregation in stabilizing nanoscale interfaces to harden metals at near-ideal Hall-Petch strength limits, through extreme grain refinement ($d \leq 50$ nm). Inevitably, grain boundary (GB) segregation is also associated with a significant deterioration of tensile ductility in nanocrystalline (nc) alloys that generally exhibit poor uniform plastic elongations below 2%. The segregation-induced ductile-to-brittle transition is well-understood in terms of two dominant deformation mechanisms at interfaces: GB embrittlement accelerating intergranular cracking, and glass-like shear localization leading to catastrophic shear banding. The proposed research aims to deploy state-of-the-art atomistic simulations and in-situ experimental studies to fundamentally understand GB solute segregation and shear localization mechanisms in binary nc Ag-Ni alloys that have not been well studied so far, as well as other nc alloys (Ag-Cu, Al-Ni, Nb-Ni and Zr-Ni) exhibiting a range of alternative segregation mechanisms. Ag-Ni alloys are of interest because past theoretical models [1] have predicted that the GB segregation behavior in these materials is intrinsically *heterogeneous*. Heterogeneous segregation is a unique behavior where solute atoms cluster along some GB regions, whereas other GB regions are left solute free. This phenomenon was also observed experimentally by others in Pt-Au alloys [2]. The ultimate goal is to advance the design of nanocrystalline alloys with new strain de-localization mechanisms induced by heterogeneous segregation that can potentially suppress GB segregation embrittlement.

Recent Progress

Roles of GB stress concentrations on segregation-induced GB-plasticity and cracking.

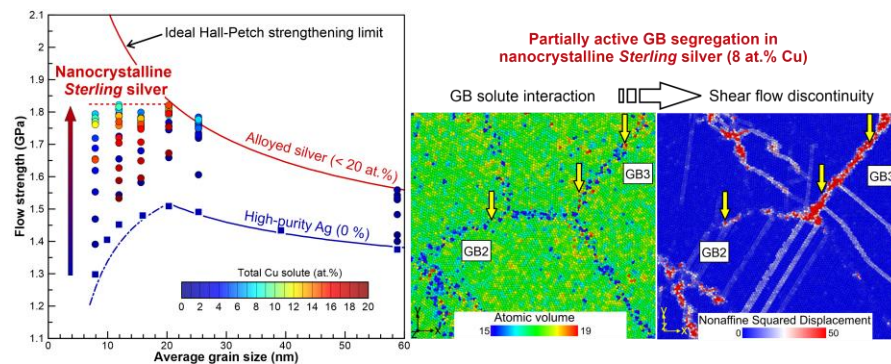


Figure 1. Hybrid Monte-Carlo and molecular dynamics (MC/MD) simulations of partially active GB segregation mechanism discovered in nc Ag-Cu alloys, termed as nc *Sterling silver*, which resulted in shear flow discontinuity and GB stress concentrations that limited the Hall-Petch strengthening effect.

Using atomistic simulations, we first studied the strength and mechanisms of GB plasticity and GB stress concentrations in columnar-grained FCC metals commonly synthesized by sputter-deposition technique. It was found that the dislocation mechanisms are the same for all FCC metals with columnar grain morphology, but most of the strengthening effects observed could be

rationalized through differences in local stress concentrations during tensile deformation. Specifically, prominent GB stress concentration and void growth at GB-twin triple junctions was found to induce a strength limit in nano-twinned Ni associated with columnar GB cracking. While focused exclusively on pure metals, this early study pointed at the important roles of GB stress concentrations and GB triple-junction plasticity on GB embrittlement in nanostructured metals.

This hypothesis was later confirmed by our team in a systematic study of the Hall-Petch breakdown in Cu-segregated Ag alloys, where three concentration-dependent regimes of plasticity were found: (1) Classical segregation strengthening behavior at low solute contents, (2) shear band-induced softening at high solute contents, and (3) a previously unknown, but extended plateau of maximum strengths for intermediate solute contents from 4 at.% to 15 at.%, which we term as nanocrystalline *Sterling* silver. Fig. 1 shows that flow strengths in nc *Sterling* alloys naturally exhibited a maximum limit at the smallest grain sizes that is well below the ideal Hall-Petch strengthening trend, because of partially active GB segregation that acted to influence interfacial plasticity in some, but not all, GB regions. This previously unknown mechanism arises from inhomogeneous Cu clustering as the local solute content exceeds the dilute limit (4-6 at.% for a 6-nm grain size). *These findings amplified the atomic nature of solute segregation and interaction at GBs and its complex roles on GB-mediated plasticity mechanisms in nc alloys.*

Ni Solute Segregation and Associated Plasticity Mechanisms in Random FCC Ag, BCC Nb and HCP Zr Polycrystals. Atomistic simulation results in Fig. 2(a) revealed that heterogeneous Ni segregation in nc Ag-Ni alloys dramatically shuts down localized shear bands during plastic deformation, while simultaneously increasing the tensile strength. In stark contrast, nc Cu-segregated Ag metals were predicted to exhibit standard homogeneous Cu segregation and a tensile strength that saturates above a solute concentration of 8 at.% due to glass-like shear localization induced by GBs. It was found that heterogeneous Ni segregation in nc Ag-Ni alloys forms Ni-rich amorphous clusters along interfaces and triple junctions, leading to strain delocalization at high strain and continuous strengthening at high solute concentrations up to 15 at.%.

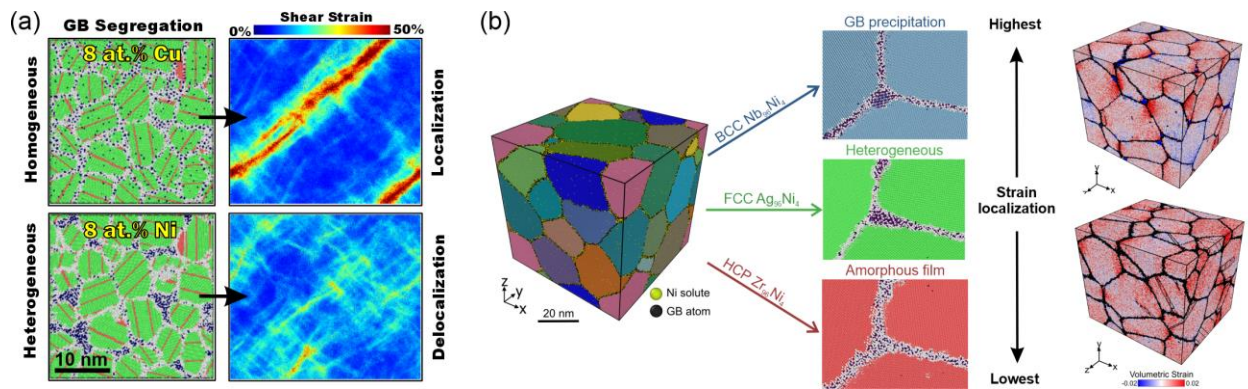


Figure 2. Large-scale hybrid MC/MD simulations of heterogeneous vs. homogeneous segregation behaviors and associated strain-localization mechanisms in different nc alloys. (a) Results showing how heterogeneous Ni solute segregation can suppress strain-localized shear bands at solute contents of 8 at.% and beyond, as opposed to homogeneous Cu solute segregation, in FCC Ag polycrystals with a 6-nm grain size. (b) Results showing different Ni solute interactions at GBs and GB triple-junctions in random FCC Ag, BCC Nb and HCP Zr polycrystals with same Ni solute content (4 at.%) and same grain size (24 nm). Strain localization evidenced by mapping the volume metric strain that characterizes free volume expansion in the vicinity of GB triple junctions, was predicted to be the largest with second-phase precipitation in BCC Nb₉₆Ni₄ polycrystals and the lowest in HCP Zr₉₆Ni₄ polycrystals.

Furthermore, we investigated the physical origin for heterogeneous segregation behavior and its existence in non-FCC alloys, Fig. 2(b). Hybrid MC/MD simulations were used to study the segregation of Ni solutes (4 at. %) into nc FCC Ag, BCC Nb and HCP Zr metals at their solubility limit temperature and a same homologous temperature ($0.405 \cdot T_m$), respectively. A range of segregation configurations was found: Fully heterogeneous segregation in $\text{Ag}_{96}\text{Ni}_4$ @ 500 K, homogeneous segregation with second-phase precipitates in $\text{Nb}_{96}\text{Ni}_4$ @ 1110 K, homogeneous segregation with small-scale Ni clusters in $\text{Nb}_{96}\text{Ni}_4$ @ 1564 K and $\text{Zr}_{96}\text{Ni}_4$ @ 464 K, and fully homogeneous segregation with amorphous intergranular films in $\text{Zr}_{96}\text{Ni}_4$ @ 1118 K. Significant variations in mechanical behavior and associated plastic deformation mechanisms were simulated for each alloy due to their different segregation behaviors. It was found that strain-localized shear banding was the most significant at interfaces with homogeneous solute segregation containing second-phase precipitates and absent in segregation leading to amorphous intergranular films, which was rationalized by a net change of free volume distribution near triple junctions, Fig. 2(b). *This work presented the first atomistic study providing a direct comparison between systems with these different crystal structures, and underscored the importance of Ni solute interactions in profoundly altering segregation and mechanical behavior in stable nanocrystalline alloys*

Quantifying short and long-range solute interactions at GBs from local atomic environments.

Analyzing GB segregation energy as a spectrum allows for a more in-depth analysis of the effects of GB atomic structure on solute segregation [3]. Here, we developed an efficient molecular-statics (MS) algorithm for predicting both short and long-range solute-solute interaction effects on GB segregation. This algorithm was applied to the segregation and interaction of Ni and Cu solutes in a $\Sigma 9$ (221) symmetric tilt grain boundary in FCC Ag. It was found that the strength of interaction between two solutes directly correlates with changes in average solute segregation energy on the local atomic environment of a fixed GB solute. Local interaction effects can be either attractive or repulsive, where an attractive effect implies the propensity for solute cluster nucleation. Given that solute clustering has correlation to heterogeneous GB segregation in polycrystals, the local environment analysis could add this level of understanding for new bulk-solute alloys without significantly increasing computational cost.

In-situ tensile SEM study of shear localization using high-resolution digital image correlation (DIC): A 500-N mini in-situ SEM tensile stage along with image acquisition software (Kamrath & Weiss) was acquired to perform high-resolution DIC in our field-emission SEM. We have successfully integrated the in-situ tensile stage to our FE-SEM, along with EBSD and DIC analysis, and then focused on the fabrication of micro tensile specimens from pure Ni and pure Ag foils of 20-microns in thickness. Our next goals are two-fold: (1) To improve the accuracy of in-situ DIC for shear localization studies and (2) to integrate synthesis and specimen microfabrication of our own sputter-deposited nc alloys.

Future Plans

The key scientific questions to be addressed in this research project:

Theoretically,

1. How do solute-solute interactions influence GB solute clustering in polycrystals?
2. How do GB character and GB triple junctions influence solute clustering in polycrystals?
3. How to understand the transition from strain-localization to delocalization in nc alloys?
4. Can deep learning accelerate and improve the atomistic simulation of GB solute segregation?

Experimentally,

5. How to quantify strain localization in nc metals and alloys at microscopic scale?
6. How do solute concentration and temperature influence strain localization mechanisms?
7. Do solute clustering and heterogeneous segregation more generally exist in other alloys?

The specific plan to answer these questions is four-fold:

- (1) **Local atomic environment analysis of GB solute interaction:** Using this year's progress on the development of an algorithm to quantify local atomic environment effects on solute-solute segregation in bicrystals, we plan to extend this line of work to random polycrystals, along with large-scale hybrid MC/MD simulations. These simulations will enable us to demonstrate that the correlation between local effects and GB clustering also exists for random polycrystals.
- (2) **Building accurate deep-learning interatomic potentials for GB solute interaction:** One of our main goals is to study the effects of local atomic environment on Ni-Ni interactions in FCC Al, BCC Nb and HCP Zr bicrystals, because preliminary MC/MD simulations have shown significant variations in Ni segregation and clustering behavior in these alloys, Fig. 2(b). A caveat, however, is that the semi-empirical interatomic potentials for these alloys in the literature were not fitted to energies of solute segregation at GBs. Therefore, a secondary goal is to address this challenge by using NequIP and DeepMD, two newly available deep-learning interatomic potential development codes, along with VASP ab-initio calculations.
- (3) **In-situ microscale quantification of shear localization:** We plan to continue the quantification of shear localization at microscopic scale using in-situ SEM/DIC tensile tests. For that purpose, we will test commercially available Ag and Ni foil materials presenting a range of grain sizes from microscopic to nanoscale, before moving to sputter-deposited binary alloy films. Experiments are necessary here because localization mechanisms in atomistic simulations are limited by their intrinsically high strain rates and ideally periodic boundaries.
- (4) **Synthesis and characterization of new alloys that suppress strain localization:** We plan to acquire a co-deposition sputtering system to make our own high purity nc alloys. The advantages of using an in-house sputtering system are (1) to allow an immediate in-situ characterization of the mechanical behavior of those alloys, which will eliminate potential issues of oxidation or contamination associated with long-term storage, to enable us to make specimens with a wider range of solute concentrations to better pinpoint the content thresholds from strain localization to delocalization mechanisms, and (3) to combine thermal annealing to control GB clustering and precipitation. Furthermore, we intend to use external facilities and expertise at the Center for Integrated Nanotechnology of the Sandia National Laboratories and the Thayer School Microscopy Center at Dartmouth College to perform STEM analysis of GB clusters and precipitates using a high angle annular dark field (HAADF) detector.

References

1. Z. Pan, V. Borovikov, M.I. Mendeleev, and F. Sansoz, *Development of a semi-empirical potential for simulation of Ni solute segregation into grain boundaries in Ag*. *Modelling and Simulation in Materials Science and Engineering* **26**, 075004 (2018)
2. N. M. Heckman, N.M., S.M. Foiles, C.J. O'Brien, M. Chandross, C.M. Barr, N. Argibay, K. Hattar, P. Lu, D.P. Adams, and B.L. Boyce, *New nanoscale toughening mechanisms mitigate embrittlement in binary nanocrystalline alloys*. *Nanoscale* **10**, 21231-21243 (2018)
3. M. Wagih, P.M. Larsen, C.A. Schuh, *Learning grain boundary segregation energy spectra in polycrystals*, *Nature communications* **11**, 1-9 (2020)

Publications

1. T. Nenninger and F. Sansoz. *Local atomic environment analysis of short and long-range solute-solute interactions in a symmetric tilt grain boundary*. Scripta Materialia, 222, 115045 (2023)
2. E. A. Picard and F. Sansoz. *Ni Solute Segregation and Associated Plastic Deformation Mechanisms into Random FCC Ag, BCC Nb and HCP Zr Polycrystals*. Acta Materialia, 240, 118367 (2022)
3. F. Sansoz and X. Ke. *Hall-Petch Strengthening Limit through Partially Active Segregation in Nanocrystalline Ag-Cu Alloys*. Acta Materialia, 225, 117560 (2022)
4. Q. Zhu, L. Kong, H. Lu, Q. Huang, Y. Chen, Y. Liu, W. Yang, Z. Zhang, F. Sansoz, H. Zhou, J. Wang. *Revealing extreme twin-boundary shear deformability in metallic nanocrystals*, Science advances 7 (36), eabe4758 (2021)
5. Q. Fang and F. Sansoz, *Columnar grain-driven plasticity and cracking in nanotwinned FCC metals*, Acta Materialia 212, 116925 (2021)
6. Q. Zhu, Z. Pan, Z. Zhao, G. Cao, L. Luo, C. Ni, H. Wei, Z. Zhang, F. Sansoz, and J. Wang, *Defect-driven selective metal oxidation at atomic scale*, Nature communications 12 (1), 1-8 (2021)
7. Z. Pan and F. Sansoz, *Heterogeneous Solute Segregation Suppresses Strain Localization in Nanocrystalline Ag-Ni Alloys*, Acta Materialia 200, 91-100 (2020)

Crack Tip Mechanisms Driving Environmental Degradation

D.K. Schreiber, C. Wang, M.J. Olszta, K. Kruska, M.L. Sushko, and K.M. Rosso

Pacific Northwest National Laboratory

Keywords: corrosion, fracture, diffusion, grain boundaries, microscopy

Research Scope

Environmental degradation and associated stress corrosion cracking (SCC) are transcendent materials science issues affecting a wide range of current and future energy systems. Despite decades of research, a seminal understanding of the crack-tip propagation mechanisms driving environmental degradation is yet to be achieved. The long-term vision of this program is to elucidate mechanisms of these fundamental processes at the atomic scale and establish their linkages to meso-to-macroscale cracking of materials under high-temperature, corrosive conditions. Currently we focus on the role of applied stress on corrosion and atomic transport behaviors and the role of altered grain boundary chemistries on further intergranular corrosion. We also seek to bridge between discreet stages of SCC (precursors, crack initiation, and propagation) to further understand how controlling mechanisms shift during crack tip evolution. To do so we integrate a cutting-edge suite of in situ and ex situ microscopy techniques, multiscale mechanistic modeling, and macroscale mechanical testing under controlled environments to produce a comprehensive picture of the roles that environment, applied stress, alloying additions, surfaces, interfaces, and microstructural defects have in the resulting behaviors. Key among these are selective oxidation, vacancy injection, and accelerated interfacial diffusion, which act together with applied stress to drive crack tip processes. Insights into these behaviors form a holistic picture of the atomic-scale processes affecting material degradation and SCC.

Recent Progress

Our research over the past several years shown how preferential, intergranular corrosion is a key contributor to alloy embrittlement and eventual SCC [1]. What has remained more elusive is if this behavior results primarily from selective oxidation itself (i.e. reactions of the less noble solute elements with the environment) or if other processes (e.g. aqueous dissolution, metastable hydroxide formation, vacancy stabilization) play a controlling role. Furthermore, the impact of corrosion on mass transport, especially along grain boundaries and oxide/metal interfaces, has been recognized as a critical issue in need of deeper investigation and fundamental understanding.

New Insights into Selective Oxidation Processes

Ni-base alloys are ideal model alloy system to investigate selective oxidation, corrosion, and grain boundary embrittlement. In addition to being relevant to energy generating systems, the alloys and various corroding environments can be readily tailored to facilitate fundamental studies. In particular, we have leveraged comparisons between dry oxidation and aqueous corrosion under similar oxidation potentials to delineate how water deviates from simpler selective oxidation alone [2]. Through this work we have noted how, in the absence of water, grain boundaries become surprisingly inert to penetrative intergranular oxidation. This observation presented an interesting question for if SCC is possible for these materials when stress is added to the dry oxidation environment. To test this, we developed a miniature 4-pt bend test apparatus that is compatible with a sealed quartz ampule with Ni-NiO

powder (so-called Rhines pack cell). Initial testing, presented in Fig. 1, have shown that the applied stress in the Rhines pack cell is generally insufficient for crack initiation on the tensile surface. In fact, most features unique to unstressed Rhines pack exposures are reproduced in the 4-pt bend sample, suggesting that SCC is unlikely to initiate in the absence of water. Further investigations are still needed to understand this result, but already it reaffirms the general premise from earlier observations in unstressed samples that other aspects of aqueous corrosion (e.g. dissolution or less protective oxide phases) may be critical to supporting SCC in these model alloy systems.

Dynamic Observation of Oxide Formation

While high-resolution ex situ microscopy provides a great amount of detail on material changes during corrosion, direct observation of material degradation in real time and at high resolution is also very insightful. In two recent studies [3, 4], we have used in situ environmental transmission electron microscopy (ETEM) to study the role of order within the oxide and underlying metal during oxidation of model Ni-Al alloys. For dilute Ni-5Al [3], oxidation in dry O₂ resulted in a

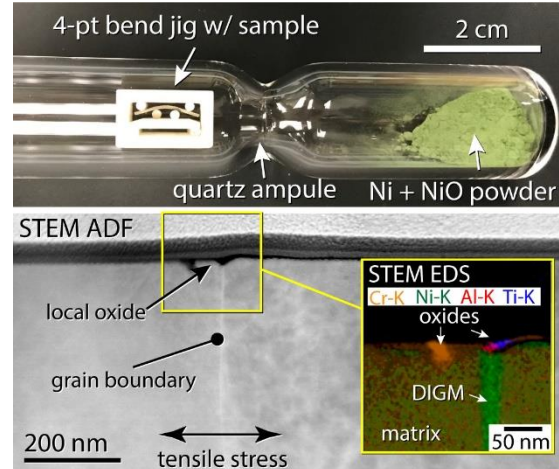


Fig. 1 – (top) A Rhines pack incorporating a 4-pt bend jig to test the effect of stress on selective oxidation in the Ni-base Alloy 600. (bottom) Preliminary STEM analyses of the 4-pt bend sample show selective oxidation near the grain boundary and diffusion induced grain boundary migration (DIGM) as Cr is depleted from the grain boundary, but no evidence for crack initiation or penetrative oxidation. [2]

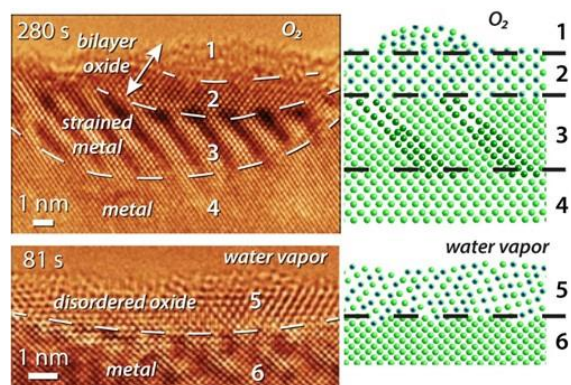


Fig. 2. In situ TEM oxidation of Ni-5Al in O₂ or water vapor reveals atomic-level structural differences. (top) Oxidation in O₂ leads to an ordered NiO layer (2) adjacent to a dislocation-rich, strained metal layer (3) which both impede overall oxidation kinetics. (bottom) Oxidation in water vapor leads to a disordered oxide layer (5) directly adjacent to the metal (6). Oxygen moves more easily through the disordered oxide, facilitating faster oxidation in water vapor. [3]

strained metal/oxide epitaxial interface (Fig 2). Conversely water vapor promotes disorder in the oxide film, without any concomitant alloy strain. Complementary density functional theory (DFT) calculations showed that protons from the water dissociation are responsible for this disorder, which also results in faster penetrative oxidation into the metal. In another study using Ni-50Al, selective oxidation of Al drives strong depletion of Al in the underlying metal [4]. This creates a high density of Al vacancies within the metal, which then order themselves into well-defined channels, as observed by TEM and supported by DFT calculations. In both cases, in situ observation of atomic scale changes provided new insights into local ordering and strain that would likely otherwise be overlooked by more conventional ex situ microscopy approaches.

Grain Boundary Diffusion via Molecular Dynamics

To further connect experimental observations of atomistic transport during corrosion with simulations, we have recently developed and validated a molecular dynamics (MD) method for predicting the temperature dependence of Ni and Cr self-diffusion in Ni-xCr (x= 0, 10, 20, 30) binary alloy compositions [5]. This is a critical first step towards MD simulations of more realistic systems to incorporate grain boundaries and vacancy sources/sinks to predict both grain boundary diffusion and mobility accompanying corrosion. In forthcoming work, we have also extended these models to incorporate grain boundary migration, observed experimentally as diffusion induced grain boundary migration (DIGM) in Fig 1. In future iterations, we intend to incorporate applied stress and to extend the method to lower temperatures (~300-500 °C) that are used experimentally to focus on interfacial diffusion at grain boundaries and oxide/metal interfaces.

Future Plans

We will continue to develop the 4-pt bend approach to test early stages of SCC in both aqueous and gaseous environments specifically targeting crack precursor and initiation events. Next steps will include testing more aggressive loading and oxidation conditions to determine if / when SCC can be initiated in the absence of water. These will be complemented by further aqueous SCC testing in 4-pt bend configuration, with a particular interest in examining if the intergranular corrosion is significantly affected by the compressive vs tensile loading configurations of the sample surface.

To further understand how water vapor affects selective oxidation processes, we will also leverage a recently established capability to directly corrode needle-shaped atom probe tomography (APT) samples using a home-built in-line reactor system [6]. A representative example of using this new system to study selective oxidation of a NiCrFeCoMn alloy is shown in Fig. 3. In addition to providing detailed nanoscale measurements of oxide film formation, the novelty of this approach is that it enables rapid exploration of oxidation conditions as analysis of the oxidized APT sample returns a pristine sample for re-exposure in the UHV attached reactor chamber. This provides a tremendous opportunity to explore the roles of temperature, pO_2 , water vapor, and other gas species on fundamental oxide formation. Isotopic tracers (e.g. ^{18}O) can also be used in this setup to employ two stage ($^{16}O / ^{18}O$) reactions to track anion redistribution as oxidation progresses. In more limited cases, it will also be possible to transfer the reacted APT sample to a TEM for more detailed examination of the oxide crystal structure, enabling directly correlated structural / nanochemical analyses. These snapshot observations will nicely complement ongoing efforts for in situ TEM observation under similar reaction conditions.

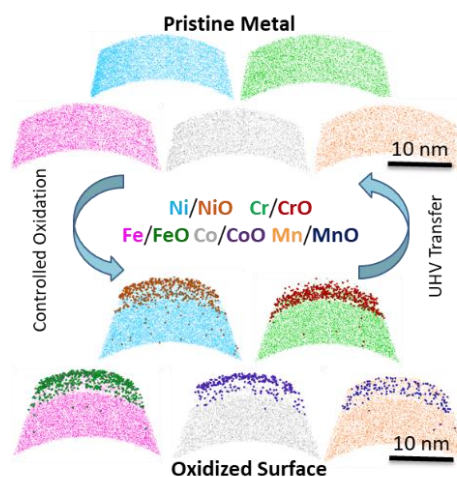


Fig. 3. Example of controlled oxidation experiments on APT samples of a compositionally complex alloy. APT analysis removes the oxidized surface, returning a pristine sample for further oxidation experiments. [6]

References

1. S.M. Bruemmer, M.J. Olszta, M.B. Toloczko, and D.K. Schreiber, *Grain boundary selective oxidation and intergranular stress corrosion crack growth of high-purity nickel binary alloys in high-temperature hydrogenated water*, Corrosion Science **131**, 310 (2018).
2. K. Kruska, Z. Zhai, B.J. Riley, and D.K. Schreiber, *Effect of Applied Stress on the Selective Oxidation of Alloy 600 Exposed to PWR Primary Water and Rhines Pack Environments*, in: Proc. of 20th International Conference on Environmental Degradation of Materials in Nuclear Power Systems – Water Reactors, AMPP, Paper No. 17328 (2022).
3. L. Luo, L. Li, D. K. Schreiber, Y. He, D. R. Baer, S. M. Bruemmer, and C. Wang, *Deciphering atomistic mechanisms of the gas-solid interfacial reaction during alloy oxidation*, Science Advances **6**, eaay8491 (2020).
4. Y. He, L. Luo, M. L. Sushko, C. Liu, D. R. Baer, D. K. Schreiber, K. M. Rosso, and C. Wang, *Vacancy ordering during selective oxidation of β -NiAl*, Materialia **12**, 100783 (2020).
5. P. Simonnin, D. K. Schreiber, and K. M. Rosso. *Predicting the temperature dependence of self-diffusion in Ni-Cr alloys via molecular dynamics*, Materials Today Communications **26**, 101982 (2021).
6. E. J. Kautz, D. K. Schreiber, A. Devaraj, and B. Gwalani. *Mechanistic insights into selective oxidation and corrosion of multi-principal element alloys from high resolution and in situ microscopy*, Materialia. **18**, 101148 (2021).

Publications (2021-2022)

1. D.K. Schreiber, E.J. Kautz, M.J. Olszta, K. Kruska, A.Y. Gerard, K.F. Quiambao-Tomko, and J.R. Scully, *Revealing the complexity of high temperature oxide formation in a 38Ni-21Cr-20Fe-13Ru-6Mo-2W (at. %) multi-principal element alloy*, Scripta Materialia **210**, 114419 (2022).
2. M. Weiser, D.K. Schreiber, K. Kruska, M.H. Engelhard, and M.J. Olszta, *Intergranular Oxidation and Oxygen Transport in Ni-20Cr During Exposure to Model Dry and Wet Oxidation Environments*, in: Proc. of 20th International Conference on Environmental Degradation of Materials in Nuclear Power Systems – Water Reactors, AMPP, Paper No. 17329 (2022).
3. D.K. Schreiber, K. Kruska, M.J. Olszta, and P.H. Chou, *Intergranular Oxidation of Unstressed Alloy 600 SA and Alloy 600TT in PWR Primary Water* in: Proc. of 20th International Conference on Environmental Degradation of Materials in Nuclear Power Systems – Water Reactors, AMPP, Paper No. 17279 (2022).
4. K. Kruska, Z. Zhai, B.J. Riley, and D.K. Schreiber, *Effect of Applied Stress on the Selective Oxidation of Alloy 600 Exposed to PWR Primary Water and Rhines Pack Environments*, in: Proc. of 20th International Conference on Environmental Degradation of Materials in Nuclear Power Systems – Water Reactors, AMPP, Paper No. 17328 (2022).
5. M. Kühbach, A.J. London, J. Wang, D.K. Schreiber, F. Mendez Martin, I. Ghamarian, H. Bilal, and A.V. Ceguerra, *Community-Driven Methods for Open and Reproducible Software Tools for Analyzing Datasets from Atom Probe Microscopy*, Microscopy & Microanalysis **28**, 1038 (2022).
6. B.P. Uberuaga, P. Simonnin, K.M. Rosso, D.K. Schreiber, and M. Asta, *The effect of Cr alloying on defect migration at Ni grain boundaries*, Journal of Materials Science **57**, 10499 (2022).
7. A. Devaraj, D.J. Barton, C.-H. Li, S.V. Lambeets, T. Liu, A. Battu, S. Vaithiyalingam, S. Thevuthasan, F. Yang, J. Guo, T. Li, Y. Ren, L. Kovarik, D.E. Perea and M.L. Sushko, *Visualizing the Nanoscale Oxygen and Cation Transport Mechanisms during the Early Stages of Oxidation of Fe–Cr–Ni Alloy Using In Situ Atom Probe Tomography*, Advanced Materials Interfaces **9**, 220134 (2022).
8. D.K. Schreiber, E. J. Kautz, M. J. Olszta, K. Kruska, G. Y. Gerard, K. F. Quiambao-Tomko, and J. R. Scully. *Revealing the complexity of high temperature oxide formation in a 38Ni-21Cr-20Fe-13Ru-6Mo-2W (at. %) multi-principal element alloy*, Scripta Materialia **210**, 114419 (2022).
9. P. Simonnin, D. K. Schreiber and K. M. Rosso. *Predicting the temperature dependence of self-diffusion in Ni-Cr alloys via molecular dynamics*, Materials Today Communications **26**, 101982 (2021).
10. E. J. Kautz, D. K. Schreiber, A. Devaraj, and B. Gwalani. *Mechanistic insights into selective oxidation and corrosion of multi-principal element alloys from high resolution and in situ microscopy*, Materialia. **18**, 101148 (2021).

Discovery and Design of Stable Nanocrystalline Alloys: The Grain Boundary Segregation Genome

Principal Investigator: Christopher A. Schuh
MIT, Department of Materials Science and Engineering

Keywords: Grain boundaries; Nanocrystalline alloys; Data Science; High-throughput; Phase-and-Defect Diagrams

Research Scope

Grain boundary segregation is the tendency for dissolved minority elements (solutes) to collect at the interfaces between crystalline grains in solid materials. This phenomenon happens with pervasive frequency in essentially all polycrystalline materials, and is of profound importance [1,2] to many properties, including strength and brittleness, thermal stability, and corrosion. Because of this broad and pervasive importance, grain boundary (GB) segregation is a materials phenomenon that engineers would increasingly like to *design for*. Unfortunately, despite its simple definition, GB segregation is an extremely complicated problem due to the multitude of possible atomic arrangements that can occur at grain boundaries. Even for simple metals these number in the millions or more, and understanding how every possible solute from across the periodic table can interact with every possible site in a GB is a vast and challenging problem.

With today's computing power and the advanced tools of data science and machine learning, it has recently become plausible to address the vast space of GB segregation. In the prior three years of DOE-BES funded work by the PI, some first steps have been taken to span the configuration space of GBs, by cataloging the sites in various metals and using data science and machine learning methods to reduce the dimensionality of the problem to a small and tractable set of computations. Combined with state-of-the-art multiscale physics models for the atomic interactions, we are now able to compute the full spectrum of interaction enthalpies for any given solute in any given base metal: with 100 carefully selected computations performed with quantum-accuracy, we can use trained machine learning models to extract a spectrum of GB segregation enthalpies representing the millions of possible sites. By repeating such calculations for many alloys, we have built a catalog of GB segregation data that is of foundational use for engineering new alloys with improved properties.

This progress in building *the spectral model of GB segregation*, however, is thorough only in the corner of a typical phase diagram: (i) in the dilute limit (alloying elements must be present at unrealistic levels below about ~1%), and (ii) at very low temperatures (near absolute zero). To address these issues requires new physical models. For issue (i) we need to compute the spectrum of solute-solute interactions at GBs, because at higher concentrations these interactions dominate the problem. For issue (ii) we need to compute the spectrum of vibrational entropy of all the GB segregation sites, as the atomic vibrations of atoms are critical to the energetics at high temperatures. The current thrust of the group is to lay out approaches to each of these problems,

which are rooted in atomistic and electronic-level computations, and extend them to cover the vast alloy and configuration space using data science and machine learning. With these advances in hand, we will be poised to develop a new engineering tool—the “phase-and-defect” diagram. In addition to showing phase equilibria (as in a phase diagram), this new tool incorporates the density of grain boundary sites (e.g., the grain size) and the chemical configuration of those boundaries as well. We are currently developing the computational methods to construct such diagrams, and a high-throughput approach to produce them for many alloys.

Recent Progress

A major advance of the PI’s group in the past few years pertains to the evaluation of the GB segregation spectrum in a high-throughput computational mode [3,4]. This advance is comprised of a number of additive achievements that incorporate the state of the art in multiscale atomistic computation as well as data science/machine learning. These achievements are summarized in Figure 1(a-c), and include:

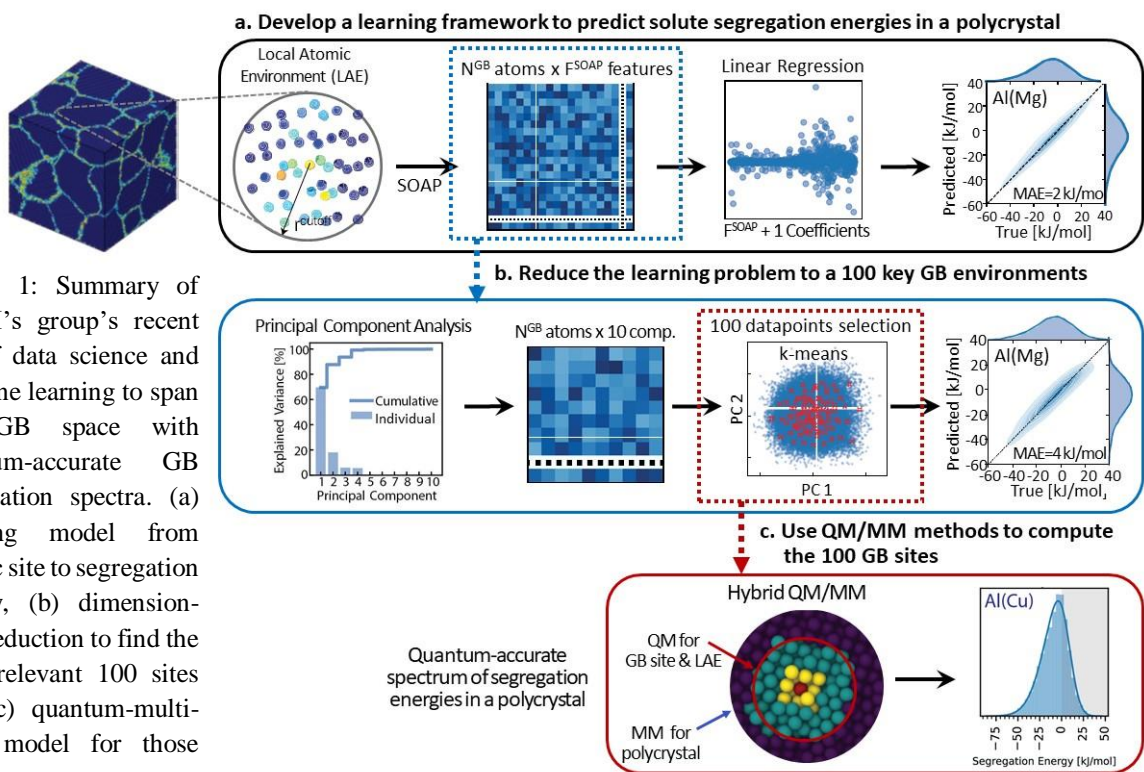


Figure 1: Summary of the PI’s group’s recent use of data science and machine learning to span the GB space with quantum-accurate GB segregation spectra. (a) learning model from atomic site to segregation energy, (b) dimensionality reduction to find the most relevant 100 sites and (c) quantum-multi-scale model for those sites.

- Figure 1 (a): The use of regression models that connect the local GB atomic structure (site configuration) to the segregation energy. These models are trained using full atomistic simulations of the kind previously seen in our work in Ref. [5], and take advantage of a machine learning-based representation of the local atomic environments using, e.g., the ‘smooth overlap of atomic positions’ (SOAP) method. This achievement dramatically

simplifies the problem of computing a segregation spectrum because no longer does each site need to be computed individually: the regression model can give the spectrum in a tiny fraction of the time (1,000 times or more faster).

- Figure 1(b): The use of dimensionality reduction methods and sampling points selection methods reduce the training need for regression models. Although in principle there are millions of different GB site types, these data science methods allow us to identify the most important 100 sites across that entire space, which, if their segregation behavior is known, can capture the full spectrum with high accuracy (less than 5% error).
- Figure 1(c): The implementation of multiscale models linking density functional theory with atomistics, for the special GB environments that best capture the full spectrum of GB segregation. We have implemented methods based on the QM/MM (quantum mechanics / molecular mechanics) multiscale coupling method, which we have validated as delivering quantum-accurate segregation enthalpies for complex GB sites. Whereas prior work has done similar things for individual boundaries, our approach solves the full polycrystal problem.

The upshot of these combined advances is potentially revolutionary for GB segregation science: for a new alloy system (for which there may not even be any existing interatomic alloy potentials), we can now conduct 100 relatively fast QM/MM computations, on carefully targeted GB sites, and the results can be fed into a regression model to yield the entire spectrum of GB segregation (representing millions of sites). These methods yield quantum-accurate thermodynamic data for many alloys inclusive of the full breadth of GB sites, and the results in Figure 2 for Al alloys represent the first such ‘atlas’ of accurate thermodynamic data for grain boundaries [4].

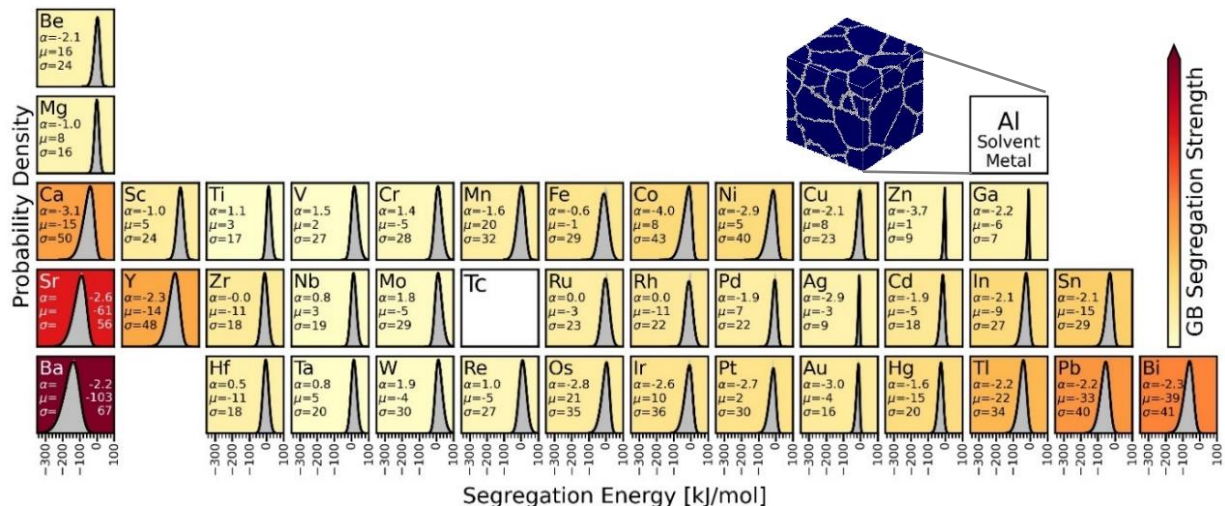


Figure 2: A first-of-its kind “atlas” of quantum-accurate GB segregation enthalpy spectra. The distributions here show the full density of states for GB segregation in polycrystals of aluminum, for all of the solute elements, and these are based on rigorous density functional theory computations.

Future Plans

- I. Effect of solute-solute interactions on GB segregation: At dilute solute concentrations, the spectrum of segregation energies will determine how solute atoms populate different GB sites. However, beyond the dilute limit, increasing solute-solute interactions at the GB will alter the nature of energetics for these GB sites, and consequently, the equilibrium segregation state. We aim to quantify – based on atomistic calculations – the magnitude and effect of solute-solute interactions on the final segregation state and nanocrystalline stability of non-dilute binary (and ternary) alloys, and develop high-throughput frameworks to extract such information across the alloy space.
- II. Effect of vibrational entropy on GB segregation: Our prior work described above was aimed specifically at exploring the configuration space of alloys. As such, it included an analysis of configurational entropy, by accounting for the variety of ways in which atoms can occupy sites in the system. However, this is only one critical component of entropy, and entirely neglects a second important contribution, namely, vibrational entropy, which accounts for the various different “microstates” that the alloy can occupy because of the atoms’ ability to vibrate on their sites. We aim to first quantify, using atomistic simulations, the vibrational contribution to entropy and its impact on the equilibrium segregation state in a polycrystal; and second, to develop data science methods to map out the entropy terms across the full alloy space.
- III. Construction of phase-and-defect phase diagrams: Once we understand the enthalpy and entropy (configurational and vibrational), then the Gibbs free energy of segregation can be minimized to calculate equilibrium at all temperatures and compositions. This free energy can be compared to that of bulk phases, which will permit the assessment of the thermodynamically favorable defect configuration in an alloy, including not only phase content, but also GB content (i.e. grain size) as well as GB composition. The resulting construct can be termed a phase-and-defect diagram, because it contains extra information about GB configuration not normally in a phase diagram, but which is indeed part of the equilibrium state. We aim to develop a high-throughput thermodynamic framework to construct phase-and-defect diagrams that quantitatively incorporate the GB state across the alloy space.

References

- [1] P. Lejček and S. Hofmann, *Thermodynamics and Structural Aspects of Grain Boundary Segregation*, Crit. Rev. Solid State Mater. Sci. **20**, 1 (1995).
- [2] D. N. Seidman, *Subnanoscale Studies of Segregation at Grain Boundaries: Simulations and Experiments*, Annu. Rev. Mater. Res. **32**, 235 (2002).
- [3] M. Wagih, P. M. Larsen, and C. A. Schuh, *Learning Grain Boundary Segregation Energy Spectra in Polycrystals*, Nat. Commun. **11**, 6376 (2020).

- [4] M. Wagih and C. A. Schuh, *Learning Grain-Boundary Segregation: From First Principles to Polycrystals*, Phys. Rev. Lett. **129**, 046102 (2022).
- [5] M. Wagih and C. A. Schuh, *Spectrum of Grain Boundary Segregation Energies in a Polycrystal*, Acta Mater. **181**, 228 (2019).

Publications

1. M. Wagih, C. A. Schuh, *Grain boundary segregation beyond the dilute limit: Separating the two contributions of site spectrality and solute interactions*. Acta Mater. 199, 63–72 (2020).
2. M. Wagih, P. M. Larsen, C. A. Schuh, *Learning grain boundary segregation energy spectra in polycrystals*. Nat. Commun. 11, 6376 (2020).
3. M. Wagih, C. A. Schuh, *Thermodynamics and Design of Nanocrystalline Alloys using Grain Boundary Segregation Spectra*. Acta Mater. 217, 117177 (2021).
4. T. P. Matson, C. A. Schuh, *Atomistic assessment of solute-solute interactions during grain boundary segregation*. Nanomaterials. 11, 2360 (2021).
5. N. Tuchinda, C. A. Schuh, *Grain size dependencies of intergranular solute segregation in nanocrystalline materials*. Acta Mater. 226, 117614 (2022).
6. C. A. Schuh, K. Lu, *Stability of nanocrystalline metals: The role of grain-boundary chemistry and structure*. MRS Bull. 46, 225–235 (2021).
7. S. A. Kube, W. Xing, A. Kalidindi, S. Sohn, A. Datye, D. Amram, C. A. Schuh, J. Schroers, *Combinatorial study of thermal stability in ternary nanocrystalline alloys*. Acta Mater. 188, 40–48 (2020).
8. E. Perrin, C. A. Schuh, *Stabilized Nanocrystalline Alloys: The Intersection of Grain Boundary Segregation with Processing Science*. Annu. Rev. Mater. Res. 51, 241–268 (2021).

New Experimental Views on the Role of Temperature in Extreme Strain Rate Mechanics

Christopher A. Schuh¹, Keith A. Nelson²

¹Department of Materials Science and Engineering, MIT, Cambridge, MA, 02139, USA

²Department of Chemistry, MIT, Cambridge, MA, 02139, USA

Keywords: High-velocity impacts, temperature evolution, material micromechanics, melting

Research Scope

This work advances the field of material mechanics by using in-situ imaging of single metallic particle impacts on metallic substrates at micrometer and nanosecond scales using laser induced particle impact tests (LIPIT), Fig. 1. The LIPIT, detailed elsewhere [1], is an all-optical table top testbed used to accelerate single particles up to $\sim 10^3$ m/s and, with in-situ ultra-high-speed imaging, capture the flight, impact, and rebound of the particle. From these images, qualitative measurements of particle size and impact and rebound velocities of particles that strike the surface are measured frame-by-frame for each impact event. With particle sizes in the range of tens of microns, these impacts can produce strain rates on the order of 10^6 - 10^9 s⁻¹. The customizability of the LIPIT allows for a wide range of experimental conditions to be tested. From previous DOE BES funding for material behavior at high strain rates, we discovered trends in mechanical properties, hydrodynamic deformation, particle size effects for bonding, temperature effects for bonding, impact induced melting, bond formation, and dynamic recrystallization. A critical component of the current project is targeted work to understand how temperature affects these phenomena.

Recent Progress

There are many processes that apply large strains at high rates, but these are rarely controllable to the degree that our LIPIT experiments are, so the processes of structural evolution that occur during such processing are often unclear. By combining LIPIT experiments of Cu on Cu impacts with STEM and electron backscatter diffraction (EBSD) we found that Cu grains experience recrystallization through nanotwinning, a process that we call nanotwinning-assisted dynamic recrystallization (ntDRX). In the ntDRX mechanism, rather than grains being partitioned by twinning, as seen in the dynamic Hall-Petch effect, they form subgrains by dislocation plasticity and reorganization, as seen in Fig. 2.

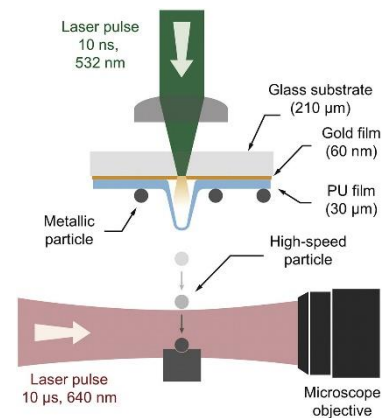


Figure 1: A schematic representation of a laser induced particle impact test (LIPIT) [1]. A laser pulse on the back of the launch pad accelerates a single microparticle towards the substrate. A second laser pulse is used to illuminate the impact event for high-speed imaging.

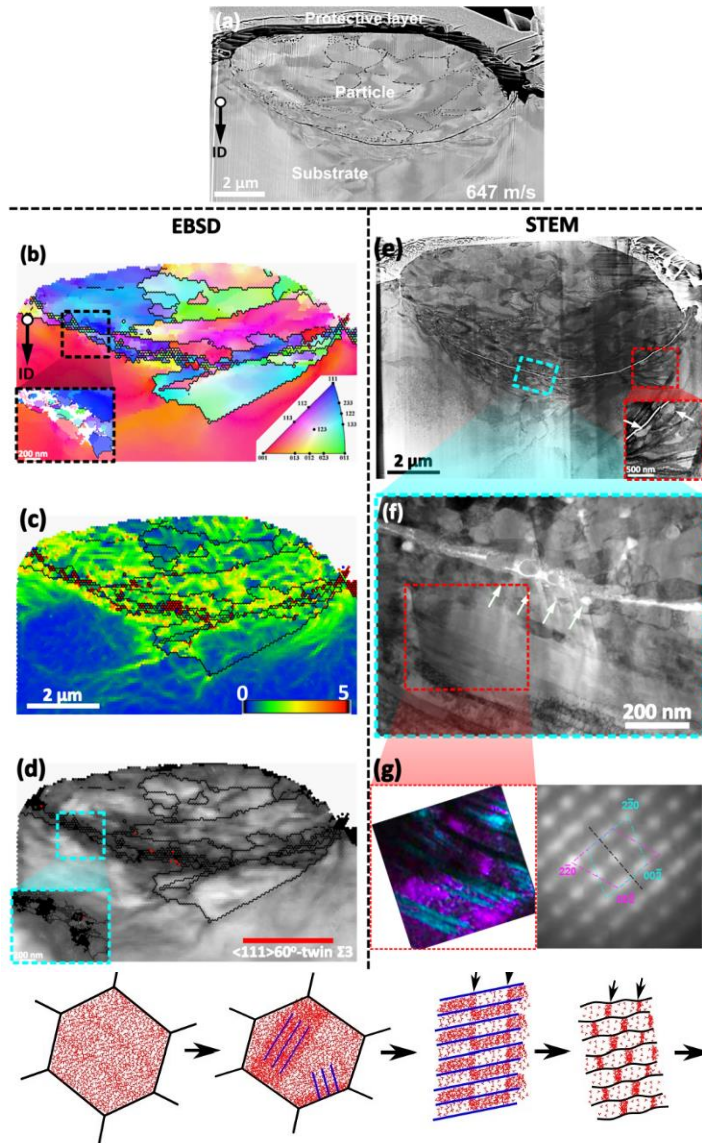


Figure 2: A cross-sectioned Cu-on-Cu impact is studied with both high resolution EBSD (left column) and STEM (right column), revealing the development of nanotwins that become partitioned into rafts of new grains under the high-strain and high-rate conditions of particle impact. The mechanism of recrystallization is termed “nanotwinning-assisted dynamic recrystallization” or ntDRX, as schematized below.

At the critical adhesion velocity, the particle and substrate are highly deformed. In the substrate at the interface, EBSD shows the presence of nanometer sized twins. When looking at the entire particle, it is seen that the deformation is most severe at the interface, by the presence of nanotwins, and less severe at the top of the particle, with only dislocation slip present. As the impact velocity is increased to 768 m/s, nanotwinning becomes extensive at the particle substrate interface and extends to the center of the particle. In the highest strained regions grain refinement through twinning and reorganization of dislocations becomes apparent through the following process: (i) deformation changes from slip to twinning; (ii) twins becomes more plastically deformed and more dislocations are generated; (iii) dislocation walls form and partition the nanotwins into blocks bounded by the twins; (iv) the twin boundaries begin to bulge outward and form hexagonally shaped nano-grains. This grain refinement and recrystallization mechanism produces finer grains than achieved by other known modes of mechanical grain refinement. We analyzed the process

quantitatively and found that other severe deformation processes (ball milling, surface mechanical attrition, machining, etc.) may also induce this mechanism.

Impacts like those that lead to ntDRX involve significant adiabatic heating, although we as yet have no direct access to the experimental temperatures that are evolved. Accordingly, we are pursuing new lines of experimentation to assess the role of temperature on plasticity and structure evolution. For example, our series of works on impact-induced melting have provided direct observations of the locations and strains at which temperature rises to the melting point of the substrate. Our most recent work has extended that work to LIPIT experiments at high temperatures specifically, with our current stage able to reach $\sim 400^\circ\text{C}$, with promise of higher temperatures in coming years.

In these experiments, the velocity at which melting is first observed (termed the melt velocity) provides a benchmark for the temperature rise in the material, i.e., a lower bound of the temperature rise is $T_m - T$, where T_m is the melting temperature and T is the ambient temperature. Changing the initial substrate temperature, T , has allowed us to identify how the melt velocity, and in turn the maximum temperature, varies for a given set of particle and initial temperature conditions. For these experiments, we use ‘hard’ microparticles that are not expected to deform under the test conditions, and impact them on low melting temperature substrates (such as Sn or Bi) at various temperatures. Via post mortem analysis of impact sites, conditions for adiabatic melting are evaluated as well as changes in substrate deformation mechanisms. It is found that as the initial substrate temperature increases, the impact velocity needed to achieve adiabatic melting lowers, as expected. The scaling of that decline is under analysis to reveal quantitative details about the adiabatic heating caused by impacts. In parallel, we are performing microstructural observations to explore if and how deformation mechanisms change as a function of substrate temperature and impact velocity for a given substrate material.

Future Plans

The use of low-melting temperature materials as witnesses to temperature rise is also a topic we are currently planning to use to evaluate plastic heating in other materials. To capture the temperature rise and dissipation around an impact site, a thin (few nm) fiducial film with a melting temperature lower than the substrate temperature is deposited on the substrate surface. The film provides an indirect temperature measurement by “illuminating” an area of melted material around the impact site, marking the lower bound of the maximum temperature rise. By changing the melting temperature of the film, a temperature profile for a given substrate-particle material pair can be generated for a range of impact velocities. Films that do not interact with the substrate allow for a temperature profile to be mapped without changing the thermal properties of the substrate material. Additionally, changing between multiple films of different T_m becomes advantageous over changing between substrates of different T_m because the properties of the substrate material being probed, such as strength, moduli, and density, remain constant between tests. What is more, using this indirect temperature measurement approach in combination with the current work of

changing the initial substrate temperature, an additional variable to refine conventional constitutive models is given.

While the above approaches map the lower bound of the maximum temperature reached, direct temperature measurements of an impact event would give a more complete understanding of the highest temperature reached during the deformation and adiabatic heating of a material. The adaptability of the LIPIT allows us to modify it in a way to do direct time-resolved in-situ temperature measure that are sensitive on the time scales (nanosecond) of a particle impact event. We are presently using microfabrication technologies to make custom launchers and targets for LIPIT experiments that should permit in-situ temperature measurements in the coming years.

References

1. M. Hassani-Gangaraj, D. Veysset, K. A. Nelson, and C. A. Schuh, *In-situ observations of single microparticle impact bonding*, Scripta Materialia **145**, 9-13 (2018).

Publications

1. M. Hassani, D. Veysset, K. A. Nelson, and C. A. Schuh, *Materials hardness at strain rates beyond $10^6 s^{-1}$ via high velocity microparticle impact indentation*, Scripta Materialia **177**, 198-202 (2020).
2. I. Dowding, M. Hassani, Y. Sun, D. Veysset, K. A. Nelson, and C. A. Schuh, *Particle size effects in metallic microparticle impact-bonding*, Acta Materialia **194**, 40-48 (2020).
3. Y. Sun, D. Veysset, K. A. Nelson, and C. A. Schuh, *The transition from rebound to bonding in high-velocity metallic microparticle impacts: Jetting-associated power-law divergence*, J. Appl. Mech. **87**, 091002 (2020).
4. Y. Sun, D. Veysset, K. A. Nelson, and C. A. Schuh, *In-situ observations of jetting in the divergent rebound regime for high-velocity metallic microparticle impact*, Appl. Phys. Lett. **117**, 134105 (2020).
5. M. Hassani, D. Veysset, Y. Sun, K. A. Nelson, and C. A. Schuh, *Microparticle impact-bonding modes for mismatched metals: From co-deformation to splatting and penetration*, Acta Materialia **199**, 480-494 (2020).
6. A. A. Tiamiyu, Y. Sun, K. A. Nelson, and C. A. Schuh, *Site-specific study of jetting, bonding, and local deformation during high-velocity metallic microparticle impact*, Acta Materialia **202**, 159-169 (2021).
7. I. Chaban, Y. Sun, D. Veysset, K. A. Nelson, and C. A. Schuh *The effect of substrate temperature on the critical velocity in microparticle impact bonding*, Appl. Phys. Lett **119**, 011903 (2021).
8. J. Lienhard, D. Veysset, K. A. Nelson, C. A. Schuh, *Melting and ejecta produced by high velocity microparticle impacts of steel on tin*, J. Appl. Mech. **88**, 111005 (2021).
9. A. A. Tiamiyu, X. Chen, E. L. Pang, Y. Sun, J. Lienhard, J. M. LeBeau, K. A. Nelson, and C. A. Schuh, *Oxide layer delamination: An energy dissipation mechanism during high-velocity microparticle impacts*, Applied Surface Science **574**, 151673 (2022).
10. A. A. Tiamiyu, E. L. Pang, X. Chen, J. M. LeBeau, K. A. Nelson, and C. A. Schuh, *Nanotwinning-assisted dynamic recrystallization at high strains and strain rates*, Nat. Mater. **21**, 786-794 (2022).

Radiation Response of Low Dimensional Carbon Systems

Lin Shao, Texas A&M University, College Station, TX 77845

Keywords: carbon, graphene, nanopore, irradiation

Research Scope

The project is aimed at understanding the fundamentals of radiation response of low dimensional carbon systems and irradiation-induced mechanical property changes, with a focus on the unique phenomena caused by their geometry, boundary, and quantum size effects. In comparison with their bulk counterparts (graphite), radiation responses of low-dimensional carbon systems are substantially different. The differences exist at almost every stage of defect development, namely, displacement creation, damage cascade, thermal spike formation defect recombination, defect clustering, and structural reconstruction. Many traditional concepts in ion-solid interaction theory do not apply at the nanoscale or require substantial modification. In our previous project, “Radiation response of low dimensional carbon systems”, we systematically studied various aspects of radiation damage development in graphene, carbon nanotubes (CNTs), and graphite. Our previous studies have mainly focused on the uniqueness of various carbon materials as substrates irradiated by ion beams.

During the current funding period, we shift focus from the substrate effect under “traditional” ion beam bombardment to the beam effect using C_{60} as a “non-traditional” projectile. C_{60} molecules are different from “traditional” monomer ions since they are clusters. Unlike other cluster ions (i.e. Ar_{3000} , bonded through weak Van der Waals forces) C_{60} molecules have a strong sp^2 covalent bond and high structural integrity. The uniqueness leads to very different irradiation behavior of C_{60} molecule compared to other molecules with unique radiation effects on various substrates. Our studies show that upon glancing angle bombardment, C_{60} molecule experiences severe deformation without breaking the molecule cells. The molecule elastically bounces off the surface without being damaged. This can lead to unique phenomena analogous to stone skimming across the water surface or to tunneling through tubes of high aspect ratios. Hence, we carried out the following parallel research tasks, which include both experimental studies and modeling simulations, driven by the dual purpose of understanding fundamentals and exploring the potential for strong technological impact.

- Elastic bouncing of C_{60} molecules from solid surface under glancing angle irradiation and determination/understanding of criteria for such elastic bouncing under various energy-substrate configurations.
- Understanding the fundamentals of C_{60} molecule channeling in nanotubes whereby C_{60} molecules “tunnel” through nanotubes via consecutive glancing elastic bounces.
- C_{60} molecule bombardment on 2D nanomaterials and the control of nanopore morphology through adjustment of irradiation parameters
- Formation of periodic nanopores on 2D nanomaterials and their technological applications.

Recent Progress

Determination of the critical angle for C_{60} molecule elastic bouncing

Measurement of C_{60} molecule scattering as a function of incident molecule angles will determine the critical angle for elastic bouncing. Figure 1 shows that a 7 keV C_{60} molecule is crushed with an incident angle 20° . At an angle of 10° , the molecule maintains its integrity and bounces off. The results were obtained using LAMMPS, a commercial molecular dynamics simulation code.

For experimental studies, the molecule incident angles can be controlled precisely by using a goniometer which can rotate with an angular resolution of 0.01 degrees. The critical angle for elastic bouncing can be measured by detecting bombardment-induced secondary electrons using a biased collector. Secondary electrons suddenly increase when the C_{60} molecule has crashed and broken apart. The second method used a time-of-flight measurement system to measure the time elapsed between molecule landing (with the first signal pulse triggered by secondary electrons) and molecule bombardment on a foil (with the second signal pulse triggered by secondary electrons). Both methods have been explored.

C_{60} molecule tunneling insider nanometer tubes

The discovery of elastic bouncing of C_{60} molecules under a glance angle bombardment triggered our interest to study the collisions of C_{60} molecules inside a tube. We have simulated the flight of one C_{60} molecule within an aluminum tunnel of 100 nm in diameter. The molecule had initial kinetic energy of 10 keV and an incident angle of 5° away from the tunnel axis. Figure 2 shows the trajectories of the C_{60} molecule's glancing-angle bouncing four times inside the tunnel. For each collision, the molecule bounced off the tube wall without being crushed. Points 1, 2, and 3 correspond to before, during, and after the first collision. At point 2, the C_{60} cage is compressed almost completely flat. Points 4, 5, and 6 correspond to the case for the fourth collision. The total flying distance by the C_{60} molecule after the fourth collision reaches about 20 microns.

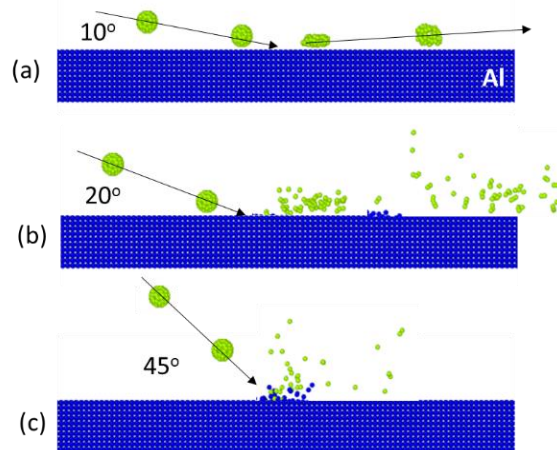


Figure 1 MD simulations of a 7 keV C_{60} molecule bombarding Al at (a) 10° , (b) 20° , and (c) 45° .

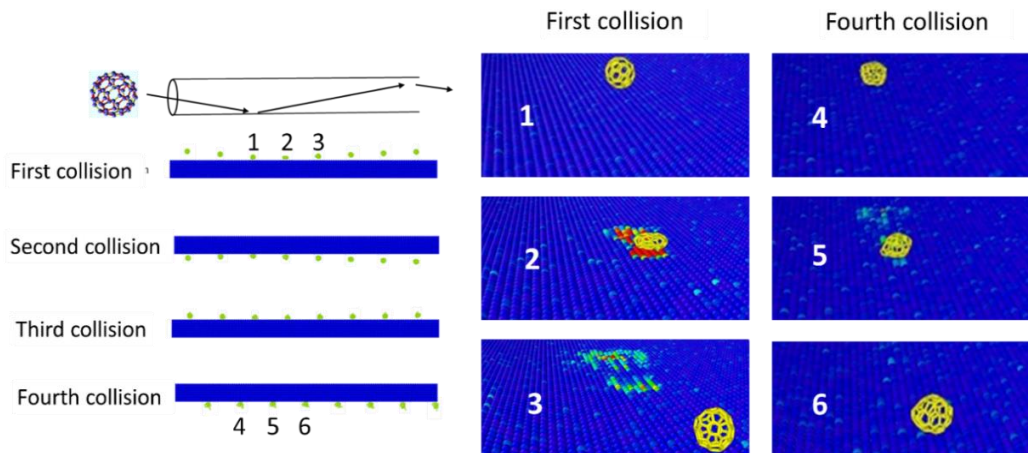


Figure 2. Molecular dynamics simulation of a C_{60} molecule transiting an Al tube of 100 nm in diameter at an initial incident angle of 5° . Note that the cage elastically bounces off the wall after each collision.

During each collision, only a very small fraction of the energy of the C_{60} molecule was lost. Figure 3 shows the kinetic energy change of a C_{60} molecule upon collision, normalized to the initial kinetic energy of 10 keV. Note that after four collisions, the total accumulated kinetic energy loss is only about 2%. This means that the C_{60} molecule is still energetic enough to continue bouncing inside the tube in a way similar to light transport inside an optical fiber. The transverse momentum of the C_{60} is slightly reduced after each collision, but the axial momentum is largely maintained. This results in a slightly reduced exit angle. In other words, after a few bounces, the molecule becomes more and more parallel to the tunnel surface, and the free-flying distance becomes larger due to the reduced exit angle. As shown in Figure 4, the flying angle of the molecule becomes smaller after each collision. For 10 keV C_{60} incident at 5° , the exit angle after four collisions reduces to 0.6° . Our simulations suggest that the C_{60} molecule can fly through a mask of $50\ \mu\text{m}$ without significant dissociation.

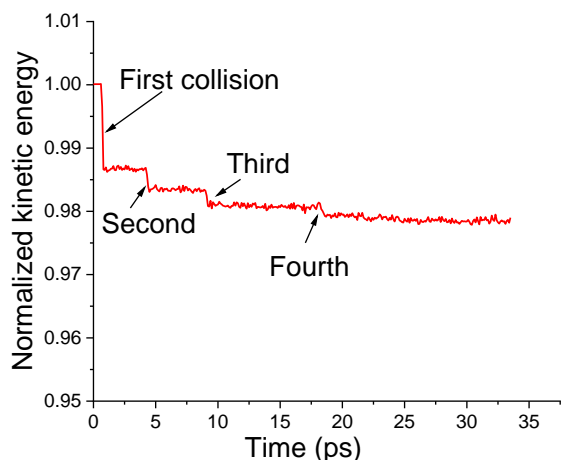


Figure 3. Kinetic energy change of a C_{60} molecule transiting an Al tube of 100 nm length at an initial incident angle of 5° , calculated using MD simulation.

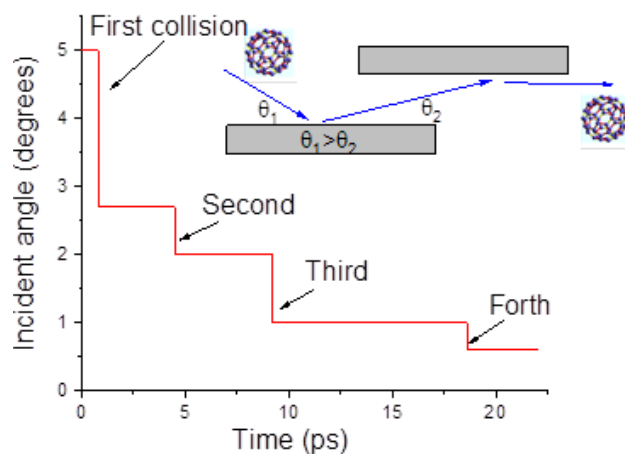


Figure 4. Flying angle changes of a C_{60} molecule transiting an Al tube of 100 nm in diameter at an initial incident angle of 5° , calculated using MD simulations.

Forming “patterned” molecule beams and periodic nanopores on 2D membranes

The discovery of “tunneling” of C_{60} molecules inside a nanotube triggered our interest to develop a method of making patterned C_{60} beams through a mask containing tunnels of high aspect ratio. Having a high aspect ratio guarantees that the fabrication of such a mask is feasible and realistic. It contains the steps of (1) “Tunneling” of C_{60} beams through a mask containing periodic nanometer tubes, (2) using the “patterned” molecules to bombard a 2D membrane to create nanopores of controllable sizes, (3) using the periodic nanopores for a wide range of industry applications, including

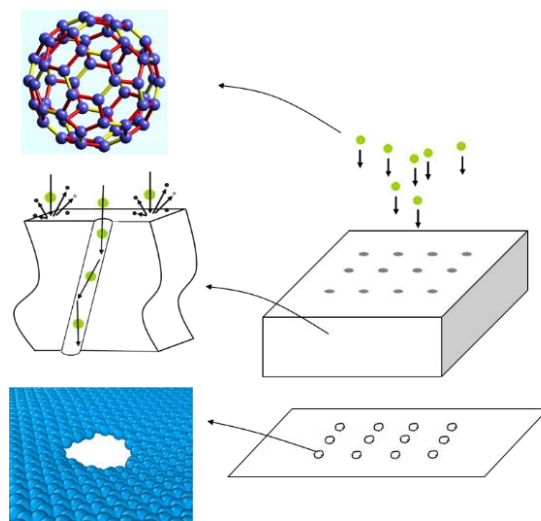


Figure 5. Schematics of experimental step to form periodic nanopores on 2D membranes.

water purification and gas sensing. Figure 5 schematically shows the concept of nanopore formation on 2D membranes.

Adjusting pore sizes by changing irradiation conditions

For C_{60} molecules bombarding along the normal direction, sputtering and pore formation occur on 2D membranes. Pore sizes are adjustable by changing irradiation conditions. As shown in Figure 6a, an 800 keV C_{60} molecule at normal irradiation creates a pore of 7 Å on a monolayer. The pore is slightly increased to 15 Å under 10 keV bombardment (Figure 6b). For 100 keV bombardment, the pore size increase to 20 Å (Figure 6c). If the substrate changes from a monolayer to a bilayer, 10 keV bombardment creates a pore size of 21 Å (Figure 6d) and 100 keV bombardment creates a pore as large as 25 Å (Figure 6e).

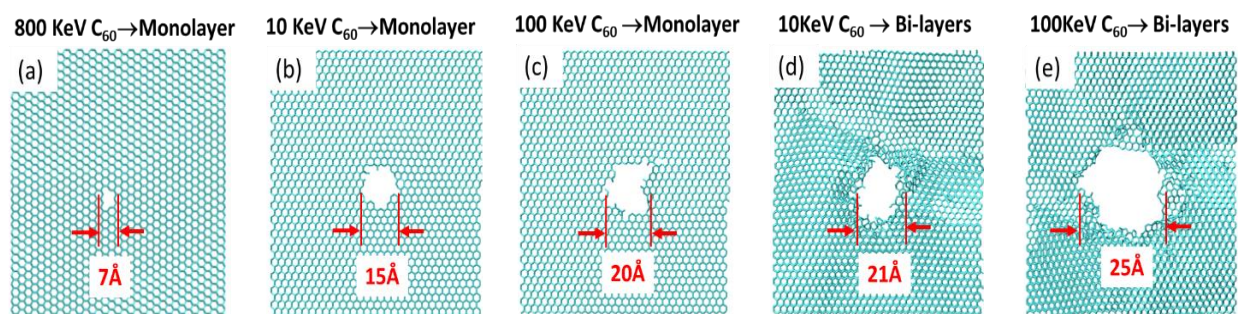


Figure 6. MD simulation-predicted pore sizes formed by C_{60} bombardment of (a) 800 keV on a graphene monolayer, (b) 10 keV on a graphene monolayer, (c) 100 keV on a graphene monolayer, (d) 10 keV on a graphene bi-layer, and (e) 100 keV on a bi-layer graphene.

Future Plans

Nanoporous graphene is unique for its tunable electronic functionality from a semimetal to a semiconductor as a device substrate, and for its excellent mechanical strength as an atomic-thick selective nanosieve. Nanoporous graphene has been proposed for a wide range of applications, including DNA sequencing, chemical sensing, molecule detection, gas separation, and water purification. However, there is currently no technology to produce periodic nanopore arrays which are suitable for large-scale, industry-level high throughput. Various methods have been developed, but most of them create randomly distributed nanopores. The project opens a door a wide range of applications.

For the coming year, we will focus on gas sensing, using graphene containing periodic nanopore arrays as the substrate in graphene-based field effect transistors (GFETs). GFETs are commercially available. Introducing nanopore arrays on graphene expect to significantly improve sensor performance, including (1) increasing gas detection limits and device sensitivity, (2) increasing resolution to differentiate gas species, and (3) increasing device repeatability and reducing device-to-device variation.

Publications (from 2020 to 2022)

1. Di Chen, Lin Shao, *Using irradiation-induced defects as pinning sites to minimize self-alignment in twisted bilayer graphene*, Applied Physics Letters **118**, 151602 (2021).
2. Joseph Wallace, Di Chen, Lin Shao, *Irradiation-enhanced torsional buckling capacity of carbon nanotube bundles*, Journal of Applied Physics **128**, 195902 (2020).
3. Jing Wang, Di Chen, Tianyi Chen, Lin Shao, *Displacement of carbon atoms in few-layer graphene*, Journal of Applied Physics **128**, 085902 (2020).
4. Zhihan Hu, Di Chen, S. Kim, R. Chauhan, Y. Li, Lin Shao, *Effect of stress on irradiation responses of highly oriented pyrolytic graphite*, Materials **15**, 3415 (2022).
5. Y. Li, R. Chauhan, D. Chen, Zhihan Hu, X.M. Wang, Lin Shao, *A method to predict texture effect on ion beam channeling analysis of polycrystals and the application to study the mosaic spreading effect in highly oriented pyrolytic graphite*, Journal of Applied Physics **131**, 225305 (2022).

Toughening mechanisms in ceramic nanocomposites

Principal Investigators: Brian W. Sheldon, Brown University; Jun Lou, Rice University

Co-Investigators: Huajian Gao and Nitin P. Padture, Brown University

Keywords: fracture, nanomaterials, small scale testing, multiscale modeling

Research Scope

The exceptional properties of many nanomaterials suggest that it should be possible to create new *composite* materials with exceptional properties. One example is multilayer coatings with small interlayer spacings (*i.e.*, laminated nanocomposites), however, these materials are highly anisotropic and they do not generally provide the same toughness enhancements observed in fiber reinforced ceramics. The promise of creating tough nanoscale ceramics *via* nanotube and nanoplatelet reinforcements is supported by prior research. However, most of the reported efforts are primarily “proof-of-concept” studies that do not explore the range of key microstructural features in this class of materials (*i.e.*, nanotube/nanofiber structure, nanotube-matrix interface properties, residual stresses, *etc.*). The research in this program is designed to substantially deepen fundamental understanding of the *mechanisms* and *material structures* that are needed to achieve high toughness, durability, and other beneficial properties in ceramics reinforced with nanomaterials. These efforts build on our prior widely-recognized work in ceramic composites at various scales, and our recent work on ceramic nanocomposites. We anticipate that this research will provide important fundamental knowledge that will significantly improve attempts to design and produce novel nanocomposites with optimal mechanical properties for a wide variety of potential energy-related and military applications.

Much of the current understanding of the mechanical behavior of ceramic nanocomposites has been obtained by extrapolating from the extensive, existing literature on micron-scale composites. However, recent evidence shows that these approaches are not always sufficient, largely due to phenomena that occur at or near atomic length scales. The research program described here is primarily directed at establishing relationships between the fracture properties and fundamental mechanisms. We have previously developed and applied new methods to investigate nanocomposites. This includes several *in situ* experimental methods which allow us to directly observe key phenomena, as well as advanced modeling techniques. The central objectives of the research in this program are to:

- Understand failure and toughening mechanisms in ceramic matrices reinforced with different nanoreinforcements. The *in situ* mechanical testing methods noted above make it possible to

investigate phenomena over a broad range of length scales. The interpretation of all of these measurements are closely integrated with related modeling and analysis.

- Quantitatively evaluate the toughening contributions from phenomena in 2-D reinforcements that have been observed in our recent work in this DOE-supported program. This includes inelastic deformation mechanisms in reduced graphene oxide (r-GO), increased fracture resistance in hexagonal boron nitride (h-BN) sheets (compared to graphene-related sheets), and strength-limited interfacial debonding at small-scales (compared to the classical energy-limited debonding that occurs at larger length scales).
- Determine how the toughening mechanisms that operate in 2-D reinforced materials differ from those that operate in 1-D reinforced materials (*e.g.*, based on comparisons between materials reinforced with r-GO and multiwalled carbon nanotubes).
- Investigate toughening with novel hybrid nanostructures consisting of both 1-D and 2-D reinforcements.

Recent Progress

Recent work has focused on studying the mechanical behavior of individual nanoplatelets and their interactions with ceramic matrices. To quantitatively evaluate toughening behavior in 2-D material reinforced ceramics, pull-out experiments were used to investigate the properties of the interface between multi-layer h-BN nanosheet and polymer-derived ceramic (PDC). By using nanoindentation-assisted micro-mechanical devices integrated with scanning electron microscopy (SEM), the interfacial sliding and failure behaviors between h-BN and PDC were systematically studied [1]. The failure process was monitored *in situ* with precise quantitative measurements of the relative displacements across the interface that were obtained with digital image correlation (DIC). An analytical cohesive shear-lag model was developed, and the interfacial modulus and strength of the h-BN/PDC interface were measured to be $5.65 \pm 1 \text{ GPa} \cdot \mu\text{m}^{-1}$ and $66.4 \pm 16.8 \text{ MPa}$, respectively. A micromechanical analysis shows that the interfacial failure in these materials is governed by the interfacial strength at small length scales, rather than the interfacial fracture energy.

Our recent work also shows that the strength / fracture toughness trade-off that occurs in the interfacial study described above and in bulk materials also extends to the fracture of 2-D materials. For example, graphene has ultrahigh intrinsic strength ($\sim 130 \text{ GPa}$) and elastic modulus ($\sim 1.0 \text{ TPa}$) but is brittle, with low fracture toughness ($\sim 4 \text{ MPa} \cdot \text{m}^{0.5}$). Hexagonal boron nitride (*h*-BN) is a dielectric 2-D material which has properties which are similar, with fracture high strength ($\sim 100 \text{ GPa}$) and elastic modulus ($\sim 0.8 \text{ TPa}$). It has long been assumed that h-BN nanosheets undergoes brittle fracture that is similar to graphene and subject to Griffith's law. Contrary to this expectation, our recent work shows that single-crystal monolayer h-BN exhibits much higher fracture toughness, with an effective energy release rate up to one order of magnitude higher than both its Griffith energy release rate and that reported for graphene [2]. Careful experiments were

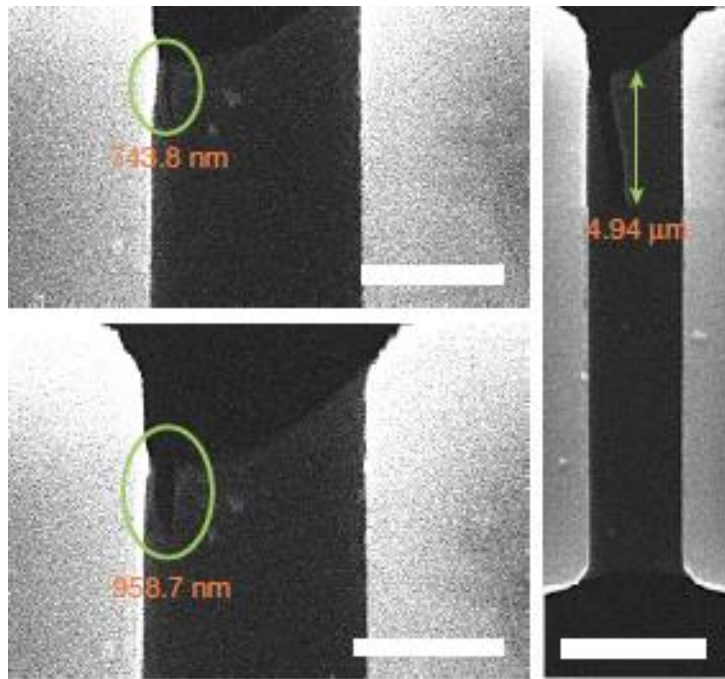


Figure. 1 SEM images showing stable crack growth from 743.8 nm to 958.7 nm and then 4.94 μm under increasing external loading. Scale bars: 2 μm left; 5 μm right

conducted to investigate stable crack propagation in monolayer *h*-BN (Figure 1). These measurements allowed us to measure the corresponding fracture resistance curves. In this material, crack deflection and branching occurs repeatedly due to asymmetry at the edge of the *h*-BN sheets, leading to asymmetry in the elastic properties at the crack tip and edge swapping during crack propagation. This mechanism toughens the *h*-BN and enables stable crack propagation. Our *in situ* experimental observations and the corresponding analysis suggest that there are added practical benefits and potential new technological opportunities for the use of monolayer *h*-BN.

Recent work in this program has also focused on evaluating the efficacy of using micron scale cantilevers and pillars for small scale mechanical testing. Others have employed these methods (primarily for monolithic materials), and our goal is to successfully apply them to nanocomposites. Detailed evaluation of these approaches demonstrates that accurate quantitative interpretation requires finite element modeling (even for monolithic materials), and that machine learning approaches can significantly improve the analysis methodologies [3,4].

Future Plans

The recent work on evaluating pull-out and fracture of *h*-BN nanosheets provides important new information about the mechanical behavior of these materials at small length scales. These measurements have turned out to be more tractable with *h*-BN rather than *r*-GO. Thus, to develop a full understanding of toughening in nanocomposites, we will focus new efforts on producing and testing full *h*-BN reinforced nanocomposites (produced by spark plasma sintering). The mechanical behavior (particularly the toughness) of these materials will then be carefully investigated with different methods. This will include the small testing methods that are described above, along with *in situ* SEM observations of crack growth and *R*-curve measurements. A detailed model of fracture in these materials will be aligned with the combined experimental results for both individual *h*-BN nanosheets and the full *h*-BN reinforced nanocomposites. Ultimately,

we will also conduct a full parallel investigation r-GO reinforced ceramics, based on analogous experiments and modeling for these materials.

References

1. B. Zhang, X. Liu, H. Guo, K. Yang, B. W. Sheldon, H. Gao, J. Lou, “Quantitative in-situ study of strength governed interfacial failure between h-BN and polymer-derived ceramic,” *Acta Materialia* **210**, 116832 (2021).
2. Y. Yang, Z. Song, G. Lu, Q. Zhang, B. Zhang, B. Ni, C. Wang, X. Li, L. Gu, X. Xie, H. Gao, and J. Lou, “Intrinsic toughening and stable crack propagation in hexagonal boron nitride,” *Nature* **594**, 57 (2021).
3. X. Liu, C. E. Athanasiou, N. P. Padture, B. W. Sheldon, and H. Gao, “A machine learning approach to fracture mechanics problems,” *Acta Materialia* **190**, 105 (2020).
4. C. E. Athanasiou, X. Liu, B. Zhang, T. Cai, C. Ramirez, N. P. Padture, J. Lou, B. W. Sheldon, and H. Gao, “Integrated simulation, machine learning, and experimental approach to characterizing fracture instability in indentation pillar-splitting of materials,” *J. Mech. Phys. Solids*, in press (2022).

Publications

- X. Liu, C. E. Athanasiou, N. P. Padture, B. W. Sheldon, and H. Gao, “A machine learning approach to fracture mechanics problems,” *Acta Materialia* **190**, 105 (2020).
- C. E. Athanasiou, T. Baba, C. Ramirez, H. Zhang, J. Xi, W. Zhang, N. P. Padture, I. Szlufarska, and B. W. Sheldon, "High toughness nanoreinforced ceramics via ion implantation," *Carbon* **163**, 169 (2020).
- Q. Wang, C. Ramirez, C.S. Watts, O. Borrero-Lopez, A.L. Ortiz, B.W. Sheldon, and N.P. Padture, "Fracture, fatigue, and sliding-wear behavior of nanocomposites of alumina and reduced graphene-oxide," *Acta Materialia* **186**, 9, (2020).
- C. E. Athanasiou, M. Y. Jin, C. Ramirez, N. P. Padture, and B. W. Sheldon, “High toughness inorganic solid electrolytes via the use of reduced graphene-oxide,” *Matter* **3**, 212 (2020).
- Y. Yang, Z. Song, G. Lu, Q. Zhang, B. Zhang, B. Ni, C. Wang, X. Li, L. Gu, X. Xie, H. Gao, and J. Lou, “Intrinsic toughening and stable crack propagation in hexagonal boron nitride,” *Nature* **594**, 57 (2021).
- Q. Wang , C.S. Watts , C.E. Athanasiou, Z. Dai, M. Hu, B.W. Sheldon, and N.P. Padture , "The effect of atmosphere on the flash-sintering of nanoscale titania ceramics," *Scripta Materialia* **199**, 113894 (2021).
- X. Liu, C. E. Athanasiou, N. P. Padture, B. W. Sheldon, and H. Gao, “Knowledge extraction and transfer in data-driven fracture mechanics,” *Proceedings National Academy of Sciences* **118**, e21047651 (2021).
- B. Zhang, X. Liu, H. Guo, K. Yang, B. W. Sheldon, H. Gao, and J. Lou, “Quantitative *in situ* study of strength governed interfacial failure between h-BN and polymer-derived ceramic,” *Acta Materialia* **210**, 116832 (2021).
- B. Ni, D. Steinbach, Z. Yang, A. Lew, B. Zhang, Q. Fang, M.J. Buehler, J. Lou, “Fracture at the two-dimensional limit,” *MRS Bulletin*, in press (2022).
- C.E. Athanasiou, X. Liu, B. Zhang, T. Cai, C. Ramirez, N.P. Padture, J. Lou, B.W. Sheldon, and H. Gao, “Integrated simulation, machine learning, and experimental approach to characterizing fracture instability in indentation pillar-splitting of materials,” *J. Mech. Phys. Solids*, in press (2022).
- Z. Dai, S. Li, X. Liu, M. Chen, C. E. Athanasiou, B. W. Sheldon, H. Gao, P. Guo, and N. P. Padture, “Dual-interface reinforced flexible perovskite solar cells for enhanced performance and mechanical reliability,” *Advanced Materials*, in press (2022).

Dynamic Fracture in Dealloying Induced Stress-Corrosion Cracking

Karl Sieradzki and Qingguo Bai, Arizona State University

Keywords: Dealloying, Nanoporous gold, Stress corrosion cracking

Research Scope

Our research is focused on understanding the detailed mechanism of stress-corrosion cracking (SCC) of model alloys such as Ag-Au. When exposed to acid electrolytes, electrochemical dealloying of silver results in the formation of nanoporous Au (NPG). In previous work, we demonstrated that monolithic NPG can undergo dynamic fracture at speeds of 200 ms^{-1} or about 0.5 of the Rayleigh speed [1]. During SCC of these alloys a NPG layer forms on the surface of these alloys that cracks, leading to the formation of a dominant crack. Within the “process zone” ahead of the crack another layer of NPG forms and the crack extends. Depending on the volume of the process zone and loading conditions, as a result of crack dynamics, the crack can extend significant distances past the process zone, into the un-dealloyed material. This process is discontinuous: a nanoporous process-zone forms around the new location of the crack, the crack propagates, and a new dealloyed process zone develops.

It is also now well known that NPG undergoes a sample-size dependent brittle/ductile transition [2,3]. For samples containing about 10^{12} gold ligaments of mean ligament diameter 100 nm or less, fracture of NPG is brittle, but as the number of ligaments in the sample is reduced, the fracture is ductile. We believe that a similar process must be operating within the nanoporous process zone that develops in front of a dominant crack during SCC. For small process zones, as measured by the number of ligaments within the volume, the behavior should be ductile and the corresponding cracking should be continuous and determined only by the current density characterizing the dealloying process. However, under suitable mechanical and dealloying conditions, large enough process zones form such that the cracking becomes discontinuous as described above.

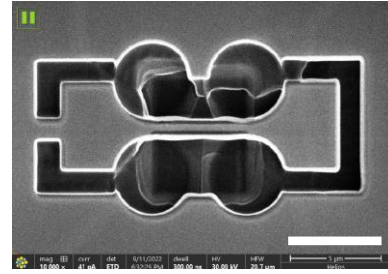
Recent Progress

In order to examine this hypothesis, we have been testing micro-scale tensile samples containing about 10^5 - 10^6 ligaments of mean ligament diameter of 40 nm. Our aim is to demonstrate that for small enough dealloyed volumes the tensile behavior is ductile. We have been using MEMS-based approaches and sputtered single-crystal Ag-Au, 1-2 μm thick films that are FIB machined in the form of dog-bone shaped samples. For the MEMS based devices we are employing, dealloying can only be accomplished under free corrosion in nitric acid prior to FIB machining. We have decided that this approach is not feasible as the yield of successful tests, as

characterized by fracture within the gage length of the sample, was only about 20%. I will discuss several reasons for the low yield of successful tests using this approach.

Future Plans

We are now transitioning to a MEMS-based push-pull device and FIB machining of NPG dog-bone single-crystal samples from bulk polycrystalline Ag-Au alloys. Since dealloying is performed prior to machining, we use electrochemical dealloying protocols developed in our group over many years. Progress on using this approach and testing of our hypothesis will be reported.



Focused Ion Beam machined dog-bone tensile sample. White bar is 10 μm .

References

1. S. Sun, X., Chen, N. Badwe, K. Sieradzki, *Nat. Mater.*, **14**, 894 (2015).
2. R. Li, K. Sieradzki, *Phys. Rev. Lett.*, **68**, 1168 (1992).
3. N. Badwe, X. Chen, K. Sieradzki, *Acta Mater.*, **129**, 251, (2017).

Publications

Xiying, Chen, Erin Karasz, Nilech Badwe, Karl Sieradzki, *Dynamic fracture and dealloying induced stress-corrosion cracking*, *Corrosion Science*, **187**, 109503 (2021).

Micromechanics of Migrating Interfaces: Martensitic Transformations

Ryan Sills, Department of Materials Science and Engineering, Rutgers University

Keywords: interfacial dislocation, disconnection, martensite, Frank-Bilby equation

Research Scope

The overall goal of this project is to quantify the relative roles of nucleation and growth of martensite to the overall rate of deformation-induced martensite transformation in steels. The primary research technique is molecular dynamics (MD) simulations, and the guiding hypothesis is that bulk and interfacial line defects—including dislocations and disconnections—dominate the nucleation and growth mechanisms. The current research scope has two major focuses: (1) insertion of specific line defect arrays in MD in order to enable quantification of phase boundary energy and mobility and (2) analysis of stability of martensitic nuclei as a function of geometry, stress, and temperature.

Recent Progress

In the first year of the project, we have focused on (1) identifying candidate defect arrays which may be present at migrating interfaces and (2) constructing a new tool for analyzing these line defects. In addition, we have leveraged other related projects to make discoveries in the areas of martensite nucleation, grain boundary complexion transitions, and dislocation wall formation.

In terms of identifying candidate defect arrays, Frank-Bilby (FB) theory provides a well-established approach. Specifically, the FB equation provides a tool for identifying line defect arrays which relieve the misfit and misorientation across a given coherent interface. There are two issues in applying FB theory to interfaces containing disconnections: (1) for a given set of Burgers vectors, many possible solutions to the FB equation exist and (2) the habit plane of the interface changes as the disconnection spacing is changed. Recently, Sanghaleh and Demkowicz [1] developed a tool called AIDA (Automated Identification of Dislocation Arrays) which exhaustively enumerates these solutions, thereby resolving issue (1) for interfaces containing dislocations. We have further solved issue (2) by extending AIDA to also solve for interfaces containing disconnection arrays. The key step is enforcement of self-consistency in the habit plane normal vector, so that the habit plane used to solve the FB equation is the same as the habit plane which results from solution of the equation. We call

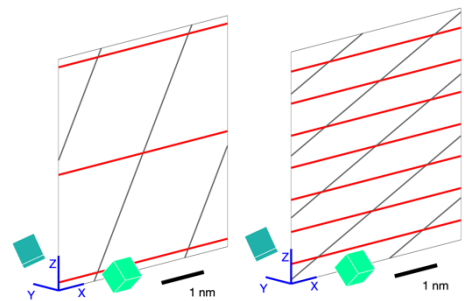


Figure 1. Line defect arrays obtained via the AIDADA code. (left) Without enforcing self-consistency in the habit plane and (right) with self-consistency. Red lines are disconnections.

the new code AIDADA (Automated Identification of Dislocation And Disconnection Arrays). Figure 1 shows an example solution obtained with AIDADA for the Nishiyama-Wasserman (NW) interface in Fe, demonstrating how the solution changes significantly upon enforcement of self-consistency.

A major challenge in MD simulation of interfaces is the identification and characterization of line defects. The dislocation extraction algorithm (DXA) is used pervasively in analysis of bulk dislocations, and was also previously extended to the case of interfacial line defects [2]. However, the user must fully define the interfacial structure in order to use it. Often, this structure is unknown and/or multiple distinct interfacial structures may exist, or may vary depending on the choice of interatomic potential. Hence, it is highly desirable to have a tool which can be used to analyze interfacial line defects which does not require user input on the interface structure. In collaboration with Alexander Stukowski at OVITO GmbH, we have developed exactly such a tool which we called ILDA (Interfacial Line Defect Analyzer). The major innovation in ILDA compared to DXA

is that we first identify coincidence sites in the interface and then use these sites to construct Burgers circuits. By coupling this approach with a surface mesh of the interfaces in a simulation, all interfacial line defects—including dislocations, disconnections, and steps—

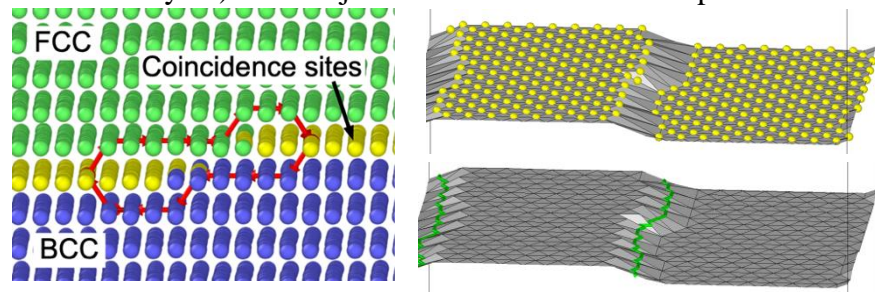


Figure 2. Depiction of the ILDA approach. (left) Burgers circuits connecting interfacial coincidence sites (yellow atoms). (right) Interfacial surface mesh connecting coincidence sites (top) and extracted disconnection lines (top).

can be identified, characterized, and localized in terms of line position and direction, Burgers vector, and step height. An example simulation for the NW interface in Fe is shown in Figure 2, where a disconnection is present whose motion causes the phase boundary to migrate. ILDA is able to identify the line position, Burgers vector, and step height of the phase boundary disconnection. No other tool is capable of analyzing a phase boundary in this way. We are preparing a manuscript to detail the new method, and will also release the code so that other researchers can utilize it. We anticipate that ILDA will have a significant impact on the interface research community.

In austenitic stainless steels, it is well established that the BCC (α') martensite phase nucleates at intersections between twin and/or HCP (ϵ) martensite slip bands. However, the precise atomic mechanism underlying this transformation has not been revealed previously. In collaboration with Xiaowang Zhou and Doug Medlin at Sandia National Labs in Livermore, we performed slip band intersection MD simulations and observed nucleation of α' martensite (see Figure 3). The orientation relationship which we observe between the γ - ϵ - α' phases matches that observed experimentally and is of the NW type [3]. To reveal the transformation mechanism, we

examine the ε - α' interface in-depth and find that coherency is established between the $(1\ 1\ 0)_{\alpha'}$ and $(0\ \bar{1}\ 1\ 1)_{\varepsilon}$ (pyramidal) planes. Furthermore, the transformation proceeds via migration of steps in the interface, likely disconnections (see Figure 3). Examining the state of coherency between these planes reveals that coherency requires a partially non-affine distortion that gives rise to a corrugated terrace plane geometry (see Figure 3). To our knowledge, a partially non-affine coherent interface of this kind has never been observed. We are in the process of applying the ILDA tool to analyze this interface and identify the disconnections which mediate transformation.

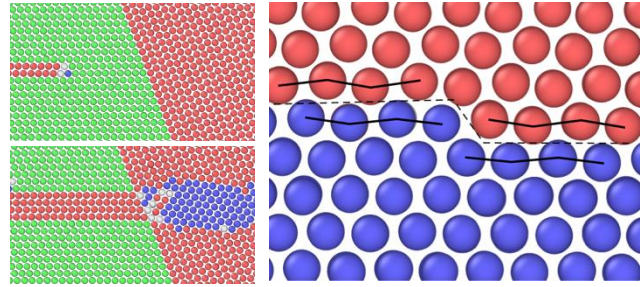


Figure 3. (left) α' -martensite nucleation at an ε -martensite slip band intersection in an Fe-Ni-Cr alloy. (right) Corrugated interface structure between α' and ε showing an interface step. green = FCC, blue = BCC, red = HCP

As a side project for undergraduate students, students have been performing simulations of grain boundary (GB) fracture in Al. While analyzing these simulations, we discovered a new phenomenon, whereby the GB structure transforms at the crack tip (see Figure 4). In different symmetric tilt GBs we observe that sometimes this transformation accelerates fracture, and sometimes it retards fracture. Recent research has revealed that these structures, called grain boundary phases or complexions, behave like distinct thermodynamic phases and that transformation from one phase to another may be dislocation mediated [4]. Analysis of the shear strain field associated with transformation reveals that the transformation is driven by migration of an edge dislocation in the boundary. In the future we hope to apply the ILDA tool to analyze these line defects.

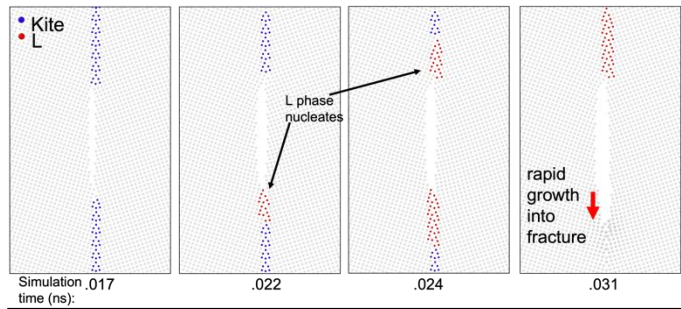


Figure 4. GB fracture simulation at a symmetric tilt $\Sigma 5(310)$ grain boundary in Al. The boundary starts in the “kite” phase, and then under applied load transitions to the “L” phase which precipitates final fracture.

Finally, leveraging progress made in a previous project, we completed a study on the formation of dislocation wall structures. Using a technique recently developed by the PI called Monte Carlo-Discrete Dislocation Dynamics (MC-DDD) [5], we demonstrated that dislocation wall structures of confined thickness can be self-stabilized by mutual short-range attractive elastic interactions. On the other hand, internal noise from long-range interactions causes the wall to thicken. These discoveries have strong implications for dislocation patterning and recrystallization.

Future Plans

Our first task this year will be to publish all of the research findings presented above. Secondly, we will perform a study to quantify the energy, stability, and mobility of martensitic interfaces containing different interfacial line defect structures. We are currently developing the ability to insert specific line defect arrays into an MD cell containing a martensitic interface. We will select these arrays based on output from the AIDADA code developed above. With these arrays inserted, we will vary the thermodynamic driving force for boundary migration to compute the interfacial mobility (velocity versus driving force). Thirdly, we will assess the stability of martensitic nuclei as a function of stress and temperature. We will insert nuclei of various sizes and geometries, and then vary the thermodynamic force on the nucleus to find the critical force needed stabilize it. These two studies will provide basic kinetic and thermodynamic insights necessary to predict the martensitic transformation rate.

References

1. A. Sangghaleh and M. J. Demkowicz, *AIDA: A tool for exhaustive enumeration of solutions to the quantized Frank-Bilby equation*, Computational Materials Science **145**, 35-47 (2018).
2. A. Stukowski, V. V. Bulatov, and A. Arsenlis, *Automated identification and indexing of dislocations in crystal interfaces*, Modell. Simul. Mater. Sci. Eng. **20**, 085007 (2012).
3. C. X. Huang, G. Lang, Y. L. Gao, S. D. Wu, and S. X. Li, Investigation on the nucleation mechanism of deformation-induced martensite in an austenitic stainless steel under severe plastic deformation, J. Mater. Res. **22**, 724-729 (2007).
4. T. Meiners, T. Frolov, R. E. Rudd, G. Dehm, and C. H. Liebscher, *Observations of grain-boundary phase transformations in an elemental metal*, Nature **579**, 375-378 (2020).
5. N. Deka and R. B. Sills, *Monte Carlo-Discrete Dislocation Dynamics: a technique for studying the formation and evolution of dislocation structures*, Modell. Simul. Mater. Sci. Eng. **30**, 024002 (2022).

Publications

1. N. Deka, C. Alleman, D. L. Medlin, and R. B. Sills, *Energy and Stochasticity: The Yin and Yang of Dislocation Patterning*, Submitted.
2. N. Deka, A. Stukowski, and R. B. Sills, *Automated Analysis of Interfacial Dislocations and Disconnections*, In Preparation.
3. D. Gordon, Y. Li, and R. B. Sills, *Self-consistent Solution of the Frank-Bilby Equation with Terraced Interfaces*, In Preparation.

Localizing energy dissipation in molecular dynamics simulations of nanostructured elastomers

David S. Simmons, Department of Chemical, Biological, and Materials Engineering, University of South Florida

Keywords: Nanocomposite, Polymer, Energy Dissipation, Toughness, Molecular Dynamics Simulation

Research Scope

Introduction of nanoparticles to elastomers and other polymers can greatly enhance mechanical toughness, an effect essential for a wide range of material

applications demanding mechanical robustness under load. At high (nonlinear) strain, the primary mechanism of this enhancement is a dramatic enhancement in energy dissipation. However, the precise molecular mechanism by which this enhanced energy dissipation occurs remains unsettled. Perhaps the central reason for this lack of understanding is an inability to resolve the questions of *where* and *when* energy is dissipated, at a microscopic level, during elastomeric nanocomposite deformation. Is the primary origin of dissipation direct particle-particle friction? Is it plastic deformation of glassy domains induced by surface interactions in gaps between particles? Is it the dragging of polymer chains across the surface, or dissipation linked to transient physical crosslinking of chains by particles? Each of these mechanisms (see Figure 1) has been proposed in the literature¹⁻³; the conditions (if any) under which each dominates remain unresolved.

The goal of this project is to resolve the nanoscale mechanisms of enhanced energy dissipation underlying nonlinear mechanical response in elastomeric nanocomposites. In order to do so, we aim to employ molecular dynamics simulations of deforming nanocomposites in order to isolate the time and location of energy dissipation events. Even in molecular simulation, this is a profoundly challenging problem. While molecular dynamics simulations innately provide information on molecular positions and motion, there is no established method for extracting temporally and spatially localized information on energy dissipation events. Since energy dissipation is essentially understandable in terms of entropy generation (irreversibility) this demands either a highly local means of decomposing nonlinear mechanical response into reversible and irreversible components, or a mechanism of effectively detecting entropy generation or energy dissipation thermodynamically. This proposal aims to establish new methods of both of these types to extract localized information on energy dissipation.

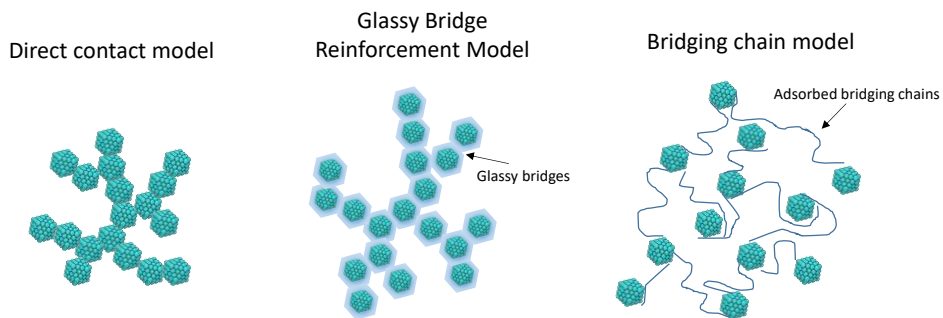


Figure 1. Proposed models of nanoparticle reinforcement of soft polymers: percolation via direct nanoparticle contacts; percolation via glassy polymer bridges between particles; and percolation via tie or interentangled chains.

In parallel to this methods development work, we will simulate nonlinear deformation in nanofilled elastomers over a range of variables implicated in controlling the roles of the mechanisms postulated above. These include the nanoparticle fractal dimension, nanoparticle loading, temperature, and particle-polymer interactions. Together with resolution of dissipative events, this matrix of simulations spanning key variables will enable us to tease out the relative roles of particle-particle friction, glassy bridge effects, and chain dragging, and establish a predictive understanding of how their interplay drives nonlinear mechanical response in these materials.

More broadly, polymer nanocomposites can be thought of the archetypal example of a broad class of ‘hybrid soft solids’ in which a material is comprised of interpenetrating rigid and soft microdomains. Other examples include glassy/rubbery block copolymers and semicrystalline polymers: in all of these materials, an interplay between the two phases mechanical response, interfacial alterations in properties, and the question of how the two domains fail under high strain, interconnect to control overall material mechanical response. The methods and physical insights developed in this work will thus lay a groundwork for advances in the understanding and design of hybrid soft solids more generally. Such advances could have considerable impacts, from emerging solid-state electrolytes of interest for next generation batteries, to separations membranes that require both toughness and high permeability, to tires, gaskets, and other high-volume elastomeric materials that underpin and mediate durability and efficiency in much of the energy and transportation economy.

Recent Progress

Recent and ongoing work on this project is focused on (1) initiation of new nanocomposite simulations (see Figure 2) and (2) development and validation of molecular dynamics simulation methods for quantification of energy dissipation at a spatially and temporally localized level. In particular, we aim to identify local energy dissipation by measuring local heating and subtracting off contributions attributable to reversible entropic heating, enabling computation of irreversible dissipative entropic heating only. In an isothermal molecular dynamics simulation, this can be done by computing the heat removed by the thermostat (the algorithm that maintains a constant temperature) as a function of time. As an initial test of this idea, we have employed this approach to compute the storage and loss moduli of an elastomer under oscillatory deformation, *from the heat flow rather than from the stress response*. Combined solution of energy and entropy balances in this situation, combined with the definitions of the storage and loss moduli, lead to the following relation between cumulative heat flow and complex modulus in the linear response regime:



Figure 2. Rendering of a nanocomposite simulation (note all particles are full icosahedra but are visually truncated by the rendering plane). Green beads are polymer segments; gold beads comprise nanoparticles.

$$-Q - \dot{Q}_{ne}t = \frac{\gamma_0^2 V}{4} \left[2G'' \omega t + G'' \sin(2\omega t) + 2G' (\sin \omega t)^2 \right], \quad (1)$$

where $-Q$ is total (integrated) heat removed by the thermostat, γ_0 is the strain amplitude of the oscillatory deformation, V is the volume of the system, G' and G'' are the storage and loss moduli, and ω is frequency. Here \dot{Q}_{ne} is heating attributable to energy generation by numerical error, an effect that can be reduced by reducing simulation timesteps but cannot be eliminated. To compute \dot{Q}_{ne} and allow for its removal from the overall signal, we perform simulations of the same system in a quiescent state and determine the rate of heat generation from numerical error. We then effectively treat this as a background, and we subtract it from the heat flow signal prior to fitting as indicated in equation (1).

As shown in Figure 3a based on this equation, one can fit integrated heat flow data to this form, employing G' and G'' as fit parameters. The functional form describes the overwhelming majority of the variation in the heat data ($R^2 > 0.999$). As shown in Figure 3c, the resulting values of G' and G'' determined from heat flow are in excellent agreement with values determined from simulated stress measurements (Figure 3b), indicating that both the overall method and subtraction of the numerical error background are successful.

In parallel to these thermal calculations, we are also computing alterations in chain conformational entropy during deformation. At very low deformation rates, we expect the reversible entropy change in the system to be dictated by the molecular strain of individual polymer strands, summed over the full system:

$$S_{rev}(t) - S_{rev,0} = -\sum_i \frac{3}{2} k \frac{(\lambda_{x,i}^2 - 1)R_{x0,i}^2 + (\lambda_{y,i}^2 - 1)R_{y0,i}^2 + (\lambda_{z,i}^2 - 1)R_{z0,i}^2}{Nb^2} \quad (2)$$

Where $\lambda_{j,i}$ is the elongation ratio of the i^{th} chain in the j^{th} direction, N is the number of segments per chain, b is the segment size, k is Boltzmann's constant, and the sum is over all polymer strands comprising the elastomer network. Combining this known result with thermodynamic balances indicates that this calculation can in turn be related to the storage modulus a

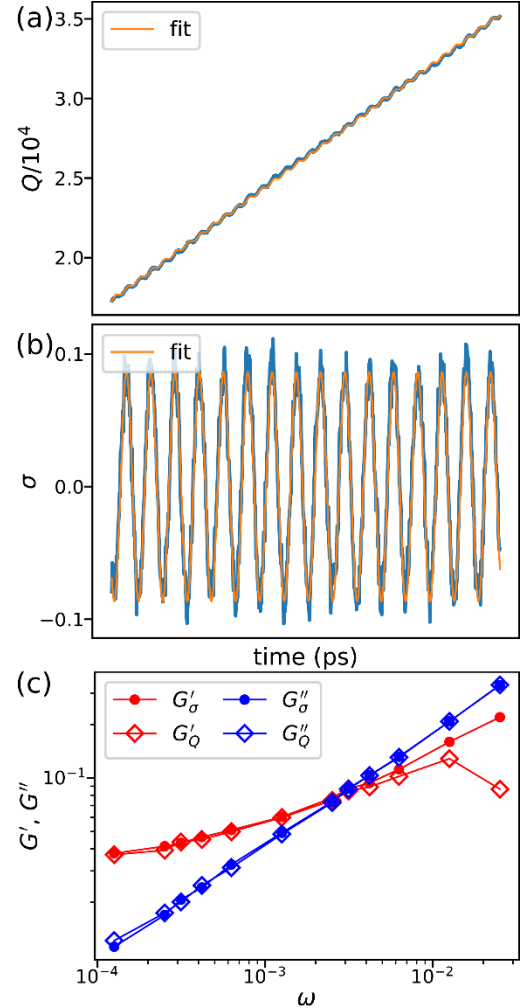


Figure 3. Top: total heat removed from the system by the thermostat during oscillatory deformation vs. time (in blue) and fit of these data to equation (1) (orange). Middle: Stress vs time (blue) during oscillatory deformation and fit to a sinusoid (orange). Bottom: storage and loss moduli as a function of oscillation frequency, as obtained from heat removed Q and from stress σ , as denoted in legend.

$$S_{rev}(t) - S_{rev,0} = -\frac{\gamma_0^2 V}{4T} 2G'(\sin \omega t)^2 \quad (3)$$

Extending to nonlinear strain, balance equations indicate that one can obtain the entropy generation (and thus dissipation) by combining the chain entropy calculation with heat measurements, as

$$TS_{gen} = T(S_{rev}(t) - S_{rev,0}) - Q \quad (4)$$

Future Plans

Our preliminary results suggest that the above approach linking chain deformation to reversible heating is correct to leading order. However, we have not yet completed simulations at low enough rates for equation (2) to hold exactly; at higher rates, higher normal mode deformation of polymer chains increases the entropy cost of deformation. We are currently extending this theoretical framework to account for higher normal mode deformation effects in order to become quantitative at more conveniently accessible deformation rates in simulation.

While these calculations presently are performed at the level of the entire simulation box, they will soon be extended to local calculations. To do so, we will apply multiple thermostats to the system, each to a distinct spatial region within the box. This will enable calculation of the heat removed from various types of regions in the box, such as polymer domains between particles vs domains near single particles vs domains far from particles. A complication here is the possibility of thermal transport between domains at rates high enough to perturb local measurements. However, initial calculations suggest that the heat transport rate in our model polymer will likely be low enough to render such effects second order at most.

Additionally, we are developing a parallel method in which the same information is extracted from local heating at constant energy, rather than from the thermostat heat extraction at local temperature. These two methods will be validated in a system involving a well-defined viscosity gradient, representing a idealized gap between two nanoparticles, such that the expected energy dissipation gradient will be well-known. After validation against known dissipation gradients in the linear regime, this will be extended to the nonlinear regime. These calculations will then be applied to full-scale elastomer nanocomposite simulations spanning the matrix of the key variables expected to underpin energy dissipation mechanisms in these systems.

References

1. Zhu, Z., Thompson, T., Wang, S.-Q., von Meerwall, E. D. & Halasa, A. Investigating Linear and Nonlinear Viscoelastic Behavior Using Model Silica-Particle-Filled Polybutadiene. *Macromolecules* **38**, 8816–8824 (2005).
2. Chen, Q., Gong, S., Moll, J., Zhao, D., Kumar, S. K. & Colby, R. H. Mechanical Reinforcement of Polymer Nanocomposites from Percolation of a Nanoparticle Network. *ACS Macro Lett.* **4**, 398–402 (2015).
3. Merabia, S., Sotta, P. & Long, D. R. A Microscopic Model for the Reinforcement and the Nonlinear Behavior of Filled Elastomers and Thermoplastic Elastomers (Payne and Mullins Effects). *Macromolecules* **41**, 8252–8266 (2008).

Role of nanoscale coherent precipitates on the thermo-mechanical response of martensitic materials

Alejandro Strachan (PI), Michael Titus (Co-PI)

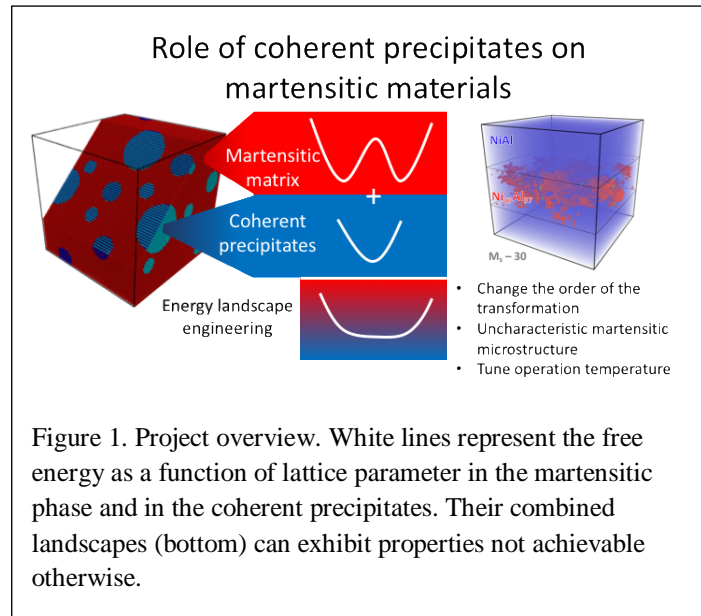
School of Materials Engineering, Purdue University, Indiana USA

Keywords: martensite microstructure, martensitic phase transition, coherent precipitates, molecular dynamics, density functional theory

Research Scope

Martensitic phase transitions are first-order, diffusionless, solid-to-solid, transformations that underlie shape memory, superelasticity, and strengthening in modern steels, impacting a wide range of technologies. While shape memory and superelasticity in traditional alloys are well understood from a mechanistic point of view, recent unexpected results by our group and others indicate a much richer set of phenomena yet to be characterized and with significant potential to result in unprecedented properties. Specifically, martensitic materials with coherent precipitates or nanoscale variations in composition have been experimentally shown to exhibit uncharacteristic martensite microstructures, broad diffraction patterns, anomalous softening and continuous stress-induced transformation [1]. From an applied point of view, ultra-high fatigue resistance [2] and low stiffness with high strength [3] have been demonstrated in martensites with coherent second phases. Our team demonstrated the ability to control the hysteresis and temperature of the phase transition [4,5], and the design of metamaterials with ultra-low stiffness [3]. We predicted Young's moduli as low as 2GPa, a value typical of soft materials, in full density and strength metallic nanomaterials. This remarkable result is possible by the stabilization of a thermodynamically unstable state with negative stiffness via interfacial stresses caused by a coherent second phase.

This effort seeks to provide a mechanistic understanding of how coherent precipitates and other second phases can be used to tune the properties of martensitic transformations, see Figure 1. Ongoing efforts include fundamental studies using density functional theory and studies of microstructural effects using large-scale molecular dynamics. In addition, an experimental effort on a NiTiHfAl alloy demonstrated how nanoprecipitates affect the martensitic transformation characteristics.



Recent Progress

This presentation summarizes the main results of our team over the last two years and is organized along three complementary topics.

Energy landscape engineering via coherent laminates

Several studies have shown that the coherent integration of a second, non-transforming phase in martensitic materials can result in unprecedented thermo-mechanical properties. Density functional theory calculations have shown the power of this approach via two applications. The first is associated with increasing the transformation temperature of Mg-Sc shape memory alloys, attractive for a wide range of applications due to their low density but limited by a low martensitic transformation temperature (173 K). Compressive strain along $[100]$ and tensile strain along $[0\bar{1}1]$ on the closest packed plane (011) stabilize the martensite phase with respect to austenite. Bi-axial strain between 5 and 7% increases the zero-temperature energy difference between the phases by over 60%. Similar stabilization of the martensite phase can be achieved by the addition of pure Mg as a coherent second phase. Superlattices with 50 at.% Mg result in an energy difference of 18.1 meV/atom between the two phases at zero temperature. These results indicate that coherency strains can be used to increase the martensitic transformation and operation temperature of Mg-Sc alloys to room temperature.[8] In a related study, we demonstrated the possibility of martensitic transformation by epitaxially combining two non-transforming materials, Mg (hexagonal closed packed) and MgLi (body centered cubic). Density functional theory calculations predict that MgLi/Mg superlattices undergo a transformation crystallographically equivalent to MgSc alloys and can be expected to result in finite temperature shape memory behavior. We predicted the zero-temperature energy of the martensite phase to be 9.3 meV/atom lower than austenite for a 50–50 at. % MgLi/Mg nanolaminate, which is expected to result in a martensitic transformation temperature of approximately 150 K. This energy difference can be tuned between 4.9 and 18.1 meV/atom by varying the fraction of the pure Mg phase in the superlattice, potentially enabling the transformation from cryogenic to room and higher temperatures. While Li diffusion might limit the applications of the systems proposed, this work opens the door to a new approach to creating martensitic materials.[9]

Uncovering the role of nanoscale precipitates on martensitic transformation and superelasticity

We characterized the role of coherent nanoscale B2 Ni₅₀Al₅₀ precipitates on the temperature- and stress-induced martensitic phase transformation in nanocrystalline Ni₆₃Al₃₇ shape memory alloys using multi-million-atoms molecular dynamics (MD) simulations.[8] We studied two types of precipitates: one with single crystal precipitates (SXP) and a second where grain boundaries cut through precipitates (PXP). Simulations reveal that the presence of B2 precipitates stabilizes the cyclic flag-shaped stress-strain response, characteristic of superelasticity, and reduces remnant strain. In contrast, single-phase nanocrystalline Ni₆₃Al₃₇ exhibits degradation of the reverse transformation during cyclic loading and, eventually,

incomplete reversible transformation within a few cycles. This is consistent with previous experimental findings of ultra-low fatigue in Ni-Ti-Cu alloys with Ti₂Cu precipitates. The simulations reveal that the presence of precipitates significantly improves the reversibility of the transformation by acting as elastic zones that partially shield the martensitic transformation and drive the reverse transformation. A detailed analysis of the MD trajectories reveals that the martensitic transformation of the matrix induces ultra-large elastic deformation in some of the B2 precipitates (approximately 12%) to the point of resulting in a martensite-like atomic structure.

Control of martensitic transformation temperatures through Heusler phase precipitation in a NiTiHf-based shape memory alloy

Significant effort has been devoted to tuning properties of martensitic transformations via compositional optimization, but recent computational and experimental work showed the great potential of utilizing nanoscale precipitates to affect the underlying free energy landscape that governs the transformation behavior and tune properties. Based on electronic structure calculations, we designed a NiTiHfAl alloy engineered to evolve coherent Ni₂TiAl Heusler precipitates upon heat treatment. This second phase is expected to stabilize the high-temperature austenite phase and, consequently, decrease the martensitic transformation temperature. The alloys were fabricated via arc melting and characterization via transmission electron microscopy (TEM) and energy-dispersive X-ray spectroscopy (EDS) confirms the expected microstructural evolution with heat treatment time. Differential scanning calorimetry (DSC) confirms the engineered depression of transformation temperature with heat treatment time as nanoscale precipitates nucleate and grow. This is followed by an abrupt increase in transformation temperature when anneal time exceeds 200 h at 700 °C. We attribute this increase to the loss of coherency between the precipitates and matrix which weakens their mechanical coupling.

Future Plans

Ongoing efforts involve the completion of the experimental work described above, specifically a more detailed characterization of the phases present via diffraction studies and the characterization of mechanical properties via nanoindentation and dynamic mechanical analysis. On the simulation side, the team is exploring the effect of dislocations on the martensitic transformation temperature and microstructure.

References

- [1] Hao, Y. L. et al. Superelasticity and Tunable Thermal Expansion across a Wide Temperature Range. *Journal of Materials Science & Technology* 32, 705–709 (2016).
- [2] Chluba, C. et al. Ultralow-fatigue shape memory alloy films. *Science*. 348, 1004–1007 (2015).
- [3] Reeve, S. T., Belessiotis-Richards, A. & Strachan, A. Harnessing mechanical instabilities at the nanoscale to achieve ultra-low stiffness metals. *Nat. Commun.* 8, 1137 (2017).

[4] Guda Vishnu, K. & Strachan, A. Shape memory metamaterials with tunable thermo-mechanical response via hetero-epitaxial integration: A molecular dynamics study. *J. Appl. Phys.* 113, 103503 (2013).

[5] Reeve, S. T., Guda Vishnu, K., Belessiotis-Richards, A. & Strachan, A. Tunability of martensitic behavior through coherent nanoprecipitates and other nanostructures. *Acta Materialia* 154, 295-302 (2018).

Publications

[6] Tripathi S, Vishnu KG, Titus MS, Strachan A. Tunability of martensitic transformation in Mg-Sc shape memory alloys: A DFT study. *Acta Materialia*. 2020 May 1;189:1-9.

[7] Tripathi S, Titus MS, Strachan A. Martensitic transformation in superlattices of two non-transforming metals. *Journal of Applied Physics*. 2021 Oct 28;130(16):165105.

[8] Tripathi S, Vishnu KG, Titus MS, Strachan A. Uncovering the role of nanoscale precipitates on martensitic transformation and superelasticity. *Acta Materialia*. 2022 May 1;229:117790.

Radiation effects and corrosion in carbides and borides

Izabela Szlufarska, Department of Materials Science & Engineering, University of Wisconsin - Madison

Keywords: RIS, corrosion, mechanochemistry, MAB phases

Research Scope

In materials with covalent or partially-covalent bonding, radiation-induced defects are characterized by a complex energy landscape, which in turn can have a profound impact on rates and mechanisms of radiation damage recovery. Specifically, in addition to migration energy barriers, defects in covalently-bonded materials can have non-negligible energy barriers to recombination. These barriers both set the critical amorphization temperature and drive an unbalanced flux of defects to interfaces such as grain boundaries (GBs), leading to significant radiation-induced segregation (RIS). The goal of this project is to discover general trends and fundamental principles that control behavior of radiation-induced defects in a broad class of materials with covalent bonding (focusing on carbides and borides) and on the role of interfaces in radiation resistance of such materials. The scientific questions pursued in this project are centered on understanding the role of off-stoichiometry (radiation-induced or inherent to the material), the role of the type of bonding (carbon vs. boron, metallic vs. covalent bonding, bond networks, 3D layering, etc.), and the role of interfaces on radiation damage recovery. In particular, coupling of the complex defect energy landscape to the radiation-induced evolution of interfaces provides opportunities for new fundamental discoveries of the role of interfaces and for design of new materials with superior radiation resistance.

Recent Progress

In this report, I would like to highlight the following major accomplishments:

1. ***Coupling of corrosion and radiation in carbides:*** Building on our earlier discovery of radiation-induced segregation (RIS) of constituent elements in ceramics¹, we have now demonstrated experimentally and in simulations, that RIS in ceramics has a significant impact on

corrosion resistance. Specifically, we have previously demonstrated that general GBs in SiC are inherently depleted in C (by as much as 4%). During radiation, C segregates to GBs, to the point where the GB can become carbon rich. We have now investigated unirradiated and irradiated high-quality SiC bicrystals to study the coupling of radiation and GB corrosion. The samples were irradiated with 6.0 MeV Si ions with a fluence of 7.5×10^{16} ions/cm² at 300 °C. Subsequently, both unirradiated and irradiated bicrystals were subjected to a corrosion test in an autoclave at 360°C with O₂ content less than 10 ppb. Surprisingly, we found that the irradiated GB have a

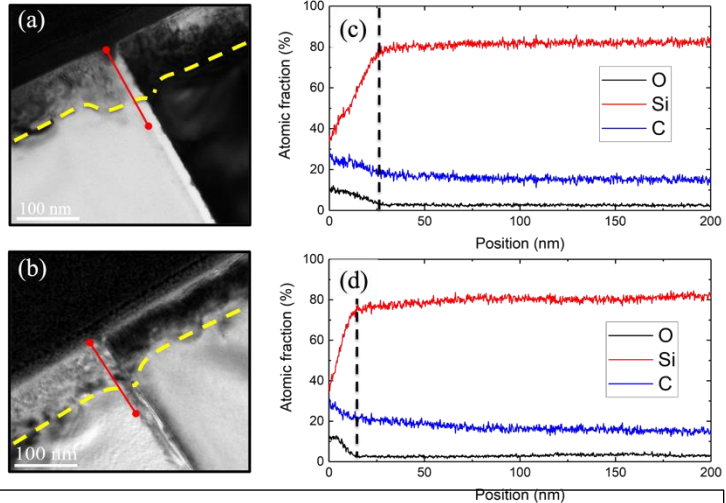


Fig. 1. TEM images and EDS spectra of the corroded bicrystal SiC samples with and without irradiation for 30 days. (a) and (b) are the TEM images of the corroded samples at 0 dpa and 3 dpa, respectively. (c) and (d) are the atomic percentage distributions of Si, C, and O determined from the EDS as a function of distance from the surface to the bulk near the GB region in the samples at 0 dpa and 3 dpa, respectively.

reduced corrosion rate. This effect is shown in Fig. 1., where compositional analysis based on EDS spectra reveals that the thickness of the corrosion region in the non-irradiated sample is larger than in the irradiated sample. In addition, our EDS analysis confirmed that the concentration of C species at GB in the irradiated sample is increased compared with the non-irradiated sample, providing further evidence of RIS in the bicrystal SiC samples. Our experimental studies demonstrate for the first time that RIS can suppress hydrothermal corrosion of SiC grain boundaries. Similar results have been observed in our atomistic simulations. The impact of C on corrosion resistance is not limited to GBs and we have explained it by investigating models of C- and Si-rich amorphous SiC samples using *ab initio* calculations.

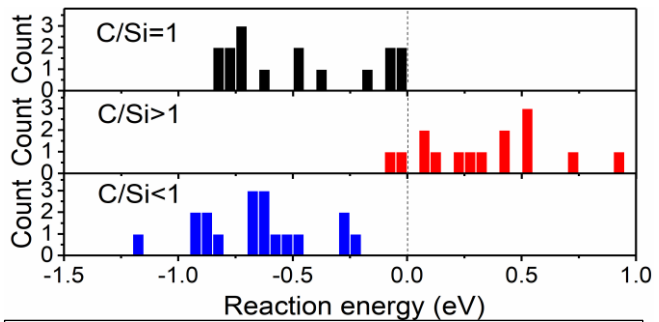


Fig. 2. Distribution of reaction energy for the hydrogen scission reaction in a-SiC with different stoichiometric conditions. Here C/Si=1, >1, and <1 represent the stoichiometric, C-rich, and Si-rich systems, respectively.

In the process of investigating the impact of radiation-induced changes in stoichiometry, we have made a fundamental discovery that the rate of surface reactions can be controlled by bulk properties, and more specifically by materials stiffness. This contrasts with what has been typically assumed that surface corrosion reactions are controlled by electronic states right at the reactive

site. The discovery was made based on *ab initio* calculations of water and oxygen reactions with stress-free amorphous SiC (*a*-SiC). The effect of bulk stiffness on surface corrosion reactivity was demonstrated by considering hydrogen scission reaction and oxygen incorporation reaction during corrosion of *a*-SiC in water and air². We chose *a*-SiC as a model of disordered general GB in SiC. We considered three different *a*-SiC systems: stoichiometric, Si-rich, and C-rich. As shown in Fig. 2, the reaction energies for C-rich system ($C/Si > 1$) are positive and higher than for the stoichiometric ($C/Si = 1$) and Si-rich ($C/Si < 1$) systems. This result demonstrates that C suppresses corrosion of SiC in water. We have further found that the major contribution to the variation of reaction energy in systems with different stoichiometries comes from the changes in the mechanical relaxation of the surrounding solid, rather than from the changes in the electronic energy associated with broken surface bonds. As C-rich system has the highest stiffness, the relaxation of energy after reaction is lowest in this system, which means that the reaction is least favorable³.

2. **Radiation effects in MAB phases (3D layered ternary borides):** MAB phases are layered ternary transition metal borides (M: transition metal, A: group III-A elements, B: B), which have been found to exhibit excellent properties, including hardness, thermal and electrical conductivities, and oxidation resistance. The layered structures of MAB phases (Fig. 3) resemble that of MAX phases, which have been shown to have highly effective defect recovery processes and excellent resistance to radiation-induced amorphization. In addition, MAB phases can be synthesized with a wide variety of M elements as well as different topologies of B networks, which creates a vast space for chemical and structural design of materials with potentially superior radiation resistance. In this study, my group combined experimental characterization based on the TEM and *ab initio* calculations to identified MAB phase materials with promising resistance to radiation and corrosion. We have also developed design rules with respect to the

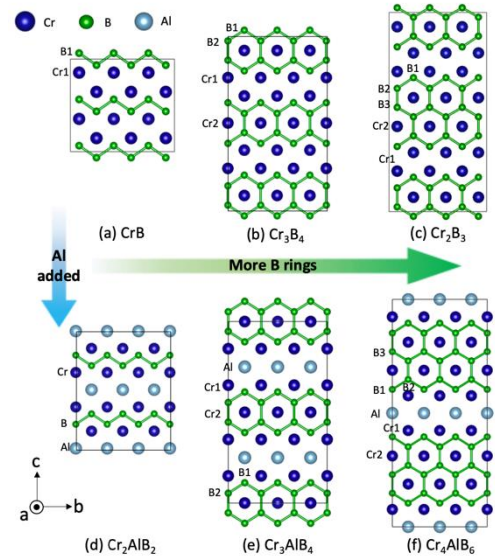


Fig. 3 Cr-B binary and Cr-Al-B ternary borides: (a) CrB, (b) Cr₃B₄, (c) Cr₂B₃, (d) Cr₂AlB₂, (e) Cr₃AlB₄, and (f) Cr₄AlB₆. The structures differ by B network and/or Al layer

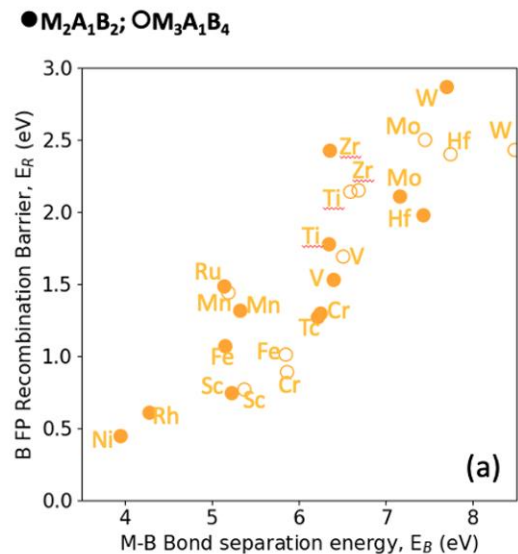


Figure 4 (a) B FP recombination (E_R) versus M-B bond separation energies (E_B), (b) schematic picture of B FP recombination process in $M_2A_1B_2$ and $M_3A_1B_4$.

transition metal and the B network. For example, we have determined that MAB compositions with two Al layers per unit cell will readily undergo radiation-induced amorphization because M interstitials are unstable in a double-Al layer. As soon as the primary knock-on atom creates a M Frenkel pair (FP), M interstitial will be transformed to and immobilized as M_{Al} antisite, producing an Al interstitial. M_{Al} have high formation energies, yet they cannot be easily annealed out, leading to a fast accumulation of damage, and driving disordering transition. We have also found that compositions with a single B chain structure (Fig. 3e) will have a better radiation resistance than those with two-chain structures (Fig. 3f) and that radiation resistance of materials with a zigzag B structure (Fig. 3d) is the worst among the different B networks. The underlying reason is the effect the B network has on recombination of B FP. We have also found that there is a correlation of the energy barrier to recombination of B FP with the strength of the M-B bond (Fig. 4) and the materials with the lowest M-B strength are predicted to have the best radiation resistance. We have also identified Cr_4AlB_3 as a promising material for applications that involve radiation and corrosion. Radiation resistance of this MAB phase is comparable to the binary Cr_4B_3 phase, but we found that the MAB phase has a significantly better corrosion resistance.

3. Multi-layered engineering of carbides with respect to radiation resistance:

We have shown that in ceramics, more interfaces does not necessarily lead to better radiation resistance and that radiation-induced phase transformation in Ti_3SiC_2 (3D layered carbide/MAX phase) can be improved by engineering multilayers or through precipitates of TiC. As shown in Fig. 5, we found that interface with SiC reduces resistance of Ti_3SiC_2 to phase transformation, whereas the interface with TiC enhances this resistance. The results were explained using *ab initio* calculations.

Future Plans: We are currently investigating RIS in binary borides to extract more general rules for the mechanisms controlling RIS in ceramics. In the future, we plan to extend our studies of radiation effects in high entropy ceramics (carbides and/or borides).

References

1. X. Wang, H. Zhang, T. Baba, H. Jiang, C. Liu, Y. Guan, O. Elleuch, T. Kuech, D. Morgan, P. Voyles, I. Szlufarska, *Radiation-induced segregation in a ceramic*, Nature Materials **9**, 992 (2020)
2. J. Xi, C. Liu, D. Morgan, I. Szlufarska, *An unexpected role of H during SiC corrosion in water*, J. Phys. Chem. C, **124**, 9394 (2020)
3. J. Xi and I. Szlufarska, *Control of surface chemical reactions through solid stiffness*, Phys. Rev. Lett. **129**, 106101 (2022)

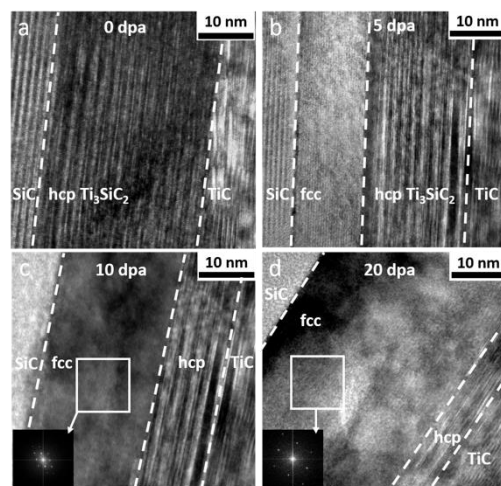


Fig. 5 HRTEM of SiC/ Ti_3SiC_2 /TiC multilayer irradiated at 150C using C ions. Images a, b, c, and d correspond to an increasing radiation dose and they reveal a growing hcp phase in Ti_3SiC_2 , which starts at the SiC interface.

Publications

1. J. Y. Kim, H. Zhang, J. Xi, I. Szlufarska, *Trends in behavior of point defects in MB and MAB phases*, Chemistry of Materials, To be published (2022)
2. J. Y. Kim, L. Gelczuk, M. P. Polak, D. Hlushchenko, D. Morgan, R. Kudrawiec, I. Szlufarska, *Native deep-level defects in transition metal dichalcogenides – experimental verification of theoretical predictions*, npj 2D Materials and Applications, To be published (2022)
3. J. Xi and I. Szlufarska, *Control of surface chemical reactions through solid stiffness*, Phys. Rev. Lett. **129**, 106101 (2022)
4. J. Y. Kim, H. Zhang, R. Su, J. Xi, S. Wei, P. Richardson, L. Liu, E. Kisi, J. H. Perepezko, I. Szlufarska, *Defect recovery processes in Cr-B binary and Cr-Al-B MAB phases: structure-dependent radiation tolerance*, Acta Materialia **235**, 118099 (2022)
5. J. Y. Kim, J. Xi, H. Zhang, I. Szlufarska, *Defect chemistry of Cr-B binary and Cr-Al-B MAB phases: Effects of covalently bonded B networks*, Phys. Rev. Mater. **5**, 113603 (2021)
6. H. Zhang, J. Xi, R. Su, X. Hu, JY Kim, S. Wei, C. Zhang, L. Shi, I. Szlufarska, *Enhancing the phase stability of ceramics under radiation via multilayer engineering*, Science Advances **7**, eabg7678 (2021)
7. J. Xi, C. Liu, I. Szlufarska, *Effects of point defect on oxidation of 3C-SiC*, J. Nucl. Mater. **538**, 152308 (September 2020)
8. H. Zhang, J. Y. Kim, R. Su, P. Richardson, J. Xi, E. Kisi, J. O'Connor, L. Shi, I. Szlufarska, *Defect behavior and radiation tolerance of MAB phases (MoAlB and Fe₂AlB₂) with comparison to MAX phases*, Acta Mater. **196**, 505 (September 2020)
9. C. Athanasiou, H. Zhang, C. Ramirez, J. Xi, T. Baba, X. Wang, W. Zhang, N. P. Padture, I. Szlufarska, B. Sheldon, *High toughness carbon-nanotube-reinforced ceramics via ion-beam engineering of interfaces*, Carbon **163**, 169 (August, 2020)
10. X. Wang, H. Zhang, T. Baba, H. Jiang, C. Liu, Y. Guan, O. Elleuch, T. Kuech, D. Morgan, P. Voyles, I. Szlufarska, *Radiation-induced segregation in a ceramic*, Nature Materials **9**, 992 (May, 2020)
11. J. Xi, C. Liu, D. Morgan, I. Szlufarska, *An unexpected role of H during SiC corrosion in water*, J. Phys. Chem. C, **124**, 9394 (April, 2020)

Grain Boundary Microstates: Exploring the Metastability of Sink Efficiency

Mitra Taheri, Johns Hopkins University, Michael Falk (Johns Hopkins University), Jaime Marian (UCLA), and David Srolovitz (University of Pennsylvania/University of Hong Kong)

Keywords: Grain boundary, metastable, microstate, defect, compositionally complex

Research Scope

Harnessing metastability to tailor radiation damage tolerance [1] is an important goal outlined in the *Basic Research Needs (BRN) Workshop for Future Nuclear Energy* report. A key challenge in bounding metastability is characterizing materials far from equilibrium. This project builds on a framework developed to understand defects in relation to metastable interfaces using a combination of theory and experiment to tackle the challenge parameterizing interfacial dynamics and resulting metastable GB states under irradiation. Our work leverages foundational understanding of GB efficiency regimes and explores the concept of how the GB and the nearby vicinity determine this efficiency.

The design of materials that incorporate self-healing or self-mitigating strategies through control of sink strength and chemical complexity are of critical importance. One such material class is high entropy alloys (HEAs), also known as compositionally complex alloys (CCAs). *The proposed multi-PI effort seeks to define how metastability is tuned by variable defect bias in CCAs. In such materials possessing a complex energetic landscape, we hypothesize that the role of the GB vicinity, in addition to the GB itself, is of paramount importance. We hypothesize that metastability thresholds in GB sink efficiency are diffuse in contrast to their counterparts in dilute alloys, which are sharp.*

To address our hypothesis, we will leverage our toolset of multiscale modeling/simulation, experiment, and machine learning tools, paving a pathway to more predictive design and optimization of reactor materials. Our approach will allow for otherwise “unseen” grain boundary structures and order landscapes to be utilized for key outcomes such as radiation tolerance, providing new insight into these critical material systems, as outlined in the *BRN Workshop for Scientific Machine Learning: Core Technologies for Artificial Intelligence*.

Recent Progress

In our current program, we are addressing key questions via experiment and modeling:

1. What role do GB micro-DOFs have on point defect absorption and denuded zone formation?
2. How does GB structure evolve during irradiation and how does any such evolution impact point defect annihilation?
3. Is it possible to saturate the GB with point defects or can the GB absorb point defects continuously or perhaps cyclically?

We have developed a toolbox to understand GB microstates, GB response, and GB local structure as a function of irradiation. Several important conclusions have emerged, listed below, with several highlights elaborated in more detail following the list:

1. GB metastability exists through microstates and other microscopic DOF changes;
2. Metastability allows for absorption to persist and for GBs to continue to act as efficient sinks;
3. When defect bias in the GB region is high, the inherent ability to realize metastable states so that the GB may continue acting as a sink are stressed, and thus, can break down (which is evidence of a limit of GB metastability);
4. Evidence of the breakdown is seen in (1) the closing of the denuded zones and (2) the development of dislocation networks adjacent to the GB;
5. GB response is dictated in part by incoming defect bias landscape, which we believe dependent on material parameters, such as alloy stoichiometry and defect formation energies.

Development of a “Fingerprint for Absorption”. Results from a suite of classical molecular dynamics, temperature accelerated dynamics, and molecular statics, coupled with quantitative in situ diffraction and imaging, have provided evidence of interfaces differing in macroscopic character displaying unique defect absorption proclivities, and that the proficiency for GBs to absorb defects is not necessarily static; GBs can exhibit substantial variability even at low irradiation doses [2]. An important outcome of our current work has been the development of a “fingerprint” for these defect absorption events, linking atomistic GB response with a mesoscale descriptor using the Nye tensor formulation. We leverage this methodology throughout our work going forward.

Mechanism behind the emergence of an observable Nye tensor signal. We are testing physical mechanisms to explain the experimental detection of nonzero GND signals near grain boundaries in the irradiated nanocrystals. As demonstrated in ref [2] when a grain boundary has saturated its capacity to absorb defect loops, defects start to accumulate in its vicinity, setting themselves up for collisions with other loops. This illustrated in **Figure 1**, which assumes that the GB is no longer able to absorb any more damage.

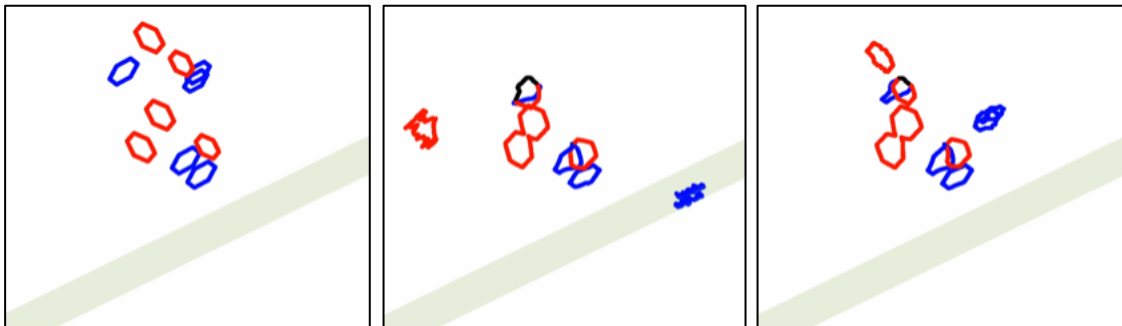


Figure 1. Three snapshots of the assembly of two families of loops (red and blue, with two different $\langle 111 \rangle$ Burgers vectors) into a ‘proto’ network simulated using Dislocation Dynamics simulations.

Specifically, the figure shows the evolution of a set of prismatic dislocation loops gliding towards a grain boundary. The loops have sizes between 2 and 4 nm across, and originate in displacement cascades in the interior of the grain. They both belong to the $\langle 111 \rangle$ Burgers vector family, one with $\mathbf{b} = \frac{1}{2}[1\bar{1}1]$ (red) and the other with $\frac{1}{2}[11\bar{1}]$ (blue). Upon contact, they can form $[100]$ junctions (in black), which are sessile. Some of the loops abut against the GB directly, which is assumed at this point to have saturated and is unable to absorb any more defects. As well, some of

the loops are seen to coalesce, creating larger loops that have a reduced mobility. The consequence of these loop reactions is the formation of an incipient dislocation network in the vicinity of the GB. Importantly, this network now gives rise to a net nonzero GND signal, as the integral of the ($\mathbf{t} \times \mathbf{b}$) product is no longer balanced along the perimeter of the resulting loops.

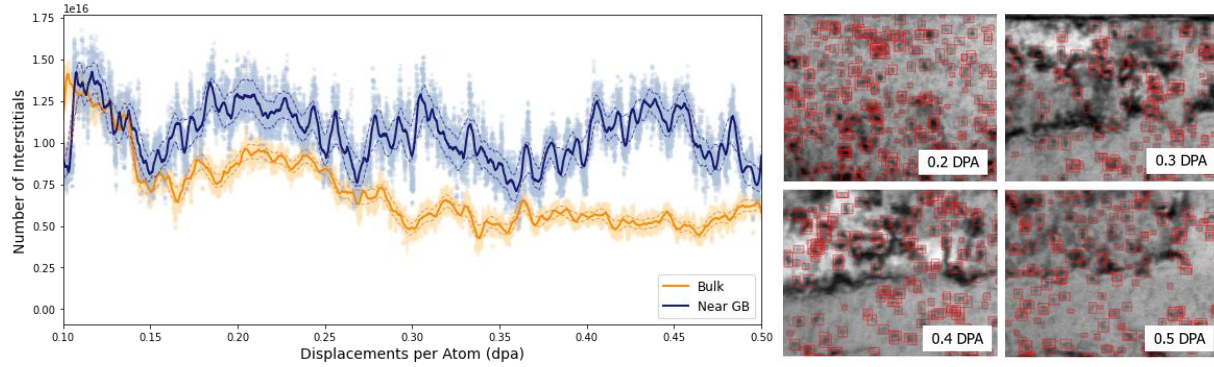


Figure 2. A) Data from YOLOv5 defect detection analysis of *in situ* TEM irradiation of a Cu bicrystal, highlighting interstitial concentration near the GB, and in the bulk region. B) Bright-field TEM images of Cu bicrystal at varying stages of radiation damage, overlain with detected defect bounding boxes as determined by YOLOv5. GB in the Cu bicrystal system is out of view at the top edge of the micrographs.

Quantification of GB Metastability Limits: Role of Defect Bias in Transient States. Through the use of the Nye Tensor fingerprinting, we were able to connect GB micro DOFs with sink efficiency [3]. Because these are microscopic and difficult to measure, they are often overlooked in descriptions of GB properties under the assumption that all boundaries with the same macroscopic character are identical. Another is the atomic density at the GB plane, which has only recently received any attention at all [1]. To reach this finding, we applied Nye Tensor analysis for a GB that experienced denuded zone collapse and see a clear correlation between GB defect density and GB effective sink efficiency [3].

Defining Regimes for GB Transient States Based on Defect Dimensionality and Bias Regimes of GB response were found to be defined not only by the GB character, but also by the damage type absorbed (single defects, clusters, or loops), resulting in system level changes. Single defects yield microstate changes while large clusters and loops give rise to disconnections. Low sigma value GBs having fewer microstates tend to be saturated after a short period of irradiation, while high sigma value GBs having multiplicity of microstates performs microstates changes to accommodate the irradiation-induced single defects over a period of time until cluster/loop absorption causing disconnection-based changes at GBs that suppress the additional defect absorption. As a result, the saturated GBs exhibit defect pileups in their neighborhoods thus building up dislocation networks. Thus, the GB state is not only a function of the GBC but perhaps more importantly the local defect production in and around the GB.

Development of Homogeneous Defect Bias in Pure and Dilute Systems. The majority of our work to date has focused on pure Fe, FeCr, and FeNi. Through various *in situ* and *ex situ* studies, we have determined that while the distribution of stable dislocation loops and clusters might vary slightly with the introduction of solute, and the dislocation loop type can be altered by temperature, both remain relatively constant for both pure and dilute systems [4]. Interestingly, this provides a

baseline for our hypothesis that CCAs will NOT exhibit a homogeneous distribution of clusters and loops, but rather due to the order-modulated energetic landscape, we would expect a much wider variation in these defects (resulting in what we refer to as a heterogeneous defect bias landscape). Moreover, our findings regarding regimes would likely show less sharp regime changes owing to the fact that all of the conclusions drawn were based on pure or dilute systems with a homogeneous defect landscape.

Utilizing Deep Learning Methods as an Indication for Sink Efficiency and Matrix Recovery. We are analyzing *in situ* microscopy video to further understand fine details regarding localized defect absorption and defect recombination at and near a grain boundary. A deep learning object detection framework (YOLOv5) was utilized to detect defects throughout *in situ* TEM irradiations [5] of a Cu bicrystal, and new analysis suggests a steady grain boundary absorptions state, with clear cycles of recombination and recovery to a stable defect concentration in the near GB matrix. We hypothesize that the data highlights the diffusivity of mobile vacancies in the presence of a steady defect sink. **Figure 2** shows an estimate on the interstitial content based on the defects detected by the YOLOv5 object detection model. The approach to a steady state condition of the bulk suggests the consistent contribution of the GB to interstitial, despite the lack of a strong defect sink as assumed by the absence of a clear denuded zone (**Figure 2B**). In addition, lack of stacking fault tetrahedra suggest the mobility of vacancies within the matrix. We hypothesize that the delayed diffusion of vacancies to recombine with interstitials in the matrix is responsible for the cycles, or momentary spikes in interstitial concentrations in the near GB region.

Future Plans

Considering that observations above hold true for pure or dilute systems, we hypothesize that the matrix defect bias, which will be significantly more heterogeneous in CCAs/HEAs, may have a profound effect in these alloys. In this context, we aim to define GB metastability in a broader context to allow for the inclusion of the matrix bias. Our hypothesis is that the regimes in which GB response leverages metastability will deviate in CCAs from that observed in pure/dilute alloys. This hypothesis is rooted in our observation of relatively homogenous defect landscapes in pure and dilute alloys, and the fact that CCAs tend to have more variable defect formation energies.

Thus, we seek to pursue the following overarching questions in our future work:

1. Will we observe more transient behavior at GBs (and thus enhanced microstate-mediated metastability) due to defect landscape heterogeneity?
2. Will this heterogeneity in defect bias spatiotemporally translate to the GB? In other words, in dilute systems, the bias should be constant, whereas in CCAs there should an increase in the heterogeneity in defect bias toward the GB by virtue of the CCA order landscape.
3. Ultimately, *will the heterogeneity allow for the GBs to leverage microstates more effectively for extended absorption efficiency?*

References

1. Han, J., Vitek, V., Srolovitz, D.J., Grain-boundary metastability and its statistical properties, *Acta Materialia* **104**, 259-273 (2016).

2. Woryk, L.M., He, S., Hopkins, E.M., Hung, C.Y., Han, J., Srolovitz, D.J., Marian, J. and Taheri, M.L., Geometrically necessary dislocation fingerprints of dislocation loop absorption at grain boundaries. *Physical Review Materials* **6(8)**, p.083804 (2022).
3. El-Atwani, O., Han, J., Leff, A.C., Hung, C.Y., Nathaniel, J.E., He, S., Hopkins, E.M., Woryk, L.M., Hattar, K., Uberuaga, B.P., Martinez, E., Marian, J., Srolovitz, D.J., Taheri M.L., Grain boundary metastability controls irradiation resistance in nanocrystalline metals, Submitted (2022).
4. Nathaniel, J.E., Vetterick, G.A., El-Atwani, O., Leff, A., Baldwin, J.K., Kirk, M.A., Hattar, K., Taheri, M.L., The influence of solute on irradiation damage evolution in nanocrystalline films. *Journal of Nuclear Materials* **543**, 152616 (2021).
5. Shen, M., Li, G., Wu, D., Yaguchi, Y., Haley, J.C., Field, K.G., Morgan, D., A deep learning based automatic defect analysis framework for in-situ TEM ion irradiations, *Computational Materials Science* **197**, 110560 (2021).

Publications

1. Woryk, L.M., He, S., Hopkins, E.M., Hung, C.Y., Han, J., Srolovitz, D.J., Marian, J. and Taheri, M.L., Geometrically necessary dislocation fingerprints of dislocation loop absorption at grain boundaries, *Physical Review Materials* **6(8)**, 083804 (2022).
2. Hung, C.Y., Vetterick, G., Hopkins, E., Balwin, J.K., Baldo, P., Kirk, M.A., Misra, A. and Taheri, M.L., Insight into defect cluster annihilation at grain boundaries in an irradiated nanocrystalline iron, *Journal of Nuclear Materials* **566**, 153761 (2022).
3. Nathaniel, J.E., El-Atwani, O., Huang, S., Marian, J., Leff, A.C., Baldwin, J.K., Hattar, K. and Taheri, M.L., Implications of Microstructure in Helium-Implanted Nanocrystalline Metals, *Materials* **15(12)**, 4092 (2022).
4. Vetterick, G., Hung, C.Y., Hopkins, E., Balwin, J.K., Baldo, P., Kirk, M.A., Misra, A., He, S., Marian, J. and Taheri, M.L., Temperature effects on the radiation damage morphology in nanocrystalline iron, *Scripta Materialia* **213**, 114607 (2022).
5. Nathaniel II, J.E., Suri, P.K., Hopkins, E.M., Wen, J., Baldo, P., Kirk, M. and Taheri, M.L., Grain boundary strain as a determinant of localized sink efficiency, *Acta Materialia* **226**, 117624 (2022).
6. Hart, J.L., Hantanasirisakul, K., Lang, A.C., Li, Y., Mehmood, F., Pachter, R., Frenkel, A.I., Gogotsi, Y. and Taheri, M.L., Multimodal spectroscopic study of surface termination evolution in Cr₂TiC₂T_x MXene, *Advanced Materials Interfaces* **8(5)**, 2001789 (2021).
7. Pate, C.M., Hart, J.L. and Taheri, M.L., RapidEELS: machine learning for denoising and classification in rapid acquisition electron energy loss spectroscopy, *Scientific reports* **11(1)**, 1-10 (2021).
8. Nathaniel II, J.E., Vetterick, G.A., El-Atwani, O., Leff, A., Baldwin, J.K., Baldo, P., Kirk, M.A., Hattar, K. and Taheri, M.L., The influence of solute on irradiation damage evolution in nanocrystalline thin-films. *Journal of Nuclear Materials* **543**, 152616 (2021).
9. Suri, P.K., Nathaniel, J.E., Li, N., Baldwin, J.K., Wang, Y., Hattar, K. and Taheri, M.L., Ion irradiation induced phase transformation in gold nanocrystalline films, *Scientific reports* **10(1)**, 1-10 (2020).
10. Anber, E.A., Foley, D., Lang, A.C., Nathaniel, J., Hart, J.L., Tadjer, M.J., Hobart, K.D., Pearton, S. and Taheri, M.L., Structural transition and recovery of Ge implanted β -Ga₂O₃, *Applied Physics Letters* **117(15)**, 152101 (2020).

Irradiation Defect Formation and Evolution in Doped Metallic Interfaces

Jason R. Trelewicz, Stony Brook University; Andrea M. Hodge, University of Southern California; David J. Sprouster, Stony Brook University

Keywords: interfaces, grain boundaries, irradiation, gas behavior, solute segregation

Research Scope

The scope of this research project is to address knowledge gaps related to the following scientific questions: (i) how are the mechanisms of bubble formation and evolution in interfaces impacted by the presence of a dopant species introduced to stabilize the interfacial network, and (ii) what is the connection to interfacial structure particularly in interphase boundaries containing high excess free volume relative to the crystalline matrix? The overarching hypothesis is at doped metallic interfaces, changes in the local energy landscape due to chemical contributions from the solute species and corresponding structural transitions will dictate the critical impurity concentration for gas bubble nucleation. The project team is employing model nano-metallic multilayer (NMM) films to access two unique interfacial configurations, doped grain boundaries (DGBs) and amorphous-crystalline interfaces (ACIs), for the isolation of interfacial effects on defect microstructure formation and evolution during gas ion implantation. Multi-modal characterization techniques are being developed to probe gas behavior with a focus on atomic and nanoscale structural changes during the incubation stages of cavity formation where electron microscopy techniques are limited in quantifying clustering behavior prior to the appearance of nascent cavities. Targeted ion irradiations are planned to introduce different concentrations of helium into DGBs and ACIs with experimental results informing molecular dynamics (MD) simulations to provide atomistic insights into the mechanisms of helium cluster formation and connections with the underlying energy landscapes of the different interfaces.

Recent Progress

Aligning with our guiding hypothesis, recent progress has been focused on: (i) synthesis of NMMs containing ACIs, (ii) synchrotron X-ray analysis for the onset of cavity formation and decoupling interface from lattice defects, and (iii) atomistic simulations of helium bubble formation in doped grain boundaries. NMMs containing ACIs in the Fe-W system were synthesized via magnetron sputtering, which required iterative process optimization to overcome challenges associated with the magnetic Fe target. The resulting parameter sets enabled tunable W concentrations via control over relative sputtering rates from the different targets. Four distinct variations of the Fe/Fe-W NMMs with either Fe-rich or W-rich amorphous layers over the range of 30 at. % < X < 70 at. % were produced to investigate the effect of composition and interface thickness on microstructural stability. The TEM micrograph in Figure 1a shows the layered nanostructure where the ~5 nm thick Fe-38 at.% W amorphous layer, which is confirmed to be X-ray amorphous in the XRD pattern, appears darker relative to the ~20 nm thick Fe crystalline layers. The differential scanning calorimetry (DSC) data suggests that the multilayer systems with

thinner (5 nm) amorphous layers are more stable based on the exothermic peaks as compared with the films containing thicker (20nm) amorphous layers (not shown here). The first peak in Figure 1b corresponds to devitrification of the amorphous phase while the second peak captures the FCC to BCC transition. In the context of our hypothesis, this system will be used in helium ion implantations to investigate the role of amorphous phases and ordering transitions on helium defect accumulation and bubble dynamics.

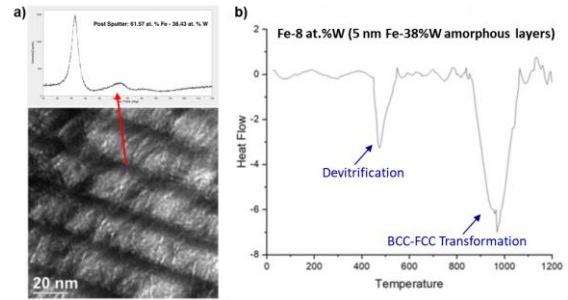


Figure 1: (a) Fe/Fe-W NMM with 20 nm thick Fe layers and 5 nm thick amorphous Fe-38 at.% W layers. The XRD pattern is specifically from the amorphous layers from glancing incidence XRD (GIXRD) (b) DSC for the sample shown in (a) with the devitrification and ferrite-to-austenite transformations identified.

In anticipation of analyzing bimodal cavity distributions that commonly form in materials containing a high density of interfaces, a multi-modal characterization approach for quantifying such size distributions including the incubation stages of helium bubble formation was developed leveraging W microstructures containing a mixture of ultrafine and nanocrystalline grains. Implantations employed 150 keV He⁺ ions at temperatures of 800 and 950°C with fluences over the range of 1x10¹⁵ - 1x10¹⁷ ions/cm². Quantified from TEM analysis, the cavity distributions are shown in Figure 2a with a bimodal distribution exhibited by the samples implanted at 950°C with large, faceted defects observed at grain boundaries and many comparatively smaller cavities distributed throughout the grain matrix. The samples implanted at 800°C had a uniform distribution of decidedly smaller cavities between the W matrix and grain boundaries.

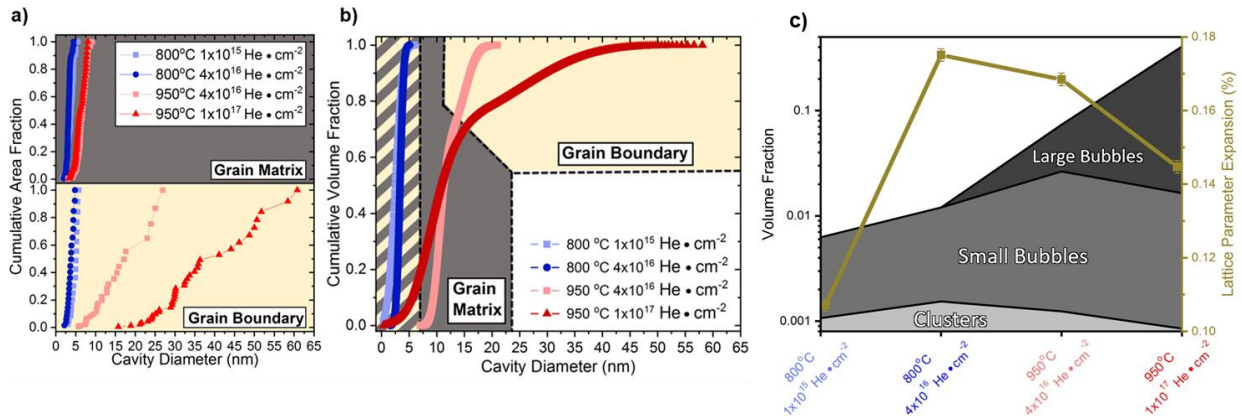


Figure 2: Cavity size distributions in helium ion implanted ultrafine grained W from (a) TEM characterization and (b) SAXS quantification with the grain matrix and boundary sizes delineated based on the bimodal distribution reported at 950 °C. (c) Volume fractions of clusters from WAXS analysis and bubbles from the TEM quantification displayed with the lattice parameter as a function of the irradiation conditions.

Refined X-ray experiments acquired 2D scattering patterns in 10 x 10 arrays on dimpled TEM disks optimized to sample the region containing the helium defects (thereby maximizing their manifestation in the absorption spectra). Following extensive processing of the scattering patterns and subsequent fitting of each spectra, the cumulative diameter distributions in Figure 2b

were extracted and shown to closely align with the distributions from TEM. Wide angle X-ray scattering (WAXS) and XRD were employed to determine the cluster volume fraction and lattice parameter expansion, respectively, which when plotted with the bubble volume fractions in Figure 2c, reveal the transition from clustering to cavity formation and its implications for swelling in the lattice (i.e., lattice parameter expansion) as a function of the irradiation conditions. These techniques will be applied to the irradiated DGB and ACI containing NMMs to probe the transition from helium clustering to cavity nucleation and growth as a function of interfacial doping aligned with our hypothesis.

The effect of doping on the formation of helium bubbles in grain boundaries were explored through MD simulations of a $\Sigma 5<100>$ tilt grain boundary in Fe with the amount of Cu doping varied to probe single, bi-, and tri-layer segregation. Helium atoms preferentially occupy grain boundary sites [1, 2] with the formation of interstitial clusters preceding the onset of bubble formation. Self-trapping has been shown to take place when 6 helium atoms cluster together without the formation of a Frenkel pair, but in the presence of vacancies, trap mutation results in the formation of helium-vacancy (He-V) complexes for clusters of larger size [3]. Adopting this transition from clustering to He-V complex formation, clusters of radii greater than 0.4 nm are defined as bubbles consistent with other recent studies [4] and allow bubble formation to be distinguished from clustering. Trends for different Cu grain boundary concentrations corresponding to single, bi-, and tri-layer segregation are shown in Figure 3 as a function of the average grain boundary helium concentration. The presence of Cu in the grain boundaries promoted the retention of smaller clusters (Figure 3a) with increasing helium concentration, which was accompanied by a higher density of smaller bubbles forming at a given helium concentration (Figure 3b,c). These findings suggest that the transition from clustering to bubble formation is independent of dopant concentration and in contradiction with the hypothesis that the critical impurity concentration for bubble nucleation will be dictated by doping. However, our results support the effect of doping on promoting distributed nucleation of bubbles, which in turn delays the critical concentration for grain boundary decohesion and potentially embrittlement.

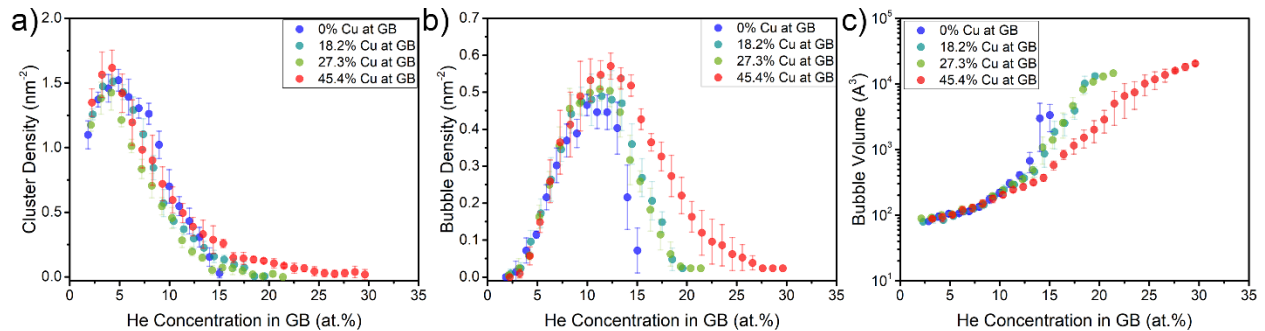


Figure 3: Helium defect density and size distributions as a function of helium concentration including (a) cluster density, (b) bubble density, and (c) bubble size. Results are from atomistic simulations of helium introduced with varying concentrations into a $\Sigma 5<100>$ tilt grain boundary doped with different concentrations of Cu (corresponding to single, bi-layer, and tri-layer segregation) relative to the pure iron grain boundary (i.e., 0% Cu).

Future Plans

Future research plans include characterization of the Fe/Fe-W NMMs in the as-deposited and annealed conditions, which will produce a matrix of samples for the helium implantation experiments. Implanted samples will be analyzed using the multi-modal approach developed under this project involving synchrotron XRD, WAXS, and SAXS in concert with focused TEM investigations. Additionally, in situ annealing experiments will be conducted on the Fe/Fe-W NMMs with thermodynamic calculations of stable segregation states performed to understand the series of configurations this system traverses as a function of temperature. Atomistic simulations are focusing on analysis of the existing simulation results on helium in Cu doped Fe grain boundaries, specifically mapping the energy landscapes, atomic strain, and their implications for defect segregation energies. This work will then be generalized to other grain boundaries selected to systematically vary the degree of structural order collectively with different dopant species to test the postulated dopant effect and further confirm that the behavior is independent of the critical impurity concentration for the formation of bubbles. Collectively mapping energy landscapes with the generalization to other grain boundaries will provide evidence to prove the postulated effect of dopants promoting distributed nucleation of bubbles – and likely disproving its role in the critical impurity concentration for the formation of bubbles. The experimental results will be analyzed in the context of the underlying mechanisms uncovered from the simulations, thereby allowing for the various components of our hypothesis to be tested and ultimately validated or disproved.

References

- [1] W.S. Cunningham, J.M. Gentile, O. El-Atwani, C.N. Taylor, M. Efe, S.A. Maloy, J.R. Trelewicz. Softening due to Grain Boundary Cavity Formation and its Competition with Hardening in Helium Implanted Nanocrystalline Tungsten, *Scientific Reports* 8 (2018) 2897.
- [2] O. El-Atwani, W.S. Cunningham, D. Perez, E. Martinez, J.R. Trelewicz, M. Li, S.A. Maloy. Temperature threshold for preferential bubble formation on grain boundaries in tungsten under in-situ helium irradiation, *Scripta Materialia* 180 (2020) 6-10.
- [3] J. Boisse, A. De Backer, C. Domain, C.S. Becquart. Modeling of the self trapping of helium and the trap mutation in tungsten using DFT and empirical potentials based on DFT, *Journal of Materials Research* 29 (2014) 2374-2386.
- [4] R. Delaporte-Mathurin, M. Ialovega, E.A. Hodille, J. Mougnot, Y. Charles, E. Bernard, C. Martin, C. Grisolia. Influence of exposure conditions on helium transport and bubble growth in tungsten, *Scientific Reports* 11 (2021) 14681.

Publications

Cunningham, W.S., Wang, W., Riano, J.S., Hodge, A.M, Trelewicz, J.R., *Unraveling Thermodynamic and Kinetic Contributions to the Stability of Nanocrystalline Alloys*, *Advanced Materials*, 2200354, (2022)

C. D. Appleget, J.S. Riaño, A.M. Hodge, “*An Overview of Nano Multilayers as Model Systems for Developing Nanoscale Microstructures*”, *Materials*, 15, 382, (2022)

Balbus, G.H., Kappacher, J., Sprouster, D.J., Wang, F., Shin, J., Eggeler, Y.M., Rupert, T.J., Trelewicz, J.R., Kiener, D., Maier-Kiener, V., Gianola, D.S., *Disordered Interfaces Enable High Temperature Thermal Stability and Strength in a Nanocrystalline Aluminum Alloy*, *Acta Materialia* 116973, (2021)

Disorder & Diffusion in Complex Oxides: Towards Prediction & Control

Matthew Janish, Cortney Kreller, Ghanshyam Pilania, Yongqiang Wang, Blas Pedro Uberuaga

Los Alamos National Laboratory

Keywords: complex oxides, radiation damage, conductivity, disordering, defect kinetics

Research Scope

To understand damage evolution in irradiated materials, it is imperative to understand how defects evolve. However, in complex oxides such as spinels, pyrochlores, and perovskites, the kinetics of defects is not a simple function of crystal structure and chemistry. As a material is irradiated, the distribution of cations changes, often from an ordered state to a disordered state. The material can undergo a phase transformation to a new structure. These changes impact the kinetic properties of those defects. This project is focused on understanding the relationship between these irradiation-induced metastable states and transport. We use irradiation as a tool to modify the structure of the material and then probe the consequences on conductivity. Experimental studies are complemented by computational modeling to provide a comprehensive view of mass transport in these systems. While in the past we have focused extensively on pyrochlores and spinels, we are shifting our attention to Ln-Ln perovskites. The phase diagrams of these Ln sesquioxides display many phases, including several that are disordered, which suggest that they may exhibit interesting behavior under irradiation. Our efforts reveal new insight into the structure-property relationship between cation ordering/disorder and mass transport, informing materials design and optimization for a wide-range of applications from nuclear energy systems to fast ion conductors.

Recent Progress

Metastability in Ln oxides: One of the consequences of irradiation is phase transformations. Irradiation introduces excess energy into a material and that ‘stored energy’ can shift the balance between the stability of different phases. However, it is still a challenge to predict what phases might be induced by irradiation, an inherently non-equilibrium phenomenon. Using DFT, we have constructed so-called metastable phase diagrams, using the Ln_2O_3 family of compounds as a prototypical system. By constructing the metastable phase diagram, we can determine the sequence of phases that would form as more stored energy is introduced into the material [1]. As highlighted in **Figure 1a**, we predict that Lu_2O_3 would transform from the cubic bixbyite C phase to first the B and then the A phase as stored energy is introduced. The only solid phase that exists in the equilibrium phase

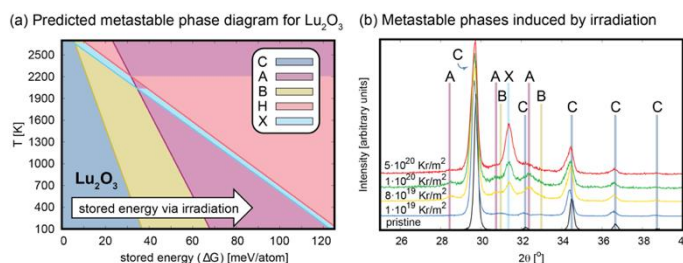


Figure 1. (a) Our predicted metastable phase diagram for Lu_2O_3 , showing how, if we gradually introduce stored energy, several phase transformations are possible. (b) GIXRD reveals that, as a function of irradiation fluence, multiple phase transformations are induced in Lu_2O_3 , as predicted.

diagram. The only solid phase that exists in the equilibrium phase diagram is the cubic bixbyite C phase. As stored energy is introduced, the system moves through the metastable phases B and A, as shown in the phase diagram. The GIXRD patterns in (b) show the evolution of the diffraction patterns as a function of irradiation fluence, with peaks corresponding to the different phases predicted in the phase diagram.

diagram for this compound is C. We have experimentally validated our predictions (**Figure 1b**) where, using low energy Kr irradiations, we have seen first the formation of the B phase and then the A and X phases with increasing fluence, just as predicted. These results not only highlight our ability to begin to predict what phases will form by irradiation, but also our ability to then control that transformation with irradiation.

Interfacial Complexity in Complex Oxides: We have studied the role that interfaces, both grain boundaries (GBs) and heterointerfaces, have in modifying cation distributions and transport. We have found that cation disorder is spatially heterogeneous, forming easier near GBs than in grain interiors. Performing Monte Carlo (MC) simulations on MgAl_2O_4 (**Figure 2a**), we found that cation disorder is easier to form at the GB [2]. This behavior occurs in real oxides as well. In recrystallized $\text{Gd}_2\text{Ti}_2\text{O}_7$ (GTO), we used 4D-scanning/transmission electron microscopy (STEM), in collaboration with the National Center for Electron Microscopy, to determine the cation disorder as a function of position. As revealed in **Figure 2b**, the level of disorder in this system is higher at the GBs than in the grain interiors. Finally, we have seen very complex response of oxide heterointerfaces under irradiation. In a series of

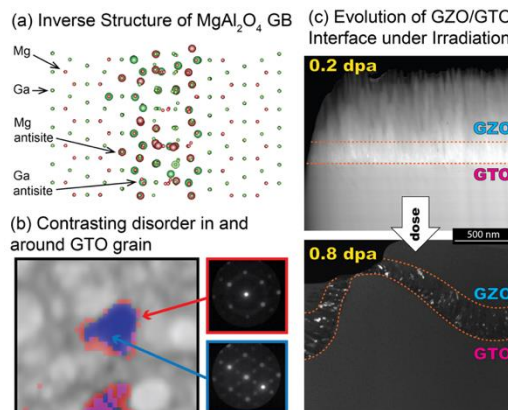


Figure 2. (a) An inverse structure forms at a GB of MgAl_2O_4 , as revealed by MC simulations. (b) In recrystallized GTO, the (blue) interior of the grains display a greater degree of ordering than the GBs (red), as indicated by the selected-area diffraction patterns. (c) The interface between GZO and GTO changes under irradiation, warping while still retaining crystallinity.

experiments [3], we synthesized a bilayer of $\text{Gd}_2\text{Zr}_2\text{O}_7$ (GZO) and GTO and irradiated the material to doses up to 0.8 dpa. As shown in **Figure 2c**, we observed several unique phenomena. The GZO, considered an amorphization resistant material, amorphized after only 0.2 dpa. We attribute this to a high density of preexisting pores in the material. However, the GZO remained crystalline at the interface. At the same time, the interface itself warped significantly, deviating from the as-synthesized flat structure into one that had undulations on the micrometer scale.

In situ Electrochemical Impedance Spectroscopy (EIS): We have developed and demonstrated an *in situ* EIS capability for measuring the conductivity of oxides as they are irradiated. **Figure 3** shows results for yttria-stabilized zirconia (YSZ), a fast ion conductor. When we study this material *ex situ*, after irradiation, we see no changes in conductivity as compared to the unirradiated material. However, *in situ*, we see the conductivity increases by a factor of 3 at 300 C. Once the beam is turned off, the material quickly recovers to its pre-irradiated state, highlighting the impact of transient defects.

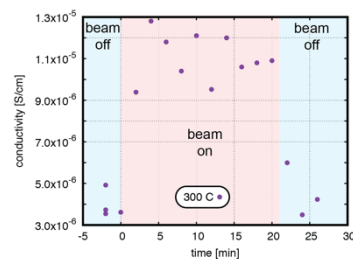


Figure 3. Results from *in situ* EIS measurements of irradiated YSZ, showing the change in conductivity as the ion beam is turned on and then turned off.

Structure and Properties of “Double” Spinels: We have discovered the possible formation of ordered “double” spinels in which the two cations on the octahedral sublattice are distinct from that on the tetrahedral sublattice and order on the octahedral sublattice. The first such compound we discovered (theoretically) was MgAlGaO_4 [4]. High-throughput DFT calculations predict the existence of several such compounds that are much more stable than MgAlGaO_4 [5]. And, using accelerated molecular dynamics simulations, we examined the kinetics of point defects in a range of Mg-Al-Ga spinel structures, finding high rates of 3+ Ga interstitial transport in some cases. This is potentially important from a battery perspective as high rates of highly charged cation transport would enable higher capacity batteries.

Future Plans

Our ongoing work focuses on four tasks that examine aspects of how irradiation modifies structure and how that modified structure impacts defect kinetics and mass transport.

Task 1: Disorder and Mass Transport in

$\text{LnLn}'\text{O}_3$ Oxides: The phase diagrams of the $\text{Ln}_2\text{O}_3+\text{Ln}'_2\text{O}_3$ oxides are rich in structure, including many disordered phases. Their propensity for disorder suggests that, upon irradiation and the large amounts of stored energy that are introduced, the material can accommodate the antisite defects that will form. In this Task, we will be using the $\text{LnLn}'\text{O}_3$ oxides as a platform for exploring how the chemical and structural changes induced by irradiation impact the mass transport characteristics of oxides. We hypothesize that (a) these compounds will exhibit higher resistance to amorphization than traditional perovskite structures due to the existence of multiple metastable states (**Figure 4**) and (b) irradiation will induce first cation disorder and then structural disorder, impacting transport mechanisms. The goal of this Task is to understand how the migration of equilibrium and non-equilibrium defects changes as the phase structure and chemistry change.

Task 2: Aliovalent Doping and the Impact on Transport in Irradiated Materials: Aliovalent doping provides opportunities to precisely control the defect content in an ionic oxide. However, how that defect content interacts with the supersaturation of defects created during irradiation is unclear. Our second Task will be to understand the impact aliovalent doping has on the response of complex oxides under irradiation. How does the high concentration of mass transport carriers impact the way the material evolves under irradiation? Will the high levels of mass transport essentially enhance the radiation tolerance of the material because of the enhanced kinetics? Two hypotheses guide this Task: (a) aliovalently-doped oxides will behave more like disordered than ordered compounds under irradiation and (b) changes in conductivity due to irradiation will be inversely related to the doping concentration. By doping LaLuO_3 to various levels with aliovalent 2+ cations, we will examine this relationship. The goal of this Task is to determine the extent to which aliovalent doping, and by extension the high concentration of carriers induced by the

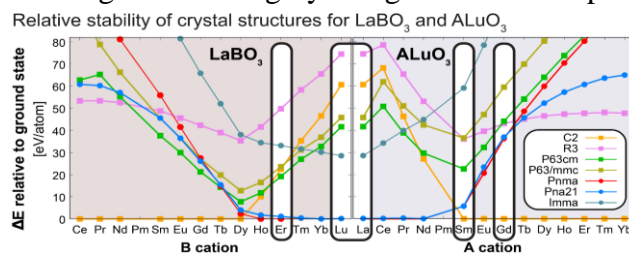


Figure 4. Predictions based on DFT calculations of the relative stability of LaBO_3 and ALuO_3 compounds. Chemistries targeted for study are highlighted.

doping, modify the radiation response of the material by changing the balance between defect generation and defect recovery.

Task 3: Oxide/Oxide Interfaces: A common theme of this project has been the interplay between interfaces (GBs and heterointerfaces), cation distributions, and defect kinetics. We will examine the role of interfaces in the evolution of cations in complex oxides near interfaces, motivated by two hypotheses: (a) the large variety of phases present in the $\text{Ln}_2\text{O}_3\text{-Ln}'_2\text{O}_3$ phase diagrams suggests that a number of new phases may form at a $\text{Ln}_2\text{O}_3/\text{Ln}'_2\text{O}_3$ interface upon irradiation and (b) the phases that form will depend on the misfit dislocation structure at the interface, which in turn depends on the chemical terminations at the interface (**Figure 5**). The goals of this Task are to identify what kinds of metastable phases form at these interfaces during irradiation and how that phase formation depends on the nature of the interface.

Task 4: Step-wise Disorder in Double Spinels: Task 4 is on double spinels. Complex oxides with multiple sublattices and multiple cations on at least one of those sublattices, such as double spinels, can exhibit multiple disordering transformations. In these materials, we will examine how disordering on just the octahedral sublattice versus combined disorder across both the octahedral and tetrahedral sublattice impacts the transport kinetics of defects and thus the rate at which the chemical order will recover. This Task is guided by two hypotheses: (a) multiple disordering transformations can be achieved in double spinels via irradiation as different sublattices disorder and (b) the transport characteristics within a double spinel will depend on which sublattices are involved in disordering. The goal is to compare how defect migration is modified by intra-sublattice versus inter-sublattice disorder.

Expected Results: Understanding how these materials evolve under irradiation begins with understanding how defects migrate within radiation-induced states. The results from the four Tasks will provide new insight into the coupling between cation disorder and mass transport in complex oxides and will aid in the design of new materials with controlled transport.

References

1. V. Kocevski, J. Valdez, B. Derby, Y. Wang, G. Pilania, and B. Uberuaga, *Predicting and Accessing Metastable Phases*, submitted.
2. B. P. Uberuaga and R. Perriot, *Spatially-Varying Inversion near Grain Boundaries in MgAl_2O_4 Spinel*, RSC Advances **10**, 11737 (2020).
3. B. Derby, Y. Sharma, J. Valdez, M. Chancey, Y. Wang, E. Brosha, D. Williams, M. Schneider, A. Chen, B. Uberuaga, C. Kreller, and M. Janish, *Interfacial Cation Mixing and Microstructural Changes in Bilayer GTO/GZO Thin Films after Irradiation*, JOM (2022). DOI: 10.1007/s11837-022-05402-0
4. G. Pilania, V. Kocevski, J. A. Valdez, C. R. Kreller, and B. P. Uberuaga, *Prediction of Structure and Cation Ordering in an Ordered Normal-Inverse Double Spinel*, Communications Materials **1**, 84 (2020).
5. V. Kocevski, G. Pilania, and B. P. Uberuaga, *High-Throughput Investigation of the Formation of Double Spinels*, Journal of Materials Chemistry A **8**, 25756 (2020).

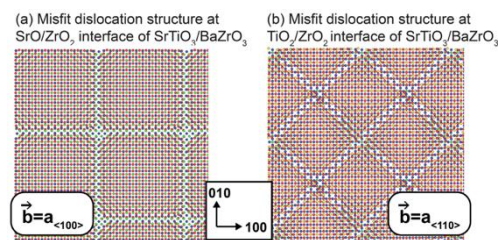


Figure 5. The misfit dislocation structure at oxide heterointerfaces depends on the chemical termination at the interface.

Publications

1. B. Derby, Y. Sharma, J. Valdez, M. Chancey, Y. Wang, E. Brosha, D. Williams, M. Schneider, A. Chen, B. Uberuaga, C. Kreller, and M. Janish, *Interfacial Cation Mixing and Microstructural Changes in Bilayer GTO/GZO Thin Films after Irradiation*, JOM (2022). DOI: 10.1007/s11837-022-05402-0
2. B. K. Derby, T. G. Holesinger, J. A. Valdez, B. P. Uberuaga, and C. R. Kreller, Microstructural Analysis of Novel $Gd_2Ti_2O_7$ Thin Films Processed via Sputter Deposition, *Materials and Design* 199, 109430 (2021).
3. V. Kocevski, G. Pilania, and B. P. Uberuaga, Modeling disorder in pyrochlores and other fluorite structural derivative oxides, *Frontiers in Chemistry* 9, 712543 (2021).
4. C. R. Kreller and B. P. Uberuaga, The role of cation ordering and disordering on mass transport in complex oxides, *Current Opinion in Solid State & Materials Science* 25, 100899 (2021).
5. M. T. Janish, M. M. Schneider, J. A. Valdez, K. J. McClellan, D. D. Byler, Y. Q. Wang, D. Chen, T. G. Holesinger, and B. P. Uberuaga, In-situ re-crystallization of heavily-irradiated $Gd_2Ti_2O_7$, *Acta Materialia* 194, 403 (2020).
6. V. Kocevski, G. P. Pilania, and B. P. Uberuaga, High-throughput investigation of the formation of double spinels, *Journal of Materials Chemistry A* 8, 25756 (2020).
7. G. Pilania, P. P. Dholabhai, and B. P. Uberuaga, Role of symmetry, geometry and termination-chemistry on misfit dislocation patterns at semicoherent oxide heterointerfaces, *Matter* 2, 1324 (2020).
8. G. Pilania, V. Kocevski, J. A. Valdez, C. R. Kreller, and B. P. Uberuaga, Prediction of Structure and Cation Ordering in an Ordered Normal-Inverse Double Spinel, *Communications Materials* 1, 84 (2020).
9. B. P. Uberuaga and R. Perriot, Spatially-Varying Inversion Near Grain Boundaries in $MgAl_2O_4$ Spinel, *RSC Advances* 10, 11737 (2020).
10. B. P. Uberuaga and G. Pilania, Inversion, Chemical Complexity, and Interstitial Transport in Spinel, *Journal of the American Ceramic Society* (2020).

Understanding the Competition between Plastic Flow and Fracture in BCC Transition Metals

Christopher R. Weinberger, Colorado State University and Gregory B. Thompson, University of Alabama

Keywords: Brittle To Ductile Transition, Fracture, Dislocations

Research Scope

The ductility and formability of body-centered-cubic (BCC) metals can vary significantly, with the origins for such differences being rather elusive. For example, molybdenum and tungsten are quite limited in their ductility and formability while niobium and tantalum easily deform. For those with limited formability, engineering solutions, such as thermomechanical processing and alloying, are primarily used improve these properties. In this program we will test the hypothesis that extrinsic point defects, *i.e.*, impurities, are more influential to the ductility of certain BCC metals than others. Through an integrated experimental and modeling approach, we will understand the origins of embrittlement regarding extrinsic impurities, both the impurity types and their concentration. The experiments will examine the change in material properties with respect to impurity level, including dislocation mobility and intrinsic fracture behavior, that will be used in a semi-analytic coupled plasticity-fracture model of the brittle-to-ductile transition temperature (BDTT). This model will enable us to fundamentally determine if and how impurities influence these BCC metals' mechanical properties lending insight into the use of alloying engineering solutions that are currently employed.

Recent Progress

The first step in understanding the role of impurities versus dislocation mobility on the brittle-to-ductile transition is through the development of a dislocation-crack model originally proposed by Giannattasio *et al.* [1]. We have successfully developed this model and have been able to simulate the BDTT in tungsten using previous dislocation mobility functions as shown in Figure 1. This model can reproduce the activation energy for this transition as well as probe the effects of model parameters on the predicted brittle-to-ductile transition. Currently, we are using a simple exponential dislocation mobility law proposed by Tarleton *et al.* [2] to predict the BDTT and its sensitivity to model inputs.

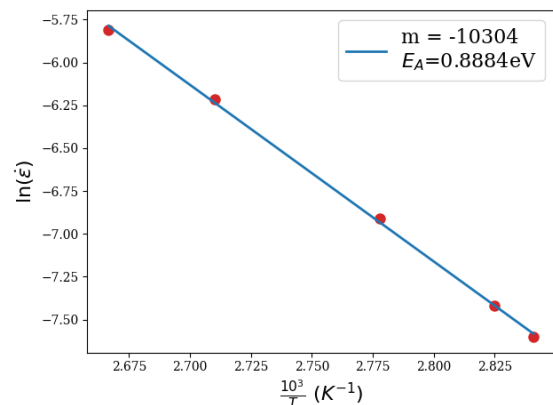


Figure 1: The logarithm of the strain rate plotted versus T^{-1}_{BDT} computed from our model to illustrate the activation energy for the brittle to ductile transition.

For example, in this model, the dislocation mobility is expressed as $v = v_0 \exp\left(-\frac{Q-\tau V}{kT}\right)$, where v_0 is the velocity prefactor, Q is the activation energy, and V is the activation volume. Values were then chosen to roughly match experiments on tungsten to predict a BDTT, T_{BDT} , between 300-400 K. We are now investigating how the v model input parameters affect the BDTT. Specifically, we are examining T_{BDT} dependency on Q , V , v_0 and their relationship on the low temperature fracture toughness K_{Ic} . Through these systematic adjustments, we are determining the model sensitivity coefficients that relate T_{BDT} .

The experimental program has focused on developing a self-contained data set of mechanical properties as a function of BCC refractory type at various impurity levels. This data will then forward feed the plasticity-fracture model of BDTT. To that end, four major tasks were performed. (1) The training of Md Tariq Islam (Graduate Research Assistant, UA) in micro-mechanical specimen preparation for K_{Ic} testing, TEM specimen preparation/microscope operation for dislocation mobility characterization, and atom probe tomography (APT) specimen preparation/instrument operation for quantifying the impurity level and spatial location. (2) Development and evaluation of focus ion-based milling procedures for micro-mechanical cantilevers for K_{Ic} measurements using either a Ga ion or Xe ion or hybrid-based method and its impact on quantitative data sets, with Figure 2 being a representative image of a tungsten sample being shaped into the required testing geometry. The aim of these milling studies is to identify potential limitations and specimen artifact effects on the measured data. (3) Installation of ambient and high temperature (up to 800 deg. C) in situ mechanical testing unit (Bruker Pi89) for K_{Ic} measurements. And (4) contaminate identification and measurement differences between various tungsten processed samples from APT. The collective training and emerging experimental work in the first year now is positioning the program to now receive self-contained, well-characterized data sets as the program enters the second year.

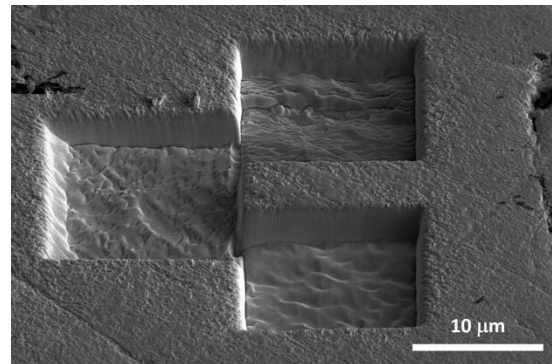


Figure 2: SEM image of a developing PFIB trrenched micro-mechanical cantilever testing geometry in a [001] orientated tungsten sample.

Future Plans

The model development will continue to completely determine the sensitivity coefficients for the simple mobility law. This is critical for understanding if changes to the dislocation mobility or fracture toughness result, as suspected with the changes in type and concentration of impurities. In addition to this modeling, we are currently fitting universal dislocation mobility activation energy curves to the available experimental data of the flow stress versus temperature. While these results will provide useful insight into the BDTT, gaps in detailed characterization and/or

especially to specific metal types is still needed remain making the development of our own, well characterized experimental data set critical. We will then use this data tied to our model to understand how the T_{BDT} changes with the new fully-parameterized dislocation mobility law for tungsten and start to compare results across the different impurity concentrations and BCC metal types. Collectively, this will enable the program in the second period of performance to begin to investigate what material properties, dislocation mobility or fracture toughness, can be responsible for the differences between the group VB and VIB metals. This will include the use of the sensitivity parameters currently being assessed to determine how much changes in K_{Ic} or differences in dislocation mobility affect the T_{BDT} .

The future plan for the experimental effort is to complete the collection of room fracture toughness measurements of different purity tungsten samples. This will be completed with the optimized milling method determined from our current work that assesses and mitigates contributions from the specimen preparation method itself. Then, K_{Ic} measurements will be carried out as a function of temperature using the same micromechanical measurements to obtain the T_{BDT} . Once self-contained tungsten data set is completed, the process will be repeated for the group VB transition metals, e.g. niobium. This will then directly given well curated experimental information from both transition group families. With completion of these fracture toughness and the T_{BDT} measurements, the experimental effort will then focus on measuring dislocation mobility in tungsten and niobium as a function of various solute impurity levels through in situ transmission electron microscopy.

References

1. A. Giannattasio , Z. Yao , E. Tarleton and S.G. Roberts, Brittle–ductile transitions in polycrystalline tungsten, *Philosophical Magazine*, **90**, 3947 (2010).
2. E. Tarleton and S.G. Roberts, Dislocation dynamic modelling of the brittle–ductile transition in tungsten, *Philosophical Magazine*, **89**, 1478 (2009).

Publications

None

Irradiation Tailoring of Deformation-Induced Phase Transformations

Janelle P. Wharry (Purdue University)

Keywords: Voids, Deformation-Induced Martensite, fcc Alloys, Phase Transformations

Research Scope

The *objective of this project is to understand how irradiation enables deformation-induced phase transformations in fcc alloys*. Low-temperature deformation of face centered cubic (fcc) metals and alloys can occur through several modes, one of which is martensitic transformation, wherein fcc γ -Fe austenite reverts to hexagonal close packed (hcp) ϵ -martensite or body centered cubic (bcc) α' -martensite. Irradiation is believed to enhance the tendency for this transformation to occur, considering that irradiation similarly enhances other low-temperature deformation modes such as dislocation channeling and deformation twinning. However, the mechanisms underlying the irradiation enhancement of martensitic transformations remain unknown. Many studies have ascribed any martensites to twinning associated with irradiation-induced dislocation loops [1-2]. But more recently, porosity has been shown to enhance the martensitic transformation in shape memory alloys [3-4] through surface energy effects. Thus, the role of both interstitial-type (e.g., loops) and vacancy-type (e.g., cavities) irradiation defects on the phase transformation must be understood. An altered tendency to phase transform can have severe implications on the performance of load-bearing materials exposed to irradiation, such as nuclear reactor structural materials. More scientifically, using irradiation to tailor the austenite-to-martensite phase transformation can facilitate materials design and innovation across numerous energy generation applications. Thus, there is a critical need to understand exactly how irradiation affects and enables the deformation-induced martensitic phase transformation.

This hypothesis will be tested using a multiscale approach that combines novel small-scale mechanical testing and *in situ* electron microscopy investigations with mechanics models that will help us interpret and expand the parametric space of our experiments. Work will focus on Fe-xMn alloys irradiated with He and/or other ions to create tailored microstructures that are dominated either by vacancy-type or interstitial-type defects, or some combination of these extremes. We will utilize small-scale mechanical testing techniques to introduce deformation. Nanoindentation will rapidly check for twinning or martensitic transformations over a range of irradiation and loading conditions, and post-indentation microstructure characterization will enable us to associate specific irradiation conditions with deformation mechanisms. Transmission electron microscopic (TEM) *in situ* deformation will reveal nano/micro-scale mechanisms of twinning and deformation-induced martensite nucleation at specific irradiation-induced defects. Molecular dynamics (MD) simulations will elucidate exactly how deformation mechanisms initiate and propagate at and around irradiation-induced defects.

Recent Progress

Experimental – We fabricated five Fe-xMn ($x = 34, 36, 39, 41, 46$ in at%) alloys that have a stable fcc austenitic structure that we believe will transform to martensite when irradiation **and**

strain are applied. Thus far, we have determined deformation mechanisms before irradiation using nanoindentation on targeted grains with subsequent focused ion beam (FIB) milling to extract transmission electron microscopy (TEM) lamellae that enable us to observe the deformation microstructure. The Fe-34Mn exhibited extensive deformation twinning, confirmed by selected area electron diffraction (SAED) at the mesoscale, with high resolution TEM (HR-TEM) revealed the atomic structure at deformation twin interfaces, and fast Fourier transformation (FFT) confirmed the twinning reflections, Figure 1(a). Near the indent (i.e., at a higher strain), deformation twins intersected with strain-induced ϵ -hcp martensite needles only a few atomic layers thick, as confirmed by streaks in the FFT pattern, Figure 1(b). Higher Mn content appeared to suppress deformation twinning and martensitic transformation in favor of dislocation-mediated deformation. In Fe-46Mn, dark field TEM of the deformation microstructure revealed a high dislocation density, especially along annealing twin boundaries, Figure 1(c-d).

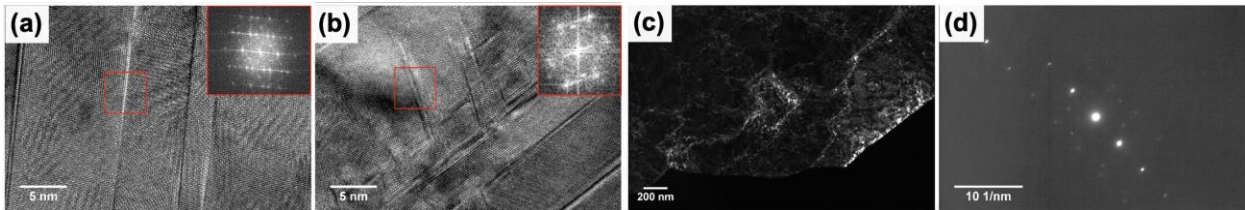


Figure 1: Nanoindentation induced deformation microstructures in (a-b) unirradiated Fe-34Mn showing HR-TEM and FFT images confirming deformation twinning; and in unirradiated Fe-46Mn showing (c) weak-beam dark field image and (d) the corresponding diffraction condition confirming dislocation-mediated deformation.

We have prepared and irradiated two sets of specimens of all five alloys. Since irradiation can compromise surface quality and subsequently make grain orientation mapping by electron backscatter diffraction (EBSD) impossible, we conducted EBSD grain orientation mapping of all five specimens in each set before irradiation. The mapped areas were marked with fiducials, and we identified at least one $\langle 100 \rangle$, $\langle 101 \rangle$, and $\langle 111 \rangle$ grain that could be identified post-irradiation. We then conducted two irradiations:

1. *Bubble-dominated microstructure:* 1 MeV He⁺ ions, 500°C, fluence 2×10^{16} ions/cm²
2. *Defect-dominated microstructure:* 2 MeV protons, 300°C, fluence 1 dpa

Simulations – An embedded-atom method (EAM) potential for Fe-Ni-Cr [5] was used to simulate strain-induced transformations in Fe-50Ni using molecular dynamics (MD). We selected this system rather than the Fe-Mn system we are studying in parallel experiments, because of a lack of a reasonable interatomic potential for Fe-Mn that can meaningfully describe fcc-bcc-hcp transformations. We set up four unique simulations that were loaded uniaxially (in the z-direction) with strain rate 0.001 ps^{-1} , to a total strain of 0.15 as follows:

1. pristine fcc single crystal – i.e., reference simulation
2. fcc single crystal with random vacancies at a concentration of 10^{-4} (atomic %)
3. fcc single crystal with 1.26 nm radius (5 atoms) spherical void at center of simulation cell
4. fcc single crystal with 2.02 nm radius (8 atoms) spherical void at center of simulation cell

Strain distributions and crystallographic orientation relationships are shown in Fig. 5 for the reference and 1.26 nm void simulations. Phase and shear strain maps of a two-dimensional slice taken parallel to the loading axis reveal that martensite phases exist wherever the shear strain is

larger than ~ 0.15 , confirming that the fcc-bcc transformation is strain-induced. High shear strain around the void (Fig. 5e) can explain the concentration of bcc phases around the void (Figs. 5c, 5f). Both the Kurdjumov-Sachs (KS) and Nishiyama-Wassermann (NW) orientation relationships (ORs) are present and are consistent across all of the simulation cells (though Fig. 5g shows only the 1.26 nm void simulation for clarity of illustration); no intermediate hcp martensite phase is found. Voids become unstable at high strains (Fig. 5h), leading to loss of material integrity, which explains the peaks in the stress-strain and bcc%-strain curves in the voided simulations.

The effect of vacancies on the strain-induced martensite transformation is not sufficiently significant to resolve, at least at the vacancy concentrations studied. By contrast, voids aid in the martensite transformation. In order for the fcc-to-bcc transformation to occur, local stress must reach a critical value to induce $1/6\{111\}\langle 211\rangle_{\text{FCC}}$ partial dislocation generation and movement. A void can cause stress concentration, increasing the likelihood that local stresses reach the critical value needed for partial dislocation generation and sliding. Additionally, strain may accumulate at the void, as the void acts as an obstacle for dislocation movement.

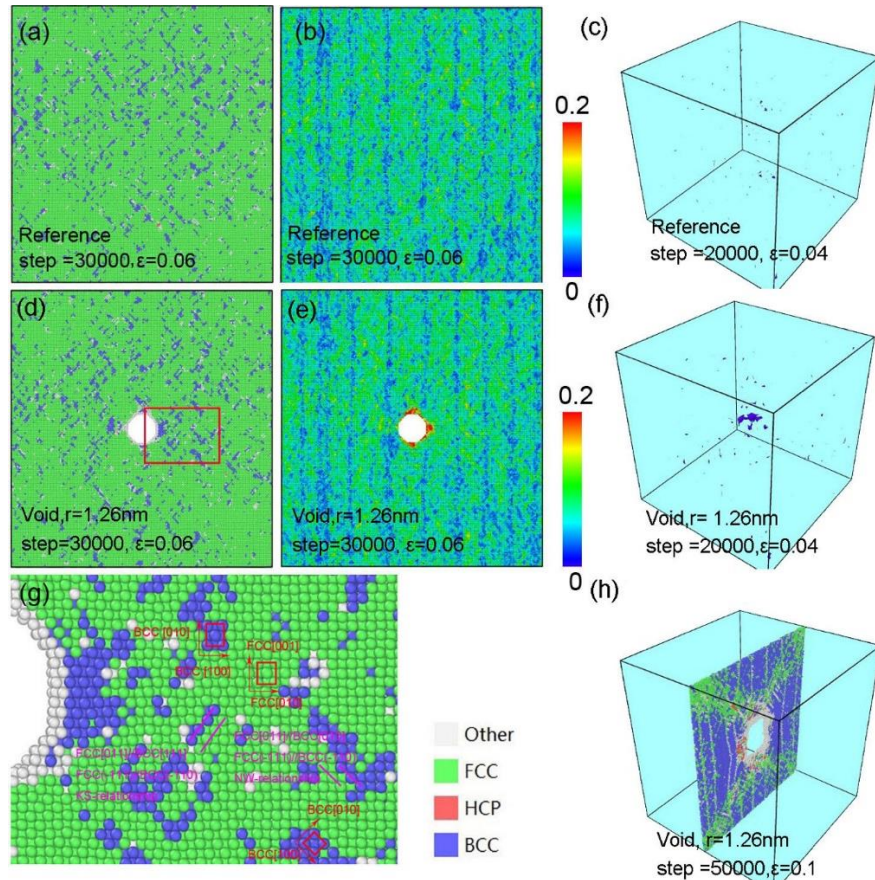


Figure 2: Snapshots of (a) reference simulation phase map, (b) shear strain map, (c) bcc surfaces in simulation box; and small void simulation (d) phase map, (e) shear strain map, (f) bcc surfaces in simulation box, (g) higher resolution view of framed region in (d) showing fcc-bcc orientation relationships, (h) high strain phase map showing void distortion and indicating the position of the 2D maps in taken from the simulation box.

Stress-Induced Transformations – We have also studied stress-induced (i.e., reversible) martensitic transformations to draw contrasts with the strain-induced transformations described previously. This avenue is a collaboration motivated by discussions with Peter Anderson from Ohio State University at the 2019 PI Meeting.

We conducted MD simulations of Ni-50Ti containing various point defects: (a) pristine, no defects; 10^{-4} at% concentration of (b) vacancies, (c) interstitials, and (d) anti-site defects; and (e) vacancy clusters formed by equilibration of 10^{-3} at% concentration of vacancies. Both the forward (B2 to B19') and reverse transformations were simulated. In this system, defects inhibited the transformation relative to the pristine simulation, with the vacancy clusters having the most pronounced effect on slowing the transformation. These results are notably different from our observations on strain-induced transformations, which suggest that cavities (which are not unlike the vacancy clusters here) should enhance the transformability by reducing the critical transformation stress. However, these results indicate that irradiation-like defects may suppress transformability to some degree. We are intrigued by these contrasting behaviors and hope to ascertain a unifying explanation for the role of defects on martensitic transformations at varying SFEs and for strain- versus stress-induced modes.

Future Plans

We intend to make considerable progress toward testing and characterization of the post-irradiation Fe-Mn specimens. We will use our pre-irradiation SEM EBSD grain orientation maps to guide us in conducting nanoindentation, conduct FIB to extract lamella, then finally use TEM/HR-TEM to characterize the deformation microstructures. We will also consider Ni-based alloys with higher SFE, in order to reveal the role of SFE on how deformation mechanisms respond to irradiation-induced defects. We have recently conducted additional ion irradiations of a model Ni alloy, consistent with those done for Fe-xMn specimens, specifically:

1. *Defect-dominated microstructure*: 2 MeV protons, 500°C, fluence 1 dpa
2. *Bubble-dominated microstructure*: 1 MeV He⁺ ions, 500°C, fluence $\sim 10^{16}$ ions/cm²

References

1. A.H. Cottrell, B.A. Bilby, *LX. A mechanism for the growth of deformation twins in crystals*, Philosophical Magazine **42**, 573-581 (1951).
2. N. Hashimoto, S.J. Zinkle, A.F. Rowcliffe, J.P. Robertson, and S. Jitsukawa, *Deformation mechanisms in 316 stainless steel irradiated at 60°C and 330°C*, Journal of Nuclear Materials **283-287**, 528-534 (2000).
3. M. Chmielus, X.X. Zhang, C. Witherspoon, D.C. Dunand, and P. Müllner, *Giant magnetic-field-induced strains in polycrystalline Ni-Mn-Ga foams*, Nature Materials **8**, 863-866 (2009).
4. W.Z. Han, J. Zhang, M.S. Ding, L. Lv, W.H. Wang, G.H. Wu, Z.W. Shan, and J. Li, *Helium nanobubbles enhance superelasticity and retard shear localization in small-volume shape memory alloy*, Nano Letters **17**, 3725-3730 (2017).
5. G. Bonny, N. Castin, and D. Terentyev, *Interatomic potential for studying ageing under irradiation in stainless steels: the FeNiCr model alloy*, Modeling and Simulation in Materials Science & Engineering **21**, 085004 (2013).

Publications

1. C. Yang and J.P. Wharry, *Role of point defects on stress-induced martensitic transformation in NiTi shape memory alloy: a molecular dynamics study*, *Physical Review B* **105**, 144108 (2022).
2. A. Hinojos, D. Hong, L. Feng, C. Yang, J.P. Wharry, X. Gao, N. Li, J. Schaffer, K. Hattar, M.J. Mills, and P.M. Anderson, *Modulating the pseudoelastic response of Nitinol using ion implantation*, *Advanced Materials & Processes* **180**, 49-53 (2022).
3. C. Yang, Y. Pachaury, A. El-Azab, and J.P. Wharry, *Molecular dynamics simulation of vacancy and void effects on strain-induced martensitic transformation in an Fe-50at%Ni concentrated solid solution alloy*, *Scripta Materialia* **209**, 114394 (2022).

Mesoscale Defect Interaction Mechanisms in Structural Alloys

Haixuan Xu, Department of Materials Science and Engineering, The University of Tennessee Knoxville

Keywords: Dislocation bias, Dislocation loop bias, Void swelling, KMC

Research Scope

This project aims to obtain a mesoscale mechanistic understanding of radiation-induced defect interaction in model structural alloys. The conventional understanding of mesoscale defect interaction in structural alloys is incomplete due to practical limitations of available tools to capture processes or phenomena in meso-timescale (nanoseconds to milliseconds or more) as they are too fast for experimental techniques like transmission electron microscopy (TEM) and too slow for conventional atomistic simulations like molecular dynamics (MD) [1]. This also limits our understanding of how microscale defects interact collectively, which leads to potential errors when extrapolating to macroscale phenomena and materials performance. This project investigates mesoscale defect dynamics and eliminates some of the assumptions or approximations in traditional models and simulations using atomistic simulations and the Self-Evolving Atomistic kinetic Monte Carlo (SEAKMC) [2,3]. Particularly this project has two specific aims: (i) Determine bias factors and sink strength of interstitial dislocation loops (especially small $\langle 100 \rangle$ loops) in *bcc* (body-centered cubic) iron and evaluate the corresponding impact on void swelling; (ii) estimate mesoscale collective interaction between multiple dislocations and multiple radiation-induced defects and compare them with the previous estimations based on the single-dislocation, single-obstacle picture. The knowledge gained will provide new insights into void swelling and radiation-induced hardening, which may lead to a useful means of avoiding failure mechanisms such as dislocation channeling. In addition, this project will advance on-the-fly KMC and energy landscape sampling computational capabilities at the mesoscale, which will be widely applicable to other fields of materials science, physics, and chemistry.

Recent Progress

Aim I. We have developed a theoretical framework to determine the bias factors and sink strengths of extended defects using the lifetime of point defects (PDs). Based on experimental observations [4], dominant types of biased sinks, sessile $\langle 100 \rangle$ dislocation loop, perfect straight $1/2\langle 111 \rangle$ screw dislocation, and $1/2\langle 111 \rangle\{110\}$ edge dislocation in *bcc* iron are included. The scheme of the KMC simulation is shown in Figure 1. This way of calculating bias extends the original method based on diffusion flux and can accurately include the complex geometry and stress/strain fields of various sinks. Additionally, the lifetime approach eliminates some of the assumptions made in previous models and allows direct comparison of different sinks under similar assumptions. The KMC model consists of different regions. In the absorption region, the mobile PDs are spontaneously absorbed by the dislocation or dislocation loop. The SEAKMC

package is used to determine the migration energy barriers (MEBs) in the core region. The dipole tensor method [5] is also employed to calculate MEBs outside of the core region, where the core effect and the difference compared with SEAKMC results are negligible. The lifetime of point defects is calculated based on defect trajectories. Following this approach, the underlying mechanism of interaction mechanisms between point defects and dislocations can be established. The capture efficiency, sink strength, and bias factors are obtained at different temperatures and dislocation densities. The bias factors and sink strengths are then used in a mean-field rate theory (MFRT) model to estimate swelling rates, which are then compared with a wide range of experimental results, including both neutron-irradiated and ion-irradiated samples at operationally relevant temperatures and defect density.

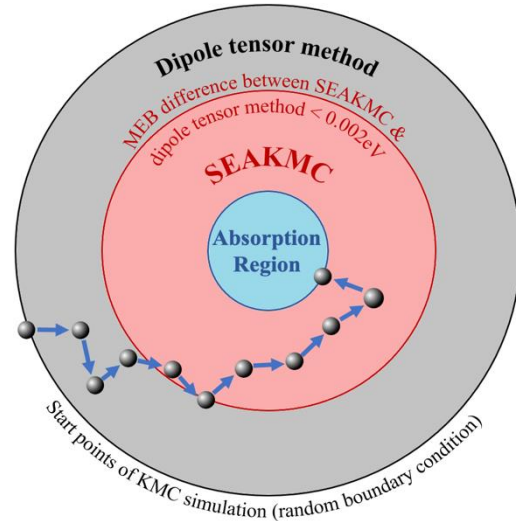


Figure 1. The schematics of the AKMC simulation setup. Random boundary condition is employed for PD diffusion. [1]

The lifetimes of PDs as a function of position to the dislocation core for a screw and an edge dislocation are calculated, as shown in Fig.2. The lifetime near the dislocation core is found highly anisotropic. The three-fold rotational symmetry of the screw dislocation is observed to influence the lifetime of both vacancies and dumbbells.

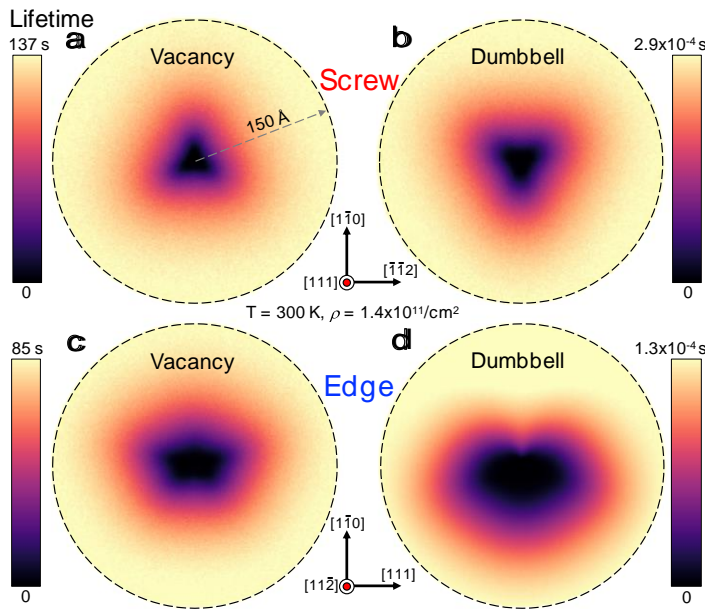


Figure 2. Defect lifetimes near a dislocation in real walks. The simulation box radius is 150 Å, the temperature is 300 K, and the dislocation density is $1.4 \times 10^{11}/\text{cm}^2$. [1]

In comparison, the lifetimes in the edge dislocation cases exhibit mirror symmetry. The gap in time scale is one of the underlying causes for the challenges associated with both experimental and computational investigations of the bias factors, as it would require atomistic resolution at a meso-timescale. For both screw and edge dislocations, the lifetime patterns of a vacancy and a dumbbell are associated with the interaction between the point defects and the strain field of the dislocations. Within the elastic region, the tensile strain favors dumbbells but not the vacancies, and the opposite behavior is observed for the compression part. This generally translates to the change of the MEBs of each type of point

defect, e.g., the MEBs of vacancies are decreased in a compression region and increased in a tensile region compared to the bulk values without strains.

The interaction between mobile PD and the dislocation loop is developed, the scheme of which is shown in Figure 3. There are two types of paths for SIA diffusion near the loop core (Figure 3a). In Path I, a mobile SIA near the habit plane of the loop tends to be absorbed by the edge of the loop following the red arrow. In Path II, the SIA over or below the habit plane of the loop diffuses along the curved arrow paths toward the habit plane region, as in Path I. This transport behavior in Path II is due to a strong repulsive interaction between the loop and the SIA, which is shown by green arrows. Comparatively, there is only one type of path for vacancy transport, wherein dislocation loops tend to attract mobile vacancies following the red arrows (Figure 3b).

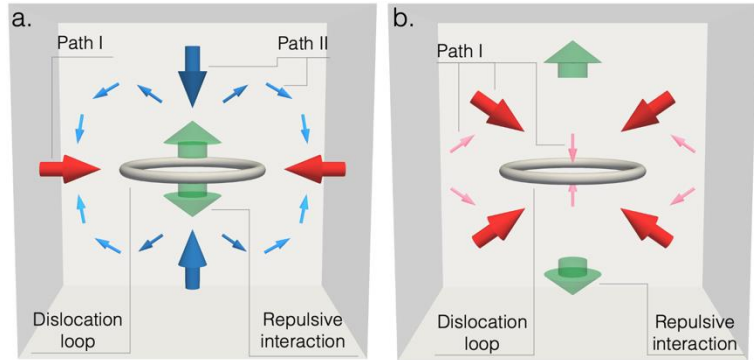


Figure 3. The PD transport mechanism of SIAs (a) and vacancies (b) both provide the paths of PD diffusion and where the repulsive interactions (green arrows) with the loop occur (white toroidal).

The capture efficiencies for a dumbbell in all sinks are higher than those for a vacancy since dumbbells are more sensitive to strain field changes than vacancies. Also, we observe the capture efficiencies for both a vacancy and a dumbbell in an edge dislocation are higher than those in a screw dislocation. Moreover, we obtain the bias factors based on the PD lifetime as a function of dislocation density and the temperature, respectively, for dislocation loops, a screw dislocation, and an edge dislocation. The comparison of bias factors between dislocation loops and straight dislocations is made. The loop bias factors are found to increase with higher loop densities and higher temperatures. On the other hand, the bias factors of both types of straight dislocations decrease with lower dislocation densities and higher temperatures.

We also carry out similar simulations in *fcc* (face-centered cubic) copper. The AKMC approach is employed to calculate the bias and sink strength of stacking fault tetrahedrons (SFTs), interstitial loops, straight dislocations, and voids in *fcc* copper. Similar to previous studies, we calculated the swelling rates at different sink densities and temperatures. Moreover, the role of each type of sink in void swelling is also studied.

Aim II. Our findings reveal that for both screw and edge dislocation cases, due to the presence of following-up dislocations, the obstacle strength of the nanovoid is weakened, and the multiple dislocation-nanovoid interactions are far more complex than the repeated single dislocation-nanovoid interaction. The presence of the following-up dislocation does not alter the interaction mechanism of screw dislocation-nanovoid interactions. However, the nanovoid will facilitate the cross-slip behavior of screw dislocation during the void-dislocation interaction. On the other hand, the interaction between a nanovoid and multiple-edge dislocations takes a different

mechanism from that of the single-edge dislocation and nanovoid interaction. In the multiple edge dislocation and nanovoid interaction, driven by the external stress, edge dislocation can enter the nanovoid before a previous edge dislocation exits the nanovoid. Resulting in an intermediate state in which both dislocations are connected to the nanovoid. In this case, the critical shear stress corresponds to the point when the edge dislocation enters the nanovoid, rather than the previous edge dislocation exiting the nanovoid. It is thereby proved that the interaction between the dislocations and the overlapping of the stress field of multiple dislocations play significant roles in the multi-dislocation nanovoid interactions. The findings for this work provide informative mechanistic inputs to larger length/time scale modeling of the plastic flow localization behavior and facilitate a more comprehensive understanding of the nano-scale interaction between dislocations and irradiation damages.

We also develop an SPS method that considerably accelerates the search for practically meaningful SPs by converting the PES to the scaled normal coordinates (SNCs), together with the dimer method. The developed method is called SNC-dimer. We benchmark the SNC-dimer using the diffusion of point defects in Fe and find that the required number of system force evaluations for an SPS is reduced by at least an order of magnitude. It should be highlighted that the SNCs could also be applied to other SPS methods that fall into the minimum-mode following type, which demonstrates the broad applicability of the developed method.

Future Plans

We plan to systematically determine the bias factors and sink strength of various sinks, including dislocation loops, dislocations, voids, and SFTs in *fcc* Ni and Fe-Ni-Cr. We will examine the similarities and differences between different *fcc* metals, e.g. Cu vs. Ni, and study the underlying cause.

References

1. Bulatov, V., Abraham, F. F., Kubin, L., Devincere, B. & Yip, S. *Connecting atomistic and mesoscale simulations of crystal plasticity*. Nature **391**, 669-672 (1998).
2. Xu, H., Osetsky, Y. N. & Stoller, R. E. *Self-evolving atomistic kinetic Monte Carlo: fundamentals and applications*. Journal of Physics: Condensed Matter **24**, 375402 (2012).
3. Xu, H., Stoller, R. E., Béland, L. K. & Osetsky, Y. N. *Self-evolving atomistic kinetic monte carlo simulations of defects in materials*. Computational Materials Science **100**, 135-143 (2015).
4. Horton, L. L., Bentley, J. & Farrell, K. *A Tem Study of Neutron-Irradiated Iron*. Journal of Nuclear Materials **108**, 222-233 (1982).
5. Carpentier, D., Jourdan, T., Le Bouar, Y. & Marinica, M.-C. *Effect of saddle point anisotropy of point defects on their absorption by dislocations and cavities*. Acta Materialia **136**, 323-334 (2017).

Publications

1. J. Hao, L. Casillas-Trujillo, & H. Xu. *Using lifetime of point defects for dislocation bias in bcc Fe*. Current Opinion in Solid State & Materials Science **26** 101021 (2022).
2. S. Hayakawa, H. Xu, *Saddle point sampling using scaled normal coordinates*, Computational Materials Science **200** 110785, (2021).
3. S. Hayakawa, J. Isaacs, H.R. Medal, H. Xu, *Atomistic model of meso-timescale processes with SEAKMC: A perspective and recent developments*, Computational Materials Science **194** 110390 (2021)
4. J. Chai, S. Jin, H. Xu, G. Lu, *Capture Efficiency and Bias from the defect dynamics near grain boundaries in bcc Fe using mesoscale simulations*, Journal of Materials Science & Technology, **93** 169 (2021)
5. J. Hao, S. Jin, G. Lu, H. Xu, *Migration energy barriers and diffusion anisotropy of point defects on Tungsten surfaces*, Computational Materials Science **184** 109893 (2020)
6. Z. Yu, H. Xu, *From Dislocation loop bias to void swelling in α -iron*, under review.
7. X. Wang, Y. Wang, W Cai, H. Xu, *Discovery of multimechanisms of screw dislocation interaction in bcc iron from open-ended saddle point searches*, under review

Deformation mechanisms of nanotwinned Al and binary Al alloys

Xinghang Zhang¹ and Jian Wang²

¹ School of Materials Engineering, Purdue University, West Lafayette, IN

² Dept. Mechanical Engineering, University of Nebraska, Lincoln, NE

Keywords: Nanotwinned metals, Aluminum alloys, Transmission electron microscopy, *In-situ* micromechanical testing, Magnetron sputtering

Program Scope

The objective of this project is to investigate the microstructural stability and deformation mechanisms of nanotwinned (nt) Al alloy films composed of a high density of **twin boundaries (TBs)** and **stacking faults (SFs)**. To achieve this goal, we tested the following hypotheses:

- 1) ***ITBs and SFs may enable high ductility in nt Al.*** Although there are abundant studies that show CTBs promote work hardening in nt Cu, there are few studies that investigate the influence of ITBs and SFs on tensile ductility of nt Al.
- 2) ***Certain solutes in nt Al alloys may enable substantial increase of strength and plasticity and significantly enhance the mechanical and thermal stability of TBs in nt Al alloys. The addition of certain solutes may enable us to tailor (reduce) the SFE of Al alloy, so that we can introduce greater density of twins/SFs in nt Al alloys, tailor strengthening and deformation mechanisms in nt Al alloys and accomplish increase of strength with little loss in ductility in nt Al alloys.***
- 3) ***Nanotwinned (nt) Al with high stacking fault energy (SFE) may have strengthening mechanisms drastically different from those of nt Cu with low SFE.***

Recent Progress

- 1) **Plastic anisotropy and tension-compression asymmetry in nanotwinned Al-Fe alloys: An *in-situ* micromechanical investigation** (Int. Journal of Plasticity 132, 102760, 2020)

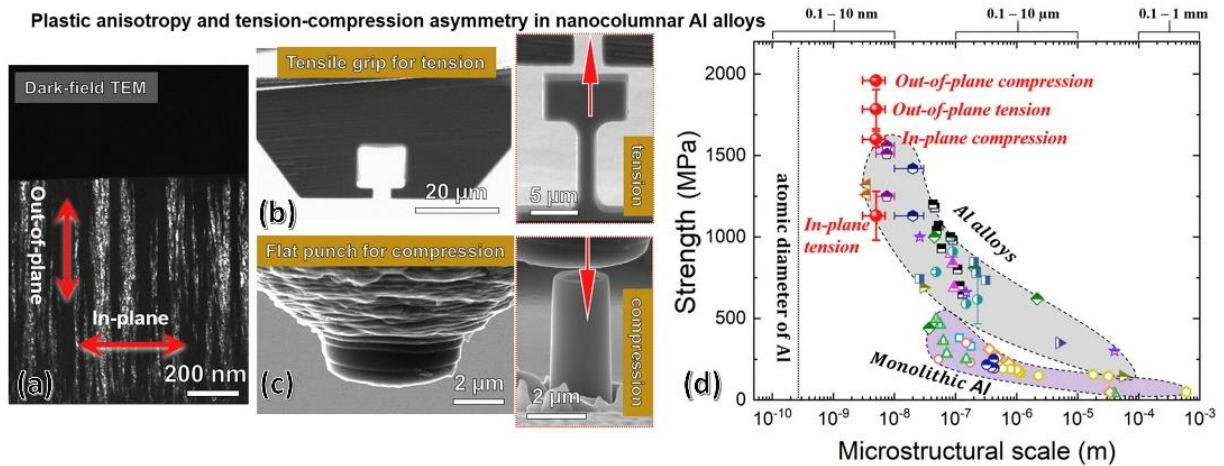


Figure 1. (a) Dark-field (DF) transmission electron microscopy (TEM) image revealing nanometer spaced columnar boundaries with an abundance of incoherent twin boundaries (ITBs). (b) Scanning electron microscopy (SEM) image showing the *in-situ* tensile grip and tensile dogbone fabricated using focused ion beam (FIB). (c) SEM image showing the flat punch and micropillar fabricated using FIB for *in-situ* micropillar compression. (d) Strength vs microstructural scale plot detailing the in-plane and out-of-plane tension-compression asymmetry for nt Al-Fe alloys and comparing it with literature.

In this study, we inspect the mechanical response of columnar nanotwinned Al-Fe alloys

with emphasis on response of grain boundaries to in-situ tension and compression tests along both in-plane and out-of-plane directions inside a scanning electron microscope. Our studies reveal ultra-high out-of-plane tensile and compressive stress, exceeding 1.8 GPa, and an in-plane tensile and compressive stress of 1.1 and 1.6 GPa, respectively. Post-mortem TEM analyses were performed to elucidate the orientation-dependent plastic anisotropy and tension-compression asymmetry in columnar nanotwinned Al–Fe alloys. This study provides an important forward step towards the understanding of deformation mechanisms in high-strength nanotwinned Al alloys and metals with nanocolumnar or non-equiaxed grains.

2) Tribological behaviors of nanotwinned Al alloys (App. Surf. Sci. 600(30), 154108, 2022)

Here we compare the tribological behaviors of ultrafine grained Al, a nanoprecipitate hardened Al 7075 alloy and nanotwinned Al–Ni alloys using the nanoscratch. The nanotwinned Al–Ni alloys exhibit lower coefficient of friction and much greater wear resistance than the Al and Al 7075 alloys. The enhanced wear properties of Al–Ni alloys arise from their high strength and the evolution of nanotwinned microstructures into gradient nanograins during wear. These findings on fundamental wear mechanisms in nanotwinned alloys may advance the discovery of wear-resistant metallic materials.

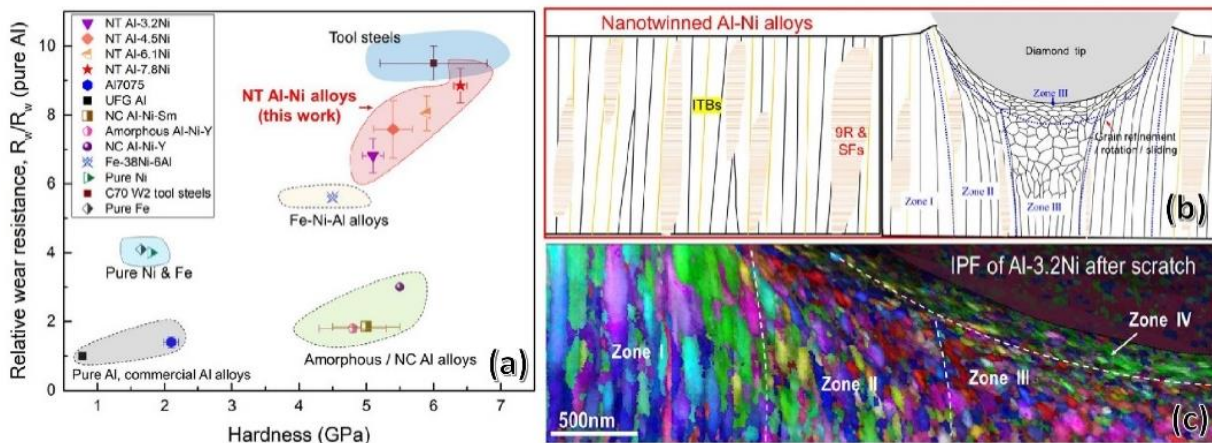


Figure 2. (a) Relative wear resistance plot highlighting the strong tribological response of nt Al-Ni alloys explored through nanoscratch testing. (b) Schematic illustrating the initial nt microstructure and its response to nanoscratch wear testing. (c) Inverse pole figure (IPF) map depicting the textural evolution of the different microstructural zones found after nanoscratch testing in nt Al-3.2Ni.

3) Exploring the deformation behavior of nanotwinned Al–Zr alloy via *in situ* compression (Editor’s pick, J. Appl. Phys. 132, 065104, 2022)

In this paper, we demonstrate the fabrication of supersaturated solid-solution Al–Zr alloys with a high density of growth twins. Incoherent twin boundaries (ITBs) are strong barriers to dislocation motion, while mobile partial dislocations promote plasticity. These deformable nanotwinned Al–Zr alloys reach a flow stress of ~ 1 GPa, as demonstrated using in situ micropillar compression tests. Density functional theory calculations uncover the role Zr solute plays in the formation and deformation of the nanotwinned microstructure. This study features a strategy for incorporating ITBs and 9R phase into Al alloys for simultaneous benefits to strength and deformability.

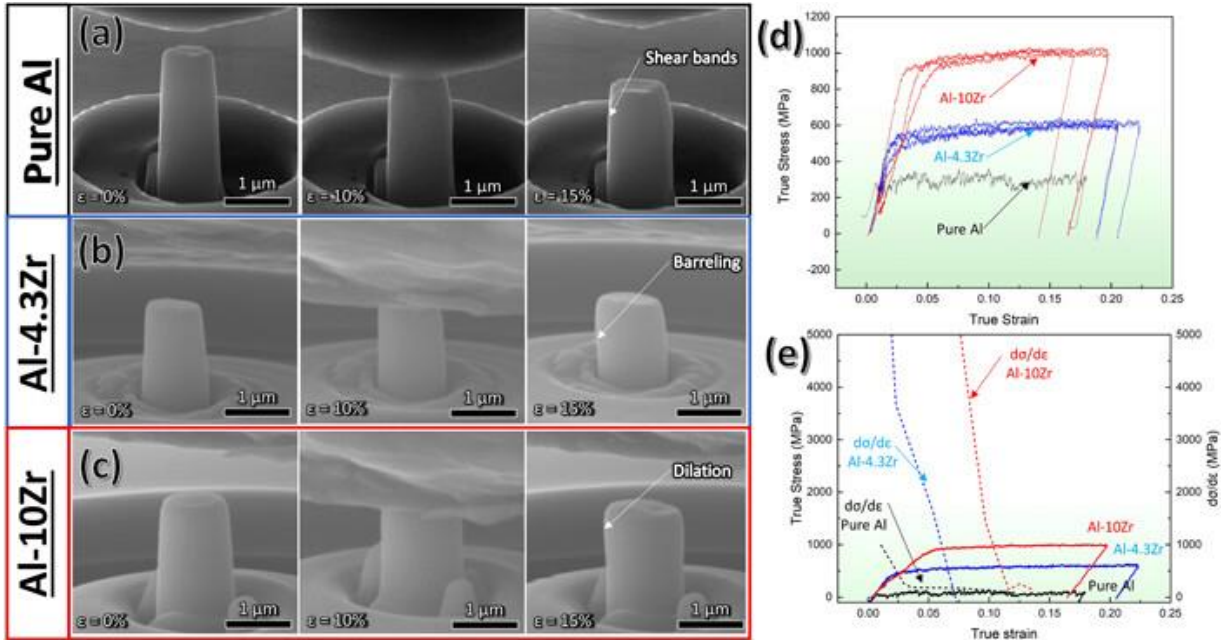


Figure 3. *In-situ* snapshots of micropillar compression tests for (a) pure Al, (b) Al-4.3Zr, and (c) Al-10Zr. These snapshots identify clear shear banding in the pure Al sample in (a), and more uniform deformation represented by (b) barreling and (c) dilation of the pillar top. (d) True stress–strain curves for the three Al–Zr alloys demonstrating increasing flow stress with Zr content. (e) The Al-10Zr sample has a higher work hardening rate than the Al-4.3Zr and Al samples.

4) First-principles calculations for understanding microstructures and mechanical properties of co-sputtered Al alloys (Nanoscale 13, 14987-15001, 2021)

Using first-principles density-functional theory (DFT) calculations, we studied the role of eleven solutes in tailoring kinetics and energetics of adatoms and clusters on Al {111} surface, stable and unstable stacking fault energies, and kinetic energy barriers for the migration of defects. The calculations show that most solutes can effectively refine columnar grain size by decreasing the diffusivity of adatoms and surface clusters. These solutes do not necessarily decrease the stacking fault energy of Al alloys but reduce the formation energy of faulted surface clusters and increase the energy barriers for the recovery of faulted surface clusters. Correspondingly, the formation of SFs is kinetically promoted during sputtering. Furthermore, solutes are segregated into the core of Shockley partial dislocations and play a pinning effect on SFs, SF arrays and twin boundaries, enhancing the thermal stability of these crystal defects. These findings provide insights into the design of high-strength Al alloys for high-temperature applications.

Future Plans

In the next fiscal year, we plan to undertake the following tasks:

- 1) Investigate the role of film texture on twin density and orientation
- 2) Explore the thermal stability of nanotwins in Al and Al alloys
- 3) Explore the solute effect on twin formation in binary Al alloy systems
- 4) Investigate the strain rate sensitivity response nanotwinned Al alloys

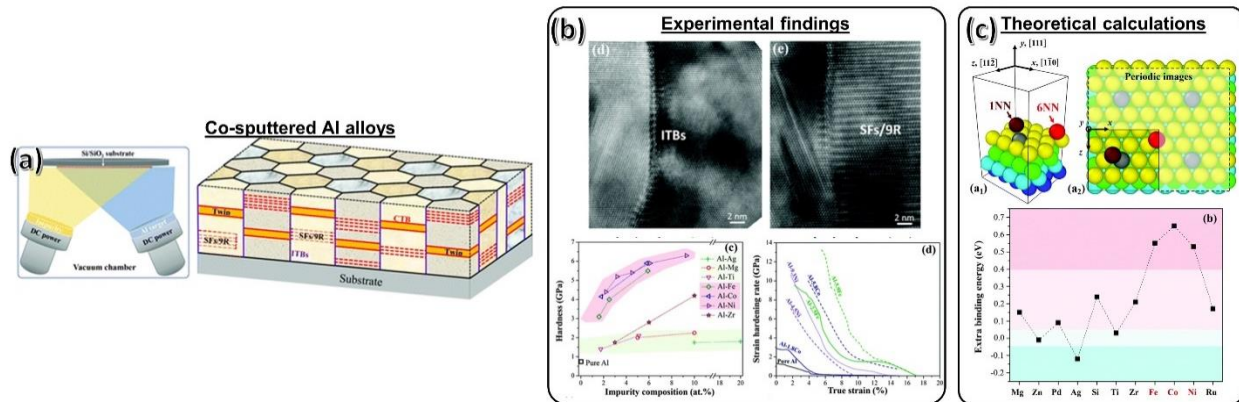


Figure 4. (a) Schematics showing the co-sputtering of Al and Al alloy films with nanotwins. (b) Microscopy of an ITB between two grains and SFs/9R phase in Al-5Mg films. Hardness as a function of solute chemistry and strain hardening rate are plotted. (c) The atomic model for DFT calculations (top left) and top view (top right). The gray atom represents the solute atoms. The red and dark red atoms indicate two possible sites for adatoms. A 2×2 periodic image is used to illustrate the order of nearest-neighbor sites. Extra-binding energy for an Al adatom due to one solute in the first atomic layer (bottom).

Publications-patents through this program, 2020-2022

1. N.A. Richter, Y. Zhang, M. Gong, T. Niu, B. Yang, S. Xue, J. Wang, H. Wang, X. Zhang, Solute synergy induced thermal stability of high-strength nanotwinned Al-Co-Zr alloys, (*Under review*).
2. N.A. Richter, M. Gong, Y. Zhang, T. Niu, B. Yang, J. Wang, H. Wang, X. Zhang, Exploring the deformation behavior of nanotwinned Al-Zr alloy via in situ compression, **Journal of Applied Physics**, 132 (2022) 065104 (*Editor's pick*).
3. Y. Zhang, T. Niu, N.A. Richter, T. Sun, N. Li, H. Wang, X. Zhang, Tribological behaviors of nanotwinned Al alloys, **Applied Surface Science**, 600(30), (2022) 154108.
4. N.A. Richter, Y. Zhang, D. Xie, R. Su, Q. Li, S. Xue, T. Niu, J. Wang, H. Wang, X. Zhang, Microstructural evolution of nanotwinned Al-Zr alloy with significant 9R phase, **Materials Research Letters**, 9(2) (2021) 91.
5. Q. Li, X. Zhang, Y. Zhang, S. Xue, H. Wang, N.A. Richter, Aluminum alloy coatings with high strength and high thermal stability and method of making the same, (U.S. patent no. 17,106,964) (2021)
6. Q. Li, J. Wang, H. Wang, X. Zhang, Achieving strong and stable nanocrystalline Al alloys through compositional design, **Journal of Materials Research**, 37 (2021) 183-207.
7. S. Xue, Y. Zhang, Q. Li, J. Ding, H. Wang, X. Zhang, Tailoring the formation of twins in Al by introducing epitaxial layer interfaces, **Scripta Materialia**, 192 (2021) 1-6.
8. Q. Li, Z. Shang, X. Sun, C. Fan, R. Su, N.A. Richter, Z. Fan, Y. Zhang, S. Xue, H. Wang, X. Zhang, High-strength and tunable plasticity in sputtered Al-Cr alloys with multistage phase transformations, **International Journal of Plasticity**, 137 (2021) 102915.
9. Q. Li, S. Xue, C. Fan, N.A. Richter, Y. Zhang, Y. Chen, H. Wang, X. Zhang, Epitaxial nanotwinned metals and alloys: synthesis-twin structure-property relations, **CrystEngComm**, 23 (2021) 6637-6649 (*review article*).
10. M. Gong, W. Wu, D. Xie, N.A. Richter, Q. Li, Y. Zhang, S. Xue, X. Zhang, J. Wang, First-principles calculations for understanding microstructures and mechanical properties of co-sputtered Al alloys, **Nanoscale**, 13 (2021) 14987-15001.
11. Qiang Li, Dongyue Xie, Zhongxia Shang, Xing Sun, Jaehun Cho, Yifan Zhang, Sichuang Xue, Haiyan Wang, Jian Wang, Xinghang Zhang, Coupled solute effects enable anomalous high-temperature strength and stability in nanotwinned Al alloys, **Acta Materialia** 200, (2020) 378-388.
12. YF Zhang, Qiang Li, M Gong, S Xue, J Ding, Jin Li, J Cho, T Niu, Ruizhe Su, NA Richter, H Wang, J Wang, X Zhang, Deformation behavior and phase transformation of nanotwinned Al/Ti multilayers, **Applied Surface Science** 527 (2020) 146776.
13. Qiang Li, Sichuang Xue, Patrick Price, Xing Sun, Jie Ding, Zhongxia Shang, Zhe Fan, Han Wang, Yifan Zhang, Youxing Chen, Haiyan Wang, Khalid Hattar, Xinghang Zhang, Hierarchical nanotwins in single-crystal-like nickel with high strength and corrosion resistance produced via a hybrid technique, **Nanoscale**, 2020, 12, 1356.
14. Qiang Li, Sichuang Xue, Yifan Zhang, Xing Sun, Haiyan Wang, Xinghang Zhang, Plastic anisotropy and tension-compression asymmetry in nanotwinned Al-Fe alloys: An in-situ micromechanical investigation, **International Journal of Plasticity**, 132 (2020)

Author Index

Aagesen, L.	80	Jiang, C.	80
Abdeljawad, Fadi	142	Jokisaari, A.....	80
Aidhy, Dilpuneet	3	Jossou, E.....	80
Aitkaliyeva, Assel	7	Kacher, Josh	111, 157
Allison, J.	9	Kesler, Michael S.	118
Anderson, Peter M.....	144	Kombaiah, Boopathy	116
Andersson, D.....	76	Krause, Amanda R.....	118
Asle Zaeem, Mohsen	14	Kreller, Cortney.....	234
Asta, Mark	167	Kruska, K.	182
Averback, Robert S.	19	Kumar, A.....	56
Bai, Qingguo	206	Lang, Maik Kurt	123
Bellon, Pascal.....	19	Lee, Seok-Woo.....	127
Beyerlein, Irene J.....	24, 137	Leonard, Aerial D. M.....	131
Boyce, Brad L.	29	Li, Qizhen.....	132
Branicio, Paulo	34	Lou, Jun.....	201
Bucsek, Ashley.....	9, 39	Mara, Nathan A.	137
Burns, James T.	44	Marian, Jaime	225
Cai, Wei	47	Marquis, Emmanuelle	142
Cao, Penghui	52	Martinez, Enrique	142
Capolungo, Laurent	56	Martini, Ashlie.....	106
Cooper, M.	76	Mathaudhu, Suveen	142
Dang, K. Q.	56	McCabe, R. J.	56
de Boer, Maarten P.....	61	Medlin, Doug	29
Demkowicz, Michael J.	64	Miller, M. P.	24
Devaraj, Arun.....	69	Mills, Michael J.	86, 144
Dickey, Elizabeth C.....	61	Minor, Andrew M.....	167
Dillon, S.	76	Mishin, Yuri	149
Dillon, Shen J.	19	Misra, Amit	9, 152
Dingreville, Remi	29	Nelson, Keith A.	192
Dongare, Avinash M.	74	Olszta, M. J.	182
Falk, Michael	225	Padtare, Nitin P.	201
Finkeldei, S.	76	Pierron, Olivier	157
Gan, J.	80	Pilania, Ghanshyam	234
Gao, Huajian	201	Pollock, Tresa M.	24
Gavini, V.....	9	Puchala, B.	9
Ghazisaeydi, Maryam.....	86	Qi, L.	9
Gill, S.....	80	Riedo, Elisa	162
Greer, Julia R.	90	Ritchie, Robert O.....	167
Gu, Wendy	93	Rohrer, Gregory S.....	61
Harley, Joel P.	118	Rosso, K. M.....	182
Hattar, Khalid.....	29	Rupert, Timothy J.	172
Hemker, Kevin J.....	96	Sansoz, Frederic	177
Hodge, Andrea M.....	230	Schneider, A.	80
Homer, Eric R.	101	Schreiber, D. K.....	182
Jacobs, Tevis D. B.....	106	Schuh, Christopher A.....	187, 192
Janish, Matthew.....	234	Sehitoglu, Huseyin.....	39

Shao, Lin.....	196
Sheldon, Brian W.	201
Sieradzki, Karl	206
Sills, Ryan.....	208
Simmons, David S.	212
Sprouster, David J.	230
Srolovitz, David	225
Strachan, Alejandro	216
Sun, C.	80
Sundararaghavan, V.	9
Sushko, M. L.....	182
Szlufarska, Izabela.....	220
Taheri, Mitra	225
Thompson, Gregory B.	101, 239
Thornton, K.....	9
Titus, Michael	216
Tome, C.	56
Tonks, Michael R.	118
Trelewicz, Jason R.	230
Uberuaga, Blas Pedro	234
Van der Ven, A.	9
Wang, C.	182
Wang, Jian	152, 252
Wang, Yongqiang.....	234
Wang, Yunzhi	144
Weinberger, Christopher R.	239
Wharry, Janelle P.	242
White, J.....	76
Xie, Kelvin Y.	64
Xu, Haixuan	247
Zhang, Xinghang	252
Zhang, Y.	80
Zhu, Ting	157

Participant List

Name	Organization	Email
Aagesen, Larry	Idaho National Laboratory	Larry.Aagesen@inl.gov
Abdeljawad, Fadi	Clemson University	fabdelj@clemson.edu
Aidhy, Dilpuneet	Clemson University	daidhy@clemson.edu
Aitkaliyeva, Assel	University of Florida	aitkaliyeva@mse.ufl.edu
Allison, John	University of Michigan	johnea@umich.edu
Anderson, Peter	The Ohio State University	anderson.1@osu.edu
Arul Kumar, Mariyappan	Los Alamos National Laboratory	marulkr@lanl.gov
Asle Zaeem, Mohsen	Colorado School of Mines	zaeem@mines.edu
Asta, Mark	Lawrence Berkeley National Laboratory	mdasta@lbl.gov
Averback, Robert	University of Illinois, Urbana-Champaign	averback@illinois.edu
Bai, Qingguo	Arizona State University	qingguo.bai@asu.edu
Bamney, Darshan	LANL (Capolungo Postdoc)	bamney@lanl.gov
Banerjee, Arunima	Johns Hopkins University	abaner11@jhu.edu
Barrios, Alejandro	Sandia National Laboratories	ajbarri@sandia.gov
Bellon, Pascal	University of Illinois, Urbana-Champaign	bellon@illinois.edu
Beyerlein, Irene	University of California, Santa Barbara	beyerlein@ucsb.edu
Bouobda Moladje, Gabriel Frank	University of Illinois, Urbana-Champaign	gfb@illinois.edu
Boyce, Brad	Sandia National Laboratories	blboyce@sandia.gov
Branicio, Paulo	University of Southern California	brancio@usc.edu
Bucsek, Ashley	University of Michigan	abucsek@umich.edu
Burns, James	University of Virginia	jtb5r@virginia.edu
Cai, Wei	Stanford University	caiwei@stanford.edu
Cao, Penghui	University of California, Irvine	caoph@uci.edu
Capolungo, Laurent	Los Alamos National Laboratory	laurent@lanl.gov
Chen, Wen-Yu	Carnegie Mellon University	wenyuche@andrew.cmu.edu
Cheng, Justin	University of Minnesota, Twin Cities	cheng316@umn.edu
Chesser, Ian	George Mason University	ichesser@gmu.edu
Dang, Khanh	Los Alamos National Laboratory	kqdang@lanl.gov
Das, Sourav	University of Illinois, Urbana-Champaign	sourav2@illinois.edu
Daza, Lina	Georgia Institute of Technology	ldaza6@gatech.edu
de Boer, Maarten	Carnegie Mellon University	mpdebo@andrew.cmu.edu
De Leo, Mauricio	University of Minnesota	trevi083@umn.edu

Demkowicz, Michael	Texas A&M University	demkowicz@tamu.edu
Devaraj, Arun	Pacific Northwest National Laboratory	arun.devaraj@pnnl.gov
Dillon, Shen	University of California, Irvine	sdillon1@uci.edu
Ding, Ruikang	University of Pittsburgh	RUD12@pitt.edu
Ding, Kunqing	Georgia Institute of Technology	kding40@gatech.edu
Dingre, Remi	Sandia National Laboratories	rdingre@sandia.gov
Dongare, Avinash	University of Connecticut	dongare@uconn.edu
Dorman, James	DOE BES	james.dorman@science.doe.gov
Egbu, James	U.S. Department of Energy	james.egbu@hq.doe.gov
Finkeldei, Sarah	University of California, Irvine	sfinkeld@uci.edu
Gan, Jian	Idaho National Laboratory	Jian.Gan@inl.gov
Gavvalapalli, Mani	U.S. Department of Energy	nagamani.gavvalapalli@hq.doe.gov
Ghazisaeidi, Maryam	The Ohio State University	ghazisaeidi.1@osu.edu
Gill, Simerjeet	Brookhaven National Laboratory	gills@bnl.gov
Greer, Julia	Caltech	jrgreer@caltech.edu
Gu, Wendy	Stanford University	xwgu@stanford.edu
Hattar, Khalid	Sandia National Laboratories	khattar@sandia.gov
He, Mo-Rigen	Johns Hopkins University	mrigen1@jhu.edu
Hemker, Kevin	Johns Hopkins University	hemker@jhu.edu
Hessong, Esther	University of California, Irvine	ehessong@uci.edu
Homer, Eric	Brigham Young University	eric.homer@byu.edu
Hu, Chongze	Sandia National Laboratories	chu@sandia.gov
Islam, Tariq	The University of Alabama	mislam37@crimson.ua.edu
Jacobs, Tevis	University of Pittsburgh	tjacobs@pitt.edu
Jiang, Chao	Idaho National Laboratory	chao.jiang@inl.gov
Jossou, Ericmoore	Brookhaven National Laboratory	ejossou@bnl.gov
Kacher, Josh	Georgia Institute of Technology	josh.kacher@mse.gatech.edu
Kannan, Aadhithyan	University of Connecticut	aadhithyan.kannan@uconn.edu
Kawak, Pierre	University of South Florida	kawak@usf.edu
Khafizov, Marat	The Ohio State University	khafizov.1@osu.edu
Kian, Cyrus	U.S. Department of Energy	kourosh.kian@hq.doe.gov
Kim, Jai-woh	U.S. Department of Energy	jai-woh.kim@hq.doe.gov
Kombaiyah, Boopathy	Idaho National Laboratory	boopathy.kombaiyah@inl.gov
Krause, Amanda	Carnegie Mellon University	krause@cmu.edu

Kreller, Cortney	Los Alamos National Laboratory	ckreller@lanl.gov
Kruska, Karen	Pacific Northwest National Laboratory	karen.kruska@pnnl.gov
Lee, Seok-Woo	University of Connecticut	seok-woo.lee@uconn.edu
Li, Qizhen	Washington State University	qizhen.li@wsu.edu
Linton, Nathan	Clemson University	nlinton@clemson.edu
Liu, Xing	Georgia Institute of Technology	xing.liu@me.gatech.edu
Lopez Pernia, Cristina	Brown University	cristina_lopez_ernia@brown.edu
Lou, Jun	Rice University	jlou@rice.edu
Mara, Nate	University of Minnesota, Twin Cities	mara@umn.edu
Marquis, Emmanuelle	University of Michigan	emarq@umich.edu
Martinez Saez, Enrique	Clemson University	enrique@clemson.edu
Martini, Ashlie	University of California, Merced	amartini@ucmerced.edu
Mathaudhu, Suveen	Colorado School of Mines	smathaudhu@mines.edu
Medlin, Douglas	Sandia National Laboratories	dlmedli@sandia.gov
Miller, Matt	Cornell University	mpm4@cornell.edu
Mills, Michael	The Ohio State University	mills.108@osu.edu
Minor, Andrew	UCB and LBNL	aminor@lbl.gov
Mishin, Yuri	George Mason University	ymishin@gmu.edu
Misra, Amit	University of Michigan	amitmis@umich.edu
Murphy-Leonard, Aerial	The Ohio State University	leonard.649@osu.edu
Nelson, Keith	Massachusetts Institute of Technology	kanelson@mit.edu
Paul, Debargha	Purdue University	paul153@purdue.edu
Pierron, Olivier	Georgia Institute of Technology	olivier.pierron@me.gatech.edu
Pollock, Tresa	University of California, Santa Barbara	pollock@engineering.ucsb.edu
Puchala, Brian	University of Michigan	bpuchala@umich.edu
Qi, Liang	University of Michigan	qiliang@umich.edu
Rabin, Aaron	University of Florida	Aaron.rabin@ufl.edu
Richter, Nicholas	Purdue University	richtern@purdue.edu
Riedo, Elisa	New York University	elisa.riedo@nyu.edu
Ritchie, Robert	Lawrence Berkeley National Laboratory	roritchie@lbl.gov
Robinson, Jarod	The University of Alabama	jrobinson6@crimson.ua.edu
Rohrer, Gregory	Carnegie Mellon University	rohrer@cmu.edu
Rosso, Kevin	Pacific Northwest National Laboratory	kevin.rosso@pnnl.gov
Rupert, Tim	University of California, Irvine	trupert@uci.edu

Sansoz, Frederic	The University of Vermont	frederic.sansoz@uvm.edu
Schrecengost, Robert	DOE FECM	robert.schrecengost@hq.doe.gov
Schreiber, Dan	Pacific Northwest National Laboratory	daniel.schreiber@pnnl.gov
Schuh, Christopher	Massachusetts Institute of Technology	schuh@mit.edu
Sehitoglu, Huseyin	University of Illinois, Urbana	huseyin@illinois.edu
Selim, Farida	Bowling Green State University	faselim@bgsu.edu
Shadle, Dalton	Cornell University	djs522@cornell.edu
Shao, Lin	Texas A&M University	lshao@tamu.edu
Sheldon, Brian	Brown University	brian_sheldon@brown.edu
Sheng, Xuanyu	Purdue University	sheng18@purdue.edu
Sheu, Emmeline	Texas A&M University	emmelinesheu@tamu.edu
Sieradzki, Karl	Arizona State University	karl.sieradzki@asu.edu
Sills, Ryan	Rutgers University	Ryan.sills@rutgers.edu
Simmons, David	University of South Florida	dssimmons@usf.edu
Simonnin, Pauline	Pacific Northwest National Laboratory	pauline.simonnin@pnnl.gov
Stangebye, Sandra	Georgia Institute of Technology	sstangebye3@gatech.edu
Strachan, Alejandro	Purdue University	strachan@purdue.edu
Sun, Cheng	Idaho National Laboratory	cheng.sun@inl.gov
Sundararaghavan, Veera	University of Michigan	veeras@umich.edu
Sushko, Peter	Pacific Northwest National Laboratory	peter.sushko@pnnl.gov
Szlufarska, Izabela	University of Wisconsin, Madison	szlufarska@wisc.edu
Taheri, Mitra	Johns Hopkins University	mtaheri4@jhu.edu
Thomas, Sam	U.S. DOE	sotirios.thomas@hq.doe.gov
Thomas, Marie	Colorado School of Mines	mthomas1@mines.edu
Thompson, Gregory	The University of Alabama	gthompson@eng.ua.edu
Thornton, Katsuyo	University of Michigan	kthorn@umich.edu
Uberuaga, Blas	Los Alamos National Laboratory	blas@lanl.gov
Verma, Akarsh	Brigham Young University	akarshverma007@gmail.com
Vetrano, John	DOE BES	john.vetrano@science.doe.gov
Wagih, Malik	Massachusetts Institute of Technology	mwagih@mit.edu
Walsh, Flynn	Lawrence Berkeley National Laboratory	fwalsh@lbl.gov
Wang, Jian	University of Nebraska, Lincoln	jianwang@unl.edu
Wang, Yifan	Stanford University	yfwang09@stanford.edu
Wang, Yunzhi	The Ohio State University	wang.363@osu.edu

Weinberger, Christopher	Colorado State University	Chris.Weinberger@colostate.edu
Wendt, Anna	Department of Energy	anna.wendt@hq.doe.gov
Wharry, Janelle	Purdue University	jwharry@purdue.edu
White, Josh	Los Alamos National Laboratory	jtwhite@lanl.gov
Wilk, Philip	DOE BES	philip.wilk@science.doe.gov
Wixom, Ryan	Sandia National Laboratories	rrwixom@sandia.gov
Xiao, Shuyang	University of Connecticut	Shuyang.xiao@uconn.edu
Xie, Kelvin	Texas A&M University	kelvin_xie@tamu.edu
Xu, Haixuan	University of Tennessee, Knoxville	xhx@utk.edu
Xu, Ke	Purdue University	xu1522@purdue.edu
Yadav, Digvijay Rajendra	Texas A&M University	digvijay.materials@tamu.edu
Yaghoobi, Mohammadreza	University of Michigan, Ann Arbor	yaghoobi@umich.edu
Yano, Kayla	Pacific Northwest National Laboratory	kayla.yano@pnnl.gov
Yuan, Suyue	University of Southern California	suyueyua@usc.edu
Zhang, Xinghang	Purdue University	xzhang98@purdue.edu
Zhang, Yongfeng	University of Wisconsin, Madison	yzhang2446@wisc.edu
Zhang, Boyu	Rice University	bz19@rice.edu
Zhu, Ting	Georgia Institute of Technology	ting.zhu@me.gatech.edu